Photophysical Properties of Single Photon Emitters in Hexagonal Boron Nitride

Prince Khatri

Supervisor: Dr. Isaac J. Luxmoore and Prof. Geoffrey Nash

College of Engineering, Mathematics, and Physical Sciences
University of Exeter

This dissertation is submitted for the degree of
Doctor of Philosophy in Engineering

December 2021

Photophysical Properties of Single Photon Emitters in Hexagonal Boron Nitride

Submitted by Prince Khatri to the University of Exeter as a thesis for the degree of
Doctor of Philosophy in Engineering
In September 2021

I certify that all material in this thesis which is not my own work has been identified and that no material has previously been submitted and approved for the award of a degree by this or any other University.

(Signature) .....

Prince Khatri

September 2021

I would like to dedicate this thesis to my loving parents and my sister Setu for always supporting me …

Declaration

I hereby declare that except where specific reference is made to the work of others, the contents of this dissertation are original and have not been submitted in whole or in part for consideration for any other degree or qualification in this, or any other university. This dissertation is my own work and contains nothing which is the outcome of work done in collaboration with others, except as specified in the text and Acknowledgements.

Prince Khatri
December 2021

Acknowledgements

My most sincere gratitude goes to my supervisor, Dr. Isaac Luxmoore for guidance and support throughout the full duration of my PhD. Thank you very much for always helping me and giving time for meetings whenever I needed. I can't thank you enough for all the work you helped me with whether it was answering my questions, assisting in experiments, reviewing my drafts and having a chat over coffee, asking how my weekend was. The support I received from you was a lot more than I expected. I am ever so grateful for the support you provided me with during Covid times and making me feel productive while I was working from home. I would also like to thank my colleagues Iago, Ralph, Simon and Valentin for helping me in the cleanroom, simulations and writing papers.

Next, I would like to thank my second supervisor, Prof. Geoff Nash for supporting me, including asking if everything is going well and being there for any help I needed. I would like to thank Geoff and Dr. Ana Neves for conducting my yearly viva and providing very helpful feedback.

I would like to thank Dr. Andrew Ramsay, Hitachi Cambridge Lab, who provided fantastic feedback for all of the projects. All this work could not have been possible without his critical reviews and guidance in theory and simulations.

Outside research, I would like to thank all the members of the Out Of Doors Society, Alan, Olivia, Jake, William, Bill, Fred, Chris, Kate, Alex and many others who made my Saturdays ever so cheerful with all the fun, walks and socials. I would also like to thank my friends, Jayesh, Kishan and Prarthana for providing me help with living in Exeter, chats and emotional support.

Finally, I would like to thank my girlfriend Olivia and her family for making me feel like home in a different country and helping with a lovely stay at their home during lockdown.

Abstract

The development of photonic based quantum technologies such as quantum encryption and quantum computing is mainly restrained by the quality of single photon emitter. Effects like phonon interaction, emission purity, stability and decoherence are the major issues. So far quantum dots are leading the race in terms of indistinguishability, emission purity and stability but low collection efficiency and operation at cryogenic/low temperature are major roadblocks. Hexagonal-Boron Nitride (hBN) is a 2D material with stable single photon emission even at 800 °C. hBN is an emerging material, attracting interest from a wider research community but information about the identity of the emitting defects is very limited. The aim of this work is to use the experimental techniques to probe the emitter and comment on the possible origins of the emission.

To understand the effects of temperature and phonon interaction with the emitter, we analysed the optical and acoustic sidebands to deduce the dimensionality of the phonon bath. We extracted the coupling parameters and other qualitative results such as number of layers in the sample and coupling mechanisms of different phonon bands. During this work we observed that some emitters suffer with stability issues, where they shift between dark and bright states. A detailed experimental study with simulations was conducted to understand the dark and bright states of the emitter and action of a repump laser in keeping the emitter bright. We also observed a repump threshold of 2.2 - 2.6 eV and a new energy level in absorption spectra. These results pointed to a carbon impurity or boron vacancy defect. To get an insight into the photophysical properties, stimulated emission depletion (STED) spectroscopy was performed to probe the emitter's ground vibrational levels. This technique is found to be greatly important to obtain map of phonon sidebands without stray emission from nearby defects and impurities. We also found that upon excitation the the emitter show lattice distortion, quantified by a shift in 200 meV peak and the emitter could be a negatively charged carbon defect. Next, building on the understanding from previous work, a practical application of STED, high resolution gated continuous wave (CW) STED microscopy has been demonstrated. We obtained a high resolution of $\sim$ 50 nm and successfully resolved two hBN emitters separated by a distance smaller than the diffraction limit.

Table of contents

List of figures

List of tables

Nomenclature

Acronyms / Abbreviations

AFM Atomic force microscopy

Al_2O_3 Aluminium oxide

APD Avalanche photodiode

ASB Acoustic phonon sideband

ATOF Acousto-optic tuneable filter

$B_3H_6N_3$ borazine

BH_6N Ammonia borane

BN Boron nitride

BNNS Boron nitride nanosheet

BPF Band pass filter

BS Beam splitter

CCD Charge-coupleddevice

CdSe Cadmium selenide

CMOS Complementary metal–oxide–semiconductor

Cs Caesium

CVD Chemical vapour deposition

CW Continuous wave

DBS dichoric beamsplitter

DFT Density function theory

DPSS Diode pumped solid state

EDX Energy dispersive X-ray

EM Electron microscopy

FT Fourier-transform

FWHM Full width half maximum

GaAs Gallium arsenide

GaInP Indium gallium phosphide

hBN hexagonal-Boron nitride

HBT Hanbury Brown and Twiss

HTHP High temperature high pressure

InAs Indium arsenide

inf infinity

InP Indium Phosphide

IRF Instrument response function

LaF_3 Lanthanum trifluoride

LA Longitudinal acoustic

LO Longitudinal optical

LP Linear polarizer

MBE molecularbeam epitaxy

MMF Multi-mode fiber

Mo Molybdenum

MOT Magneto-optical trap

MOVPE Metalorganic vapour-phase epitaxy

NV Nitrogen vacancy

ODMR Optically detected magnetic resonance

OPSB Optical phonon sideband

PLE Photo luminescence excitation

PL Photoluminescence

PMMA Poly(methyl methacrylate)

PMT Photomultiplier tube

PSB Phonon sideband

QD Quantum dot

QED quantum electrodynamic

QIP Quantum information processing

QKD Quantum key distribution

Rb Rubidium

SCL Supecontinuum laser

SEM Scanning electron microscopy

SiO_2 Silicon dioxide

Si Silicon

SiV Continuous wave

SMF Single mode fiber

SPDC Spontaneous parametric down-conversion

SPE Single photon emitter

STED Stimulated emission depletion

STIRAP Stimulated Raman adiabatic passage

TCSPC Time-correlated single photon counting electronics

TEM Transmission electron microscopy

TMDC Transition metal di-chalcogen

TO Transverse optical

UV Ultra violet

WSe_2 Tungsten diselenide

YAG Yttrium aluminium garnet

YOS Yttrium orthosilicate

EELS Electron energy loss spectroscopy

ZnO Zinc oxide

SiC Silicon carbide

Zn Zinc

ZPL Zero phonon line

Chapter 1

Introduction

1.1 Quantum photonics Technology

At the beginning of 21^{st} century a new technology race began. This time the race is not for more powerful computing, smaller transistors, efficient programming or smaller size but it is for a completely new type of computer called quantum computer, where only 300 qubits can perform more operations than the known number of atoms in the universe [1]. Tech giants such as Google, IBM, Microsoft and Intel are all trying to build the first quantum computer to gain the economic and strategic advantage. Google has recently demonstrated quantum supremacy with their 54 qubit Sycamore chip. In their latest Google Input/Output (I/O) event in May 2021, Google unveiled their quantum computing research efforts and the future plan for the technology [2]. This is a huge feat for quantum computing research field as big companies are understanding that the classical computing is on its limits now and the only way forward is quantum. Moreover, the classical computers are struggling to cater for technologies like artificial intelligence (AI), secure communication and complex simulation for biology and physics.

Here, we focus more on the application of quantum technology for secure communication- Quantum key distribution (QKD). A quantum computer is also capable of decoding any classical encryption into seconds so it is very important to first have QKD in practice so all the information can be secure once commercial quantum computers are available. Fortunately, QKD is a more mature technology with commercial availability [3] and successful long distance demonstrations [4]. The most secure and efficient approach for QKD is to use a single photon emitter (SPE), which generates only one photon at a time and information such a polarization can be encoded onto that photon. Ideally all the communication such as credit card transactions, data sharing and messaging should be quantum encrypted but

the cost of QKD is the main hurdle and especially a cheap and versatile SPE. QKD and its implementation is discussed in details in the background chapter of this thesis

In this thesis, we focus on single photon emitting properties of emitters in hexagonal-Boron Nitride (hBN), an emerging 2D material which shows ultra bright single photon emission [5, 6] even at temperature of 800 °C [7]. It has a variety of properties like low density(2.27 g/cm^3) [8], exceptional electric insulation with thermal conductivity of $\sim 300-200\mathrm{Wm}^{-1}\mathrm{K}^{-1}$ [9] and is used in high temperature electronics. The emitters show a wide spectral range from UV to near infrared [10–14]. hBN is very inexpensive and being a 2D material it can be incorporated to chip style, mass production devices. Properties of hBN are discussed in details in the background chapter.

1.2 Objectives of the Thesis

The main goal of this thesis is to understand the photophysical properties of emitters in hBN. We did a variety of experiments to comment on the origins of the emitter, effects of phonons and new phenomena such as optical gating. Currently, we have a plethora of density functional theory (DFT) calculations [15–17] for various SPE candidates in hBN but a few experimental studies to link them with the observed emitters [18]. We focused on using techniques such as photoluminescence excitation (PLE) and stimulated emission depletion (STED) to gain an insight into the absorption and emission processes. These studies are required to engineer hBN based quantum devices where emitter's spectral properties, location and response to temperature and stress/strain are of paramount importance to their scalability and integration. The results can help in designing and manufacturing chip based robust QKD devices. We also used computational methods to simulate the experiment and extract different time constants and rates involved during a cycle of excitation and emission.

In particular, the following research challenges are addressed:

- Developing theories and computational models to understand the emission processes and phonon coupling with the emitter.
- On demand optical switching of emitters based on excitation laser energy and reporting new absorption energy levels.
- Identifying the origins of the emitter based on optical signatures in excitation and stimulated emission.

- Demonstrating super high resolution imaging capability and opening new frontiers in bio-medical applications.

1.3 Thesis outline

Chapter 2: In the second chapter, a detailed nano-photonics background is given, necessary to understand this thesis. This chapter also includes an overview of different SPEs and a discussion of their advantages and disadvantages. A brief introduction of the physical properties of hBN and its applications are discussed along with the SPE properties. Finally, QKD and quantum computing are introduced as the ultimate application of hBN SPEs.

Chapter 3: An independent boson model, typically used for quantum dots is used in this chapter to understand the phonon coupling mechanisms with the defect. The acoustic and optical sidebands are analysed to address the dimensionality of the phonon bath. It was observed that longitudinal optical phonon band peak can give insight into the coupling mechanisms and number of layers in the sample.

Chapter 4: All hBN emitters are not same and each of them respond differently depending on the excitation energy. In this chapter we present the optical switching of hBN emitters between bright and dark states. A detailed multilevel theoretical model addresses the repump energy threshold for various defects along with time correlated optical experiments.

Chapter 5: In this chapter a detailed study about the origins of the emitter is presented using a new spectroscopic technique called STED. This is complementary to PLE for mapping the vibronic modes in the ground state without interference from nearby emitters. With STED it is possible to distinguish the noise peaks in the spectrum that are not from the emitter under observation and vibronic levels of the ground and excited state of the emitter can be mapped precisely. Adding to the understanding of negatively charged defects, it was observed that when defect excites, it undergoes a lattice distortion of 2.6 %.

Chapter 6: After detailed study of the effects of STED on hBN emitters, In this chapter an important real world application in the field of bio-imaging is presented. We demonstrated that hBN emitters can be used as fluorophores and a high resolution of $\sim$ 50 nm can be achieved using STED microscopy assisted with gated technique. We resolved two emitters separated by 250 nm, which is less than the diffraction limit. We found that average STED cross section of hBN emitters compare favorably with color centers in diamond and organic dye molecules.

Chapter 7: In this chapter, the conclusions of the thesis and suggestions for further related work are discussed.

1.4 Journal Papers

- Phonon Sidebands of Color Centers in Hexagonal Boron Nitride.

  Prince Khatri, Isaac J. Luxmoore and Andrew J. Ramsay, Physical Review B 2019 100 (12), 125305- 125312, DOI: 10.1103/PhysRevB.100.125305.

- Optical Gating of Photoluminescence from Color Centers in Hexagonal Boron Nitride.

  Prince Khatri, Andrew J. Ramsay, Ralph Nicholas Edward Malein, Harold M. H. Chong, and Isaac J. Luxmoore, Nano Letters 2020 20 (6), 4256-4263, DOI: 10.1021/acs.nanolett.0c00751.

- Stimulated Emission Depletion Spectroscopy of Color Centres in Hexagonal Boron Nitride.

  Ralph N. E. Malein, **Prince Khatri**, Andrew J. Ramsay and Isaac J. Luxmoore, ACS Photonics 2021 8(4), 1007–1012, DOI: 10.1021/acsphotonics.0c01917.

- Stimulated Emission Depletion Microscopy of Color Centres in Hexagonal Boron Nitride.

  Prince Khatri, Ralph N. E. Malein, Andrew J. Ramsay and Isaac J. Luxmoore, ACS Photonics 2021 8(7), 2081–2087, DOI: 10.1021/acsphotonics.1c00423.

References

[1] Charles Q. Choi. How many qubits are needed for quantum supremacy? https://spectrum.ieee.org/qubit-supremacy, Jun 2021.

[2] Google. Google i/o 2021. Available at https://events.google.com/io/?lng=en, August 2021.

[3] Anton Pljonkin and Pradeep Kumar Singh. The review of the commercial quantum key distribution system. In *2018 Fifth International Conference on Parallel, Distributed and Grid Computing (PDGC)*. IEEE, December 2018.

[4] Sheng-Kai Liao, Wen-Qi Cai, Wei-Yue Liu, Liang Zhang, Yang Li, Ji-Gang Ren, Juan Yin, Qi Shen, Yuan Cao, Zheng-Ping Li, Feng-Zhi Li, Xia-Wei Chen, Li-Hua Sun, Jian-Jun Jia, Jin-Cai Wu, Xiao-Jun Jiang, Jian-Feng Wang, Yong-Mei Huang, Qiang Wang, Yi-Lin Zhou, Lei Deng, Tao Xi, Lu Ma, Tai Hu, Qiang Zhang, Yu-Ao Chen, Nai-Le Liu, Xiang-Bin Wang, Zhen-Cai Zhu, Chao-Yang Lu, Rong Shu, Cheng-Zhi Peng, Jian-Yu Wang, and Jian-Wei Pan. Satellite-to-ground quantum key distribution. *Nature*, 549(7670):43–47, August 2017.

[5] Toan Trong Tran, Kerem Bray, Michael J. Ford, Milos Toth, and Igor Aharonovich. Quantum emission from hexagonal boron nitride monolayers. *Nature Nanotechnology*, 11(1):37–41, October 2015.

[6] L. J. Martínez, T. Pelini, V. Waselowski, J. R. Maze, B. Gil, G. Cassabois, and V. Jacques. Efficient single photon emission from a high-purity hexagonal boron nitride crystal. *Physical Review B*, 94(12), September 2016.

[7] Mehran Kianinia, Blake Regan, Sherif Abdulkader Tawfik, Toan Trong Tran, Michael J. Ford, Igor Aharonovich, and Milos Toth. Robust solid-state quantum system operating at 800 k. *ACS Photonics*, 4(4):768–773, March 2017.

[8] Haotian Yang, Hailiang Fang, Hui Yu, Yongjun Chen, Lianjun Wang, Wan Jiang, Yiquan Wu, and Jianlin Li. Low temperature self-densification of high strength bulk hexagonal boron nitride. *Nature Communications*, 10(1), February 2019.

[9] Cem Sevik, Alper Kinaci, Justin B. Haskins, and Tahir Çağın. Characterization of thermal transport in low-dimensional boron nitride nanostructures. *Physical Review B*, 84(8), August 2011.

[10] Toan Trong Tran, Christopher Elbadawi, Daniel Totonjian, Charlene J. Lobo, Gabriele Grosso, Hyowon Moon, Dirk R. Englund, Michael J. Ford, Igor Aharonovich, and Milos Toth. Robust multicolor single photon emission from point defects in hexagonal boron nitride. *ACS Nano*, 10(8):7331–7338, July 2016.

[11] T. Q. P. Vuong, G. Cassabois, P. Valvin, A. Ouerghi, Y. Chassagneux, C. Voisin, and B. Gil. Phonon-photon mapping in a color center in hexagonal boron nitride. *Physical Review Letters*, 117(9), August 2016.

[12] Romain Bourrellier, Sophie Meuret, Anna Tararan, Odile Stéphan, Mathieu Kociak, Luiz H. G. Tizei, and Alberto Zobelli. Bright UV single photon emission at point defects in h-BN. *Nano Letters*, 16(7):4317–4321, June 2016.

[13] Xiangzhi Li, Gabriella D. Shepard, Andrew Cupo, Nicolas Camporeale, Kamran Shayan, Yue Luo, Vincent Meunier, and Stefan Strauf. Nonmagnetic quantum emitters in boron nitride with ultranarrow and sideband-free emission spectra. *ACS Nano*, 11(7):6652–6660, May 2017.

[14] Brian Shevitski, S. Matt Gilbert, Christopher T. Chen, Christoph Kastl, Edward S. Barnard, Ed Wong, D. Frank Ogletree, Kenji Watanabe, Takashi Taniguchi, Alex Zettl, and Shaul Aloni. Blue-light-emitting color centers in high-quality hexagonal boron nitride. *Physical Review B*, 100(15), October 2019.

[15] Viktor Ivády, Gergely Barcza, Gergő Thiering, Song Li, Hanen Hamdi, Jyh-Pin Chou, Örs Legeza, and Adam Gali. Ab initio theory of the negatively charged boron vacancy qubit in hexagonal boron nitride. *npj Computational Materials*, 6(1), April 2020.

[16] Sherif Abdulkader Tawfik, Sajid Ali, Marco Fronzi, Mehran Kianinia, Toan Trong Tran, Catherine Stampfl, Igor Aharonovich, Milos Toth, and Michael J. Ford. First-principles investigation of quantum emission from hBN defects. *Nanoscale*, 9(36):13575–13582, 2017.

[17] Yağmur Aksu Korkmaz, Ceyhun Bulutay, and Cem Sevik. Defect states in monolayer hexagonal BN: A comparative DFT and DFT-1/2 study. *Physica B: Condensed Matter*, 584:411959, May 2020.

[18] Akbar Basha Dhu al-jalali-wal-ikram Shaik and Penchalaiah Palla. Optical quantum technologies with hexagonal boron nitride single photon sources. *Scientific Reports*, 11(1), June 2021.

Chapter 2

Background

2.1 Single Photon Emission

2.1.1 Light: Neither a particle nor a wave

In quantum mechanics light is considered as a stream of elementary massless particles called photons. The nature of photons in quantum mechanics is often stated " neither a wave nor a particle" which means that they exhibit wave-particle duality.

The light interference experiment, commonly known as 'Young's double slit experiment' which was first performed by an English physicist Thomas Young in 1807 demonstrated the wave nature of light. Later in 1887, Heinrich Hertz observed the photoelectric effect which was not satisfactorily explained until 1905 when Albert Einstein gave the laws of the photoelectric effect and established that light also has a particle nature. In his theory each quantum of light has an energy equal to the frequency of light multiplied by a constant h which was later called Plank's constant. The particle nature of light also helped Compton to explain the wavelength shift in scattered X-rays in 1923. Gilbert N. Lewis, a prominent American physical chemist first used the term "photon" for the quanta of light.

Generally, light is regarded as stream of photons to study the interaction with matter where photons are absorbed and emitted and light is regarded as wave to understand propagation. Neither of the assumptions are wrong but depend on the experiment and interactions.

2.1.2 Photons and light sources

In the quantum picture of light the elementary particle of light is a photon, a term coined by Gilbert Lewis in 1926 [1] after the formulation of Plank's theory of black body radiation

in 1900 and the discovery of the photoelectric effect by Einstein in 1905. A photon is an elementary excitation of a single mode of quantised electromagnetic field with energy $E = h\nu$ [2], where h is Plank's constant and ν is the frequency of the electromagnetic field.

Light sources can be classified into three broad categories based on the fluctuation of photons in time - bunched, coherent and antibunched. Thermal light source, for example, an incandescent bulb is an example of bunched source which emits multiple photons at the same time. This type of emission statistics is called super-Poissonian distribution. This is the most common light source and can not be used for quantum technology as no information can be encoded on spatially and temporally uncontrolled stream of photons. Coherent sources such as light from a laser have nearly constant intensity with all emitted photons having the same frequency and hence the same energy. Such sources obey Poissonian distribution and can be used in technologies like fibre optic communication. Information is encoded onto the pulse train which can travel thousand of miles with repeaters every 40 to 60 miles. Fast modern internet is based on fibre optics for example- 3,800 mile long Apollo North optic cable connecting USA and UK. Antibunched sources (example quantum dot emitters) emit one photon at a time with all photons having the same energy and following a sub-Poissonian distribution. These sources can be used in quantum technologies to encode information on individual photons in terms of polarization, time or spatial mode. Quantum encryption is a prime example where secure satellite to ground quantum key exchange has been demonstrated by Liao *et. al* [3]. To quantify the quality of single photon emission from a source, correlation experiments are used and in particular, the Hanbury Brown and Twiss (HBT) experiment.

2.1.3 Hanbury Brown and Twiss experiment

HBT experiment is one of the most important measurement to asses the quality of a single photon emitter (SPE). The main principle behind HBT is that the intensity fluctuations of a light source are related to its coherence [4]. The original experiment was performed by Robert Hanbury Brown and Richard Q. Twiss in 1956 [5] with more detailed theoretical explanation in 1957 [6] and an experimental test for a partially coherent light source in 1958 [7].

Consider a partially coherent (chaotic) light source, say a mercury lamp where different atoms emit at a different time, the light intensity $I(t)$ fluctuates with time on a scale comparable to the coherence time, τ_c. Fig. 2.1 shows an example time dependent intensity plot for a chaotic light source. The intensity $I(t)$ fluctuates around the average value $\langle I \rangle$ of the source.

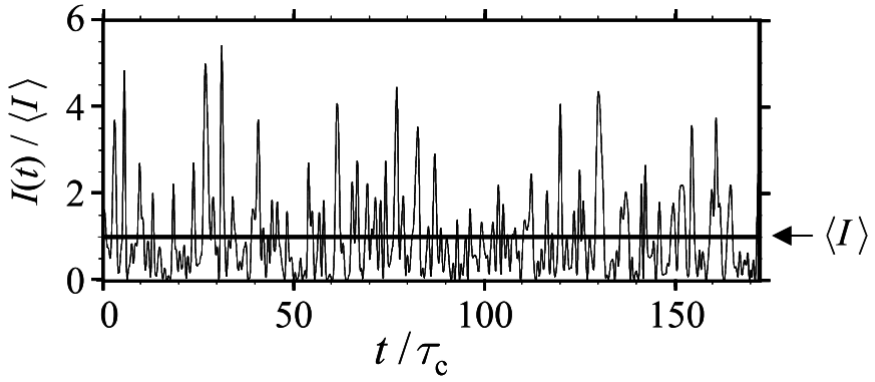

Fig. 2.1 Computer simulation of light intensity emitted by a chaotic source with average intensity $\langle I \rangle$ and coherence time τ_c [4].

We can define the fluctuations as $\Delta I(t)$. The chaotic light source intensity can be written as:

$$I(t) = \langle I \rangle + \Delta I(t) \tag{2.1}$$

Fig. 2.2 shows the setup for HBT intensity correlation experiment. The incoming light from a mercury lamp is filtered to get only 435.8 nm emission line incident on a half-silvered mirror. Photomultiplier tubes PMT1 and PMT2 detect the light intensity $I_1(t)$ and $I_2(t)$ in path 1 and 2 respectively. AC coupled amplifiers filter and amplify the signal from both PMTs. The two fluctuating signals were sent to an electronic multiplier-integrator with a time delay τ in the path of PMT2. A linear translation stage is used to move the PMT1 to change the distance d between the two light signals for investigating spatial coherence. When $d = 0$ the output of the multiplier-integrator is:

$$\langle \Delta I(t) \rangle \langle \Delta I(t+\tau) \rangle \tag{2.2}$$

Let's assume a case when there is no time delay in PMT2 i.e $\tau = 0$. The output is:

$$\langle \Delta I(t) \rangle \langle \Delta I(t+\tau) \rangle_{\tau=0} = \langle \Delta I(t)^2 \rangle \tag{2.3}$$

By definition $\langle \Delta I(t) \rangle = 0$ but $\langle \Delta I(t)^2 \rangle$ is nonzero and depends on the magnitude of fluctuation. A highly chaotic source will give a high $\langle \Delta I(t)^2 \rangle$ value.

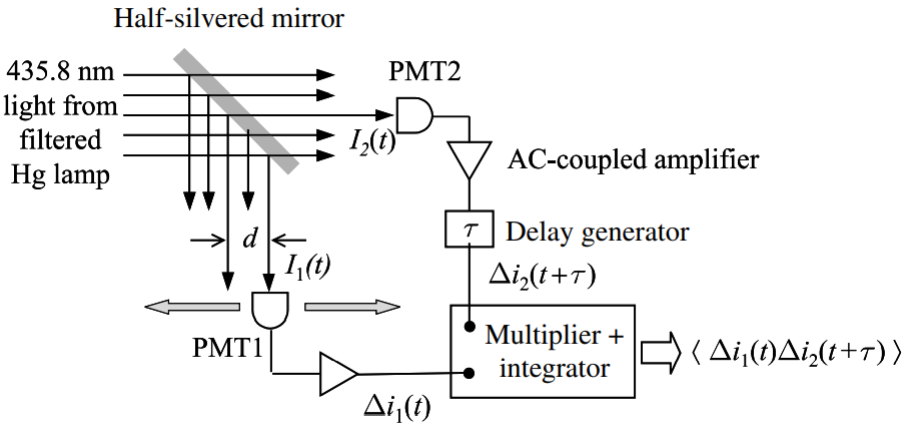

Fig. 2.2 Schematic representation of HBT intensity correlation experiment. The 435.8 nm filtered light from mercury lamp incident on half silvered mirror. The two photomultiplier tubes PMT1 and PMT2 detects the light intensity $I_1(t)$ and $I_2(t)$, respectively. The photocurrent is filtered, amplified and time delay τ is added in one of them. The two fluctuating signals $\Delta i_1(t)$ and $\Delta i_2(t+\tau)$ are fed into an electronic multiplier-integrator, giving output $\langle \Delta i_1(t)\Delta i_2(t+\tau)\rangle$. To investigate the spatial coherence in range d, PMT1 is placed on a translation stage [4, 5].

In other case, when the delay time is much larger than the coherence time, $\tau >> \tau_c$. This results in completely uncorrelated fluctuation and the output will be zero:

$$\langle \Delta I(t)\rangle \langle \Delta I(t+\tau)\rangle_{\tau>>\tau_c} = 0 \tag{2.4}$$

In this way the coherence time of a light source can be directly measured with the help of changing time delay. Hanbury Brown and Twiss in their original experiment also studied the spatial coherence by changing d while keeping $\tau = 0$. When d is increased, the correlation between the two intensity fluctuations decreased and the output signal reduced to zero. Their method provided a very robust way of determining the spatial coherence of a light source and is now used to assess the quality of coherent sources.

2.1.4 The second-order correlation function

We have seen in the previous section that the HBT experiment is a powerful technique, not only to assess the spatial coherence of a light source, but to determine the coherence time as

well. Our motive in SPE research is to quantify the purity of the single photon emission, so how can the HBT experiment help us to measure photon counting statistics? The answer lies in the second-order correlation function, $g^{(2)}(\tau)$, which is defined as [4] :

$$g^{(2)}(\tau) = \frac{\langle I(t)I(t+\tau)\rangle}{\langle I(t)\rangle\langle I(t+\tau)\rangle} \tag{2.5}$$

Let's consider a stable light source with constant average intensity:

$$\langle I(t)\rangle = \langle I(t+\tau)\rangle \tag{2.6}$$

From now, using second-order correlation function, we are investigating the temporal coherence using spatially coherent light from a small area of the source. Using Eq. 2.1 the output for condition $\tau >> \tau_c$ is:

$$\begin{aligned}\langle I(t)\rangle\langle I(t+\tau)\rangle_{\tau>>\tau_c} &= \langle[\langle I\rangle + \Delta I(t)][\langle I\rangle + \Delta I(t+\tau)]\rangle \\ &= \langle I\rangle^2 + \langle I\rangle\langle\Delta I(t)\rangle + \langle I\rangle\langle I(t+\tau)\rangle + \langle\Delta I(t)\Delta I(t+\tau)\rangle \\ &= \langle I^2\rangle\end{aligned} \tag{2.7}$$

Where we used Eq. 2.4 and the fact that $\langle\Delta I(t)\rangle = 0$ and $\langle\Delta I(t+\tau)\rangle = 0$. Now $g^{(2)}(\tau)$ function can be expressed as:

$$g^{(2)}(\tau)_{\tau>>\tau_c} = \frac{\langle I(t)I(t+\tau)\rangle}{\langle I(t)\rangle\langle I(t+\tau)\rangle} = \frac{\langle I(t)\rangle^2}{\langle I(t)\rangle^2} = 1 \tag{2.8}$$

In case of delay time $\tau << \tau_c$ and $\tau = 0$

$$g^{(2)}(0) = \frac{\langle I(t)^2\rangle}{\langle I(t)\rangle^2} \geq 1 \tag{2.9}$$

For a perfectly coherent source with time independent intensity $g^{(2)}(\tau) = 1$, for all values of τ as $I(t) = I(t+\tau) = I$. For any other source $g^{(2)}(0) > 1$ because $\langle I(t)^2\rangle > \langle I(t)\rangle^2$. Using these results and Eq. 2.8 we plot the $g^{(2)}(\tau)$ function for both chaotic and coherent sources in Fig 2.3. At $\tau = 0$ the $g^{(2)}(\tau)$ function for a chaotic source is higher than unity and a larger

value of $g^{(2)}(\tau)$ implies more chaotic emission. As τ increases the $g^{(2)}(\tau)$ function tends towards unity and aligns with that of a coherent source.

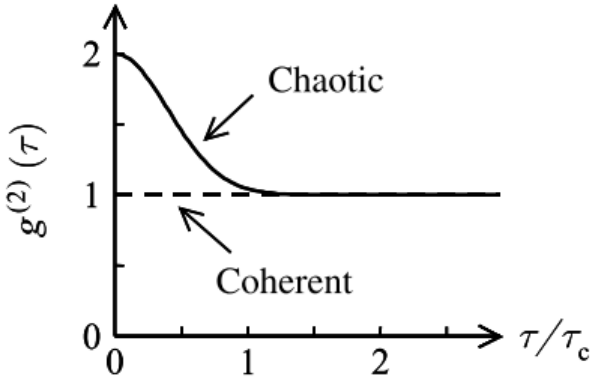

Fig. 2.3 Second order correlation function $g^{(2)}(\tau)$ for perfectly coherent and a Doppler-broadened chaotic source with coherence time τ_c [4].

Until now we have not discussed the HBT experiment in terms of photons and how it can be used to comment on the purity of single photon emission. In the next section I will discuss how the HBT experiment and $g^{(2)}(\tau)$ combine for photon counting and correlation.

2.1.5 The second-order correlation function for photons

Fig. 2.4 shows a HBT experiment setup for measuring photon statistics. The incoming photon stream incident on a 50:50 beam splitter randomly sends photons either to detector D1 or D2. The detector generates an electronic signal commonly called a "click" when it senses a photon. Clicks from both D1 and D2 are sent to a counting device. When a click is received from D1 a timer starts, until a click from D2 is received and time difference between a click from D1 and D2 is calculated for plotting the $g^{(2)}(\tau)$ function.

A stream of photons from a light source can be classified in three groups. Fig. 2.5 represents these cases in the photon picture of light. In antibunching, the photons are distributed with the same time delay between each. In the bunching case, the photons arrive in groups with one or more photons at the same time whereas in the randomly coherent case, the photons have random time intervals between them, but no grouping.

The $g^{(2)}(\tau)$ function for photon counting is [4]:

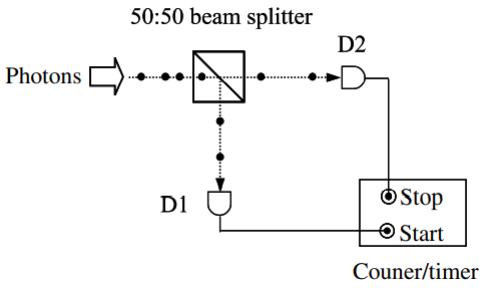

Fig. 2.4 HBT experiment with photons. The incoming stream of photons incident on a 50:50 beam splitter sends photons to detector D1 and D2. Electronic signal "click" from D1 starts the timer until a click signal arrives from D2 [4].

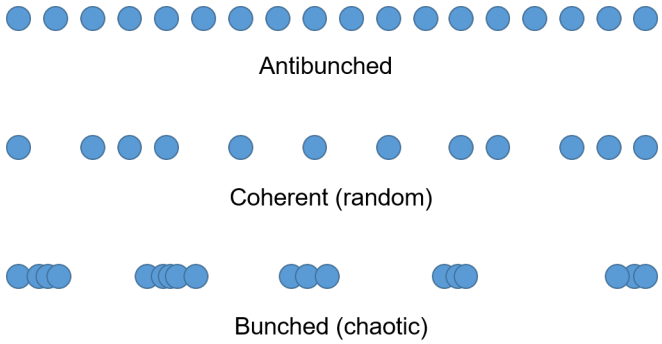

Fig. 2.5 Schematic representation of photon streams for antibunched, coherent and bunched light.

$$g^{(2)}(\tau) = \frac{\langle n_1(t) n_2(t+\tau) \rangle}{\langle n_1(t) \rangle \langle n_2(t+\tau) \rangle} \tag{2.10}$$

Where $n_i(t)$ is the number of counts registered on detector i at time t. A simple way of understanding $g^{(2)}(\tau)$ is that - It is the conditional probability of detecting a second photon at $t = \tau$ given that one has been detected at $t = 0$. Let's now consider the $g^{(2)}(\tau)$ function for each case:

Coherent

In the case of a coherent source, the time interval between photons is random, so once a photon is detected there is an equal probability of detecting another photon at $\tau = 0$ to any other value of τ. This gives $g^{(2)}(\tau) = 1$, for all $g^{(2)}(\tau)$, which is the same result as we get with a coherent light source in the wave picture.

Bunching

In case of bunching the photons arrive in groups. The time interval between the photons in a group is much smaller than the time interval between the groups. This means, once a photon is detected at $\tau = 0$ there is a much higher possibility of detecting another one at shorter times rather than longer. This gives $g^{(2)}(0) > 1$ similar to the chaotic source in Eq. 2.9 proving that bunching is same as chaotic light in wave picture. As τ increases $g^{(2)}(\tau)$ start approaching unity, shown in Fig. 2.3. The scale of bunching for an emitter is proportional to $g^{(2)}(0) - g^{(2)}(\infty)$.

Antibunching

In antibunching no two photons arrive at the same time making $g^{(2)}(0) = 0$. As τ increases the probability to detect another photon increases and after $\tau_a > 0$, where τ_a is the emitter's lifetime, the function $g^{(2)}(\tau_a)$ becomes unity. More the antibunching more will be the spacing between the photons increasing the τ_a making the transition between $g^{(2)}(0) = 0$ to $g^{(2)}(\tau_a) = 1$ slower, indicating an increase in emitter's lifetime. Antibunched light is a clear indication of a SPE and quantum nature of light. Fig. 2.6 show three curves representing the antibunching scenarios. The red curve shows $g^{(2)}(\tau)$ for a single photon emitter with no bunching whereas blue represent signal from a SPE with some degree of grouping/bunching but still satisfying the condition of only one photon at a time. Green represents a SPE similar to red but with more time spacing between the photons.

Fig. 2.7 shows $g^{(2)}(\tau)$ measurement from a single hBN emitter. Note that the $g^{(2)}(0)$ value is not equal to zero even though the emission is from a single photon source. This is because more than one SPE is excited at the same time which increase the probability of detecting two photons at $\tau = 0$. The $g^{(2)}(0)$ value for n excited SPE is $(1 - 1/n)$, so for two or more SPE, $g^{(2)}(0) \geq 0.5$. Thus, it is widely acceptable that if $g^{(2)}(0) \leq 0.5$, the emission is from a single photon source because it means that the collection is predominantly from a single SPE with minor contribution from a nearby SPE or impurity.

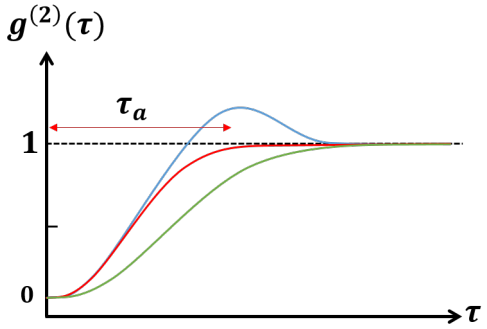

Fig. 2.6 Second order correlation function $g^{(2)}(\tau)$ for three forms of antibunched photon stream. Red represents single photon stream with no bunching, blue shows some degree of grouping (τ_a is the emitter lifetime for red and blue case) and green shows a case similar to red but with larger temporal spacing.

it is not possible for bunched or coherent sources to have a probability of detecting another photon at $\tau = 0$ less than half compared to $\tau >> 0$. Also note that the $g^{(2)}(\tau)$ function is plotted for $+\tau$ as well as $-\tau$. This is because in reality the photon counter assigns a time stamp to each photon detected at the two channels and later the computer program subtract start channel from stop channel time stamps to get the τ value. If the stop channel gets a click before start channel then the τ value will be negative. One can neglect these negative time counts and plot only the positive side. This does not affect the efficacy of the $g^{(2)}(\tau)$ whatsoever. In literature, the $g^{(2)}(\tau)$ is shown with both sides because the symmetry helps in verifying that both the detector and channels are identical.

2.1.6 Qualities of a quantum emitter

An ideal single photon source [8] satisfies the following properties:

1. **Deterministic**- A single photon can be emitted on-demand i.e at any arbitrary time defined by the user.

2. **Purity**- The source should emit only a single photon at a time and the probability for multiple photon generation should be zero i.e $g^{(2)}(0) = 0$.

3. **Indistinguishability**- The emitted photons should be indistinguishable from each other i.e every photon should have precisely the same wavelength, polarization, spatial mode etc.

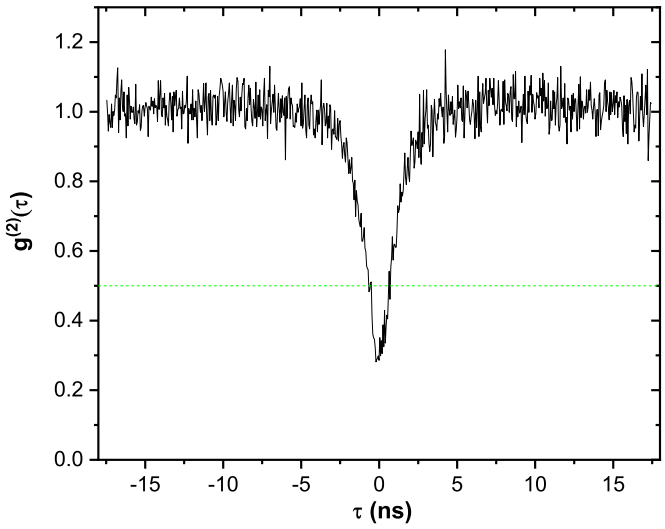

Fig. 2.7 Example of a second order correlation measurement of a typical hBN emitter. The $g^{(2)}(\tau)$ function at $\tau = 0$ ns dips below 0.5 confirming that the emission is from a single photon source.

4. **Repeatability**- The source should be able to emit photons at an arbitrary high repetition rate whilst satisfying the above three qualities.

Along with the above basic properties a few more qualities are desirable for versatile and robust use of a SPE. Qualities such as- stable emission at high temperature, ability to integrate with other materials, low manufacturing and operation costs and small size. All these properties will be discussed in later sections. So far we have discussed the single photon measurement technique and the properties of an ideal SPE. In reality no SPE is ideal, some SPEs are closer to ideal characteristics than other. In the next section we will discuss some candidates that show single photon emission and their advantages and disadvantages.

2.1.7 Different sources of single photons

The basic requirement for a SPE is a two level system which can be excited by an external pump source and the system relaxes by emitting a photon similar to the energy difference between the two levels, which is less than the excitation energy. The excess energy can create an optical or acoustic phonon so that the whole process obeys the law of conservation of energy. Single photon emission was first demonstrated by Kimble et al. [9] in 1977 using atomic transition in sodium atoms but the efficiency and the controlability were low.

Following are some SPEs commonly used in research these days. First, we briefly discuss the non-solid state SPEs and then the solid state SPEs in more detail.

Single neutral atoms and ions

The generation of single photons from cold single alkali atoms such as Cs (Caesium) and Rb (Rubidium) is cumbersome and require high level of precision and complex setup [10–15]. Fig. 2.8 shows the experimental scheme for generations of single photons from a Rb atom. A magneto-optical trap (MOT) first cools down the atoms which is then switched off to allow them to fall under the action of gravity inside a high finesse optical cavity and an optical trap is turned on. The aim is to trap only one atom inside the cavity for a pure single photon emission. The atom has a Λ type energy level (i.e one excited state and two ground states). The resonance of the optical cavity aligns with one ground to excited state and the pump laser pulse aligns with the other. With precise control of pump laser and cavity coupling resonance a single photon is generated via stimulated Raman adiabatic passage (STIRAP) [16]. The purity of the single photon emission via this process can be close to unity showing $g^{(2)}(0) = 0.06$ [17] but the emission probability is very low, close to 4.8 %. Fluctuating cavity mode coupling [18], limited trapping time [17] and large operating costs are major hurdles for single atom sources.

In similar fashion, a single ion showing a Λ-type energy level is trapped using a radio frequency ion trap and single photon is emitted via STIRAP technique [19–21]. Ion sources are better than single atom sources to get high emission rate [20] by stably localizing the ion at the centre of the optical cavity with a precision of few nanometers but still the emission rates are not high enough for practical applications. Problems such as strong spontaneous decay rates competing with emission of radiation into the cavity mode and the ion residing in the ground state at the end of the excitation pulse without generation of a photon hampers the emission rates. Both single atom and ion sources have very high purity but share the same problem of low emission rates and setup complexity [22]. Although complex and expensive, trapped ion based quantum computing has already gained market interest with initial public offering in IonQ, a trapped ion based quantum computing company [23].

2.1.8 Solid state emitters

In terms of stability, purity and possibility of commercial applications, the most promising single photon sources are solid state SPEs based on atom like emitters. These emitters can be single molecules embedded in solid state host matrix, quantum dots (QD) or defects in

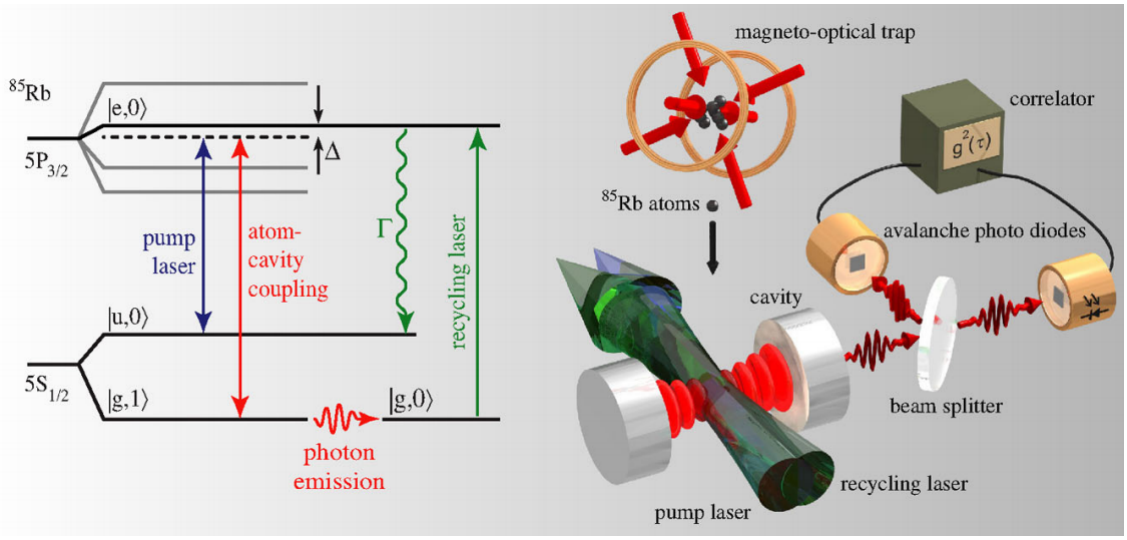

Fig. 2.8 Experiment scheme for single photon emission from Rb atom. Left shows the energy levels and transitions in ^{85}Rb with atomic states involved in Raman process labelled as $|u\rangle$, $|e\rangle$ and $|g\rangle$. $|0\rangle$ and $|1\rangle$ represents the photon number in cavity. Right shows the experimental setup where a cloud of atoms are are released from a MOT into an optical trap. The pump and recycling laser overlaps with the cavity mode. The emission can be directed into a HBT measurement setup to confirm the single photon emission [10].

materials such as diamond and 2D materials like hBN which can be easily scaled and does not require traps or a complex setup.

Single molecules in solid matrix

First candidate for solid state emitters is a single molecule source embedded in a solid state host matrix [24, 25]. The vibrational energy levels can be approximated as singlet ground and singlet excited state with a triplet dark state. The molecule is optically excited and a single photon is generated when it relaxes into the ground state. This process continues until it gets trapped into the dark state which lowers the emission rate and results in blinking of the emitter shown by bunching in $g^{(2)}(\tau)$ at longer times [26]. To reduce the random blinking of the emitter a continuous wave (CW) pump laser is applied along with sinusoidal external electric field to sweep the molecule's absorption energy which modulates the emission rate [27]. The purity of the emission from a single molecule is not appreciable due to the possibility of the laser exciting more than one molecule at a time [28]. Moreover, like other sources, molecule sources show poor indistinguishably and $g^{(2)}(0)$ values at a temperature higher than 8 Kelvin [29, 28] due to phonon interactions.

Quantum dots

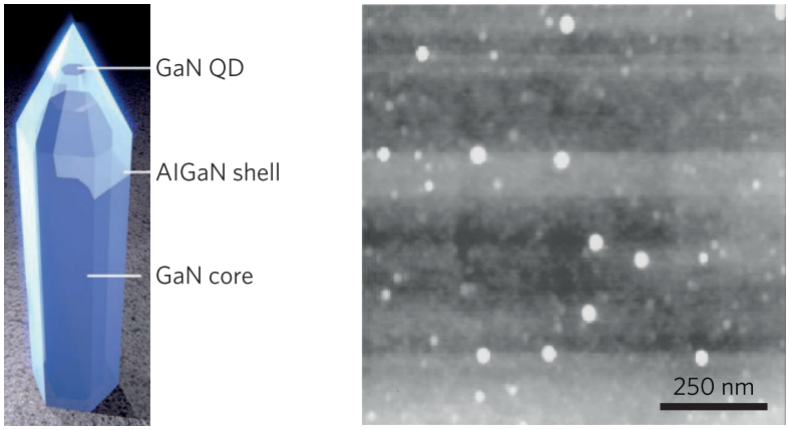

Fig. 2.9 Quantum dots as SPE. Left: Nitride QD embedded in nanowire waveguide for enhanced emission. Right: Self assembled InAs QDs, the first system used to demonstrate triggered single photon emission [30].

The discrete energy structure for electrons and holes in a quantum dot (QD) allow single photon emission with radiative lifetime ≤ 1 nanosecond via radiative recombination of the electron-hole pair (exciton) [31–38, 34, 39–47]. The exciton can be produced on demand by an excitation signal which can be optical or electrical depending on the device structure. For optically excited QD (CdSe/Zn [48], InP/GaInP [49] and InAs/GaAs [50]), a photon is absorbed, which puts the QD into the excited state, from where it relaxes radiatively by emitting a single photon. In case of electrically excited QD (InAs [47] and InP [37]), the charge or charge pair is directly injected with the help of a p-n junction where it can be done controllable [51]. Semiconductor quantum dots (QD) such as InGaAs are fabricated using molecular beam epitaxy where small islands of InGaAs are embedded in GaAs layers which has a larger band gap than InGaAs [52]. A simpler chemical synthesis process is used for making colloidal quantum dots such as CdSe/ZnS [48]. Fig. 2.9 shows some examples of SPE QD. The quantum dots can emit in any direction so it is important to control the direction of emission for photonic applications. Distributed Bragg reflection mirrors can be fabricated on both sides of a QD to get the desired emission direction. Other techniques such as integrating with microcavities like micro disk, sphere and pillars [32, 40, 42, 44–46] to enhance the emission rate via the Purcell effect [53]. Recently, QDs has been demonstrated as highly-efficient entangled-photon source [54]

Even though the probability of creating a photon from correct excitation is close to 1 but still the emission efficiency is low. The quantum dot when excited can also form a biexciton state which is different in energy. Each QD is unique which makes the photon indistinguishability poor from one emitter to the other. Moreover, the small carrier wave function limits their operation to cryogenic temperatures only [22].

Crystal colour centres

These are point defects in a crystal that are fluorescent and emit one photon at a time. For photon indistinguishability, these emitters need to be separate enough from each other so that only one defect can be excited at a time. Most of these emitters, Fig. 2.10 are in wide bandgap semiconductors like Diamond [55–59], SiC [60, 61], ZnO [62] and rare earth ion impurities in crystals such as Yttrium aluminium garnet (YAG) [63–65], Yttrium orthosilicate (YOS) [66] and Lanthanum trifluoride LaF_3 [67] with energy levels embedded deep in the bandgap, further away from the valance and conduction band. This gives colour centres a major advantage of stable room temperature operation which is not possible in other candidates like single atom, ion or molecule. Let's discuss the leading crystal colour centre sources one by one.

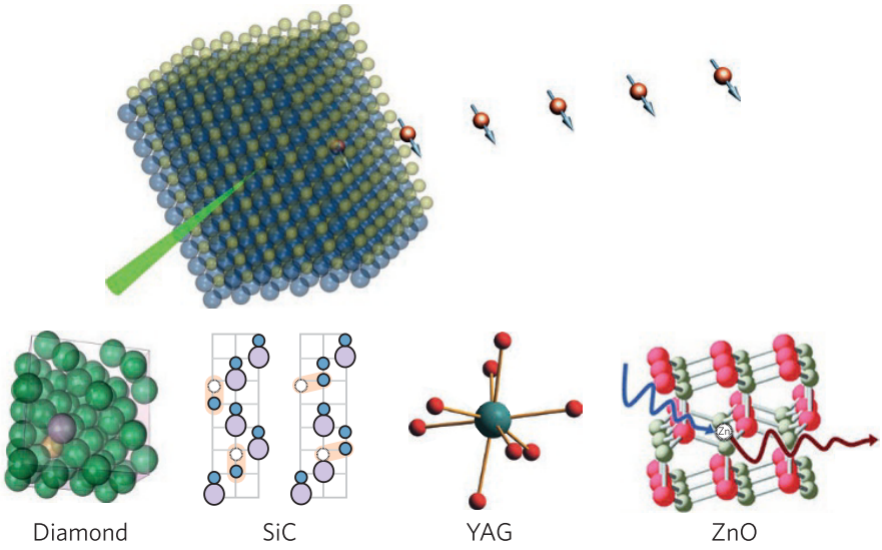

Fig. 2.10 Colour centres in bulk 3D crystals that shows single photon emission when excited optically. Top shows a schematic diagram of excitation laser exciting a defect in a 3D crystal which generates polarized single photons upon relaxation. Bottom shows different candidates such as Diamond, Silicon Carbide, Yttrium aluminium garnet and Zinc Oxide crystal. [30]

Two of the most studied defects in diamond are the nitrogen vacancy (NV) and the silicon vacancy (SiV) [55]. Theoretical calculations such as density functional theory (DFT) and photoluminescence experiments have been carried out on these defects [55]. These defects are found naturally in diamond and can also be created by a process like laser writing, electron beam and ion implantation- where an ion is bombarded with the diamond target to create these defects [68]. They exhibit a narrow ZPL linewidth which is highly desirable for indistinguishability and efficiency [57, 56]. The NV centres are sensitive to strain in the crystal due to their non zero electric dipole movement, whereas SiV defects with inversion symmetry are less susceptible. However the brightness of diamond defects is still low owing to low quantum efficiency of the defect [30]. Other defects such as Germanium vacancies are promising candidates for a bright single photon emission [69, 70]. Nickel NE8 and Nitrogen H3 defects are currently under research to understand their structure and dynamics, but have no pathway for their controlled fabrication [55].

Another very competitive SPE candidate is charged carbon vacancy defects in SiC [61]. These emitters are bright at room temperature and SiC is a compound semiconductor which is used in semiconductor application with industrial scale production. However, the identity and origins of the defect with precise emission properties is still missing [71]. A major advantage of SiC emitters is zero nuclear spin state, allowing a long coherence time for colour centre spin state [72–76] which means the defect can retain the spin state for sufficiently long time. This allows the defect to be used as a qubit for quantum computing, where the electron spin can be initialized, manipulated and read optically [77].

The II-VI compound wide bandgap semiconductor ZnO also shows single photon emission [62]. However, the origin of the defect species and detailed study is still missing. These emitters also suffer from bleaching and blinking [78–81]. Fabricating a stable p-doped ZnO important for p-n junction device is still a challenge. YAG and YOS show single photon emission properties and their defect structures are very well studied [63–66] but long excited state lifetime ($>$ 100 millisecond) and multiple competing relaxing pathways are still a big hurdle which significantly drops the emission rate.

2D materials

A variety of 2D materials such as monolayer tungsten diselenide WSe_2, a member of transition metal di-chalcogens (TMDCs) family [82–84] and hBN [85] show single photon emission. In TMDCs, emitters are localized excitons which operate at cryogenic temperatures where emission is often observed at 2D flake edges shown in Fig 2.11. The emission is detuned by a few milli-electronvolt from the exciton transition and brightness varies from

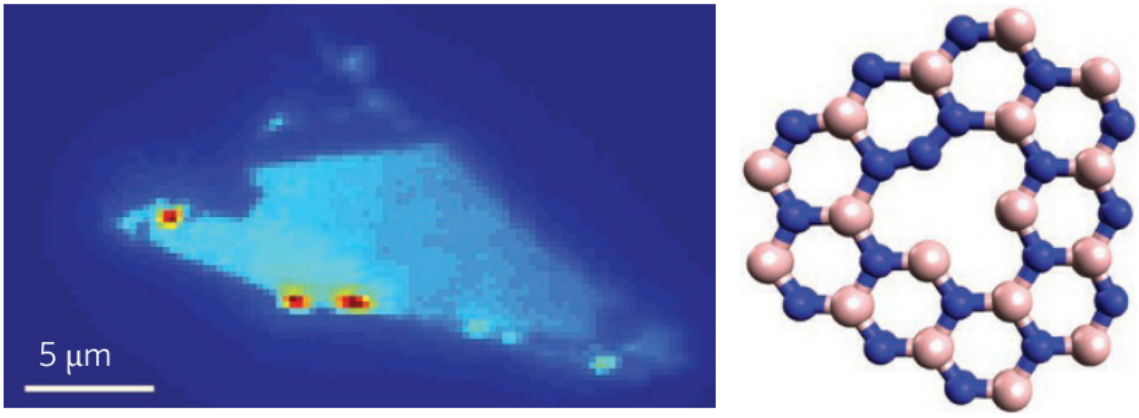

Fig. 2.11 SPE in 2D hosts. Left: Three distinct emitters revealed via confocal microscopy in a WSe_2 flake at cryogenic temperature. Right: A schematic diagram of hBN flake with a missing atom and an atom substitution representing a defect which exhibits room temperature single photon emission [30].

sample to sample. The detailed origins of emission from TMDCs is not clear but highly localized strain gradients are often liked to the origin of these emitters which can trap the excitons [86]. Although a strain gradient helps in funneling the exciton, crystallographic defects may play a significant role in emission by localizing the point defects [87, 88]. The $g^{(2)}(\tau)$ measurement for single photon emitters in WSe_2 monolayer flakes show $g^{(2)}(0) \approx 0.2$ [83], whereas resonant spectroscopy reduces it to $g^{(2)}(0) \approx 0.02$ [89] with 60% emission in ZPL. Recently, WSe_2 flakes grown with chemical vapour deposition (CVD) and encapsulated with hBN shows lifetime ≥ 200 ns [90]. A recent detailed review from Chakraborty *et. al* [86] can be referred for SPEs in TMDCs. These emitters are still in the early research phase with a rapidly growing interest among the nanophotonics community.

Another emerging candidate for robust SPE is hBN [85, 91]. Defect centres in hBN are bright, have narrow linewidth with stable single photon emission up to 800° C [92] which is a remarkable feat for any SPE thanks to its transition levels embedded deep in the 6 eV band gap. These emitters in 2D materials opens endless possibilities of integration with photonic devices. 2D emitters are best suited for interation with plasmonic structures.

In next section we will discuss the hBN in more detail, understanding the advantages, applications and challenges.

2.1.9 Emitter lifetime and decoherence

When a SPE is subjected to continuous-wave (CW) laser, the rate of photon generation Γ_{rad}, is determined by emission lifetime τ_f and is related to other parameters by [93]-

$$\Gamma_{rad} = \frac{1}{\tau_f} = \frac{4|\mu_{eg}^2|}{3n4\pi\varepsilon_0\hbar}\left(\frac{\omega}{c}\right)^3 \tag{2.11}$$

where n is the refractive index of the medium, ω, transition frequency, μ_{eg}, dipole movement between ground and excited state. ε_0, c and $\hbar$ are vacuum permittivity, speed of light and modified Plank's constant. The fluctuation of the electric field at the location of the emitter induces the decay into ground state. The rate of photon generation depends on the refractive index of the environment and how many modes of electromagnetic wave it can support [93]. For a bright emitter, we need a very high rate of photon generation without losing indistinguishability i.e keeping the linewidth narrow.

When radiative decay is the only contributor for broadening, the linewidth achieved is called Fourier-transform limited (FT) linewidth. In reality, the linewidth from an SPE is few orders of magnitude more than the FT limited value because of dephasing and spectral diffusion arising from fast and slow fluctuations of the transition frequency. The dephasing time of the emitter, T_2, excited state lifetime, T_1 and pure dephasing time (time during which system interacts with phonon bath) T_2^* are related as-

$$\frac{1}{T_2} = \frac{1}{2T_1} + \frac{1}{T_2^*} \tag{2.12}$$

In the absence of slow spectral diffusion, the FWHM, $\Delta\nu$ is given by-

$$\Delta\nu = \frac{1}{2\pi T_1} + \frac{1}{\pi T_2^*} \tag{2.13}$$

When dephasing due to the phonon bath is negligible i.e $T_2^* = \text{inf}$, Eq. 2.13 gives the lifetime limited linewidth. At room temperature, the dephasing time is dramatically shortened by phonon interactions. Most SPE characterization experiments are carried out at cryogenic temperatures to reduce the effects of dephasing into the phonon bath. For robust SPE, it would be ideal to operate at room temperature with least phonon interaction. Spectral diffusion is another contributor of linewidth broadening which arises from the nearby charged impurities

and mechanical stress in the vicinity of the emitter [94]. For emitters in hBN, working well below the saturation power helps in reducing the spectral diffusion by reducing the phonon interaction [95].

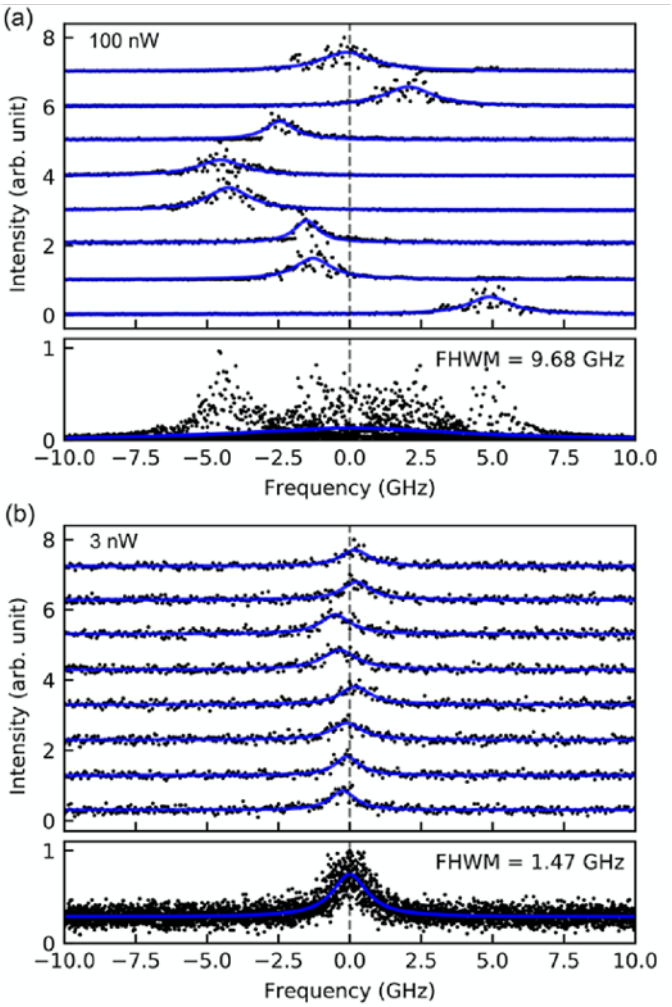

Fig. 2.12 Individual photoluminiscence excitation (PLE) (see Chapter Methods for information about PLE) scans (top) and corresponding integrated PLE spectrum (bottom) for a hBN emitter showing (a) significant spectral diffusion at high pump power of 100 nWatt and (b) negligible for lower pump power of 3 nWatt [95].

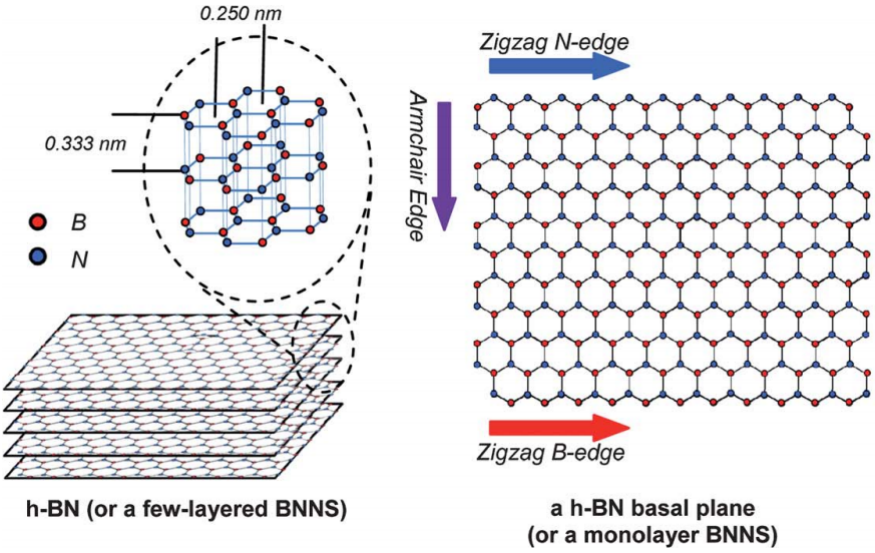

Fig. 2.13 Crystal structure of hexagonal Boron Nitride. Left: A few layered boron nitride nanosheet (BNNS) sample with layers arranged in AA' type stacking. The distance between the centre of two BN rings is 0.25 nm with B − N bond length as 0.14 nm, whereas the interlayer separation is 0.333 nm. Right: A monolayer BNNS showing three types of edges- Armchair, Zigzag N and Zigzag B-edge due to the presence of nitrogen and boron atoms on the edges [96].

2.2 Hexagonal Boron Nitride

2.2.1 hBN crystal structure and properties

Boron Nitride exists in variety of structures depending upon the arrangement of Boron and Nitrogen atoms. The amorphous form [97] has no long range order whereas cubic and wurtzite [98] form shows an arrangement similar to that of diamond and lonsdaleite form of carbon. The main focus of this thesis is on the hexagonal form of Boron nitride which shows stable and high single photon emission rate [85, 91] even at high temperature of $\sim 800°C$ [92]. This structure is sometimes referred as "graphitic boron nitride" due to similar structure as that of graphene. In a layer, the Boron and Nitrogen atoms are arranged as hexagonal pattern held together with strong covalent bonds. In multi-layer sample the layers are held together with weak van-der-Walls forces in such a way that a Boron atom from one layer is perfectly aligned with Nitrogen atom from the layer above and below [99]. This arrangement is also known as AA' sequence [100]. The B-N bond length is 1.446 $A°$ and the interlayer

separation is 3.331 A° [96], shown in Fig. 2.13. Alternative stacking patters like AA, AB etc are also possible in hBN and presented in Ref. [101].

Thanks to the layer structure of hBN, it can be exfoliated into few or mono-layers using simple and inexpensive methods such as tape-exfoliation [102] where an ordinary tape is used for repeated peeling, similar to graphene [103]. Ball milling [104] and solvent exfoliation [105] are other techniques, which allow more control over the number of layers and size of the flake. However, extracting hBN monolayers is difficult compared to that of graphene due to strong intralayer AA' interaction [106, 107].

hBN is an indirect bandgap semiconductor with an energy gap of ~ 6 eV [108]. It has a variety of properties like low density (2.27 g/cm^3) [109], high temperature stability and inertness up to 1000 °C [110]. It is also an exceptional electrical insulator with thermal conductivity $\sim 300-200$ Wm^{-1}K^{-1} [111] and is used in high temperature electronics. Strong B-N bonds and low atomic number allow highly energetic in-plane phonon modes giving hBN a high thermal conductivity. However, multilayer hBN is less thermally conductive perpendicular to the plane of the flake due to decrease in interlayer phonon scattering. Monolayer hBN is one of the strongest materials with mechanical strength ~ 260 Nm^{-1}, which is slightly lower than that of graphene monolayers [112].

Among the various properties of hBN, one of the most interesting is emission of single photons which is the theme of this PhD thesis. In the next section we will discuss the single photon emission from hBN in more detail.

2.2.2 SPE in hBN

Atomic defects in hBN result in energy levels deep in the band gap which can be optically active. SPE in hBN were first reported in 2016 [85] and since then a significant research has been done to understand the emission properties and limits. The measured brightness of hBN SPEs is 3×10^6 counts/sec which is linearly polarized and stable up-to 10 minutes [85]. From CVD grown hBN $g^{(2)}(0) \leq 0.1$ has been shown with emission wavelength ~ 580 nm and linewidth 3 nm [114, 115]. The hBN emitters are excited optically where the defect is pumped from ground to excited state. For a two level defect the excited state relaxes into the ground state by emitting a single photon. If the relaxation does not generate a phonon then the emitted photon is said to originate from zero phonon line (ZPL), but if the emission involves an optical or acoustic photon generation then it is said to be in the optical and acoustic phonon sideband. Fig. 2.14 shows the photoluminescence (PL) spectrum for a single hBN emitter and corresponding transitions in the energy level diagram. For an ideal hBN SPE a

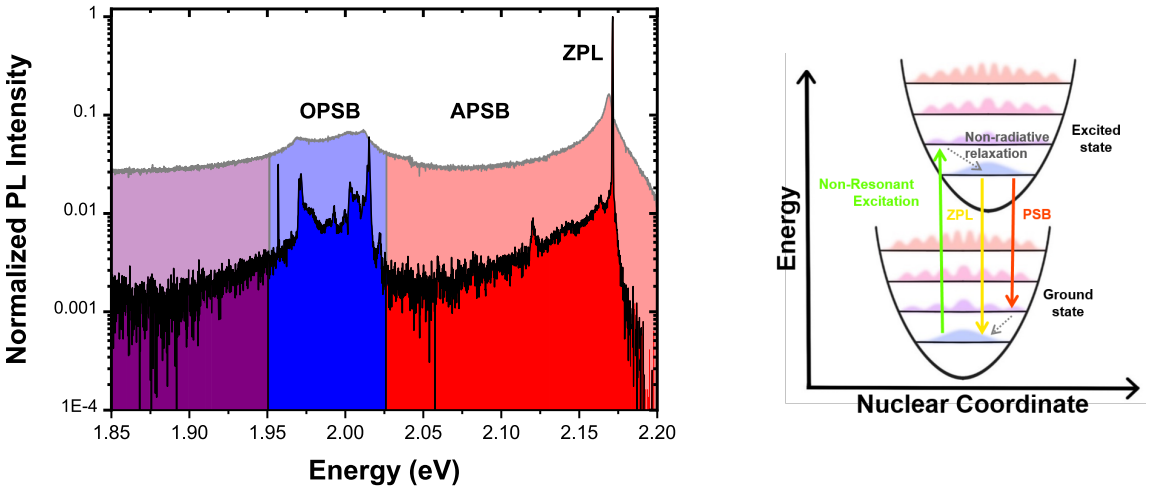

Fig. 2.14 Single photon emission in hBN. Left: PL spectrum for a single hBN emitter at 20 K and 275 K. The ZPL emission from this particular defect is at 2.17 eV which decreases in intensity with rising temperature. Next to ZPL is acoustic phonon sideband (ASB) in red and optical phonon sideband (OPSB) in blue, which indicates the strength of phonon coupling with the emitter [113]. Right: Energy level diagram representing the excitation and the emission from a two level system such as hBN emitters with phonon interaction.

narrow linewidth and maximum emission into ZPL is desirable. The emitters shows a wide spectral range from UV to near infrared [116–120].The large bandgap allows bright ZPL at room temperature because of low electron-phonon coupling and reduced non-radiative recombinations. The in-plane dipole results in highly polarized emission [121]. For most hBN defects the in-plane dipole coincides with the emission dipole [85] but it does differ in some cases [122] (See further discussion in chapter 5).

A point like defect in hBN adds trap states into the bandgap which can be regarded as a two level system. Despite efforts made in group theory and DFT [123–126], the precise nature of defects is still unclear and under debate. Out of many theoretically studied candidates only few such as C_BV_N (carbon in place of boron and vacant nitrogen), V_NN_B (vacant nitrogen and nitrogen in place of boron) ,V_BC_N (vacant boron and carbon in place of nitrogen) and V_B (vacant boron) are identified to have the correct allowed transitions for single photon emission. It is difficult to compare the calculated defects with experimentally studied ones because the ZPL energies coincide with allowed transitions of multiple emitters. Moreover, DFT calculation consider monolayer supercells to efficiently use the computing resources because adding more atoms increases the demand for computing power and time exponentially. This creates a mismatch between DFT calculated energy values and experimentally observed ZPL energy because in most experiments the sample is a multilayer

finite flake with nearby charged species, defects and impurities. The emission from mono and multilayer hBN samples have significant differences [85].

The ZPLs in most of the hBN emitters bunch in three groups around- 560 nm [127, 113, 128, 129], 590 nm [115], 640 nm [85, 116] and 710 nm [116]. The understanding so far is that a point-like defect is responsible for each group and local crystal strain/impurities are responsible for the spread around these wavelengths. Similar phonon sideband shape [113] in these groups further confirms this reasoning. The ZPL's that do not fall in any of these categories have a different phonon sideband (PSB) and are likely to originate from surface contamination [130].

Other applications of hBN

Apart from providing a single photon source, hBN SPEs can also be employed for optically detected magnetic resonance (ODMR) [131, 132] which can be used to initialize the spin state of a negatively charged defect. hBN is an excellent 2D material for encapsulating heterostructure of TMDC and other 2D materials particularly graphene [133]. When graphene is encapsulated with hBN the electron mobility increases dramatically because of shielding from local environment [134–136]. The mobility of this hBN/graphene/hBN heterostructure can only be increased by suspending a single graphene sheet which significantly hampers the application possibilities. This heterostructure can also show ballistic transport at cryogenic temperature [137]. The anisotropic crystal structure and polar bonds allow its application in IR nanophotonics [138, 139]. hBN based moiré-heterostrcture show novel electrical and optical properties as a function of layer's rotation angle [140–142].

2.2.3 Choosing the right SPE

So far, SPE based quantum computers are in research phase but QD based systems are leading the race [143]. Fig. 2.15 shows an optical quantum information processor (QIP) setup based on InAs/GaAs QD as SPE [144]. We have discussed the optical properties of the QDs as a SPE in section 2.1.8. Here, we discuss some of the major advances in QDs applicable for quantum key distribution (QKD) and QIP technologies.

A major breakthrough has been made by QDs which emits in telecommunication band. Optical fibers for telecommunication has low optical losses in $\sim$ 1300 nm (O-band) and $\sim$ 1500 nm (C-band) wavelength region. Therefore, it is very important to make SPEs with similar emission wavelengths, especially ones that emits in C-band region because it has the least amount of losses and is promising for satellite based communication [3]. InAs/InP

offer high purity and efficient emission in the C-band [145–147]. This is considered a major breakthrough for QD SPE and open doors for their commercial use.

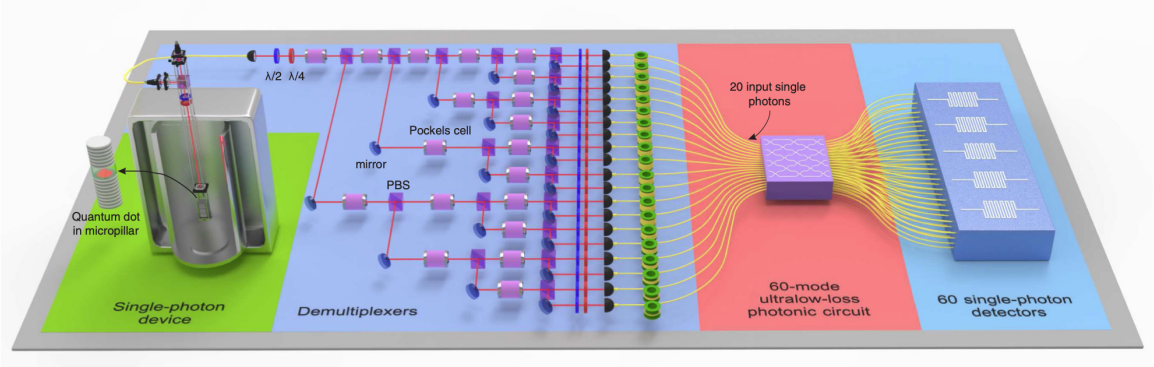

Fig. 2.15 Experimental setup for optical QIP based on boson sampling platform [144]. Highly efficient, pure and indistinguishable stream of single photons are obtained from InAs/GaAs QD, which is resonantly coupled to a microcavity.

To tackle the problem of low photon extraction efficiency, Takemoto *et. al* used optical horn structure for InAs/InP QD and demonstrated a fully operational QKD system capable of delivering secure keys up-to 120 km [146]. The highly indistinguishable photons are extracted with efficiency $\sim 11\%$ from emission at ~ 1559 nm having linewidth $= 0.29$ nm. The experiment was carried out at 4K and QD show high purity with $g^{(2)}(0) = 0.0051$. Later, Miyazawa *et. al* demonstrated a $g^{(2)}(0) = 4.4 \times 10^{-4}$ at 8 K under quasi-resonant excitation with similar optical horn structure and InAs/InP QD [145]. They anticipated that this could extend the QKD range up-to 200 km, similar distance as London to Cardiff. In another study, Muller *et. al* demonstrated that with highly symmetric InAs/InP QDs, grown using metalorganic vapour-phase epitaxy (MOVPE) epitaxy, maintains photon entanglement generated via biexciton cascade emission process even at a temperature of ~ 93 K, which can be achieved with just nitrogen cooling [148]. Using similar QDs, a successful demonstration of quantum teleportation was made where QDs exhibit a long coherence time of ~ 1 ns [149]. More details about the state of the art QD based SPEs can be found in a rececent review article by Arakawa *et. al* [147].

Although QDs are leading the race, but they still require temperature below 10 K for low $g^{(2)}(0)$ values. For example, InAs/InP QDs show $g^{(2)}(0) = 4.4 \times 10^{-4}$ at 8 K [148] but for operational temperature, at 80 K, the purity reduces to $g^{(2)}(0) = 0.34$ [150]. Moreover, the process of fabricating structures like optical horns are not cheap and easy and can increase the cost of of the SPE. We ideally want an inexpensive SPE which can operate at high

temperature without loosing the emission purity and easy to integrate with photonic devices. Colour centres in hBN are promising candidates with single photon emission even at 800 K and with purity $g^{(2)}(0) < 0.1$ [92] and near unity light collection efficiency with coupling to metallo-dielectric antennas [151]. We have discussed the optical and mechanical properties of hBN in depth in section 2.2. Although the purity of emitters in hBN is not as high as QDs but they satisfy the criteria for future chip-scale hand-held QKD devices [152]. With some more research breakthroughs in terms of emitter origins, stability and improvement in purity at high temperature, hBN could be competing/leading the race of SPE of choice in future QKD technologies [153]. Table 2.1 compares characteristics of emerging solid state SPEs.

Table 2.1 Comparison of different SPE characteristics [30]

Emitter	Temperature	Wavelength	Count rate	Linewidth	$g^{(2)}(0)$	Reference
Diamond SiV	300 K	738 nm	3×10^6	Lifetime-limited	≤ 0.1	[154]
Diamond NV	300 K	600-800 nm	1×10^6	Lifetime-limited	≤ 0.3	[155]
SiC defects	300 K	488 nm	60×10^3	N/A	≤ 0.1	[156]
ZnO defects	300 K	516 nm	1×10^5	N/A	≤ 0.2	[62]
TMDC (WSe_2)	4 K	730-750nm	3.7×10^5	N/A	~ 0.2	[83]
InAs QD	5 K	907 nm	1×10^7	Lifetime-limited	0.009	[157]
GaN QD	300 K	280 nm	N/A	1.5 meV	0.13	[158]
hBN defects	4 K	UV-NIR	3×10^6	~ 1 nm	~ 0.01	[153]
	300 K	UV-NIR	7×10^6	~ 10 nm	≤ 0.2	[159, 153]

2.3 Synthesis of hBN

2.3.1 Bulk crystals

To manufacture a high quality bulk hBN crystals, high temperature high pressure (HTHP) method is used [160, 161]. The Taniguchi group at the National Institute for Materials Science (NIMS), Japan is world renowned for producing high quality 2D materials including bulk and layered hBN [162]. The hBN powder (commercial hBN powder is synthesised synthetically by reaction of boron trioxide (B_2O_3) or boric acid (H_3BO_3) with ammonia (NH_3) or urea ($CO(NH_2)_2$) in a nitrogen atmosphere) is first heated at >2000 °C under an inert gas. The powder is then mixed with an alkali solvent like $Ba_3B_2N_4$ and packed in Molybdenum (Mo) chamber at a pressure of 40,000 atm and heated to 1,600 °C for a few days. The Mo chamber is then dissolved using aqua regia and hBN crystals are washed with water. Fig. 2.16 shows the uncrystallized BN powder before and synthesized hBN crystal after the process. The quality and purity of crystals can be estimated from its appearance.

Colourless crystals imply low density of defects, grain boundaries and impurities. This method produces ultra-pure hBN crystals which can be used as a substrate to study the properties of graphene [163–165], as it provides a perfectly flat surface that does not interact with graphene's fast travelling electrons. However, ultra-pure hBN is not ideal for studying the SPEs because defects and impurities are required for the formation of colour centres [85].

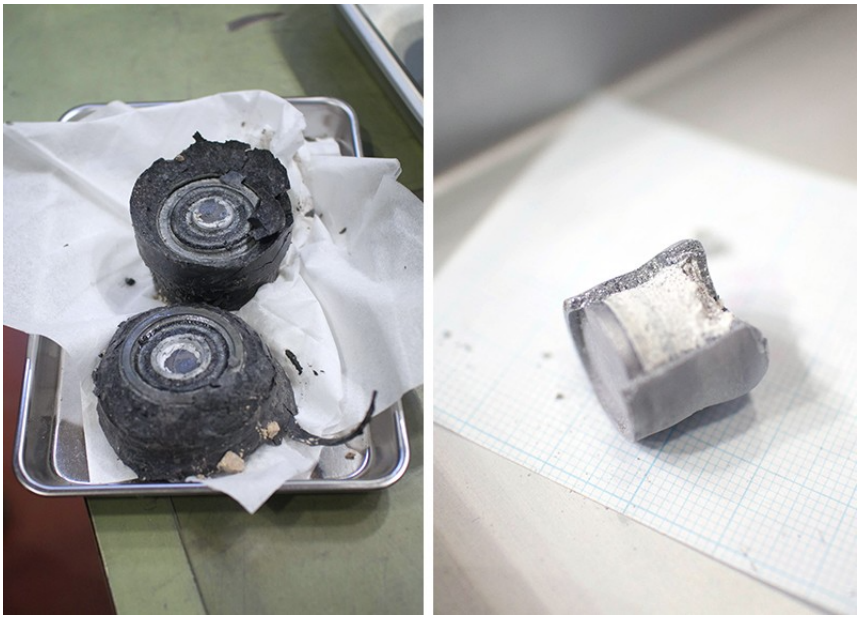

Fig. 2.16 Left: Synthesized hBN crystals by Taniguchi *et. al* after the HTHP process. Right: Uncrystallized BN powder in a Mo chamber before loading into the hydraulic press for few days. [162].

2.3.2 Multilayer flakes

Multilayer flakes can be extracted from commercial bulk crystals by either a top-down or bottom-up method.

The "Scotch tape method" is a common top-down exfoliation technique [102]. This process is repeated until flakes of desired size and thickness are obtained. These flakes are then transferred onto a substrate and heated at $\sim 400°$ C to remove any residuals of tape adhesive. This process gives clean flakes but it suffers from limitations such as random orientation and distribution of hBN layers. It also lacks scalability, essential for commercial application. Hence, this process is only used in labs for research purposes.

A ball milling process can efficiently produce hBN nanosheets on a large scale [104]. In this method shear forces from oxide beads exfoliates nanosheets from micron size hBN powder. The sheet size, number of layers, yield and efficiency can be controlled by milling parameters like milling speed, ball-to-powder ratio, milling ball size and milling agent [166]. It is found that under optimum conditions small balls of 0.1-0.2 mm can exfoliate $0.5-1.5\ \mu m$ wide nanosheets with 14% yield. The majority of applications from this technique are in the oil industry for the purpose of lubrication and adds significantly high density of defects compared to tape method.

Solvent exfoliation is another top-down method [105] that uses sonication force and appropriate solvent to exfoliate a thick flake into thinner ones. Along with hBN, this method can be used for a variety of 2D materials such as MoS_2, WS_2, $MoSe_2$ etc. [167]. Further additions such as surfactant-assisted aqueous exfoliation [168] and mixed-solvent strategy [169] are used to extract thinner flakes and achieve more extraction control. Review article from Nicolosi *et. al* [105] can be referred for further reading on solvent exfoliation. A limitation of this method is lack of control especially the number of hBN monolayers in the flake.

Bottom-up approaches, such as chemical vapor deposition (CVD) and molecular beam epitaxy (MBE) give an outstanding advantage over the control of layer size and thickness [170]. CVD is the most promising process because it allows mass production and flexible controllability during the growth process by adjusting parameters like temperature, pressure, precursor concentration etc. The growth mechanism has three major steps-

1. Decomposition of precursors such as ammonia borane (BH_6N) and borazine ($B_3H_6N_3$) into species containing boron and nitrogen under high temperature.

2. Deposition of boron and nitrogen containing species onto metal subsatrate such as copper and nickel to start the nucleation process for a pure hBN layer.

3. Continuous growth of these nucleation sites into islands with uniform rate. These islands ultimately coalesce to form one large layer.

After growth, the substrate is spin coated with a carrier polymer- poly(methyl methacrylate) (PMMA) and the substrate is etched away using an appropriate etchant. The polymer film now only has monolayer hBN attached to it. It can be transferred to the target substrate and the PMMA can be dissolved using organic solvents. CVD techniques can also be used for in-plane growth of heterostructures between hBN and other 2D materials such as graphene [171].

2.3.3 Characterization

The most direct technique to characterize hBN is atomic force microscopy (AFM) where a mechanical probe scans the sample. AFM is a real space imaging technique and has 0.37 nm resolution which can further be modified using ambient conditions such as low amplitude excitation of higher eigenmodes of the scanning cantilever [172] and can resolve even the hexagonal structure. It can determine surface roughness, flake thickness, edge type and other topological data. This technique requires considerable amount of time and additional steps and also the scan size is usually small. Another powerful imaging technique is electron microscopy (EM), where high energy electrons with wavelength 2.5 pm at 200 KeV are focused with magnetic lenses providing a resolution of 50 nm and magnification 10^7 times depending on the EM technique [173]. Most commonly used techniques for characterizing hBN flakes are scanning electron microscopy (SEM) which only scans the surface and transmission electron microscopy (TEM) which gives in depth information about hBN crystal [96]. Composition characteristics can be obtained by methods such as energy dispersive X-ray (EDX) [174] or electron energy loss spectroscopy (EELS) [175] which are an auxiliary feature of SEM and TEM. Another non-invasive technique is optical microscopy (OM) where hBN flake is placed on a contrasting surface such as silicon substrate coated with 80 nm thick silicon dioxide (SiO_2) [176] to optimize the viewing conditions and get an estimation of number of layers [177, 178]. Although this method is not accurate but it is quick and very convenient for preliminary checks on hBN flakes before using another sophisticated technique. Raman spectroscopy (a technique that probes the vibration modes of a system via elastic scattering) is also used to determine number of layers by probing the E_{2g} optical phonon coupling(See chapter- 4, phonon sideband analysis for details on E_{2g} phonon mode). Increase in number of layers increases the inter-layer interactions and the stretching E_{2g} phonon mode energy decreases [178]. A detailed study of phonon coupling is presented later in this thesis which can be used to estimate the number of layers in the sample by just observing the PL spectra [113].

References

[1] GILBERT N. LEWIS. The conservation of photons. *Nature*, 118(2981):874–875, December 1926.

[2] Claude Cohen-Tannoudji, Jacques Dupont-Roc, and Gilbert Grynberg. *Photons and Atoms*. Wiley, March 1997.

[3] Sheng-Kai Liao, Wen-Qi Cai, Wei-Yue Liu, Liang Zhang, Yang Li, Ji-Gang Ren, Juan Yin, Qi Shen, Yuan Cao, Zheng-Ping Li, Feng-Zhi Li, Xia-Wei Chen, Li-Hua Sun, Jian-Jun Jia, Jin-Cai Wu, Xiao-Jun Jiang, Jian-Feng Wang, Yong-Mei Huang, Qiang Wang, Yi-Lin Zhou, Lei Deng, Tao Xi, Lu Ma, Tai Hu, Qiang Zhang, Yu-Ao Chen, Nai-Le Liu, Xiang-Bin Wang, Zhen-Cai Zhu, Chao-Yang Lu, Rong Shu, Cheng-Zhi Peng, Jian-Yu Wang, and Jian-Wei Pan. Satellite-to-ground quantum key distribution. *Nature*, 549(7670):43–47, August 2017.

[4] Mark Fox. *Quantum optics: an introduction*. Oxford master series in atomic, optical, and laser physics. Oxford Univ. Press, Oxford, 2006.

[5] R. HANBURY BROWN and R. Q. TWISS. Correlation between photons in two coherent beams of light. *Nature*, 177(4497):27–29, January 1956.

[6] Interferometry of the intensity fluctuations in light - i. basic theory: the correlation between photons in coherent beams of radiation. *Proceedings of the Royal Society of London. Series A. Mathematical and Physical Sciences*, 242(1230):300–324, November 1957.

[7] Interferometry of the intensity fluctuations in light. II. an experimental test of the theory for partially coherent light. *Proceedings of the Royal Society of London. Series A. Mathematical and Physical Sciences*, 243(1234):291–319, January 1958.

[8] Brahim Lounis and Michel Orrit. Single-photon sources. *Reports on Progress in Physics*, 68(5):1129–1179, April 2005.

[9] H. J. Kimble, M. Dagenais, and L. Mandel. Photon antibunching in resonance fluorescence. *Phys. Rev. Lett.*, 39:691–695, Sep 1977.

[10] M Hennrich, T Legero, A Kuhn, and G Rempe. Photon statistics of a non-stationary periodically driven single-photon source. *New Journal of Physics*, 6:86–86, July 2004.

[11] Markus Hijlkema, Bernhard Weber, Holger P. Specht, Simon C. Webster, Axel Kuhn, and Gerhard Rempe. A single-photon server with just one atom. *Nature Physics*, 3(4):253–255, March 2007.

[12] Axel Kuhn, Markus Hennrich, and Gerhard Rempe. Deterministic single-photon source for distributed quantum networking. *Physical Review Letters*, 89(6), July 2002.

[13] T. Wilk, S. C. Webster, H. P. Specht, G. Rempe, and A. Kuhn. Polarization-controlled single photons. *Physical Review Letters*, 98(6), February 2007.

[14] B. Dayan, A. S. Parkins, T. Aoki, E. P. Ostby, K. J. Vahala, and H. J. Kimble. A photon turnstile dynamically regulated by one atom. *Science*, 319(5866):1062–1065, February 2008.

[15] Takao Aoki, A. S. Parkins, D. J. Alton, C. A. Regal, Barak Dayan, E. Ostby, K. J. Vahala, and H. J. Kimble. Efficient routing of single photons by one atom and a microtoroidal cavity. *Physical Review Letters*, 102(8), February 2009.

[16] U. Gaubatz, P. Rudecki, M. Becker, S. Schiemann, M. Külz, and K. Bergmann. Population switching between vibrational levels in molecular beams. *Chemical Physics Letters*, 149(5-6):463–468, September 1988.

[17] J. McKeever. Deterministic generation of single photons from one atom trapped in a cavity. *Science*, 303(5666):1992–1994, March 2004.

[18] L.-M. Duan, A. Kuzmich, and H. J. Kimble. Cavity QED and quantum-information processing with "hot" trapped atoms. *Physical Review A*, 67(3), March 2003.

[19] Christian Maurer, Christoph Becher, Carlos Russo, Jürgen Eschner, and Rainer Blatt. A single-photon source based on a single caion. *New Journal of Physics*, 6:94–94, July 2004.

[20] Matthias Keller, Birgit Lange, Kazuhiro Hayasaka, Wolfgang Lange, and Herbert Walther. Continuous generation of single photons with controlled waveform in an ion-trap cavity system. *Nature*, 431(7012):1075–1078, October 2004.

[21] H G Barros, A Stute, T E Northup, C Russo, P O Schmidt, and R Blatt. Deterministic single-photon source from a single ion. *New Journal of Physics*, 11(10):103004, October 2009.

[22] M. D. Eisaman, J. Fan, A. Migdall, and S. V. Polyakov. Invited review article: Single-photon sources and detectors. *Review of Scientific Instruments*, 82(7):071101, July 2011.

[23] Ian Bezek. Nasdaq ionq. Available at https://www.nasdaq.com/articles/ionq-is-the-first-publicly-traded-quantum-computing-firm-2021-10-21, October 2021.

[24] Christian Brunel, Brahim Lounis, Philippe Tamarat, and Michel Orrit. Triggered source of single photons based on controlled single molecule fluorescence. *Physical Review Letters*, 83(14):2722–2725, October 1999.

[25] S. C. Kitson, P. Jonsson, J. G. Rarity, and P. R. Tapster. Intensity fluctuation spectroscopy of small numbers of dye molecules in a microcavity. *Physical Review A*, 58(1):620–627, July 1998.

[26] A. Kiraz, S. Fälth, C. Becher, B. Gayral, W. V. Schoenfeld, P. M. Petroff, Lidong Zhang, E. Hu, and A. Imamoğlu. Photon correlation spectroscopy of a single quantum dot. *Physical Review B*, 65(16), March 2002.

[27] B. Lounis and W. E. Moerner. Single photons on demand from a single molecule at room temperature. *Nature*, 407(6803):491–493, September 2000.

[28] A. Kiraz, M. Ehrl, Th. Hellerer, Ö. E. Müstecaplıoğlu, C. Bräuchle, and A. Zumbusch. Indistinguishable photons from a single molecule. *Physical Review Letters*, 94(22), June 2005.

[29] Li Zhang, Yun-Jie Yu, Liu-Guo Chen, Yang Luo, Ben Yang, Fan-Fang Kong, Gong Chen, Yang Zhang, Qiang Zhang, Yi Luo, Jin-Long Yang, Zhen-Chao Dong, and J. G. Hou. Electrically driven single-photon emission from an isolated single molecule. *Nature Communications*, 8(1), September 2017.

[30] Igor Aharonovich, Dirk Englund, and Milos Toth. Solid-state single-photon emitters. *Nature Photonics*, 10(10):631–641, September 2016.

[31] Satoshi Kako, Charles Santori, Katsuyuki Hoshino, Stephan Götzinger, Yoshihisa Yamamoto, and Yasuhiko Arakawa. A gallium nitride single-photon source operating at 200 k. *Nature Materials*, 5(11):887–892, October 2006.

[32] Andrew J. Shields. Semiconductor quantum light sources. *Nature Photonics*, 1(4):215–223, April 2007.

[33] A. J. Bennett, D. C. Unitt, P. Atkinson, D. A. Ritchie, and A. J. Shields. High performance single photon sources from photolithographically defined pillar microcavities. *Optics Express*, 13(1):50, 2005.

[34] P. Michler. A quantum dot single-photon turnstile device. *Science*, 290(5500):2282–2285, December 2000.

[35] Charles Santori, David Fattal, Jelena Vučković, Glenn S. Solomon, and Yoshihisa Yamamoto. Indistinguishable photons from a single-photon device. *Nature*, 419(6907):594–597, October 2002.

[36] Z. Yuan. Electrically driven single-photon source. *Science*, 295(5552):102–105, December 2001.

[37] V. Zwiller, T. Aichele, W. Seifert, J. Persson, and O. Benson. Generating visible single photons on demand with single InP quantum dots. *Applied Physics Letters*, 82(10):1509–1511, March 2003.

[38] A. J. Shields, M. P. O'Sullivan, I. Farrer, D. A. Ritchie, R. A. Hogg, M. L. Leadbeater, C. E. Norman, and M. Pepper. Detection of single photons using a field-effect transistor gated by a layer of quantum dots. *Applied Physics Letters*, 76(25):3673–3675, June 2000.

[39] Oliver Benson, Charles Santori, Matthew Pelton, and Yoshihisa Yamamoto. Regulated and entangled photons from a single quantum dot. *Physical Review Letters*, 84(11):2513–2516, March 2000.

[40] E. Moreau, I. Robert, J. M. Gérard, I. Abram, L. Manin, and V. Thierry-Mieg. Single-mode solid-state single photon source based on isolated quantum dots in pillar microcavities. *Applied Physics Letters*, 79(18):2865–2867, October 2001.

[41] Charles Santori, Matthew Pelton, Glenn Solomon, Yseulte Dale, and Yoshihisa Yamamoto. Triggered single photons from a quantum dot. *Physical Review Letters*, 86(8):1502–1505, February 2001.

[42] Matthew Pelton, Charles Santori, Jelena Vuc
ković, Bingyang Zhang, Glenn S. Solomon, Jocelyn Plant, and Yoshihisa Yamamoto. Efficient source of single photons: A single quantum dot in a micropost microcavity. *Physical Review Letters*, 89(23), November 2002.

[43] D C Unitt, A J Bennett, P Atkinson, K Cooper, P See, D Gevaux, M B Ward, R M Stevenson, D A Ritchie, and A J Shields. Quantum dots as single-photon sources for quantum information processing. *Journal of Optics B: Quantum and Semiclassical Optics*, 7(7):S129–S134, June 2005.

[44] A. Kress, F. Hofbauer, N. Reinelt, M. Kaniber, H. J. Krenner, R. Meyer, G. Böhm, and J. J. Finley. Manipulation of the spontaneous emission dynamics of quantum dots in two-dimensional photonic crystals. *Physical Review B*, 71(24), June 2005.

[45] S. Laurent, S. Varoutsis, L. Le Gratiet, A. Lemaître, I. Sagnes, F. Raineri, A. Levenson, I. Robert-Philip, and I. Abram. Indistinguishable single photons from a single-quantum dot in a two-dimensional photonic crystal cavity. *Applied Physics Letters*, 87(16):163107, October 2005.

[46] David Press, Stephan Götzinger, Stephan Reitzenstein, Carolin Hofmann, Andreas Löffler, Martin Kamp, Alfred Forchel, and Yoshihisa Yamamoto. Photon antibunching from a single quantum-dot-microcavity system in the strong coupling regime. *Physical Review Letters*, 98(11), March 2007.

[47] M. B. Ward, T. Farrow, P. See, Z. L. Yuan, O. Z. Karimov, A. J. Bennett, A. J. Shields, P. Atkinson, K. Cooper, and D. A. Ritchie. Electrically driven telecommunication wavelength single-photon source. *Applied Physics Letters*, 90(6):063512, February 2007.

[48] X. Brokmann, E. Giacobino, M. Dahan, and J. P. Hermier. Highly efficient triggered emission of single photons by colloidal CdSeZnS nanocrystals. *Applied Physics Letters*, 85(5):712–714, August 2004.

[49] G. J. Beirne, P. Michler, M. Jetter, and H. Schweizer. Single-photon emission from a type-b InPGaInP quantum dot. *Journal of Applied Physics*, 98(9):093522, November 2005.

[50] Neil S. Beattie, Patrick See, Guillaume Zoppi, Palat M. Ushasree, Martial Duchamp, Ian Farrer, David A. Ritchie, and Stanko Tomić. Quantum engineering of InAs/GaAs

quantum dot based intermediate band solar cells. *ACS Photonics*, 4(11):2745–2750, October 2017.

[51] Saniya Deshpande, Junseok Heo, Ayan Das, and Pallab Bhattacharya. Electrically driven polarized single-photon emission from an InGaN quantum dot in a GaN nanowire. *Nature Communications*, 4(1), April 2013.

[52] D. Leonard, M. Krishnamurthy, C. M. Reaves, S. P. Denbaars, and P. M. Petroff. Direct formation of quantum-sized dots from uniform coherent islands of InGaAs on GaAs surfaces. *Applied Physics Letters*, 63(23):3203–3205, December 1993.

[53] E. M. Purcell, H. C. Torrey, and R. V. Pound. Resonance absorption by nuclear magnetic moments in a solid. *Physical Review*, 69(1-2):37–38, January 1946.

[54] Yan Chen, Michael Zopf, Robert Keil, Fei Ding, and Oliver G. Schmidt. Highly-efficient extraction of entangled photons from quantum dots using a broadband optical antenna. *Nature Communications*, 9(1), July 2018.

[55] Igor Aharonovich and Elke Neu. Diamond nanophotonics. *Advanced Optical Materials*, 2(10):911–928, July 2014.

[56] A. Sipahigil, K. D. Jahnke, L. J. Rogers, T. Teraji, J. Isoya, A. S. Zibrov, F. Jelezko, and M. D. Lukin. Indistinguishable photons from separated silicon-vacancy centers in diamond. *Physical Review Letters*, 113(11), September 2014.

[57] A. Sipahigil, M. L. Goldman, E. Togan, Y. Chu, M. Markham, D. J. Twitchen, A. S. Zibrov, A. Kubanek, and M. D. Lukin. Quantum interference of single photons from remote nitrogen-vacancy centers in diamond. *Physical Review Letters*, 108(14), April 2012.

[58] Elke Neu, David Steinmetz, Janine Riedrich-Möller, Stefan Gsell, Martin Fischer, Matthias Schreck, and Christoph Becher. Single photon emission from silicon-vacancy colour centres in chemical vapour deposition nano-diamonds on iridium. *New Journal of Physics*, 13(2):025012, February 2011.

[59] Tim Schröder, Friedemann Gädeke, Moritz Julian Banholzer, and Oliver Benson. Ultrabright and efficient single-photon generation based on nitrogen-vacancy centres in nanodiamonds on a solid immersion lens. *New Journal of Physics*, 13(5):055017, May 2011.

[60] A. Lohrmann, N. Iwamoto, Z. Bodrog, S. Castelletto, T. Ohshima, T.J. Karle, A. Gali, S. Prawer, J.C. McCallum, and B.C. Johnson. Single-photon emitting diode in silicon carbide. *Nature Communications*, 6(1), July 2015.

[61] S. Castelletto, B. C. Johnson, V. Ivády, N. Stavrias, T. Umeda, A. Gali, and T. Ohshima. A silicon carbide room-temperature single-photon source. *Nature Materials*, 13(2):151–156, November 2013.

[62] Anthony J. Morfa, Brant C. Gibson, Matthias Karg, Timothy J. Karle, Andrew D. Greentree, Paul Mulvaney, and Snjezana Tomljenovic-Hanic. Single-photon emission and quantum characterization of zinc oxide defects. *Nano Letters*, 12(2):949–954, January 2012.

[63] R. Kolesov, K. Xia, R. Reuter, R. Stöhr, A. Zappe, J. Meijer, P.R. Hemmer, and J. Wrachtrup. Optical detection of a single rare-earth ion in a crystal. *Nature Communications*, 3(1), January 2012.

[64] Kangwei Xia, Roman Kolesov, Ya Wang, Petr Siyushev, Rolf Reuter, Thomas Kornher, Nadezhda Kukharchyk, Andreas D. Wieck, Bruno Villa, Sen Yang, and Jörg Wrachtrup. All-optical preparation of coherent dark states of a single rare earth ion spin in a crystal. *Physical Review Letters*, 115(9), August 2015.

[65] Roman Kolesov, Kangwei Xia, Rolf Reuter, Mohammad Jamali, Rainer Stöhr, Tugrul Inal, Petr Siyushev, and Jörg Wrachtrup. Mapping spin coherence of a single rare-earth ion in a crystal onto a single photon polarization state. *Physical Review Letters*, 111(12), September 2013.

[66] T. Utikal, E. Eichhammer, L. Petersen, A. Renn, S. Götzinger, and V. Sandoghdar. Spectroscopic detection and state preparation of a single praseodymium ion in a crystal. *Nature Communications*, 5(1), April 2014.

[67] Ippei Nakamura, Tatsuya Yoshihiro, Hironori Inagawa, Satoru Fujiyoshi, and Michio Matsushita. Spectroscopy of single pr3 ion in LaF3 crystal at 1.5 k. *Scientific Reports*, 4(1), December 2014.

[68] Andrey A. Shiryaev, Jonathan A. Hinks, Nigel A. Marks, Graeme Greaves, Felipe J. Valencia, Stephen E. Donnelly, Rafael I. González, Miguel Kiwi, Alexander L. Trigub, Eduardo M. Bringa, Jason L. Fogg, and Igor I. Vlasov. Ion implantation in nanodiamonds: size effect and energy dependence. *Scientific Reports*, 8(1), March 2018.

[69] V. G. Ralchenko, V. S. Sedov, A. A. Khomich, V. S. Krivobok, S. N. Nikolaev, S. S. Savin, I. I. Vlasov, and V. I. Konov. Observation of the ge-vacancy color center in microcrystalline diamond films. *Bulletin of the Lebedev Physics Institute*, 42(6):165–168, June 2015.

[70] Takayuki Iwasaki, Fumitaka Ishibashi, Yoshiyuki Miyamoto, Yuki Doi, Satoshi Kobayashi, Takehide Miyazaki, Kosuke Tahara, Kay D. Jahnke, Lachlan J. Rogers, Boris Naydenov, Fedor Jelezko, Satoshi Yamasaki, Shinji Nagamachi, Toshiro Inubushi, Norikazu Mizuochi, and Mutsuko Hatano. Germanium-vacancy single color centers in diamond. *Scientific Reports*, 5(1), August 2015.

[71] Benjamin Lienhard, Tim Schröder, Sara Mouradian, Florian Dolde, Toan Trong Tran, Igor Aharonovich, and Dirk Englund. Bright and photostable single-photon emitter in silicon carbide. *Optica*, 3(7):768, July 2016.

[72] William F. Koehl, Bob B. Buckley, F. Joseph Heremans, Greg Calusine, and David D. Awschalom. Room temperature coherent control of defect spin qubits in silicon carbide. *Nature*, 479(7371):84–87, November 2011.

[73] Abram L. Falk, Bob B. Buckley, Greg Calusine, William F. Koehl, Viatcheslav V. Dobrovitski, Alberto Politi, Christian A. Zorman, Philip X.-L. Feng, and David D. Awschalom. Polytype control of spin qubits in silicon carbide. *Nature Communications*, 4(1), May 2013.

[74] D. Riedel, F. Fuchs, H. Kraus, S. Väth, A. Sperlich, V. Dyakonov, A. A. Soltamova, P. G. Baranov, V. A. Ilyin, and G. V. Astakhov. Resonant addressing and manipulation of silicon vacancy qubits in silicon carbide. *Physical Review Letters*, 109(22), November 2012.

[75] David J. Christle, Abram L. Falk, Paolo Andrich, Paul V. Klimov, Jawad Ul Hassan, Nguyen T. Son, Erik Janzén, Takeshi Ohshima, and David D. Awschalom. Isolated electron spins in silicon carbide with millisecond coherence times. *Nature Materials*, 14(2):160–163, December 2014.

[76] Matthias Widmann, Sang-Yun Lee, Torsten Rendler, Nguyen Tien Son, Helmut Fedder, Seoyoung Paik, Li-Ping Yang, Nan Zhao, Sen Yang, Ian Booker, Andrej Denisenko, Mohammad Jamali, S. Ali Momenzadeh, Ilja Gerhardt, Takeshi Ohshima, Adam Gali, Erik Janzén, and Jörg Wrachtrup. Coherent control of single spins in silicon carbide at room temperature. *Nature Materials*, 14(2):164–168, December 2014.

[77] Giulia Pacchioni. Spin qubits: Useful defects in silicon carbide. *Nature Reviews Materials*, 2(8), July 2017.

[78] Oliver Neitzke, Anthony Morfa, Janik Wolters, Andreas W. Schell, Günter Kewes, and Oliver Benson. Investigation of line width narrowing and spectral jumps of single stable defect centers in ZnO at cryogenic temperature. *Nano Letters*, 15(5):3024–3029, March 2015.

[79] N. R. Jungwirth, Y. Y. Pai, H. S. Chang, E. R. MacQuarrie, K. X. Nguyen, and G. D. Fuchs. A single-molecule approach to ZnO defect studies: Single photons and single defects. *Journal of Applied Physics*, 116(4):043509, July 2014.

[80] Nicholas R. Jungwirth, Hung-Shen Chang, Mingde Jiang, and Gregory D. Fuchs. Polarization spectroscopy of defect-based single photon sources in ZnO. *ACS Nano*, 10(1):1210–1215, December 2015.

[81] Sumin Choi, Brett C. Johnson, Stefania Castelletto, Cuong Ton-That, Matthew R. Phillips, and Igor Aharonovich. Single photon emission from ZnO nanoparticles. *Applied Physics Letters*, 104(26):261101, June 2014.

[82] Ajit Srivastava, Meinrad Sidler, Adrien V. Allain, Dominik S. Lembke, Andras Kis, and A. Imamoğlu. Optically active quantum dots in monolayer WSe2. *Nature Nanotechnology*, 10(6):491–496, May 2015.

[83] Yu-Ming He, Genevieve Clark, John R. Schaibley, Yu He, Ming-Cheng Chen, Yu-Jia Wei, Xing Ding, Qiang Zhang, Wang Yao, Xiaodong Xu, Chao-Yang Lu, and Jian-Wei Pan. Single quantum emitters in monolayer semiconductors. *Nature Nanotechnology*, 10(6):497–502, May 2015.

[84] M. Koperski, K. Nogajewski, A. Arora, V. Cherkez, P. Mallet, J.-Y. Veuillen, J. Marcus, P. Kossacki, and M. Potemski. Single photon emitters in exfoliated WSe2 structures. *Nature Nanotechnology*, 10(6):503–506, May 2015.

[85] Toan Trong Tran, Kerem Bray, Michael J. Ford, Milos Toth, and Igor Aharonovich. Quantum emission from hexagonal boron nitride monolayers. *Nature Nanotechnology*, 11(1):37–41, October 2015.

[86] Chitraleema Chakraborty, Nick Vamivakas, and Dirk Englund. Advances in quantum light emission from 2d materials. *Nanophotonics*, 8(11):2017–2032, August 2019.

[87] Lukas Linhart, Matthias Paur, Valerie Smejkal, Joachim Burgdörfer, Thomas Mueller, and Florian Libisch. Localized intervalley defect excitons as single-photon emitters in wse_2. *Phys. Rev. Lett.*, 123:146401, Sep 2019.

[88] Yu Jie Zheng, Yifeng Chen, Yu Li Huang, Pranjal Kumar Gogoi, Ming-Yang Li, Lain-Jong Li, Paolo E. Trevisanutto, Qixing Wang, Stephen J. Pennycook, Andrew T. S. Wee, and Su Ying Quek. Point defects and localized excitons in 2d WSe2. *ACS Nano*, 13(5):6050–6059, May 2019.

[89] Santosh Kumar, Mauro Brotóns-Gisbert, Rima Al-Khuzheyri, Artur Branny, Guillem Ballesteros-Garcia, Juan F. Sánchez-Royo, and Brian D. Gerardot. Resonant laser spectroscopy of localized excitons in monolayer WSe_2. *Optica*, 3(8):882, August 2016.

[90] Chandriker Kavir Dass, Mahtab A. Khan, Genevieve Clark, Jeffrey A. Simon, Ricky Gibson, Shin Mou, Xiaodong Xu, Michael N. Leuenberger, and Joshua R. Hendrickson. Ultra-long lifetimes of single quantum emitters in monolayer WSe 2 /hBN heterostructures. *Advanced Quantum Technologies*, 2(5-6):1900022, April 2019.

[91] L. J. Martínez, T. Pelini, V. Waselowski, J. R. Maze, B. Gil, G. Cassabois, and V. Jacques. Efficient single photon emission from a high-purity hexagonal boron nitride crystal. *Physical Review B*, 94(12), September 2016.

[92] Mehran Kianinia, Blake Regan, Sherif Abdulkader Tawfik, Toan Trong Tran, Michael J. Ford, Igor Aharonovich, and Milos Toth. Robust solid-state quantum system operating at 800 k. *ACS Photonics*, 4(4):768–773, March 2017.

[93] Sonia Buckley, Kelley Rivoire, and Jelena Vučković. Engineered quantum dot single-photon sources. *Reports on Progress in Physics*, 75(12):126503, November 2012.

[94] Janik Wolters, Nikola Sadzak, Andreas W. Schell, Tim Schröder, and Oliver Benson. Measurement of the ultrafast spectral diffusion of the optical transition of nitrogen vacancy centers in nano-size diamond using correlation interferometry. *Physical Review Letters*, 110(2), January 2013.

[95] Simon White, Connor Stewart, Alexander S. Solntsev, Chi Li, Milos Toth, Mehran Kianinia, and Igor Aharonovich. Phonon dephasing and spectral diffusion of quantum emitters in hexagonal boron nitride. *Optica*, 8(9):1153, August 2021.

[96] Yi Lin and John W. Connell. Advances in 2d boron nitride nanostructures: nanosheets, nanoribbons, nanomeshes, and hybrids with graphene. *Nanoscale*, 4(22):6908, 2012.

[97] Seokmo Hong, Chang-Seok Lee, Min-Hyun Lee, Yeongdong Lee, Kyung Yeol Ma, Gwangwoo Kim, Seong In Yoon, Kyuwook Ihm, Ki-Jeong Kim, Tae Joo Shin, Sang Won Kim, Eun chae Jeon, Hansol Jeon, Ju-Young Kim, Hyung-Ik Lee, Zonghoon Lee, Aleandro Antidormi, Stephan Roche, Manish Chhowalla, Hyeon-Jin Shin, and Hyeon Suk Shin. Ultralow-dielectric-constant amorphous boron nitride. *Nature*, 582(7813):511–514, June 2020.

[98] A. Nagakubo, H. Ogi, H. Sumiya, K. Kusakabe, and M. Hirao. Elastic constants of cubic and wurtzite boron nitrides. *Applied Physics Letters*, 102(24):241909, June 2013.

[99] Kenji Watanabe, Takashi Taniguchi, Kenta Miya, Yoshitaka Sato, Kazuhito Nakamura, Takahiro Niiyama, and Masateru Taniguchi. Hexagonal boron nitride as a new ultraviolet luminescent material and its application—fluorescence properties of hBN single-crystal powder. *Diamond and Related Materials*, 20(5-6):849–852, May 2011.

[100] Hyo Ju Park, Janghwan Cha, Min Choi, Jung Hwa Kim, Roland Yingjie Tay, Edwin Hang Tong Teo, Noejung Park, Suklyun Hong, and Zonghoon Lee. One-dimensional hexagonal boron nitride conducting channel. *Science Advances*, 6(10), 2020.

[101] S Matt Gilbert, Thang Pham, Mehmet Dogan, Sehoon Oh, Brian Shevitski, Gabe Schumm, Stanley Liu, Peter Ercius, Shaul Aloni, Marvin L Cohen, and Alex Zettl. Alternative stacking sequences in hexagonal boron nitride. *2D Materials*, 6(2):021006, mar 2019.

[102] K. S. Novoselov, D. Jiang, F. Schedin, T. J. Booth, V. V. Khotkevich, S. V. Morozov, and A. K. Geim. Two-dimensional atomic crystals. *Proceedings of the National Academy of Sciences*, 102(30):10451–10453, July 2005.

[103] K. S. Novoselov. Electric field effect in atomically thin carbon films. *Science*, 306(5696):666–669, October 2004.

[104] Lu Hua Li, Ying Chen, Gavin Behan, Hongzhou Zhang, Mladen Petravic, and Alexey M. Glushenkov. Large-scale mechanical peeling of boron nitride nanosheets by low-energy ball milling. *Journal of Materials Chemistry*, 21(32):11862, 2011.

[105] V. Nicolosi, M. Chhowalla, M. G. Kanatzidis, M. S. Strano, and J. N. Coleman. Liquid exfoliation of layered materials. *Science*, 340(6139):1226419–1226419, June 2013.

[106] Oded Hod. Graphite and hexagonal boron-nitride have the same interlayer distance. why? *Journal of Chemical Theory and Computation*, 8(4):1360–1369, February 2012.

[107] Aleksey Falin, Qiran Cai, Elton J.G. Santos, Declan Scullion, Dong Qian, Rui Zhang, Zhi Yang, Shaoming Huang, Kenji Watanabe, Takashi Taniguchi, Matthew R. Barnett, Ying Chen, Rodney S. Ruoff, and Lu Hua Li. Mechanical properties of atomically thin boron nitride and the role of interlayer interactions. *Nature Communications*, 8(1), June 2017.

[108] G. Cassabois, P. Valvin, and B. Gil. Hexagonal boron nitride is an indirect bandgap semiconductor. *Nature Photonics*, 10(4):262–266, January 2016.

[109] Haotian Yang, Hailiang Fang, Hui Yu, Yongjun Chen, Lianjun Wang, Wan Jiang, Yiquan Wu, and Jianlin Li. Low temperature self-densification of high strength bulk hexagonal boron nitride. *Nature Communications*, 10(1), February 2019.

[110] Lu Hua Li, Jiri Cervenka, Kenji Watanabe, Takashi Taniguchi, and Ying Chen. Strong oxidation resistance of atomically thin boron nitride nanosheets. *ACS Nano*, 8(2):1457–1462, January 2014.

[111] Cem Sevik, Alper Kinaci, Justin B. Haskins, and Tahir Çağın. Characterization of thermal transport in low-dimensional boron nitride nanostructures. *Physical Review B*, 84(8), August 2011.

[112] H. Şahin, S. Cahangirov, M. Topsakal, E. Bekaroglu, E. Akturk, R. T. Senger, and S. Ciraci. Monolayer honeycomb structures of group-IV elements and III-v binary compounds: First-principles calculations. *Physical Review B*, 80(15), October 2009.

[113] P. Khatri, I. J. Luxmoore, and A. J. Ramsay. Phonon sidebands of color centers in hexagonal boron nitride. *Physical Review B*, 100(12), September 2019.

[114] Chi Li, Zai-Quan Xu, Noah Mendelson, Mehran Kianinia, Milos Toth, and Igor Aharonovich. Purification of single-photon emission from hBN using post-processing treatments. *Nanophotonics*, 8(11):2049–2055, July 2019.

[115] Noah Mendelson, Zai-Quan Xu, Toan Trong Tran, Mehran Kianinia, John Scott, Carlo Bradac, Igor Aharonovich, and Milos Toth. Engineering and tuning of quantum

emitters in few-layer hexagonal boron nitride. *ACS Nano*, 13(3):3132–3140, February 2019.

[116] Toan Trong Tran, Christopher Elbadawi, Daniel Totonjian, Charlene J. Lobo, Gabriele Grosso, Hyowon Moon, Dirk R. Englund, Michael J. Ford, Igor Aharonovich, and Milos Toth. Robust multicolor single photon emission from point defects in hexagonal boron nitride. *ACS Nano*, 10(8):7331–7338, July 2016.

[117] T. Q. P. Vuong, G. Cassabois, P. Valvin, A. Ouerghi, Y. Chassagneux, C. Voisin, and B. Gil. Phonon-photon mapping in a color center in hexagonal boron nitride. *Physical Review Letters*, 117(9), August 2016.

[118] Romain Bourrellier, Sophie Meuret, Anna Tararan, Odile Stéphan, Mathieu Kociak, Luiz H. G. Tizei, and Alberto Zobelli. Bright UV single photon emission at point defects in h-BN. *Nano Letters*, 16(7):4317–4321, June 2016.

[119] Xiangzhi Li, Gabriella D. Shepard, Andrew Cupo, Nicolas Camporeale, Kamran Shayan, Yue Luo, Vincent Meunier, and Stefan Strauf. Nonmagnetic quantum emitters in boron nitride with ultranarrow and sideband-free emission spectra. *ACS Nano*, 11(7):6652–6660, May 2017.

[120] Brian Shevitski, S. Matt Gilbert, Christopher T. Chen, Christoph Kastl, Edward S. Barnard, Ed Wong, D. Frank Ogletree, Kenji Watanabe, Takashi Taniguchi, Alex Zettl, and Shaul Aloni. Blue-light-emitting color centers in high-quality hexagonal boron nitride. *Physical Review B*, 100(15), October 2019.

[121] Milos Toth and Igor Aharonovich. Single photon sources in atomically thin materials. *Annual Review of Physical Chemistry*, 70(1):123–142, June 2019.

[122] Annemarie L. Exarhos, David A. Hopper, Richard R. Grote, Audrius Alkauskas, and Lee C. Bassett. Optical signatures of quantum emitters in suspended hexagonal boron nitride. *ACS Nano*, 11(3):3328–3336, March 2017.

[123] Sherif Abdulkader Tawfik, Sajid Ali, Marco Fronzi, Mehran Kianinia, Toan Trong Tran, Catherine Stampfl, Igor Aharonovich, Milos Toth, and Michael J. Ford. First-principles investigation of quantum emission from hBN defects. *Nanoscale*, 9(36):13575–13582, 2017.

[124] Mehdi Abdi, Jyh-Pin Chou, Adam Gali, and Martin B. Plenio. Color centers in hexagonal boron nitride monolayers: A group theory and ab initio analysis. *ACS Photonics*, 5(5):1967–1976, April 2018.

[125] A. Sajid, Jeffrey R. Reimers, and Michael J. Ford. Defect states in hexagonal boron nitride: Assignments of observed properties and prediction of properties relevant to quantum computation. *Physical Review B*, 97(6), February 2018.

[126] Viktor Ivády, Gergely Barcza, Gergő Thiering, Song Li, Hanen Hamdi, Jyh-Pin Chou, Örs Legeza, and Adam Gali. Ab initio theory of the negatively charged boron vacancy qubit in hexagonal boron nitride. *npj Computational Materials*, 6(1), April 2020.

[127] Tobias Vogl, Geoff Campbell, Ben C. Buchler, Yuerui Lu, and Ping Koy Lam. Fabrication and deterministic transfer of high-quality quantum emitters in hexagonal boron nitride. *ACS Photonics*, 5(6):2305–2312, April 2018.

[128] Prince Khatri, Andrew J. Ramsay, Ralph Nicholas Edward Malein, Harold M. H. Chong, and Isaac J. Luxmoore. Optical gating of photoluminescence from color centers in hexagonal boron nitride. *Nano Letters*, 20(6):4256–4263, May 2020.

[129] Ralph Nicholas Edward Malein, Prince Khatri, Andrew J. Ramsay, and Isaac J. Luxmoore. Stimulated emission depletion spectroscopy of color centers in hexagonal boron nitride. *ACS Photonics*, 8(4):1007–1012, April 2021.

[130] Stefania Castelletto, Faraz A Inam, Shin ichiro Sato, and Alberto Boretti. Hexagonal boron nitride: a review of the emerging material platform for single-photon sources and the spin–photon interface. *Beilstein Journal of Nanotechnology*, 11:740–769, May 2020.

[131] Andreas Gottscholl, Matthias Diez, Victor Soltamov, Christian Kasper, Andreas Sperlich, Mehran Kianinia, Carlo Bradac, Igor Aharonovich, and Vladimir Dyakonov. Room temperature coherent control of spin defects in hexagonal boron nitride. *Science Advances*, 7(14):eabf3630, April 2021.

[132] A. Sajid, Kristian S. Thygesen, Jeffrey R. Reimers, and Michael J. Ford. Edge effects on optically detected magnetic resonance of vacancy defects in hexagonal boron nitride. *Communications Physics*, 3(1), August 2020.

[133] Gwan-Hyoung Lee, Young-Jun Yu, Xu Cui, Nicholas Petrone, Chul-Ho Lee, Min Sup Choi, Dae-Yeong Lee, Changgu Lee, Won Jong Yoo, Kenji Watanabe, Takashi

Taniguchi, Colin Nuckolls, Philip Kim, and James Hone. Flexible and transparent MoS2 field-effect transistors on hexagonal boron nitride-graphene heterostructures. *ACS Nano*, 7(9):7931–7936, August 2013.

[134] A. V. Kretinin, Y. Cao, J. S. Tu, G. L. Yu, R. Jalil, K. S. Novoselov, S. J. Haigh, A. Gholinia, A. Mishchenko, M. Lozada, T. Georgiou, C. R. Woods, F. Withers, P. Blake, G. Eda, A. Wirsig, C. Hucho, K. Watanabe, T. Taniguchi, A. K. Geim, and R. V. Gorbachev. Electronic properties of graphene encapsulated with different two-dimensional atomic crystals. *Nano Letters*, 14(6):3270–3276, May 2014.

[135] C. R. Dean, A. F. Young, I. Meric, C. Lee, L. Wang, S. Sorgenfrei, K. Watanabe, T. Taniguchi, P. Kim, K. L. Shepard, and J. Hone. Boron nitride substrates for high-quality graphene electronics. *Nature Nanotechnology*, 5(10):722–726, August 2010.

[136] Achim Woessner, Mark B. Lundeberg, Yuanda Gao, Alessandro Principi, Pablo Alonso-González, Matteo Carrega, Kenji Watanabe, Takashi Taniguchi, Giovanni Vignale, Marco Polini, James Hone, Rainer Hillenbrand, and Frank H. L. Koppens. Highly confined low-loss plasmons in graphene–boron nitride heterostructures. *Nature Materials*, 14(4):421–425, December 2014.

[137] G. X. Ni, A. S. McLeod, Z. Sun, L. Wang, L. Xiong, K. W. Post, S. S. Sunku, B.-Y. Jiang, J. Hone, C. R. Dean, M. M. Fogler, and D. N. Basov. Fundamental limits to graphene plasmonics. *Nature*, 557(7706):530–533, May 2018.

[138] S. Dai, Z. Fei, Q. Ma, A. S. Rodin, M. Wagner, A. S. McLeod, M. K. Liu, W. Gannett, W. Regan, K. Watanabe, T. Taniguchi, M. Thiemens, G. Dominguez, A. H. C. Neto, A. Zettl, F. Keilmann, P. Jarillo-Herrero, M. M. Fogler, and D. N. Basov. Tunable phonon polaritons in atomically thin van der waals crystals of boron nitride. *Science*, 343(6175):1125–1129, March 2014.

[139] Joshua D. Caldwell, Andrey V. Kretinin, Yiguo Chen, Vincenzo Giannini, Michael M. Fogler, Yan Francescato, Chase T. Ellis, Joseph G. Tischler, Colin R. Woods, Alexander J. Giles, Minghui Hong, Kenji Watanabe, Takashi Taniguchi, Stefan A. Maier, and Kostya S. Novoselov. Sub-diffractional volume-confined polaritons in the natural hyperbolic material hexagonal boron nitride. *Nature Communications*, 5(1), October 2014.

[140] G. X. Ni, H. Wang, J. S. Wu, Z. Fei, M. D. Goldflam, F. Keilmann, B. Özyilmaz, A. H. Castro Neto, X. M. Xie, M. M. Fogler, and D. N. Basov. Plasmons in graphene moiré superlattices. *Nature Materials*, 14(12):1217–1222, September 2015.

[141] S. S. Sunku, G. X. Ni, B. Y. Jiang, H. Yoo, A. Sternbach, A. S. McLeod, T. Stauber, L. Xiong, T. Taniguchi, K. Watanabe, P. Kim, M. M. Fogler, and D. N. Basov. Photonic crystals for nano-light in moiré graphene superlattices. *Science*, 362(6419):1153–1156, December 2018.

[142] Hongyi Yu, Gui-Bin Liu, Jianju Tang, Xiaodong Xu, and Wang Yao. Moiré excitons: From programmable quantum emitter arrays to spin-orbit–coupled artificial lattices. *Science Advances*, 3(11):e1701696, November 2017.

[143] Pascale Senellart, Glenn Solomon, and Andrew White. High-performance semiconductor quantum-dot single-photon sources. *Nature Nanotechnology*, 12(11):1026–1039, November 2017.

[144] Jianwei Wang, Fabio Sciarrino, Anthony Laing, and Mark G. Thompson. Integrated photonic quantum technologies. *Nature Photonics*, 14(5):273–284, October 2019.

[145] T. Miyazawa, K. Takemoto, Y. Nambu, S. Miki, T. Yamashita, H. Terai, M. Fujiwara, M. Sasaki, Y. Sakuma, M. Takatsu, T. Yamamoto, and Y. Arakawa. Single-photon emission at 1.5 m from an InAs/InP quantum dot with highly suppressed multi-photon emission probabilities. *Applied Physics Letters*, 109(13):132106, September 2016.

[146] Kazuya Takemoto, Motomu Takatsu, Shinichi Hirose, Naoki Yokoyama, Yoshiki Sakuma, Tatsuya Usuki, Toshiyuki Miyazawa, and Yasuhiko Arakawa. An optical horn structure for single-photon source using quantum dots at telecommunication wavelength. *Journal of Applied Physics*, 101(8):081720, April 2007.

[147] Yasuhiko Arakawa and Mark J. Holmes. Progress in quantum-dot single photon sources for quantum information technologies: A broad spectrum overview. *Applied Physics Reviews*, 7(2):021309, June 2020.

[148] T. Müller, J. Skiba-Szymanska, A. B. Krysa, J. Huwer, M. Felle, M. Anderson, R. M. Stevenson, J. Heffernan, D. A. Ritchie, and A. J. Shields. A quantum light-emitting diode for the standard telecom window around 1, 550 nm. *Nature Communications*, 9(1), February 2018.

[149] M. Anderson, T. Müller, J. Huwer, J. Skiba-Szymanska, A. B. Krysa, R. M. Stevenson, J. Heffernan, D. A. Ritchie, and A. J. Shields. Quantum teleportation using highly coherent emission from telecom c-band quantum dots. *npj Quantum Information*, 6(1), January 2020.

[150] Ł. Dusanowski, M. Syperek, J. Misiewicz, A. Somers, S. Höfling, M. Kamp, J. P. Reithmaier, and G. Sęk. Single-photon emission of InAs/InP quantum dashes at 1.55 m and temperatures up to 80 k. *Applied Physics Letters*, 108(16):163108, April 2016.

[151] Xiangzhi Li, Robert A. Scully, Kamran Shayan, Yue Luo, and Stefan Strauf. Near-unity light collection efficiency from quantum emitters in boron nitride by coupling to metallo-dielectric antennas. *ACS Nano*, 13(6):6992–6997, May 2019.

[152] Joshua D. Caldwell, Igor Aharonovich, Guillaume Cassabois, James H. Edgar, Bernard Gil, and D. N. Basov. Photonics with hexagonal boron nitride. *Nature Reviews Materials*, 4(8):552–567, July 2019.

[153] Akbar Basha Dhu al-jalali-wal-ikram Shaik and Penchalaiah Palla. Optical quantum technologies with hexagonal boron nitride single photon sources. *Scientific Reports*, 11(1), June 2021.

[154] Elke Neu, David Steinmetz, Janine Riedrich-Möller, Stefan Gsell, Martin Fischer, Matthias Schreck, and Christoph Becher. Single photon emission from silicon-vacancy colour centres in chemical vapour deposition nano-diamonds on iridium. *New Journal of Physics*, 13(2):025012, feb 2011.

[155] Tim Schröder, Friedemann Gädeke, Moritz Julian Banholzer, and Oliver Benson. Ultrabright and efficient single-photon generation based on nitrogen-vacancy centres in nanodiamonds on a solid immersion lens. *New Journal of Physics*, 13(5):055017, may 2011.

[156] P. Siyushev, K. Xia, R. Reuter, M. Jamali, N. Zhao, N. Yang, C. Duan, N. Kukharchyk, A. D. Wieck, R. Kolesov, and J. Wrachtrup. Coherent properties of single rare-earth spin qubits. *Nature Communications*, 5(1), May 2014.

[157] Luca Sapienza, Marcelo Davanço, Antonio Badolato, and Kartik Srinivasan. Nanoscale optical positioning of single quantum dots for bright and pure single-photon emission. *Nature Communications*, 6(1), July 2015.

[158] Mark J. Holmes, Kihyun Choi, Satoshi Kako, Munetaka Arita, and Yasuhiko Arakawa. Room-temperature triggered single photon emission from a III-nitride site-controlled nanowire quantum dot. *Nano Letters*, 14(2):982–986, January 2014.

[159] Gabriele Grosso, Hyowon Moon, Benjamin Lienhard, Sajid Ali, Dmitri K. Efetov, Marco M. Furchi, Pablo Jarillo-Herrero, Michael J. Ford, Igor Aharonovich, and Dirk Englund. Tunable and high-purity room temperature single-photon emission from atomic defects in hexagonal boron nitride. *Nature Communications*, 8(1), September 2017.

[160] Kenji Watanabe, Takashi Taniguchi, and Hisao Kanda. Direct-bandgap properties and evidence for ultraviolet lasing of hexagonal boron nitride single crystal. *Nature Materials*, 3(6):404–409, May 2004.

[161] T. Taniguchi and K. Watanabe. Synthesis of high-purity boron nitride single crystals under high pressure by using ba–BN solvent. *Journal of Crystal Growth*, 303(2):525–529, May 2007.

[162] Mark Zastrow. Meet the crystal growers who sparked a revolution in graphene electronics. *Nature*, 572(7770):429–432, August 2019.

[163] Yuan Cao, Valla Fatemi, Shiang Fang, Kenji Watanabe, Takashi Taniguchi, Efthimios Kaxiras, and Pablo Jarillo-Herrero. Unconventional superconductivity in magic-angle graphene superlattices. *Nature*, 556(7699):43–50, March 2018.

[164] Yuan Cao, Valla Fatemi, Ahmet Demir, Shiang Fang, Spencer L. Tomarken, Jason Y. Luo, Javier D. Sanchez-Yamagishi, Kenji Watanabe, Takashi Taniguchi, Efthimios Kaxiras, Ray C. Ashoori, and Pablo Jarillo-Herrero. Correlated insulator behaviour at half-filling in magic-angle graphene superlattices. *Nature*, 556(7699):80–84, March 2018.

[165] Guorui Chen, Aaron L. Sharpe, Patrick Gallagher, Ilan T. Rosen, Eli J. Fox, Lili Jiang, Bosai Lyu, Hongyuan Li, Kenji Watanabe, Takashi Taniguchi, Jeil Jung, Zhiwen Shi, David Goldhaber-Gordon, Yuanbo Zhang, and Feng Wang. Signatures of tunable superconductivity in a trilayer graphene moiré superlattice. *Nature*, 572(7768):215–219, July 2019.

[166] Deepika, Lu Hua Li, Alexey M. Glushenkov, Samik K. Hait, Peter Hodgson, and Ying Chen. High-efficient production of boron nitride nanosheets via an optimized ball milling process for lubrication in oil. *Scientific Reports*, 4(1), December 2014.

[167] J. N. Coleman, M. Lotya, A. O'Neill, S. D. Bergin, P. J. King, U. Khan, K. Young, A. Gaucher, S. De, R. J. Smith, I. V. Shvets, S. K. Arora, G. Stanton, H.-Y. Kim, K. Lee, G. T. Kim, G. S. Duesberg, T. Hallam, J. J. Boland, J. J. Wang, J. F. Donegan, J. C. Grunlan, G. Moriarty, A. Shmeliov, R. J. Nicholls, J. M. Perkins, E. M. Grieveson, K. Theuwissen, D. W. McComb, P. D. Nellist, and V. Nicolosi. Two-dimensional nanosheets produced by liquid exfoliation of layered materials. *Science*, 331(6017):568–571, February 2011.

[168] Ronan J. Smith, Paul J. King, Mustafa Lotya, Christian Wirtz, Umar Khan, Sukanta De, Arlene O'Neill, Georg S. Duesberg, Jaime C. Grunlan, Gregory Moriarty, Jun Chen, Jiazhao Wang, Andrew I. Minett, Valeria Nicolosi, and Jonathan N. Coleman. Large-scale exfoliation of inorganic layered compounds in aqueous surfactant solutions. *Advanced Materials*, 23(34):3944–3948, July 2011.

[169] Kai-Ge Zhou, Nan-Nan Mao, Hang-Xing Wang, Yong Peng, and Hao-Li Zhang. A mixed-solvent strategy for efficient exfoliation of inorganic graphene analogues. *Angewandte Chemie International Edition*, 50(46):10839–10842, September 2011.

[170] Hongwei Liu, Chae Young You, Jingwei Li, Patrick Ryan Galligan, Jiawen You, Zhenjing Liu, Yuting Cai, and Zhengtang Luo. Synthesis of hexagonal boron nitrides by chemical vapor deposition and their use as single photon emitters. *Nano Materials Science*, April 2021.

[171] Teng Gao, Xiuju Song, Huiwen Du, Yufeng Nie, Yubin Chen, Qingqing Ji, Jingyu Sun, Yanlian Yang, Yanfeng Zhang, and Zhongfan Liu. Temperature-triggered chemical switching growth of in-plane and vertically stacked graphene-boron nitride heterostructures. *Nature Communications*, 6(1), April 2015.

[172] Vladimir V. Korolkov, Alex Summerfield, Alanna Murphy, David B. Amabilino, Kenji Watanabe, Takashi Taniguchi, and Peter H. Beton. Ultra-high resolution imaging of thin films and single strands of polythiophene using atomic force microscopy. *Nature Communications*, 10(1), April 2019.

[173] Rolf Erni, Marta D. Rossell, Christian Kisielowski, and Ulrich Dahmen. Atomic-resolution imaging with a sub-50-pm electron probe. *Physical Review Letters*, 102(9), March 2009.

[174] Manoj Kumar Gupta, Jayashree Bijwe, and Meghashree Padhan. Role of size of hexagonal boron nitride particles on tribo-performance of nano and micro oils. *Lubrication Science*, 30(8):441–456, July 2018.

[175] Frédéric Fossard, Lorenzo Sponza, Léonard Schué, Claudio Attaccalite, François Ducastelle, Julien Barjon, and Annick Loiseau. Angle-resolved electron energy loss spectroscopy in hexagonal boron nitride. *Physical Review B*, 96(11), September 2017.

[176] Roman V. Gorbachev, Ibtsam Riaz, Rahul R. Nair, Rashid Jalil, Liam Britnell, Branson D. Belle, Ernie W. Hill, Kostya S. Novoselov, Kenji Watanabe, Takashi Taniguchi, Andre K. Geim, and Peter Blake. Hunting for monolayer boron nitride: Optical and raman signatures. *Small*, 7(4):465–468, January 2011.

[177] Dheeraj Golla, Kanokporn Chattrakun, Kenji Watanabe, Takashi Taniguchi, Brian J. LeRoy, and Arvinder Sandhu. Optical thickness determination of hexagonal boron nitride flakes. *Applied Physics Letters*, 102(16):161906, April 2013.

[178] Yeonghoon Jin, Yoonhyuk Rah, Junghoon Park, Jaeho Shim, and Kyoungsik Yu. Rapid and broad-range thickness estimation method of hexagonal boron nitride using raman spectroscopy and optical microscope. *Applied Physics Letters*, 116(8):081104, February 2020.

Chapter 3

Methods

3.1 Sample Fabrications

The samples for all the work presented in this thesis are made with basic drop casting technique. We sourced hBN solution from graphene supermarket which comes in a batch of 100 mL vial containing pristine hBN flakes suspended in ethanol/water solution (product name - Boron Nitride (BN) Pristine Flakes in Solution, 100 ml, Graphene Supermarket). The flake size is typically 50-200 nm with average of 1-5 monolayers with 5.4 mg/L concentration. The solution is pure (>99% in dry phase) and appears white translucent in colour compared to milky white for suspended micro-sized hBN solutions. The vendor does not provide publicly the technique for manufacturing the solution and hBN exfoliation but we suspect, most likely, ball milling is employed. This solution is not made specifically for single photon emission/nanophotonics research but for a wide variety of applications such as- dielectric layer in transistors, hybrid materials, inks, insulating films in microelectronics and protective coating. Hence, the nature, type, location and density of defects are uncontrolled. This helps in keeping the sample inexpensive and provides a very wide range of emitters to study.

We use a 6 inch bulk silicon wafer and dice it into $\sim 6 \times 6$ mm sized substrates. It is then cleaned and the hBN solution is drop cast before the sample undergoes a process of rapid thermal annealing in nitrogen atmosphere to stimulate defect formation [1]. The temperature is ramped up-to 850°C in 7 min and held for 8 min before being allowed to cool. After this the sample is ready for optical experiments. In each of the experimental chapters presented in this thesis, we altered the process a little bit such as adding a layer of aluminium oxide Al_2O_3 [2] to the silicon (Si) substrate or the annealing process with just heating the sample on hot plate to evaporate the solvent. This has been discussed in the methods section of

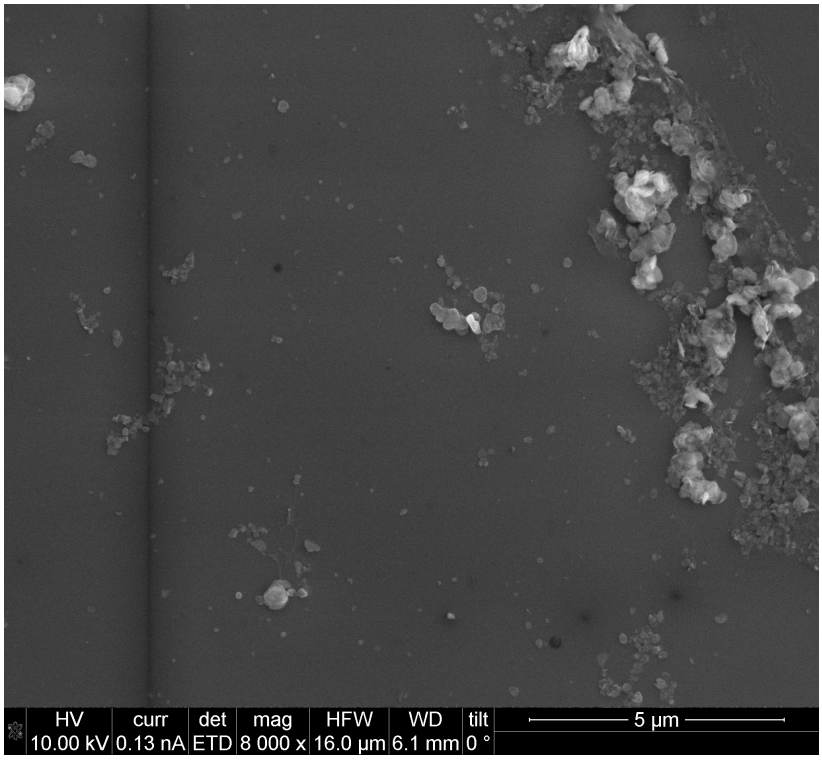

Fig. 3.1 A SEM image of hBN flakes drop cast from solution on silicon substrate. The SEM parameters are at the bottom. Note that drop casting randomly orientate and distribute the hBN flakes.

each chapter. The sample in the end has randomly orientated and distributed flakes with a significant possibility of overlapping (Fig. 3.1), depending on the amount of hBN solution used.

3.2 Fluorescence confocal microscopy

The fluorescence microscopy is the most basic optical microscopy technique to study material that shows fluorescence. A laser beam is used to excite the material which then emits photons at a lower energy. The emission follows the same path as excitation until it is separated by a dichoric beamsplitter (DBS). The emission signal is a direct measurement of the fluorescent material in real time. This technique has two sub parts- wide-field and scanning. In wide-field technique a very large area of the sample is illuminated and the emission can be seen as live video of the sample. This technique is commonly used in biology to study the molecules and movement of enzymes in the tissue. For studying emitters in a 2D material such as hBN

this technique has a major limitation- it excites many emitters at once and decreases signal to noise ratio. To study single photon emitters we employ the scanning technique. This technique is also called photoluminescence (PL) measurement in nanophotonics literature.

Fig. 3.2 (a) shows a basic scanning fluorescence confocal microscopy setup. A diode pumped solid state (DPSS) laser emits at 532 nm in CW mode. The beam is filtered using a 532 nm band pass filter and then passed through a linear polarizer. A half wave plate $\lambda/2$ changes the excitation polarization to the desired angle, or sometimes a quarter wave plate $\lambda/4$ is used to generate circularly polarized light, which is then fed into an objective through a DBS. A pinhole aperture is often used before the DBS for spatial filtering of the laser spot by removing the side fringes. The objective lens is mounted on a XYZ piezo stage to focus and scan the sample. For low temperature measurements, the sample is placed in vacuum chamber of the cryostat (3.2 K closed cycle optical cryostat, Montana Instruments). The emitted signal is then diverted using the same DBS into a fibre coupler. At the other end of the multimode fibre a spectrometer senses the PL signal to generate the spectrum. The DBS can not block all the excitation signal from the emission beamline so a low pass filter is used before the fibre coupler as a safety mechanism to protect the spectrometer's charge-coupled device (CCD). A linear polarizer checks the polarizing plane of the emission.

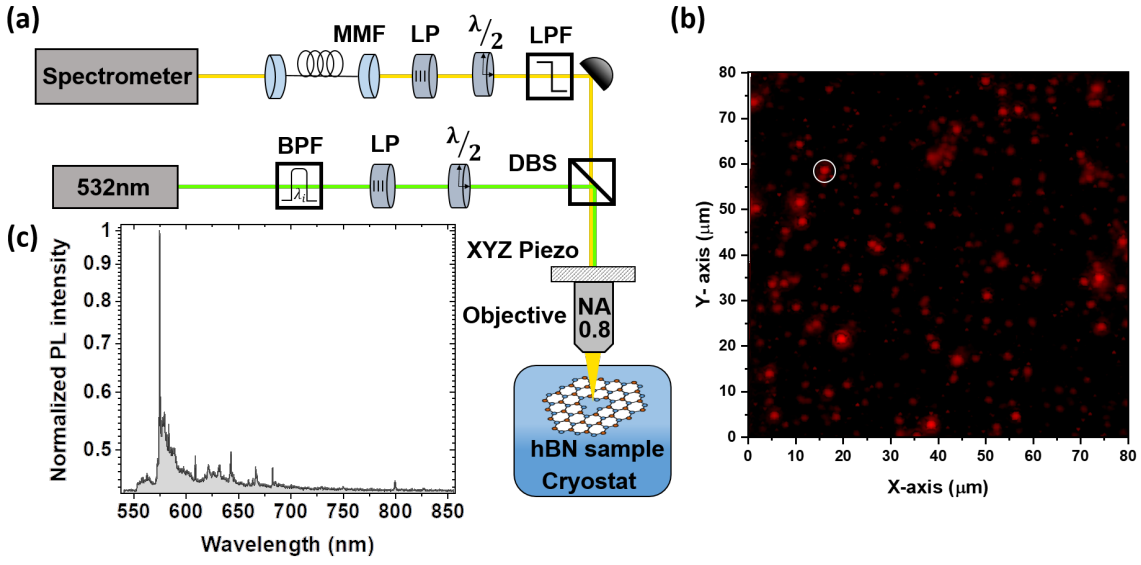

Fig. 3.2 (a) Photoluminescence (PL) measurement setup. BPF = band pass filter; LP = linear polarizer; $\lambda/2$ = half wave plate; DBS= dichroic beam splitter; LPF = long pass filter; MMF = multimode fibre. (b) PL map of a typical hBN flake. The bright spots shows the emitting centres which can be from a single or a group of defects. (c) PL spectrum of an emitter marked with circle in (b) showing a sharp ZPL at 575 nm.

During measurement, the excitation spot size (d) on the sample is kept minimum, closer to the diffraction limited spot size $d = 0.61\lambda/NA$, where λ is the wavelength of the light used for excitation and NA is the numerical aperture of the objective lens. This allows excitation of the smallest possible area on the sample and if emitters are separated by a distance more than d, we can successfully excite only one emitter. The whole sample is scanned in a raster fashion using a XYZ piezo stage. Each scan point generates a PL spectrum (Fig. 3.2 (c)) which is later processed based on the area under the whole spectrum or under a particular energy range to generate the PL map. This method takes a considerable amount of time and is not very quick. The scan time depends on step size, scan area and signal accumulation time for each step. Correct focusing of the Z axis is critical for sharp and well resolved PL maps. Usually a large area of the sample is first scanned with large steps and once interesting locations are identified, smaller maps are acquired with small step size and large integration time.

Fig. 3.2 (b) shows a 80×80 μm^2 PL map with 0.5 μm step size in ratser scan. Note that all the bright spots are not essentially single emitters, there can be more than one emitter with small spatial distribution which can not be resolved using confocal microscopy. This is a major drawback of this technique. In this thesis we will discuss the work done on stimulated emission depletion (STED) microscopy where we achieved 60 nm resolution with confocal like setup [3].

3.3 Autocorrelation measurement and time resolved spectroscopy

Fig. 3.3a shows a basic setup for an auto-correlation experiment. An excitation beam from 532 nm diode pumped solid state (DPSS) laser is passed through a linear polarizer and a half wave plate to allow polarization only in one plane. The angle of polarization can be changed by the half wave plate. It is then directed into the objective lens using a dichroic beam splitter. The XYZ piezo stage aligns and focuses the laser spot on the target emitter. The output signal is passesed through a set of tuneable filters (low pass and high pass) to filter only the ZPL. The signal is then divided into two paths using a 50:50 beam splitter and coupled to a multimode fibre. Each fibre is connected to an avalanche photodiode (APD) which registers the photons and generates an electronic signal called "click". This click is then sent to time tagger / time-correlated single photon counting electronics (TCSPC) (Swabian instruments, model- Time tagger 20) channels to produce a $g^{(2)}(\tau)$ plot (See background chapter section

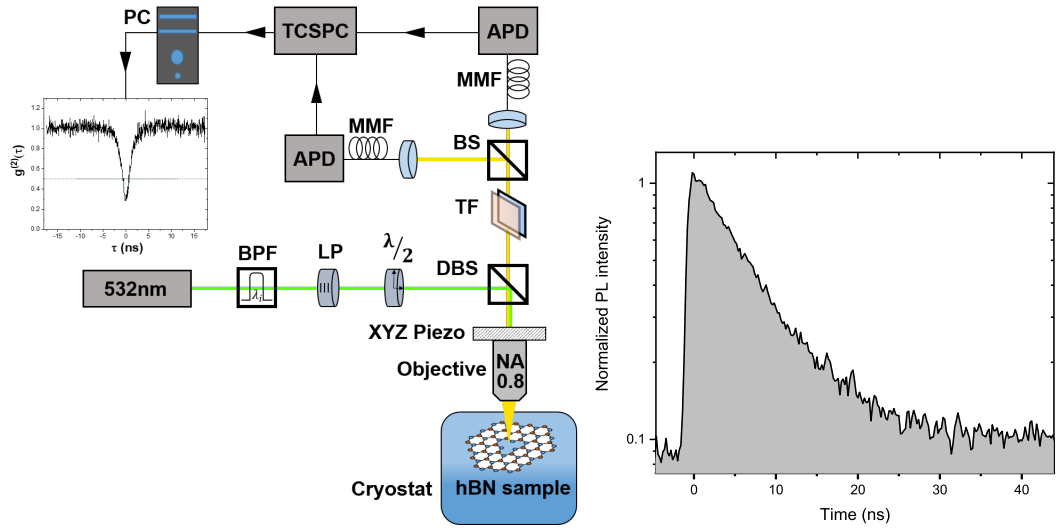

(a) (b)

Fig. 3.3 (a) Setup for $g^{(2)}(\tau)$ measurement. BPF = band-pass filter; LP = linear polarizer; $\lambda/2$ = half-waveplate; DBS = dichroic beam splitter; TF = tuneable filters; BS = 50:50 beam splitter; MMF = multimode fibre; APD = avalanche photodiode; TCSPC = time-correlated single photon counting electronics. (b) A typical time trace from an hBN emitter showing single exponential decay with decay time 6.8 ns.

2.1.5 for details on processing timestamps and Fig. 2.7 for example $g^{(2)}(\tau)$ from a typical hBN emitter).

A similar setup is also used for time resolved spectroscopy where we study the time dependent excitation and emission from an emitter. In this case, the DPSS laser is used in pulsed mode and we remove the 50:50 beam splitter and the inactive APD. The TCSPC now receives click signals from the active APD and the trigger signal from DPSS laser. The Matlab program calculates the time difference between the excitation pulse and photons registered by the APD. Fig. 3.3b shows the output generated after the calculation, commonly known as time trace. Most photons show a very small time delay between excitation and emission and the time trace shows an exponential decay. The inverse of the decay rate of this exponential gives us emitter's radiative lifetime. This technique is used in the experimental chapters presented in this thesis.

3.4 Photoluminescence excitation measurement

In confocal microscopy or time resolved spectroscopy we only observe the emission properties of the emitter once it is excited by the laser system. In the excited state the emitter

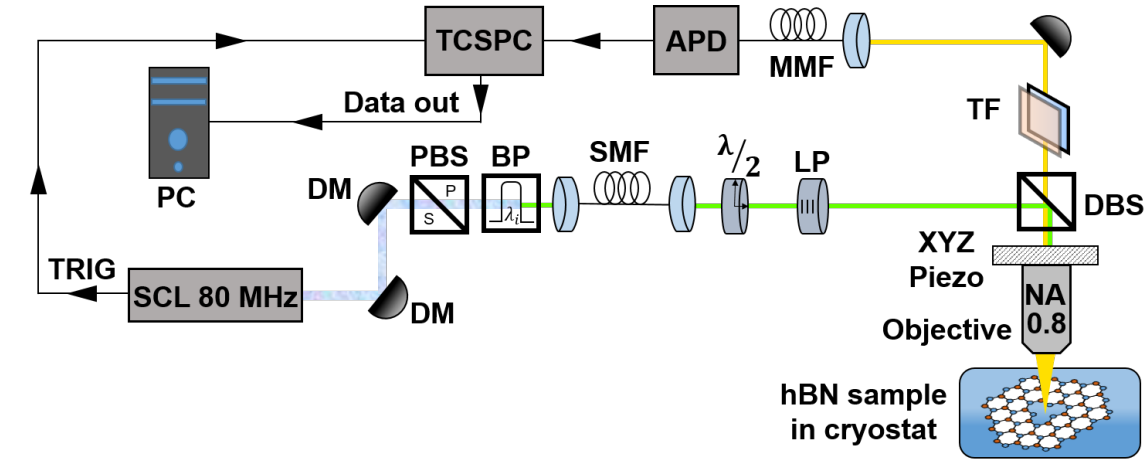

(a)

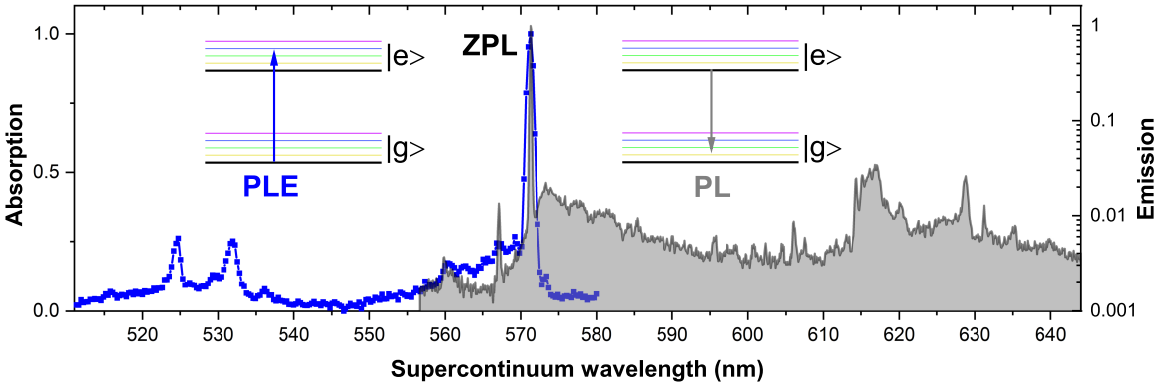

(b)

Fig. 3.4 (a) Setup for photoluminescence excitation (PLE) measurement. SCL= Supercontinuum laser; DM = dielectric mirror; SMF = single-mode fibre; MMF = multimode fibre; PBS = polarizing beam splitter; BPF = band-pass filter; LP = linear polarizer; DBS = dichroic beam splitter; APD = avalanche photodiode; $\lambda/2$ = half-waveplate; TCSPC-time-correlated single photon counting electronics. (b) Comparison of PL and PLE measurement. PLE (blue) probes the vibronic modes in the excited state while PL represents radiative decay of an emitter from excited state to vibronic modes of the ground state. Note that the PLE has a poor resolution compared to PL because PLE resolution depends on the SCL step size and instrument response function of the APD.

relaxes to the ground vibronic level before relaxing to the ground state. Now the emitter can relax into ground state with or without a change in quantum vibrational number giving PSB or ZPL respectively (See Fig. 3.4 (b) emission spectra on right). In this way we are probing the vibrational modes of the ground state, getting only half the picture. To study the excitation dynamics we use a technique called photoluminescence excitation (PLE). A supercontinuum laser (NKT Photonics, SuperK COMPACT supercontinuum laser), along

with an acousto-optic tunable filter (ATOF), provides a narrow linewidth ($\sim$1 nm) laser pulse (pulsewidth $\sim$ 1 ps) . For the PLE experiment, we first do a PL test to see the ZPL energy of the emitter. Once an emitter is selected, a wavelength filter allows only the optical PSB from emission into the fibre coupler (sometime ZPL is used, depending on the experiment, the reason for this will be discussed later in chapter 5). An APD and TCSPC on the other side of the fibre do the photon counting and statistics. The setup is shown in Fig. 3.4 (a) . This preliminary PL test also helps in determining the energy sweep range for the supercontinuum laser. Ideally this sweep range should start from a bit lower than the ZPL to more than one optical phonon band higher than the ZPL energy. Fig. 3.4 (b) shows the PL and PLE from an hBN emitter. For an energy lower than ZPL, we do not see any emission because the energy is not sufficient to excite the emitter. When the PLE energy is same as the ZPL we see maximum emission as expected. Depending on the optical and acoustic phonon coupling we also see the PSB in absorption. This technique helps to study the differences between the ground and excited state and how material behaves during a cycle of absorbption and emission. This technique is used in experimental chapters 5, 6 and 7 presented in this thesis [4, 5, 3].

3.5 Stimulated emission depletion spectroscopy

Stimulated emission depletion (STED) spectroscopy is based on the fact that an excited fluorophore can be depleted via stimulated emission which reduces the ZPL emission intensity while increasing the phonon sideband emission. If the depletion laser energy matches with the emitter's PSB energy, we see a drastic reduction in the ZPL emission. Chapter 6 and 7, presented in the thesis are based on this technique and it will be discussed in great detail along with experimental setup and results. A major advantage of STED over fluorescence microscopy is that it directly probes the vibronic modes of the ground state and filters out the noise/stray emission from neighbouring impurities. The ability to deplete the defect via PSB is used in chapter 7 to achieve high resolution maps of hBN emitters without the interference from nearby species.

References

[1] Nicholas R. Jungwirth, Brian Calderon, Yanxin Ji, Michael G. Spencer, Michael E. Flatté, and Gregory D. Fuchs. Temperature dependence of wavelength selectable zero-phonon emission from single defects in hexagonal boron nitride. *Nano Letters*, 16(10):6052–6057, September 2016.

[2] Xiangzhi Li, Gabriella D. Shepard, Andrew Cupo, Nicolas Camporeale, Kamran Shayan, Yue Luo, Vincent Meunier, and Stefan Strauf. Nonmagnetic quantum emitters in boron nitride with ultranarrow and sideband-free emission spectra. *ACS Nano*, 11(7):6652–6660, May 2017.

[3] Prince Khatri, Ralph Nicholas Edward Malein, Andrew J. Ramsay, and Isaac J. Luxmoore. Stimulated emission depletion microscopy with color centers in hexagonal boron nitride. *ACS Photonics*, June 2021.

[4] Ralph Nicholas Edward Malein, Prince Khatri, Andrew J. Ramsay, and Isaac J. Luxmoore. Stimulated emission depletion spectroscopy of color centers in hexagonal boron nitride. *ACS Photonics*, 8(4):1007–1012, April 2021.

[5] Prince Khatri, Andrew J. Ramsay, Ralph Nicholas Edward Malein, Harold M. H. Chong, and Isaac J. Luxmoore. Optical gating of photoluminescence from color centers in hexagonal boron nitride. *Nano Letters*, 20(6):4256–4263, May 2020.

Chapter 4

Phonon sideband analysis of hBN emitters

4.1 Introduction

With the general framework about SPEs established, especially colour centres in hBN, it is now possible to start exploring the first hurdle in the path of an SPE - phonons. The effects of temperature are unavoidable and it is important to make SPEs robust so that they can be operated efficiently at room temperature or higher. Although cooling down the SPE is an option but cryostat costs makes the whole setup expensive.

In Chapter 2, section 2.1.9 we have discussed how increase in temperature increases the emitter's linewidth. When SPE is used at high temperature, a wavelength filter is used to select only a narrow, $\sim$ 1 nm wide, most intense wavelength from the ZPL. If the ZPL linewidth is wide, the filter rejects a large percentage of emitted photons and reduces the SPE's brightness. Phonons are quanta of lattice vibrations and with increase in temperature the lattice can support more phonons. It is impossible to remove them from the system but we can reduce the effects by techniques like Purcell enhancement where emission is coupled to a cavity mode [1]. What we ideally want is reduced phonon interactions, which increases the coherence, resulting in a lifetime limited linewidth.

So far, InAs quantum dots demonstrate the best optical coherence properties with lifetime limited linewidth, and about 96% emission into the zero-phonon line [2]. We have discussed the properties of QDs in Chapter 2 and how a low operating temperature is the limiting factor. The large carrier wavefunction in QDs gives a small (1.3 meV) electron phonon cutoff energy (This is calculated in reference [3]). This means if phonons with energy more than 1.3 meV exist in the system, they can interact with the QD emitter and reduce the emission quality. To

let this happen the temperature of the system should only exceed $\hbar\omega_c/k_B = 16$ K, restricting the use at high temperature.

Although, it is possible to keep the QD under low temperature for quantum technology applications but this significantly increases the operation costs and size, making it impractical and uneconomical for the industry. That is why, it is important to search for a SPE that could give comparable emission quality to QDs while operating at high temperature. As discussed in chapter 2, section 2.2.3, colour centres in hBN can be a promising candidate with reported single photon emission upto 800 K [4]. Whilst there are reports of room temperature single photon emission in InGaN quantum dots [5, 6], colour centres in diamond [7] and SiC [8], h-BN stand out for the high ZPL fraction (ZPL emission/total emission). Being a 2D material it is important to know if the phonon bath in hBN is effectively 3D or 2D, and if so, does the reduced dimensionality have an advantage for the optical coherence properties of the emitter. The issue has been experimentally investigated for quantum dots in carbon nanotubes with a 1D-phonon bath [9] and Vuong *et al* [10] have analyzed the acoustic phonon sidebands of emitters in bulk h-BN, and explain the results in terms of a 3D acoustic phonon-bath. There are also a couple of reports that fit the acoustic and optical sidebands at room [11] and low temperature [12].

In this chapter we analyze the phonon sideband of colour centre in multi-layer flakes of hBN in detail. By comparison of acoustic sidebands of PL data to an independent boson model, typically used for quantum dots, [13] we infer that the phonon bath is effectively 2D. This arises due to deformation coupling of LA-phonons to in-plane k-vector, due to the in-plane polarization of the longitudinal acoustic (LA)-phonons in h-BN, [14] and a phonon dispersion that is nearly independent of k_z for phonon energies larger than 10 meV. The optical phonon band has a number of resonances coinciding with turning points (phonon energy where slope of the phonon dispersion curve ($d\omega/dk$) is zero, implying a zero phonon group velocity) in the phonon dispersion. We propose that a peak at 200 meV detuned from the ZPL, also reported by others [12] is a signature of a few layer sample. The peaks associated with transverse optical (TO)-phonons are best described by a deformation coupling proportional to in-plane lattice displacement. Combined with the near degeneracy of the TO-band with respect to out-of-plane momentum, [15] the TO-bath is also effectively two dimensional. By contrast, although the polarization vector of longitudinal optical (LO)-phonons is in-plane, we infer that the Fröhlich coupling depends on interactions between the layers. This may partly explain variations in the optical-phonon sidebands between different emitters, as they can be in a flake with different number of layers. Compared to emitters in a 3D host material, this work identifies qualitative differences in the emitter-phonon coupling

that arise from the layered structure of h-BN. For a second-emitter, evidence for coupling to out-of-plane polarized phonon modes is reported.

This work has been published and is here adapted from Phys. Rev. B 100, 125305 (2019). Copyright 2019 American Physical Society. For this work, my contributions were- numerical simulation to fit the data and inputs for the paper. This paper was written and submitted by Dr. Andrew Ramsay.

For this topic, the contributions are; Prince Khatri- numerical model simulation, fitting the data, inputs for the paper. Dr. Isaac Luxmoore- model and theory guidance, inputs for the paper and preparing the figures. Dr. Andrew Ramsay- Collecting the data, model and theory guidance, writing and submitting the paper.

4.2 Photoluminescence measurements

The sample consists of few-layer flakes of hBN drop-cast onto a silicon substrate. See chapter 3, section 3.1 for more details. For a 532 nm pump laser, the density of emitters is low, under 1 per 100 μm^2. We focus on two colour centres emitting close to 2.17 eV.

The identity of the colour centre is unknown, and the subject of some debate. However, in ref. [16], in monolayer hBN samples where the emitters are at approximately 580 nm, the dominant defects in TEM was found to be the boron vacancy. Therefore, the defects studied here may be the V_B^-.

Fig. 4.1 compares the micro-photoluminescence spectra of emitter I using a 532 nm pump at temperatures of 20 and 275 K. Close to room temperature, the spectrum consists of a bright, narrow line at 2.171 eV. We attribute this peak to the zero phonon line (ZPL) emission of the colour centre, since the intensity of the peak is sensitive to temperature. The energy of the ZPL is 159 meV less than the photon energy of the pump laser, similar to the energy of an optical phonon. Defects emitting at similar energies have been previously reported [17]. At 275 K, there is a slight asymmetry of the ZPL, which is clearly revealed as the temperature is decreased. In fig. 4.1(a), the spectrum is colour-coded to indicate red-detuned sidebands due to acoustic phonon emission assisted radiative recombination (detuning $<$150 meV)(red), and optical phonon emission assisted radiative recombination (150$<$detuning$<$200 meV)(blue).

At low temperature, approximately 18% of the emitted photons are from the zero phonon line at 571 nm. This is high compared to 12%, 3.7% at 575 nm, and 682 nm reported in ref. [17], and considerably smaller than the (80% at 623 nm) reported in ref. [18]. The coupling of the colour centre to the vibronic modes, as evident in the temperature dependent

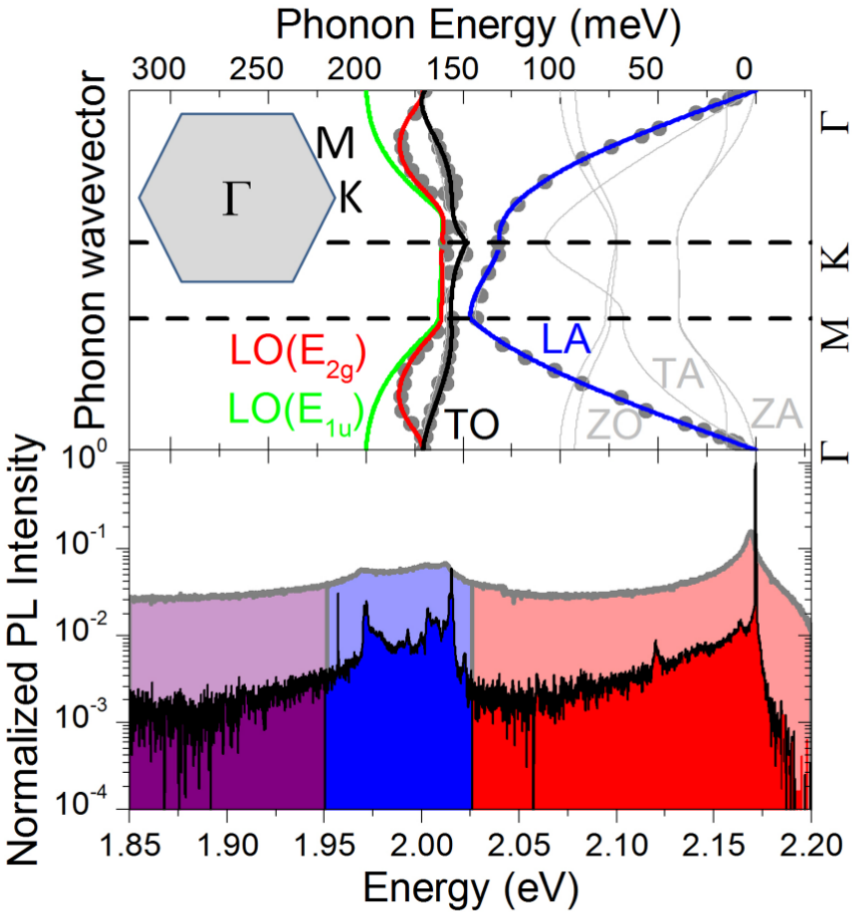

Fig. 4.1 Comparison of PL at 20 K and 275 K for emitter I. The ZPL can be identified by its large drop in intensity with temperature. (above) By comparison to the phonon dispersion curves [14] the acoustic and optical sidebands can be identified. The markers indicate data points, and lines are fits to data from ref. [14]. For the LO(E_{1u})-band, a fit to ab-initio calculations in ref. [14] is used. (inset) 2D Brillouin zone.

spectra of Fig. 4.1, leads to the observed reduction in the relative intensity of the ZPL as the temperature is increased. About 19 % of the emission is into the optical phonon band, indicating that coupling to optical phonons is efficient, and the broad acoustic phonon band accounts for the rest.

4.3 Analysis of the acoutic phonon sideband

In order to analyse the acoustic phonon sideband we consider a two level system which is coupled to a phonon bath. The system is excited to energy level $|1\rangle$ at $t = 0$ which then decay to ground energy level $|0\rangle$ via some phonon coupling as shown in Fig. 4.2. Note that this model is based on the Ref. [13], where it is used to study phonon interaction with QDs. In this chapter, we implemented this model for emitters in hBN, similar to Ref. [10].

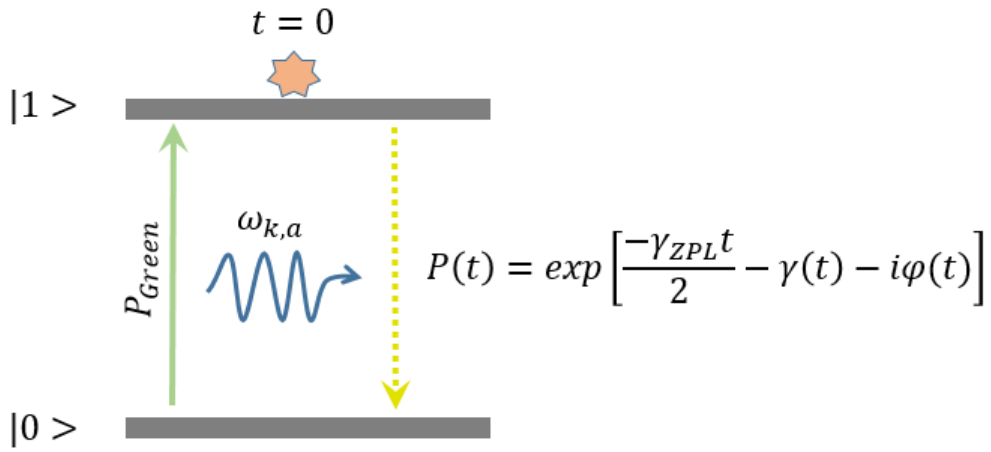

Fig. 4.2 Two level system coupling to a phonon bath. System is excited from $|0> \rightarrow |1>$ with a green laser, shown in the diagram as P_{Green}. At $t = 0$ the system is in excited state. The decay from $|1> \rightarrow |0>$ is coupled with the bulk phonon modes $\omega_{k,a}$. The allowed phonon energy in Brillouin zone can be deduced from phonon dispersion curves of bulk hBN shown in Fig. 4.1 [14].

The electronic polarization $P(t)$ of the defect is related to the fixed incident field E by

$$P(t) = \varepsilon\chi(t)\mathbf{E} \tag{4.1}$$

where ε is the electric permittivity of the medium and $\chi(t)$ is the time dependent linear susceptibility, which captures all the phonon phenomena.

For our two level system, the linear susceptibility is defined as [10]

$$\chi(t) = exp\left[\sum_{a,k} |\gamma_{a,k}|^2 (e^{-i\omega_a(\mathbf{k})t} - N(\omega_a(\mathbf{k}),T)|e^{-i\omega_a(\mathbf{k})t} - 1|^2 - 1)\right] \tag{4.2}$$

here j is the phonon band, k is the propagation wave vector for the phonon, $\gamma_{j,k}$ is a dimensionless coupling strength of the phonon band with the two level system, $\omega_j(k)$ is the energy of the phonon band along vector k and $N(\omega_j(k),T)$ is Bose-Einstein distribution.

To consider the phonon assisted broadening of the ZPL we multiply the susceptibility with $exp^{-\Gamma_{ZPL}t/2\hbar}$, where Γ_{ZPL} is the full with half maxima of the ZPL and can be obtained by a Lorentz fit to the PL data. Susceptibility can now be written as

$$\tilde{\chi}(t) = \chi(t) exp^{-\Gamma_{ZPL}t/2\hbar} \tag{4.3}$$

For simplicity and better understanding we can consider emission polarization and use equation 4.2 and 4.3 to write time dependent polarization as

$$P(t) \cong exp\left(-\frac{\Gamma_{ZPL}t}{2} - \gamma(t) - i\Phi(t)\right) \tag{4.4}$$

where $\Gamma_{ZPL}t/2\hbar$ represents dephasing to account for the finite width of the zero-phonon line from Eq. 4.3 and $\gamma(t)$ and $i\Phi(t)$ represents the part of linear susceptibility from Eq. 4.2.

$$-\gamma(t) - i\Phi(t) = \sum_{a,k} |\gamma_{a,k}|^2 (e^{-i\omega_a(\mathbf{k})t} - N(\omega_a(\mathbf{k}),T)|e^{-i\omega_a(\mathbf{k})t} - 1|^2 - 1) \tag{4.5}$$

The emission spectra is given by the real part of the fourier transform of polarization

$$S(\omega) \cong real\left(\int_0^\infty e^{-i\omega t} P(t)\right) \tag{4.6}$$

Using Euler's formula $e^{i\phi} = cos\phi + isin\phi$, we can separate Eq. 4.5 into a real and imaginary parts and write $\gamma(t)$ and $\Phi(t)$ as

$$\gamma(t) = \sum_{a,k} |\gamma_{k,a}|^2 [1 - cos\omega_a(\mathbf{k})t][2N(\omega_a(\mathbf{k}), T) + 1] \tag{4.7}$$

$$\Phi(t) = \sum_{a,k} |\gamma_{k,a}|^2 [2sin\omega_a(\mathbf{k})] \tag{4.8}$$

we can change summation to integral by including density of states as $\sum \longrightarrow \int d^d n$. For a d-dimentional k space of volume V_d Equation 4.7 can be written as

$$\gamma(t) = \sum_j \frac{V_d}{(2\pi)^d} \int d^d k |\gamma_{k,a}|^2 [1 - cos\omega_a(\mathbf{k})t][2N(\omega_a(\mathbf{k}), T) + 1] \tag{4.9}$$

Coupling constant $\gamma_{k,a}$ can be expresed as

$$\gamma_{k,a} = \frac{g_{k,a}}{\omega_a(\mathbf{k})} \tag{4.10}$$

where $g_{k,a} = g^{(1)}_{k,a} - g^{(0)}_{k,a}$ is the difference in the electron-phonon coupling strength between the upper $|1\rangle$ and lower energy level$|0\rangle$ of the two level system. Combining 4.9 and 4.10 gives us the final form $\gamma(t)$ and $\Phi(t)$

$$\gamma(t) = \sum_a \int \frac{V_d d^d k}{(2\pi)^d} \left| \frac{g_{k,a}}{\omega_{k,a}} \right|^2 (1 - cos\omega_{k,a}t)(2N(\omega_{k,a}, T) + 1) \tag{4.11}$$

$$\Phi(t) = \sum_a \int \frac{V_d d^d k}{(2\pi)^d} \left| \frac{g_{k,a}}{\omega_{k,a}} \right|^2 sin\omega_{k,a} \tag{4.12}$$

In the following analysis the bulk phonon modes are assumed. The energy dispersion is obtained from a fit to the data in [14]. We have phonon energies only in $\Gamma - K$ and $\Gamma - M$ directions. To interpolate the phonon energies across the whole 2D Brillouin zone we used $\omega(\mathbf{k})$ as a function of k and θ where k goes from 0 to edge K of the Brillouin zone and θ from 0 to $\pi/6$

$$\omega^2(k,\theta) = \frac{1}{2}\left(\omega^2_{\Gamma-K}(k) + \omega^2_{\Gamma-M}(k)\right) + \frac{1}{2}\left(\omega^2_{\Gamma-K}(k) - \omega^2_{\Gamma-M}(k)\right) cos6\theta \tag{4.13}$$

To describe electron phonon coupling we expand the term $g_{k,a}$ which accounts for how strongly each phonon mode couples with the system [13].

$$g^{(b)}_{k,a} = \frac{1}{\sqrt{2\rho_d V_d \hbar\omega_{k,a}}}(i.\mathscr{M}^{(b)}_a + \mathbf{k}.\hat{u}_a\mathscr{D}^{(b)}_a) f^{(b)}_a(k) \tag{4.14}$$

The prefactor normalizes the energy of the phonon mode to $\hbar\omega_{k,a}$. ρ_d is d-dimensional mass density. $f^{(b)}_a(k)$ is form factor and defined as the overlap between the electron desity of state (b) and phonon wave function (k,a). In other words, form factor can be defined as the size of the emitter in the brillouin zone, which is fourier transform of the physical size of the emitter in real space. Since the phonon mode is a travelling wave $f^{(b)}_a(k)$ is simply the fourier transform of the electron probability density, $f^{(b)}_a(0) = 1$ by definition. The $\mathscr{M}$-term describes a piezo-like change in the energy proportional to the lattice displacement, and the $\mathscr{D}$-term a deformation-like coupling proportional to the strain. For acoustic phonons, the $\mathscr{D}$-term dominates since the strain changes the separation between neighbouring lattice sites. The unit-vector $\hat{u}_a$ is the polarization of the phonon mode of band-a.

Our goal here is to understand the electron phonon coupling by comparing the data with the model. A number of fitting parameters can be reduced to ease out the fitting process and stop over-parametrization. The difference in coupling strength of level $|1\rangle$ and $|0\rangle$ is responsible for the phonon sideband in PL so we can drop parameter b here

$$g_{k,a} = g^{(1)}_{k,a} - g^{(0)}_{k,a}$$
$$\implies \mathscr{M}_a = \mathscr{M}^{(1)}_a - \mathscr{M}^{(0)}_a \quad , \quad \mathscr{D}_a = \mathscr{D}^{(1)}_a - \mathscr{D}^{(0)}_a \quad \text{and} \quad f_a = f^{(1)}_a - f^{(1)}_a$$

In the unlikely case that $\mathscr{M}^1_a = \mathscr{M}^{(0)}_a$, the form-factor and coefficient are redefined such that $f(k \to 0) = k^2$, since the probability density is real. In the case of a quantum dot, the envelope of the carrier wavefunction spans more than 10^3 lattice constants and is relatively unaffected by lattice vibrations. The electron-phonon coupling arises from a change in band-gap and hence is a property of the host material [13]. For a deep defect, the intra-band transition is insensitive to changes in the bandgap. However, since the carrier envelope is

similar in size to a lattice constant, the confinement potential is strongly influenced by lattice vibrations, and hence a coupling constant that is a property of the defect is expected.

4.3.1 Coupling dimension and isotropicity

To help identify the dimension and coupling mechanism we need to simplify equation 4.11 and 4.12. The $(1-cos\omega_{k,a}t)(2N(\omega_{k,a},T)+1)$ term becomes 0 as $\omega_{k,a}\to 0$. We can remove this problem by:

$$(1-cos\omega_{k,a}t) = 2sin^2\left(\frac{\omega_{k,a}t}{2}\right) = 2\left(\frac{\omega_{k,a}t}{2}\right)^2\frac{sin^2\left(\frac{\omega_{k,a}t}{2}\right)}{\left(\frac{\omega_{k,a}t}{2}\right)^2} = 2\left(\frac{\omega_{k,a}t}{2}\right)^2 sinc^2\left(\frac{\omega_{k,a}t}{2}\right)$$

$$\lim_{\omega_{k,a}\to\infty} sinc^2\left(\frac{\omega_{k,a}t}{2}\right) = 1$$

The term $(2N(\omega_{k,a},T)+1) = coth\left(\frac{\hbar\omega_{k,a}}{2K_bT}\right)$ becomes ∞ as $\omega_{k,a}\to 0$. To remove the singularity we modify the term:

$$(2N(\omega_{k,a},T)+1) = \frac{1}{\omega_{k,a}}\left(\omega_{k,a}coth\frac{\hbar\omega_{k,a}}{2K_bT}\right)$$

$$\lim_{\omega\to\infty}\omega_{k,a}coth\left(\frac{\hbar\omega_{k,a}}{2K_bT}\right) = \frac{2K_bT}{\hbar}$$

Using these two modifications the $\gamma(t)$ can be rewritten as

$$\gamma(t) = \sum_a\int\frac{V_d d^dk}{(2\pi)^d}\left|\frac{g_{k,a}}{\omega_{k,a}}\right|^2\left(\frac{\omega_{k,a}t^2}{2}\right)\left(sinc^2\frac{\omega_{k,a}t}{2}\right)\left(\omega_{k,a}coth\frac{\hbar\omega_{k,a}}{2K_bT}\right) \tag{4.15}$$

For a two-dimensional isotropic phonon coupling

$$\int\frac{V_d d^dk}{(2\pi)^d} = \frac{A}{(2\pi)^2}\int d^2k$$

To include phonon anisotropicity this can be further modified as

$$\frac{A}{(2\pi)^2}\int d^2k = \frac{A}{(2\pi)^2}12\int d\theta \int kdk$$

where k goes from 0 to edge K of the Brillouin zone and θ from 0 to $\pi/6$. The factor 12 comes from the fact that integral only covers $1/12th$ of the brillouin zone. The strength term $g_{k,a}$ is same for both isotropic and anisotropic coupling. To include anisotropicity the phonon energy should also be anisotropic and eq. 4.13 for $\omega(k,\theta)$ should be used. For a two-dimensional anisotropic case using equation 4.10:

$$g_{k,a} = \frac{1}{\sqrt{2\rho_A A\hbar\omega_{k,\theta,a}}}(i.\mathscr{M}_a + \mathbf{k}.\hat{u}_a\mathscr{D}_a)f_a(k)$$

Combining all the results,$\gamma(t)$ for anisotropic two-dimensional LA deformation type coupling is:

$$\gamma(t)_{LA} = \frac{3D^2}{2\pi^2\rho_A\hbar}\int_0^{\pi/6} d\theta \int_0^K \frac{k^3}{\omega_{k,\theta}^2} f(k)dk\left(\frac{t^2}{2}\right)\left(sinc^2\frac{\omega_{k,\theta}t}{2}\right)\left(\omega_{k,\theta}coth\frac{\hbar\omega_{k,\theta}}{2K_bT}\right) \tag{4.16}$$

For n-dimensional isotropic

$$\gamma(t)_{LA} = \frac{D^2}{4\pi^m\rho_n\hbar}\int_0^K \frac{k^{n+1}}{\omega_k^2} f(k)dk\left(\frac{t^2}{2}\right)\left(sinc^2\frac{\omega_k t}{2}\right)\left(\omega_k coth\frac{\hbar\omega_k}{2K_bT}\right) \tag{4.17}$$

where $m = n-1$ if $n \geq 2$ and $m = 1$ if $n = 1$. $\phi(t)$ for all casses can be calculated easily using the same method. For calculations we considered three types of form factor

$$f^2(k) = e^{-k\sigma} \qquad Exponential \tag{4.18}$$

$$f^2(k) = e^{\frac{-k^2\sigma^2}{2}} \qquad Gaussian \tag{4.19}$$

$$f^2(k) = \frac{\sigma^2}{\sigma^2+k^2} \qquad Lorentzian \tag{4.20}$$

where σ is a measure of the size of the electron density. Fig. 4.3 shows calculated spectra for different form factors. To make comparison easy 2D isotropic deformation type coupling is used and $\mathscr{D}_{2D} = 8.8\ eV$ for all calculations. We used $\mathscr{D}_{2D} = 8.8\ eV$ here such that the calculated spectra in 4.3 (b) are approximately close to the data points to see clearly which form factor follows to correct trend. Note that a fitting to obtain precise value of $\mathscr{D}_{2D}$ is presented in 4.4.

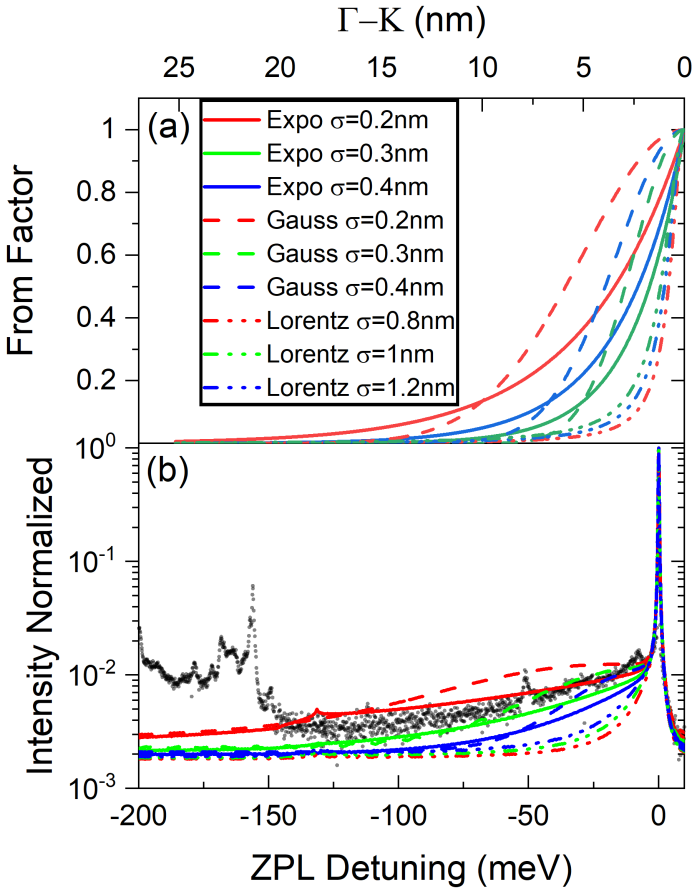

Fig. 4.3 Different form factors used for calculations. (a) represents form factor in brillouin zone alone $\Gamma - K$ direction. (b) Calculated 2D-deformation anisotropic LA coupling spectra. $\mathscr{D}_{2D} = 8.8\ eV$ for all calculations. Only exponential form factor (solid lines) with appropriate σ can fit the LA sideband data.

In Fig. 4.4, a close-up of the acoustic phonon sideband is shown, which indicates that an exponential form factor most closely fits the experimental data

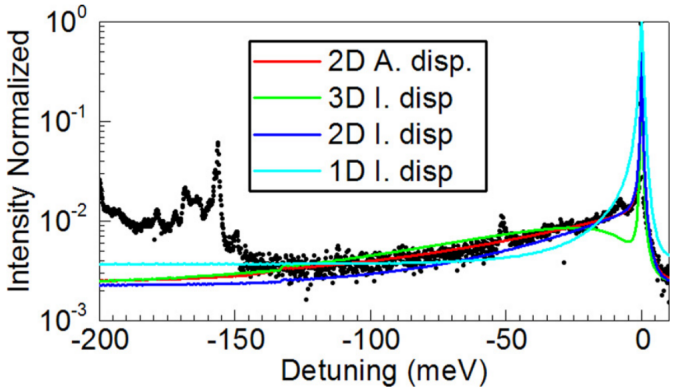

Fig. 4.4 Close up of acoustic phonon sideband. Lines are calculations that assume electron phonon spectral densities of order n=1 (cyan), 2 (blue), 3 (green). Qualitatively, the n=2 case fits best. The red line shows the case n=2, using Eq. 4.16 to estimate the anisotropy of the nonlinear dispersion curves, and gives a slightly better fit to data. The parameters used are: $\mathscr{D}_{1D} = 4$ eV, $\rho_{1D} = 1.65 \times 10^{-16}$ kg.m^{-1}, $\sigma_{1D} = 0.21$ nm; $\mathscr{D}_{2D} = 10.5$ eV, $\rho_{2D} = 0.76$ mg.m^{-2}, $\sigma_{2D} = 0.35$ nm; $\mathscr{D}_{3D} = 26$ eV, $\rho_{3D} = 2.18 \times 10^{3}$ kg.m^{-3}, $\sigma_{3D} = 0.49$ nm.

Note that the acoustic sideband is quite smooth, even on logarithmic Y scale, and do not show any sharp peaks near 75 meV and 100 meV, implies that the Z-axis optical (ZO) phonons do not play a significant role. To identify the order of the electron-phonon interaction, a set of calculations assuming deformation coupling, and that $\mathscr{D}^{(1)} \neq \mathscr{D}^{(0)}$, are made for longitudinal acoustic phonon-baths with linear dispersion of different dimension $n = 1, 2, 3$, and are shown alongside the data in Fig. 4.4. Only $n = 2$ can describe the data. Therefore, to conclude, the acoustic sideband arises from deformation coupling to a phonon bath that is effectively two-dimensional. Since the form-factor restricts the contributing phonons to low-k, it is difficult to distinguish between contributions from TA and LA phonons. An additional calculation using Equation 4.16 to approximate the anisotropy and include the nonlinearity of the dispersion is also made, see Fig. 4.4, and provides a slightly better description of the data at higher phonon energy.

An effective two dimensional coupling can arise if the integrand of Eq. 4.15 is independent of out-of-plane k-vector k_z. Since the polarization $\hat{u}_a$ of the LA and TA phonon modes is in-plane, the deformation coupling is to in-plane momentum, $g_{k,LA} \sim \mathscr{D}_{LA}\mathbf{k}.\hat{u}_{LA} \rightarrow \mathscr{D}_{LA}k_{\perp}$. In addition, for phonon energies $\hbar\omega_k > 10$ meV the dispersion curves of the LA and TA-phonons are also independent of k_z [14]. Hence, due to the in-plane polarization of the phonon modes, for most energies of interest the electron-phonon coupling is effectively two-dimensional, although this is a multi-layer sample.

If we assume that only LA-phonons contribute, since $\mathbf{k}.\hat{u}_{TA} = 0$, we extract a value $\mathscr{D}_{2D} \approx 10.5$ eV, using $\rho_{2D} = 0.76$ mg.m^{-2} [19]. $\sigma_{LA} = 0.35$ nm which is about 2.4 times the nearest neighbour separation of 0.144 nm [20].

The deformation coupling strength is close to the $\mathscr{D}_{LA}$=*11 eV* found for UV-emitting defect-bound excitons coupled to 3D phonon-bath in bulk h-BN [10], and is close to values found for excitons in GaAs QDs [21]. However, it is relatively large compared to deformation coupling constants of up to 0.6 eV measured under static strain conditions for hBN colour centres emitting at 2.14 eV [22].

4.4 Analysis of the optical phonon sideband

To gain insight into the interaction of the colour centre with optical phonons, we compare the dispersion curve of hBN presented in ref. [14] (Note that the experiment to measure the data is not performed by Serrano *et al* [14]) to a close-up of the optical phonon sideband of the emission spectra taken at 20 K, see Fig. 4.5. The red and green curves indicate bulk LO-phonon branches with E_{2g} and E_{1u} symmetry at the Γ-point, where neighbouring planes oscillate in-phase or anti-phase, respectively. The black curve shows the bulk TO-branch. The over-bending of the in-phase LO(E_{2g})-band results from a spring-constant that changes sign with the separation between lattice sites, see table I of ref. [15]. For multi-layers, [15] adjacent out-of-phase layers ($k_z \neq 0$) generate an in-plane electric-field via the Coulomb interaction increasing the spring constants. This increases the energy of the $LO(E_{1u})$ with respect to the $LO(E_{2g})$ band, suppresses the over-bending, and results in energies that depend on the number of layers, as seen for example in other 2D materials such as graphene [23], MoS_2, and WS_2 [24, 25]. To aid identification, construction lines are drawn from the turning points in the bulk dispersion curves, corresponding to energies where the phonon density of states is high.

Table 4.1 compares the features labelled A-I with turning points in the dispersion curves [14] of the optical sidebands, where the phonon density of states are high. The strong peak-A at 200 meV, also seen in [12] can be unambiguously identified as the $LO(E_{1u})$ band at the Γ-point of bulk h-BN [15].

The lowest energy peak (I) corresponds to TO(K). The strongest peak (H) at 156 meV correspond to the TO-branch near to the first Brillouin zone edge. The relative strength of this peak compared to the LO-peak (A) is suggestive of a sample with few layers, rather than a single layer, as the relative DOS of the TO-branch compared with the LO-branches is higher since the degeneracy of the TO-branches is not lifted by the Coulomb interaction

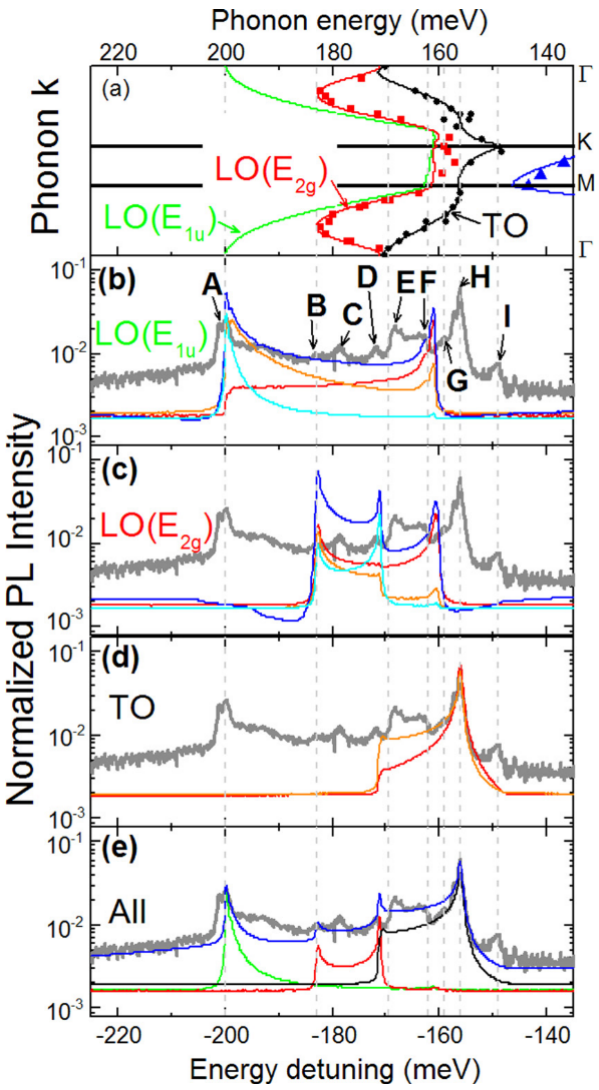

Fig. 4.5 (a) Dispersion curves of the optical phonon branches. The markers are data, and the lines are fits to data taken from Serrano *et al* [14]. The LO(E_{1u})-band is a fit to ab-initio calculation of ref. [14]. Vertical lines are aligned to turning points in the dispersion curves where the density of states is high. Comparison of data to calculations considering a single band: (b) $LO(E_{1u})$ (c) $LO(E_{2g})$ (d) TO. We consider a Fröhlich (blue,cyan) and deformation (red,orange) coupling with (blue, $\varepsilon_{eff} = 22.2, \sigma = 0$); (cyan,$\varepsilon_{eff} = 33.3, \sigma = 0.2$ nm);(red, $\mathscr{M} = 72$ eV.nm^{-1}); (orange,$\mathscr{M} = 341.5$ eV.nm^{-1}). For the TO-branch only the deformation coupling is presented. (e) A fit to data assuming Fröhlich coupling to two LO-branches, and deformation coupling to the TO. Values of $\varepsilon_{eff}(LO(E_{1u})) = 33.3, \varepsilon_{eff}(LO(E_{2g})) = 66.7, \sigma_{LO} = 0.2$ nm, $\mathscr{M}_{TO} = 153$ eV.nm^{-1}, $\sigma_{TO} = 0.1$ nm are used.

[15]. The presence of peak (E) suggests the turn-on of the electron-TO interaction at low momentum as the phonon energy decreases. Peak (D) is assigned to $\mathrm{LO}(\mathrm{E_{2g}},\Gamma)$ assuming the energy is slightly higher than the $\mathrm{TO}(\Gamma)$ point. It is also reproduced by the calculations, see Fig. 4.5(c). Peaks (F) and (G) are near the Brillouin edge of the LO bands, and we use the energy ordering to assign (F) to $\mathrm{LO}(\mathrm{E_{1u}},\mathrm{M}-\mathrm{K})$ and (G) to $\mathrm{LO}(\mathrm{E_{2g}},\mathrm{M}-\mathrm{K})$. Peak B corresponds to the energy of the turning point in $\mathrm{LO}(\mathrm{E_{2g}},\mathrm{T})$.

Peak	detuning (meV)	identity
A	200	$\mathrm{LO}(E_{1u},\Gamma)$
B	183	$\mathrm{LO}(E_{2g},T)$
C	178	?(Not Sure)
D	172	$\mathrm{LO}(E_{2g},\Gamma)$
E	169	$\mathrm{TO}(\Gamma)$
F	163	$\mathrm{LO}(\mathrm{E_{1u}},\mathrm{M}-\mathrm{K})$
G	159	$\mathrm{LO}(\mathrm{E_{2g}},\mathrm{M}-\mathrm{K})$
H	156	TO(M),TO(T)
I	149	$\mathrm{TO}(K)$

Table 4.1 List of optical phonon peaks observed in Fig. 4.5. Most peaks can be linked to turning points in the dispersion. (T) labels a turning point away from the first Brillouin zone edge.

To model the electron-phonon interaction, we consider a Fröhlich-like coupling (coupling which arises due to microscopic electric field produced by the LO phonons which interact with the electrons) to the LO-branch of dimension $d = 2$ given by [26]

$$|g_{k,\alpha,LO}|^2 = \frac{e^2\omega_{k,\alpha,LO}}{2^{4-d}\hbar\varepsilon_0 V_d k_\perp^{d-1}\varepsilon_{eff,\alpha}} f_{LO}^2(k) \tag{4.21}$$

where ε_{eff} is treated as a fitting parameter. For a single conduction band electron

$$\frac{1}{\varepsilon_{eff}} = \frac{1}{\varepsilon_\infty} - \frac{1}{\varepsilon_s} \tag{4.22}$$

where ε_∞ and ε_s are the high frequency and static dielectric constants respectively. The other parameters are the permittivity of free-space ε_0, and the electron charge e. The anisotropy of the dispersion of the optical phonons is approximated according to Eq. (4.15) with $\omega_{k,\theta}$ from Eq. 4.13. Note that qualitatively, there is no difference in $\gamma(t)$ for a 2D or 3D Fröhlich interaction, and we cannot use the data to distinguish between them. To find $\gamma(t)$ for 2D anisotropic Fröhlich coupling Eq. 4.11 can be modified as:

$$\gamma(t)_{2D,frohlich} = \frac{12A}{(2\pi)^2}\int_0^{\pi/6} d\theta \int_0^K dk \left|\frac{g_{k,\theta}}{\omega_{k,\theta}}\right|^2 (1-cos\omega_{k,\theta}t)(2N(\omega_{k,\theta},T)+1) \quad (4.23)$$

For optical phonons $\hbar\omega_k >> 2K_bT$

$$(2N(\omega_{k,\theta},T)+1) = coth\left(\frac{\hbar\omega_{k,\theta}}{2K_bT}\right) \to 1$$
$$(1-cos\omega_{k,\theta}) = 2sin^2\left(\frac{\omega_{k,\theta}t}{2}\right)$$

Using Eq. 4.21, 4.23 and above results

$$\gamma(t)_{2D,frohlich} = \frac{3e^2}{2\pi^2\hbar\varepsilon_0\varepsilon_{eff}}\int_0^{\pi/6} d\theta \int_0^K dk \frac{1}{\omega_{k,\theta}} sin^2\left(\frac{\omega_{k,\theta}t}{2}\right) \quad (4.24)$$

The polarization of the LO-branch is in-plane, hence the argument in Eq. (4.21) is $k \to k_\perp$. For a $\mathcal{N}$-layer sample [15], there are $\mathcal{N}$ LO-branches, labelled by the index α according to the relative phase between adjacent layers (i.e. k_z). The dispersion depends on the index α, and the number of layers $\mathcal{N}$. In Fig. 4.5(a), the LO-branches with $k_z c = 0, \pi$ (i.e. $LO(E_{2g}), LO(E_{1u})$ respectively), are shown for a bulk material. The volume $V_d \to \mathcal{N}V_2$, and a sum over $\mathcal{N}$ branches is made in Eq. 4.14. Calculation for 25-layer sample is presented in Fig. 4.6. The phonon dispersion curves are calculated from [15]. The saw-like n-peak pattern in calculation between 200-170 meV is absent in the data. Moreover, the multi-layer calculation suggest that as $\mathcal{N}$ increases the 200 meV feature should become weaker contrary to the experimental data. This implies that increasing the number of layers will only diverge the fitting. 1-layer sample lacks any phonon feature around 200 meV [15]. This strongly indicates that only bulk phonon modes presented in Serrano *et al* [14] should be considered for the optical calculations.

In addition to the Fröhlich interaction, it is expected that both the LO and TO modes will exhibit a coupling proportional to the optical displacement. For optical-phonons, this is often referred to as deformation coupling [27], but can be treated as the $\mathcal{M}$-term from Eq.4.14 in Eq. 4.11. $\gamma(t)$ for 2D anisotropic optical deformation coupling can be written as:

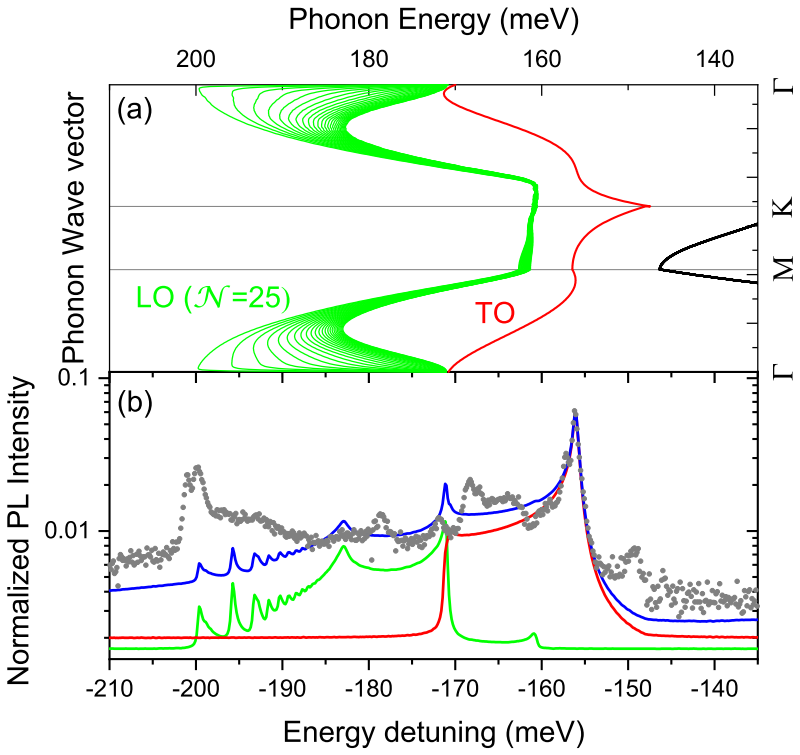

Fig. 4.6 Optical sideband calculation considering a case of 25 layer sample. The phonon dispersions in (a) are calculated from [15]. (b) n+1 peaks are expected for n-layer calculations. The saw-like pattern in calculation from 200-170 meV is absent in the data. All LO optical peaks (green) are caluclated with same fitting parameters $\varepsilon_{eff} = 22.2, \sigma = 0.2$ *nm* and 2D Frohlich coupling. Red shows deformation coupling with $\mathscr{M}_{TO} = 164$ eV.nm^{-1}, $\sigma_{TO} =$ 0.2 nm and blue is calculated spectrum including LO, TO and LA ($\mathscr{D}_{LA} = 9.5$ eV, $\sigma_{LA} =$ 0.4 nm) bands.

$$\gamma(t)_{2D,OD} = \frac{3\mathscr{M}^2}{2\pi^2\rho_A\hbar}\int_0^{\pi/6} d\theta \int_0^K \frac{k^2}{\omega_{k,\theta}^2} f(k)dk \left(\frac{t^2}{2}\right)\left(sinc^2\frac{\omega_{k,\theta}t}{2}\right)\left(\omega_{k,\theta}coth\frac{\hbar\omega_{k,\theta}}{2K_bT}\right) \tag{4.25}$$

Fig. 4.5 compares calculations of the different bands contributions to the spectrum. The contribution to $\gamma(t)$ of both the Fröhlich interaction and the optical deformation coupling depends mostly on the inverse group velocity of the band. In Fig. 4.5(d), the TO-branch is unaffected by additional layers [15], so should be less open to interpretation. The strongest peak (H) is reproduced with $\mathscr{M}_{TO}$=72-341 eV.nm^{-1}, depending on the σ_{TO} used. This appears high, however the origin of the coupling is the deformation of the lattice, and at the

Brillouin edge the 'acoustic' deformation coupling required to give the same shift in energy is: $\mathscr{D} = \mathscr{M}_{TO}a/\pi = 3.3 - 15.6$ eV, which is not unreasonable. Peak (I) is not reproduced, this is attributed to the higher group velocity of the approximate dispersion curve used in our calculations.

In Fig. 4.5(b), it is clear that 200-meV peak can only be explained by Fröhlich interaction to a bulk-like $LO(E_{1u})$ mode, since the $\mathscr{M}$-term has no peak at the Γ-point where $k_\perp = 0$. Naively, one would expect the defect to couple to all of the LO-modes equally. In Fig. 4.5(c), the $LO(E_{2g})$ band has a higher DOS since the spread in energies is lower. Hence if the coupling were equal, this would imply that the peak at the LO(T) point would be stronger than the 200-meV peak. This implies that for this defect, the Fröhlich coupling is stronger for LO-modes where adjacent layers oscillate out-of-phase. This may suggest that dipole fields generated by adjacent layers cancel or enhance the E-field generated by LO-phonon, or may relate to which layer the defect resides. The strength of the interaction given by $\varepsilon_{eff}^{-1} = 0.03$ is small compared with the value of 0.056 for a single electron in bulk h-BN [28]. This is to be expected since it is the difference in the charge distribution of the energy-levels of optical transition that matters.

Fig. 4.5(e) presents a fit to the optical sideband using two LO bands with Fröhlich coupling and a TO-band with deformation coupling. We note that the model is over-specified, and the numbers used should not be considered as accurate. The discrepancy at high energy may suggest that more layers need to be considered, or that $\sigma_{LO} < 0.2$ nm.

4.5 Emitter II

There is considerable variation in the phonon sidebands of the colour centres. To make this point, Fig.4.7 presents the photoluminescence spectrum of emitter II. Although the emission energies are similar, the spectrum is more complicated than for emitter-I. Peak-B is the strongest, and the peak intensity falls strongly with temperature. Hence we assign peak-B as a ZPL. In Fig. 4.1, the ZPL is the highest energy peak, consistent with our two-level model. However, for emitter II the highest photon energy peak is the weaker peak-A. We cautiously suggest that peak-A is also a ZPL, either indicating a fine-structure or a second colour centre. If we assign peaks A and B to ZPLs, then peaks C-G match turning points in the ZA and ZO dispersion curves relative to peak-A. The energies of peaks C and G also match expected turning points relative to peak-B. The energies of peaks H to O match turning points of in-plane polarized phonon modes. The suggested identities of the peaks are presented in table 4.2. The out-of-plane polarized phonon modes have B_{1g}-symmetry [14]. Observation of ZA

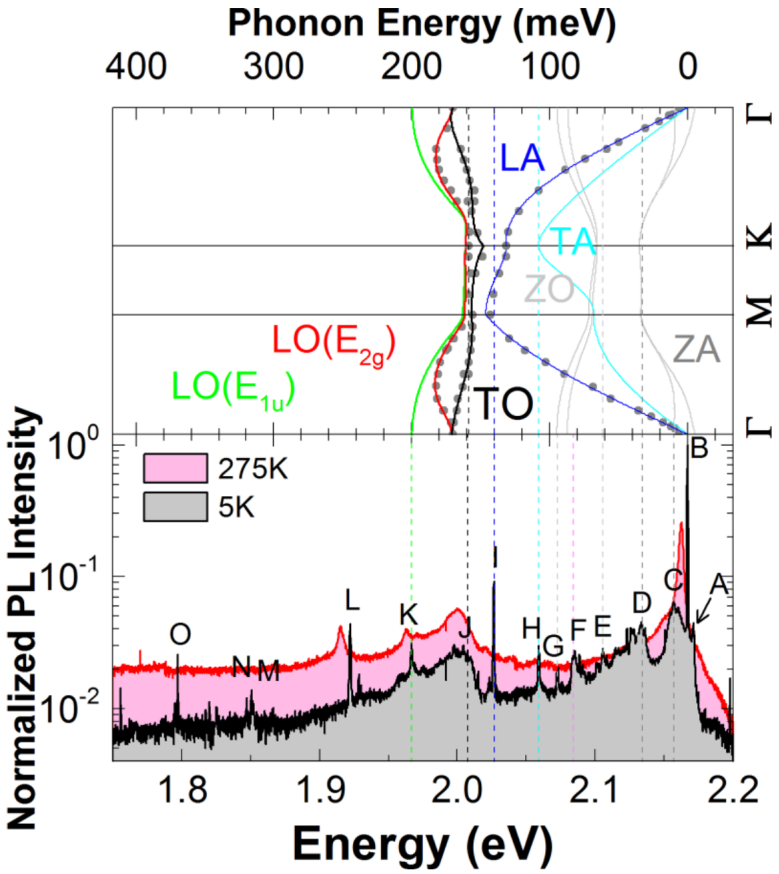

Fig. 4.7 Photoluminescence spectra of emitter II. (top) Dispersion curves of bulk-phonon modes. The markers are data points, and the lines fits to data or ab-initio calculations of ref. [14]. The z-polarized ZA and ZO branches are shifted to the blue by 5.5 meV to match peak-A. The peaks A-O are identified in table 4.2. To aid comparison a number of construction lines aligned with peaks in PL have been drawn.

and ZO-phonon assisted emission suggests that one of the electron states of ZPL_A couples to this symmetry, possibly indicating a p_z orbital [29]. We note that peak (I) is especially strong, sharp, and sensitive to temperature. This could indicate a ZPL at 610 nm, or the LA(M) point with respect to peak-B. Peaks (H) TA(K), and L(LA(M)+TA(K)) are prominent and correspond to displacements along the bond direction of the heavier Nitrogen sub-lattice. Once again, there is a 200-meV peak of the $\mathrm{LO}(\mathrm{E}_{1\mathrm{u}},\Gamma)$ point, indicating the sample has a few layers. Otherwise the in-plane optical phonon sideband has fewer features than emitter I, possibly due to broadening with ZA-phonons, or the emitter preferentially couples to TO

Peak	detuning (meV)	identity
A	-5.5	ZPL_z
B	0	ZPL_x
C	9.8	$\bar{ZA}(\Gamma)_z$ or $ZA(B_{1g},\Gamma)_x$
D	32.7	$ZA(M,K)_z$
E	61	$TA(M)_z$?
F	83.2	$ZO(\Gamma)_z$
G	94	$\bar{ZO}(\Gamma)_z$ or $ZO(\Gamma)_x$
H	107.6	$TA(K)_x$
I	140	$LA(M)_x$
J	159	$TO(M)_x$
K	200	$\bar{LO}(E_{1u},\Gamma)_x$
L	244.5	$LA(M)_x + TA(K)_x$
M	315.5≈ 2(158)	$2\mathrm{TO(M)_x}, 2\mathrm{LO(M,K)_x}$
N	319.8≈ 149+170	$\mathrm{TO(K)_x} + [\mathrm{LO(E_{2g},\Gamma)}, \mathrm{TO(\Gamma)}]_\mathrm{x}$
O	369.4≈ 200+170	$\mathrm{LO(E_{1u},\Gamma)_x} + \mathrm{TO(\Gamma)_x}$

Table 4.2 List of peaks identified in Fig. 4.7 for emitter II. Peaks *A* and *B* are identified with ZPL lines labeled *z* and *x*. The other peaks are identified relative to these two peaks. The bar labels modes where layers oscillate in anti-phase. For peaks C and G the energy matches phonon energies with respect to both peaks A and B.

along the K-direction where the DOS is less peaked. The energies of peaks M-O, match two phonon resonances given in table 4.2.

This suggests that either emitter I and II are from different species of defect, despite their similar emission energies 2.171 (emitter I) vs 2.167 eV (emitter II), or the local environment of emitter II somehow activates the out-of-plane transition.

Note that it is possible that these spectral lines could be from a nearby emitter or charged species. In Chapter 6, we present stimulated emission depletion spectroscopy, a powerful technique to remove spectral line which are not from the emitter under observation.

4.6 Conclusions

The phonon sidebands of a colour centre in h-BN emitting close to 2.17 eV have been analyzed using an independent boson model usually applied to quantum dots [13]. Key differences in the electron-phonon coupling that arise due to the layered structure of h-BN are identified as follows. For emitter I, the acoustic sideband can be described by deformation coupling to an effective two-dimensional phonon-bath with exponential form-factor. This

arises because the LA-phonons are polarized in-plane, and deformation couple to in-plane momentum, and for phonon energies larger than 10 meV, the acoustic phonon dispersion is degenerate with respect to the out-of-plane momentum. For a two-dimensional system, this results in an intrinsic sub-Lorentzian broadening of the ZPL [30], and could limit the optimum photon indistinguishability that could be achieved. The identification of the order of the electron-phonon spectral density is important, since this determines a number of coherence properties, such as the power laws of intensity damping [21], and ZPL broadening [17, 31–34].

In optical phonon band, A peak at 200 meV, which can be attributed to Fröhlich coupling to an $LO(E_{1u})$-phonon where neighboring layers vibrate in anti-phase is prominent in both emitters, and is reported in ref. [12]. We propose that this is a signature of a multi-layer flake with $\mathcal{N} > 3$. The LO-phonons are Fröhlich coupled. From the data, we infer that contrary to our simple model, the Fröhlich interaction strength depends on the relative phase between adjacent layers, i.e. k_z. Furthermore, much of the variation in the optical phonon sideband between different emitters, may be down to the number of layers in the sample. The TO-electron coupling can be described by a deformation coupling proportional to the in-plane lattice displacement. Combined with the near degeneracy of the TO-band with respect to out-of-plane k-vector, the TO-bath is effectively two-dimensional.

For emitter II, we argue that a second weak ZPL coupled to z-polarized phonons is present.

We note that the cut-off length is small $\sigma_{LA} \approx 0.4$ nm, and indicates small carrier wave-functions. Due to the high speed-of-sound, this corresponds to a cut-off temperature of $\hbar\omega_c/k_B = \frac{\hbar v}{\sigma k_B} \approx 400\ K$, where v is the angle-averaged speed of sound, explaining the temperature robustness of the ZPL.

For bulk-phonon modes, an exponential form-factor implies a Lorentizan-like [35] electron density in real-space. The size of the electron density σ varies between phonon branches. Within the independent boson model, this may arise from the use of a single form-factor, and a different ratio of the coupling strength to the upper and lower energy levels of the optical transition between bands. However, this may also hint that short-lived phonon modes localized to the defect may be involved. How these should be treated in this model is an open question.

References

[1] Jake Iles-Smith, Dara P.S. McCutcheon, Ahsan Nazir, and Jesper Mørk. Phonon scattering inhibits simultaneous near-unity efficiency and indistinguishability in semiconductor single-photon sources. *Nature Photonics*, 11(8):521–526, 2017.

[2] P. Borri, W. Langbein, S. Schneider, U. Woggon, R. L. Sellin, D. Ouyang, and D. Bimberg. Ultralong dephasing time in ingaas quantum dots. *Physical Review Letters*, 87(15):157401–157401–4, 2001.

[3] A. J. Ramsay, T. M. Godden, S. J. Boyle, E. M. Gauger, A. Nazir, B. W. Lovett, A. M. Fox, and M. S. Skolnick. Phonon-induced Rabi-frequency renormalization of optically driven single InGaAs/GaAs quantum dots. *Physical Review Letters*, 105(17):1–4, 2010.

[4] Mehran Kianinia, Blake Regan, Sherif Abdulkader Tawfik, Toan Trong Tran, Michael J. Ford, Igor Aharonovich, and Milos Toth. Robust Solid-State Quantum System Operating at 800 K. *ACS Photonics*, 4(4):768–773, 2017.

[5] Mark J. Holmes, Kihyun Choi, Satoshi Kako, Munetaka Arita, and Yasuhiko Arakawa. Room-temperature triggered single photon emission from a III-nitride site-controlled nanowire quantum dot. *Nano Letters*, 14(2):982–986, 2014.

[6] Mark J. Holmes, Satoshi Kako, Kihyun Choi, Munetaka Arita, and Yasuhiko Arakawa. Single Photons from a Hot Solid-State Emitter at 350 K. *ACS Photonics*, 3(4):543–546, 2016.

[7] N. Mizuochi, T. Makino, H. Kato, D. Takeuchi, M. Ogura, H. Okushi, M. Nothaft, P. Neumann, A. Gali, F. Jelezko, J. Wrachtrup, and S. Yamasaki. Electrically driven single-photon source at room temperature in diamond. *Nature Photonics*, 6(5):299–303, 2012.

[8] A. Lohrmann, N. Iwamoto, Z. Bodrog, S. Castelletto, T. Ohshima, T. J. Karle, A. Gali, S. Prawer, J. C. McCallum, and B. C. Johnson. Single-photon emitting diode in silicon carbide. *Nature Communications*, 6, 2015.

[9] Christophe Galland, Alexander Högele, Hakan E. Türeci, and Ataç Imamoğlu. Non-Markovian decoherence of localized nanotube excitons by acoustic phonons. *Physical Review Letters*, 101(6):1–4, 2008.

[10] T. Q.P. Vuong, G. Cassabois, P. Valvin, A. Ouerghi, Y. Chassagneux, C. Voisin, and B. Gil. Phonon-Photon Mapping in a Color Center in Hexagonal Boron Nitride-supplementary. *Physical Review Letters*, 117(9):3–5, 2016.

[11] Annemarie L. Exarhos, David A. Hopper, Richard R. Grote, Audrius Alkauskas, and Lee C. Bassett. Optical Signatures of Quantum Emitters in Suspended Hexagonal Boron Nitride. *ACS Nano*, 11(3):3328–3336, 2017.

[12] Matthew A. Feldman, Alex Puretzky, Lucas Lindsay, Ethan Tucker, Dayrl P. Briggs, Philip G. Evans, Richard F. Haglund, and Benjamin J. Lawrie. Phonon-induced multicolor correlations in hBN single-photon emitters. *Physical Review B*, 99(2):1–5, 2019.

[13] B. Krummheuer, V. M. Axt, and T. Kuhn. Theory of pure dephasing and the resulting absorption line shape in semiconductor quantum dots. *Physical Review B*, 65(19):195313, 2002.

[14] J. Serrano, A. Bosak, R. Arenal, M. Krisch, K. Watanabe, T. Taniguchi, H. Kanda, A. Rubio, and L. Wirtz. Vibrational properties of hexagonal boron nitride: Inelastic X-ray scattering and Ab Initio calculations. *Physical Review Letters*, 98(9):12–15, 2007.

[15] K. H. Michel and B. Verberck. Phonon dispersions and piezoelectricity in bulk and multilayers of hexagonal boron nitride. *Physical Review B - Condensed Matter and Materials Physics*, 83(11):1–14, 2011.

[16] Jiandong Feng, Hendrik Deschout, Sabina Caneva, Stephan Hofmann, Ivor Lončarić, Predrag Lazić, and Aleksandra Radenovic. Imaging of Optically Active Defects with Nanometer Resolution. *Nano Letters*, 18(3):1739–1744, 2018.

[17] Nicholas R. Jungwirth, Brian Calderon, Yanxin Ji, Michael G. Spencer, Michael E. Flatté, and Gregory D. Fuchs. Temperature Dependence of Wavelength Selectable

Zero-Phonon Emission from Single Defects in Hexagonal Boron Nitride. *Nano Letters*, 16(10):6052–6057, 2016.

[18] Toan Trong Tran, Kerem Bray, Michael J. Ford, Milos Toth, and Igor Aharonovich. Quantum emission from hexagonal boron nitride monolayers. *Nature Nanotechnology*, 11(1):37–41, 2016.

[19] The mass density is estimated using a nearest neighbor lattice constant of 0.144nm [20].

[20] R Geick, C. H. Perry, and G. Rupprecht. Normal modes in Hexagonal Boron Nitride. *Physical Review*, 146(2):543–547, 1966.

[21] A. J. Ramsay, Achanta Venu Gopal, E. M. Gauger, A. Nazir, B. W. Lovett, A. M. Fox, and M. S. Skolnick. Damping of exciton rabi rotations by acoustic phonons in optically excited InGaAs/GaAs quantum dots. *Physical Review Letters*, 104(1):20–23, 2010.

[22] Gabriele Grosso, Hyowon Moon, Benjamin Lienhard, Sajid Ali, Dmitri K. Efetov, Marco M. Furchi, Pablo Jarillo-Herrero, Michael J. Ford, Igor Aharonovich, and Dirk Englund. Tunable and high-purity room temperature single-photon emission from atomic defects in hexagonal boron nitride. *Nature Communications*, 8(1):1–8, 2017.

[23] A. C. Ferrari, J. C. Meyer, V. Scardaci, C. Casiraghi, M. Lazzeri, F. Mauri, S. Piscanec, D. Jiang, K. S. Novoselov, S. Roth, and A. K. Geim. Raman spectrum of graphene and graphene layers. *Physical Review Letters*, 97(18):1–4, 2006.

[24] A. Molina-Sánchez and L. Wirtz. Phonons in single-layer and few-layer MoS2 and WS2. *Physical Review B - Condensed Matter and Materials Physics*, 84(15):1–8, 2011.

[25] Changgu Lee, Hugen Yan, Louis E. Brus, Tony F. Heinz, James Hone, and Sunmin Ryu. Anomalous lattice vibrations of single- and few-layer MoS2. *ACS Nano*, 4(5):2695–2700, 2010.

[26] F. M. Peeters, Wu Xiaoguang, and J. T. Devreese. Ground-state energy of a polaron in n dimensions. *Physical Review B*, 33(6):3926–3934, 1986.

[27] X. B. Zhang, T. Taliercio, S. Kolliakos, and P. Lefebvre. Influence of electron-phonon interaction on the optical properties of III nitride semiconductors. *Journal of Physics Condensed Matter*, 13(32):7053–7074, 2001.

[28] 'Ioffe semiconductors database' http://www.ioffe.ru/SVA/NSM/Semicond/.

[29] Mehdi Abdi, Jyh Pin Chou, Adam Gali, and Martin B. Plenio. Color Centers in Hexagonal Boron Nitride Monolayers: A Group Theory and Ab Initio Analysis. *ACS Photonics*, 5(5):1967–1976, 2018.

[30] G M Palma, K A Souminen, and A K Ekert. Quantum computers and dissipation. *Proceedings of the Royal Society A*, (452):567–584, 1996.

[31] Bernd Sontheimer, Merle Braun, Niko Nikolay, Nikola Sadzak, Igor Aharonovich, and Oliver Benson. Photodynamics of quantum emitters in hexagonal boron nitride revealed by low-temperature spectroscopy. *Physical Review B*, 96(12):1–5, 2017.

[32] Elke Neu, Christian Hepp, Michael Hauschild, Stefan Gsell, Martin Fischer, Hadwig Sternschulte, Doris Steinmüller-Nethl, Matthias Schreck, and Christoph Becher. Low-temperature investigations of single silicon vacancy colour centres in diamond. *New Journal of Physics*, 15, 2013.

[33] T. Müller, I. Aharonovich, Z. Wang, X. Yuan, S. Castelletto, S. Prawer, and M. Atatüre. Phonon-induced dephasing of chromium color centers in diamond. *Physical Review B - Condensed Matter and Materials Physics*, 86(19):4–9, 2012.

[34] Kay D. Jahnke, Alp Sipahigil, Jan M. Binder, Marcus W. Doherty, Mathias Metsch, Lachlan J. Rogers, Neil B. Manson, Mikhail D. Lukin, and Fedor Jelezko. Electron-phonon processes of the silicon-vacancy centre in diamond. *New Journal of Physics*, 17, 2015.

[35] In 1D the Fourier transform of an exponential is a Lorentzian. In 2D it is a bit different.

Chapter 5

Optical Gating of Photoluminescence

5.1 Introduction

In the previous chapter, the emitter is resonantly excited with a 532 nm CW laser and a phonon mediated emission process was studied. For qualitative SPE measurements, we have to search for a bright emitter (for high signal to noise ratio) with "clean spectra" (Intense ZPL with narrow linewidth, clear PSB peaks and no other intense peaks which can be from a nearby species) such as emitter I in chapter 4. The drop casting technique and annealing at high temperature facilitates many such emitters in the sample and a $80 \times 80\ \mu m^2$ PL map (See Fig. 3.2 in chapter 3) can reveal a number of them. The next issue is the stability of these emitters. During experiment we observed that some emitters fluctuate in intensity, some are stable over time and some switch off after few minutes of illumination. Since no one is clear about the origin of these emitters, it is not possible to predict the stability by just looking at the spectra, one needs to illuminate the emitter for a long time while tracking its photon count rate. Instability in emission makes hBN emitters unreliable for application in quantum technologies. The ideal scenario would be to make an emitters stable rather than hunting for a stable one that may or may not have the desired wavelength, linewidth etc.

Typically, the choice of excitation laser plays a crucial role in the optical control of quantum emitters. For example, in stabilizing and enhancing the photoluminescence (PL) yield, of colour centres in diamond [1–5] and SiC [6–8], and of InGaAs quantum dots [9]. In hBN there have been fewer studies in this area, but the choice of excitation energy has been shown to play a role in the absorption efficiency [10, 11], in stabilisation and enhancement of the PL emission [12] and in photochemical modification of the defect [13].

For the work in this chapter, we use multicolour excitation to investigate the photophysical dynamics of yellow emitting colour centres in hBN. Typically a green excitation is used to

study such defects. The addition of a blue repump laser dramatically enhances the PL yield of certain colour centres, but has a weak effect on others. We investigate two defects in detail using photoluminescence, and photoluminescence excitation (PLE), spectroscopy. Through comparison with a rate equation model we find that the observed dynamics can be explained in terms of photo-induced switching between two states. The colour centres are pumped into a dark state by resonant, or quasi-resonant, excitation and require a higher energy laser to repump back to the bright state. The repump spectrum is step-like with a defect specific threshold between 2.25 and 2.6 eV. This indicates a discrete to band repump transition, and points to charge state conversion as the origin of this behavior.

This work has been published and is here adapter from Nano Lett., 20, 6, 4256–4263 (2020). [14] Copyright 2020 American Chemical Society. For this work, my contributions were- numerical simulation to fit the data, measurements in the lab and programming the devices, inputs for the paper and contribution towards plotting the figures. This paper was written and submitted by Dr. Isaac Luxmoore.

5.2 Sample Preparation and Experimental Setup

For this experiment, before drop casting hBN, the Si substrate is coated with 5 nm of Al_2O_3 [15] followed by annealing. See Chapter 3, section 3.1 for process and details. Fig.5.1 shows the experimental setup. The three lasers used in the experiment are co-aligned and coupled to a microscope objective of N.A=0.8, which focuses the laser light to a diffraction limited spot of approximately 1μm diameter. The luminescence from the sample is collected using the same objective and sent to a monochromator/CCD for spectroscopy, or filtered using a pair of tunable long and short pass filters resulting in an allowed bandwidth of $\sim$1 nm and detected with avalanche photo diodes (APD), for time-resolved and autocorrelation measurements. Blue and green continuous wave (CW) excitation is provided by a 450 nm (2.76 eV) diode laser and a 532 nm (2.33 eV) diode pumped solid state (DPSS) laser, respectively. A function generator is used to provide trigger signal for the two lasers and TCSPC (time correlated single photon counter). A pair of half wave plate ($\lambda/2$) and linear polarizer (LP) are used at the input before DBS to set the excitation polarization. On emission side, before tuneable filters, another set of $\lambda/2$ and LP detect emission polarization. For the PLE experiment a supercontinuum laser (SCL) is filtered with an acousto-optic tunable filter (AOTF) to give a $\sim$1 nm bandwidth and a pulsewidth of $\sim$5 ps. The AOTF can be driven with a superposition of radio frequencies to create a filter with multiple passbands that can be independently controlled (wavelength and transmittance). This means that AOTF can allow two or more

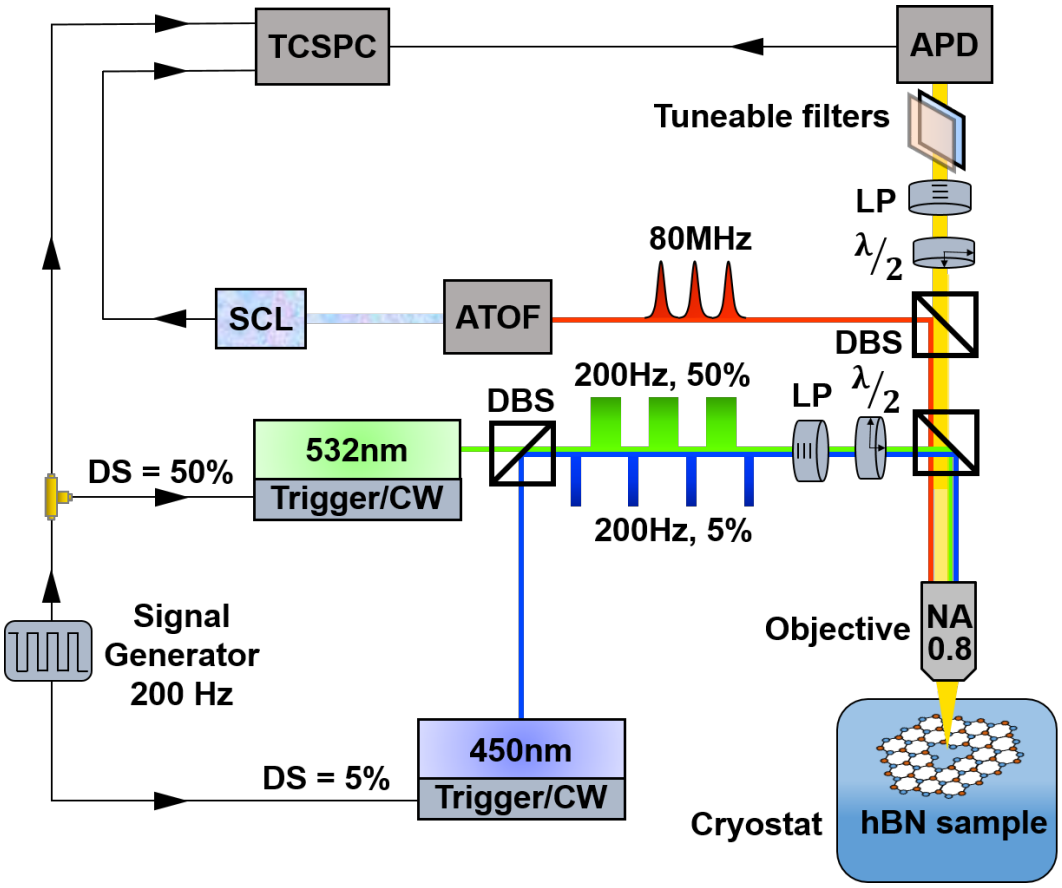

Fig. 5.1 Schematic diagram for photocharging setup. PBS=polarizing beam-splitter; LP= linear polarizer; DBS=dichroic beam-splitter; SCL=supercontinuum laser; AOTF=acousto-optic tunable filter; DS=duty cycle; APD=avalanche photodiode; $\lambda/2$=half-waveplate; TCSPC=time-correlated single photon counting electronics. For PL measurements signal is sent to spectrometer instead of tuneable filters and APD.

spectral lines with full control over intensity and wavelength individually. However, the pulse frequency is same for each spectral line and can be controlled using the SCL (frequency = 80 Mhz). This enables PLE measurements with simultaneous resonant excitation, as shown in Fig. 5.8(a).

5.3 Multicolour Excitation

Fig. 5.2 illustrates the enhancement of photoluminescence from colour centres in hBN using multicolour excitation. Fig. 5.2(a) shows a typical PL map recorded with green CW excitation, which shows a number of bright spots resulting from individual, and small clusters

of, colour centres in hBN flakes. In Fig. 5.2(b), the same region of the sample is mapped using co-aligned green and blue CW laser beams, resulting in an approximately two-fold increase in the number of luminescent centres. Two representative emitters are highlighted in the PL maps and defined as defect-A and defect-B. Defect-A appears bright in both maps, whereas defect-B is dark under green excitation, but bright when blue illumination is added. To verify that defects-A and -B are individual colour centres we measure the second order auto-correlation function, $g^{(2)}(\tau)$

5.3.1 Second order autocorrelation measurements

To verify that we are probing individual colour centres, we use a HBT interferometer to measure the second order autocorrelation function, $g^{(2)}(\tau)$, of defects A and B. Fig. 5.3 summarises these measurements, where the data is presented without background subtraction. Note that the $g^{(2)}(\tau)$ is normalised by dividing the second order autocorrelation data by $(C_{R1} \times C_{R2} \times W_{bin} \times t_{int})$, where C_{R1} and C_{R2} are the photon count rates on APD1 and APD2, W_{bin} and t_{int} are the data bin-width and integration time of the experiment. In Fig. 5.3(a) the $g^{(2)}(\tau)$ function is plotted for a relatively low green power, P_G, of 0.36 mW and decreases to $\sim$0.25 at zero time delay, unambiguously confirming the antibunching in the emission. The calculated (this calculation with the theoretical 3 level model will be discussed later) $g^{(2)}(\tau)$ goes to zero at zero time delay and therefore deviates from the experimental data. However, it is well known that the value of $g^{(2)}(0)$ is limited by the timing resolution of the setup. In our case, the measured instrument response function (IRF) is well fit by a Gaussian function with FWHM of 905 ps. A convolution of the calculated $g^{(2)}(\tau)$ and the Gaussian IRF is plotted in In Fig. 5.3(a) showing improved agreement with the experimental data.

In the presence of bunching (reason for the bunching behaviour will be discussed later, in model section, and is not relevant at this point) the criterion for single photon emission is modified and the $g^{(2)}(0)$ threshold becomes half of the maximum bunched amplitude [16]. This is the case for high green power (P_G =4.3 mW), as shown for defect-B in Fig. 5.3(e), where the maximum bunching reaches $\sim$3.28, but $g^{(2)}(0) \approx$1.2, again satisfying the criterion for single photon emission.

Similar measurements are made for defect-A. In this case only green excitation is used and there is considerable bunching, even at low green power, P_G =0.36 mW (Fig. 5.3(a)). In this case the experimental data dips to $g^{(2)}(0) \approx$0.5, considerably below half the maximum bunching, again confirming single photon emission. When the green power is increased beyond saturation, to P_G =4.3 mW, the bunching increases, the radiative lifetime is reduced

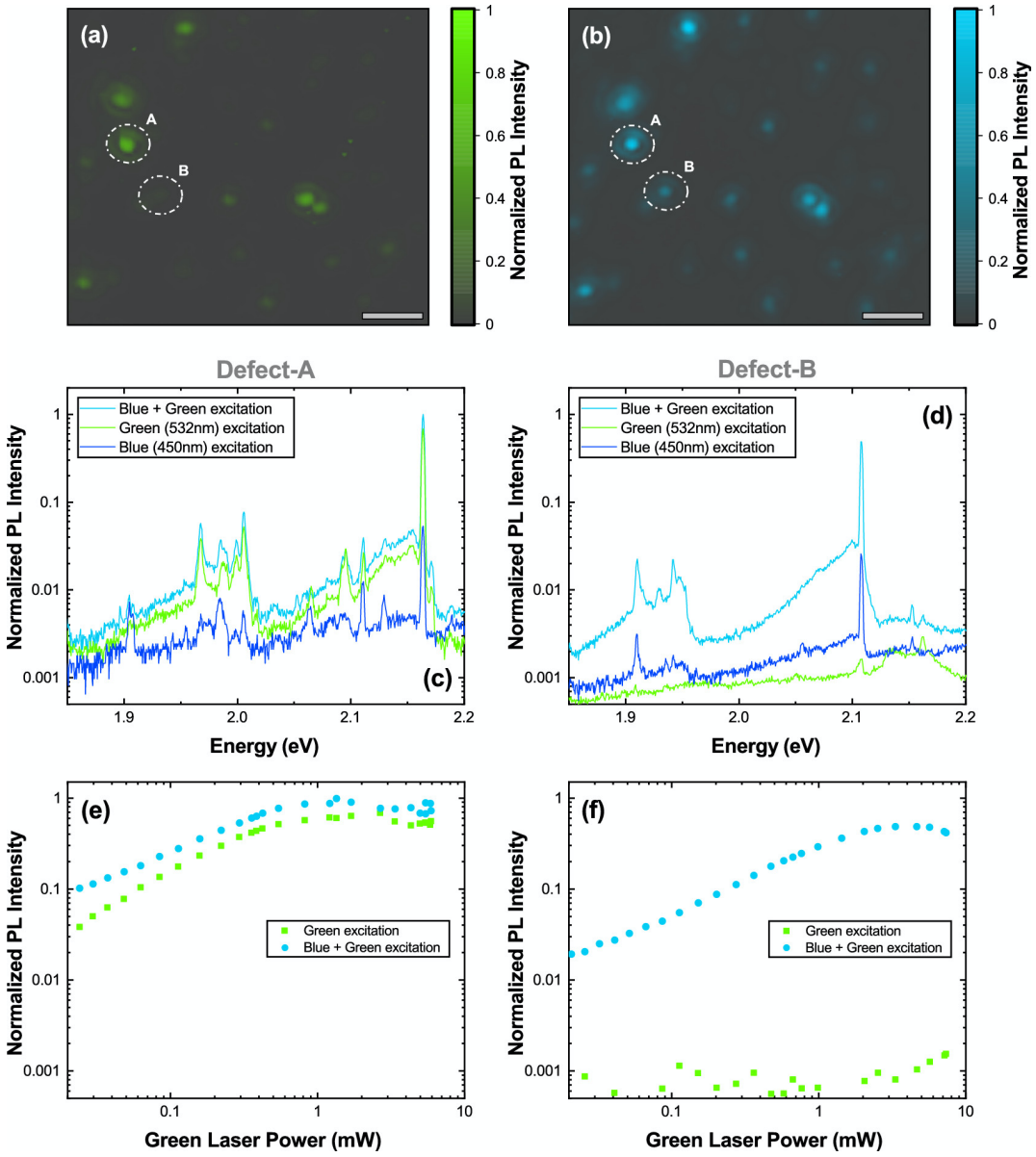

Fig. 5.2 (a) and (b) Spatial maps of integrated photoluminescence emission (spectral range from 2.06 to 2.15 eV) under (a) green(532 nm, 2.33 eV) only and (b) green plus blue (450 nm, 2.76 eV) excitation. The scale marker in (a) and (b) is 5μm. (c) and (d) Photoluminescence spectra recorded under green, blue and green plus blue excitation conditions for the two defects circled in the PL maps, (c) defect-A and (d) defect-B. The green and blue excitation powers are $\sim 700\mu W$. (e) and (f) Green laser power dependent intensity of the zero phonon line PL emission for (e) defect-A and (f) defect-B, with (blue circles) and without (green squares) the blue repump laser. In (c) to (f) the PL intensity is normalized to the peak counts of defect-A. In (e) and (f) the blue power is $\sim 700\mu W$.

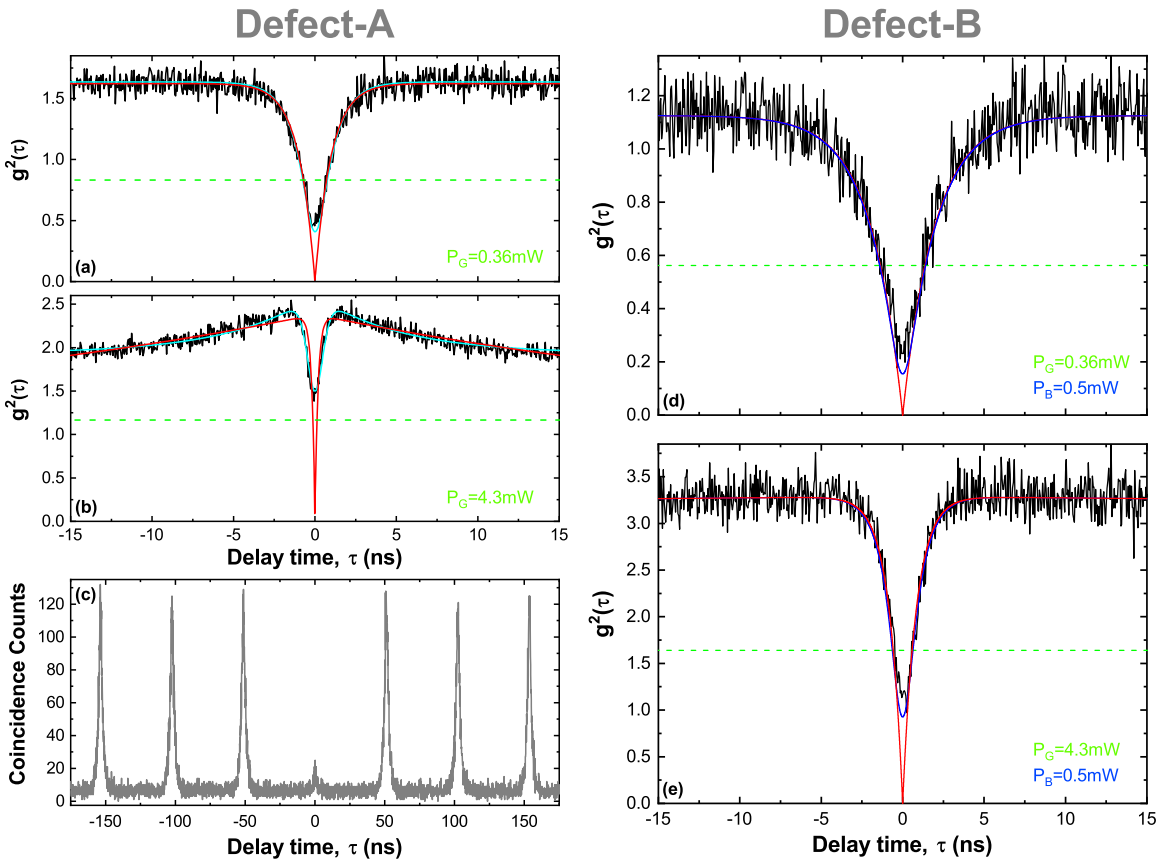

Fig. 5.3 Second order autocorrelation function $g^{(2)}(\tau)$ of defects A and B. (a) and (b) CW $g^{(2)}(\tau)$ for defect-A with (a) green laser power of 0.36mW and (b) green power of 4.3 mW. In (a) and (b) the cyan (red) lines show fits to a 3-level model with (without) convolution of a Gaussian instrument response function with FWHM of 905 ps. The dashed green lines show the threshold for single photon emission. (c) Pulsed $g^{(2)}(\tau)$ for defect-A with green peak power of $\sim$5 mW. (d) and (e) CW $g^{(2)}(\tau)$ for defect-B with (d) green laser of 0.36 mW and blue power of 0.5 mW and (e) green power of 4.3 mW and blue power of 0.5 mW. In (d) and (e) the blue (red) lines show the calculated $g^{(2)}(\tau)$ function with (without) convolution of a Gaussian instrument response function with FWHM of 905 ps. The dashed green lines show the threshold for single photon emission.

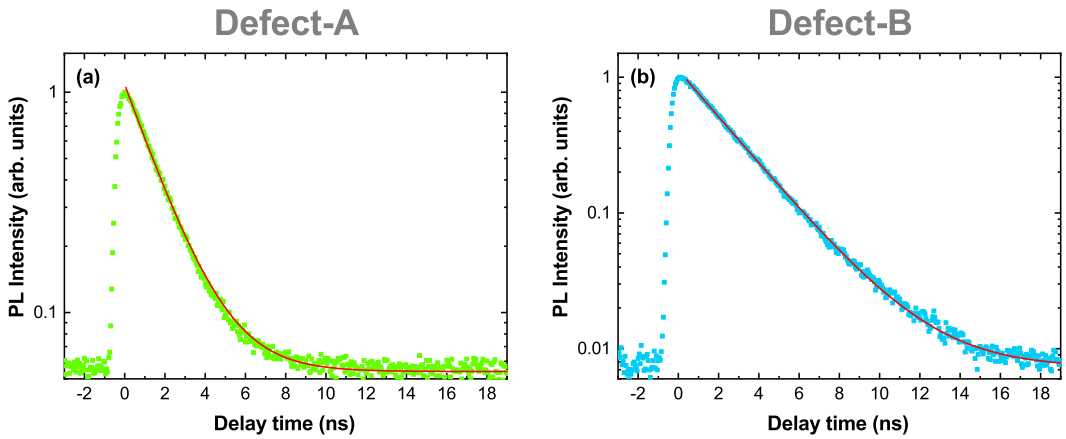

Fig. 5.4 Time-resolved photoluminescence decay of the zero-phonon line of (a) defect-A and (b) defect-B. The red solid line shows exponential fits to the data with decay rates of 600 MHz and 380 MHz for defects-A and -B, respectively.

and the experimental $g^{(2)}(0)$ no longer dips below half the maximum bunching amplitude (Fig. 5.3(b). However, this is due to the limited timing resolution of our setup, combined with the considerably faster radiative decay of 1.67ns for defect-A compared to 2.63 ns for defect-B (Fig. 5.4). This is highlighted by the good agreement shown between the experimental data and the ideal 3-level behaviour convolved with the Gaussian IRF (Fig. 5.3(b)). As a final proof that we are measuring the emission from a single defect, even at these high excitation powers, we perform a pulsed $g^{(2)}(\tau)$ measurement with a laser power above saturation (peak green power $\sim$5 mW), shown in Fig. 5.3(c). In this case, the criterion for single photon emission is clearly satisfied, with the area of the zero time delay peak 0.07 when normalized to the mean area of the six other peaks shown.

5.3.2 Behaviour under different illumination conditions

Further detail is shown in the PL spectra of the two defects under different illumination conditions (Fig. 5.2(c) and (d)). Under green excitation the spectrum of defect-A, in Fig. 5.2(c), consists of a bright ZPL at 2.167 eV, with optical and acoustic phonon sidebands (PSB) that are consistent with previous reports [17, 11, 18]. Addition of the blue laser, results in a small enhancement of the overall PL intensity. With blue excitation alone, the ZPL intensity is reduced by a factor of $\sim$20, for the same excitation power. A comparison of the green laser power dependence of the ZPL of defect-A is made in Fig. 5.2(e), with and without the blue laser. The presence of the blue laser increases the PL intensity at all powers of the green

laser, including those beyond saturation, indicating that the blue laser is not just providing extra power, but increasing the PL yield of the defect.

In the case of defect-B, the choice of excitation conditions plays a much greater role. The PL spectrum, shown in Fig. 5.2(d), is similar to that of defect-A, with a single ZPL at 2.107 eV and similar optical and acoustic PSBs. However, this is only the case for simultaneous excitation with blue and green lasers. With only blue excitation, the ZPL intensity is reduced by a factor of $\sim$20, whereas for only green excitation the intensity is reduced by a factor of $\sim$400. The power dependence (Fig. 5.2(f)) shows that even with a green laser power up to several mW the PL yield is still hundreds of times less intense without the blue laser.

5.4 Time Resolved PL Measurements

To further investigate this behavior, we use time-resolved photoluminescence to study the dynamics of defect-B. Fig. 5.5(a) illustrates the experiment, where a pulse train of alternating blue and green pulses excite the defect, whilst the PL from the ZPL is directed to an APD. Fig. 5.5(b) plots a typical PL time trace recorded during this experiment, with and without the blue laser. With no blue laser pulses, the photoluminescence from the defect is weak and directly follows the intensity profile of the green laser. We term this the *dark* state of the defect.

When the blue laser pulses are applied, weak PL is observed for the duration of the pulse. However, the blue pulse also prepares the defect in a *bright* state, resulting in a strong PL signal at the start of the following green pulse. The initial peak PL increases linearly with blue power, and saturates at a few μW of the blue pump power (Fig. 5.5(g)). Under green illumination, the bright state lives for tens of μs. The PL decays exponentially with a decay-rate that is quadratic with green laser power, indicating that the *bright* to *dark* transition is mediated by a two-photon process (Fig.5.5(f)).

5.4.1 Rate equation model

For qualitative understanding, we construct a simple rate equation model motivated by the experimental observations and illustrated in Fig. 5.7(c). The model consists of four energy levels: G and E are the ground and excited levels of the bright state; S represents the dark shelving state of the defect; and C the conduction band or some higher energy levels of the system. Γ_R is the radiative decay of the bright state and Γ_{CS}, and Γ_{CE} are non-radiative

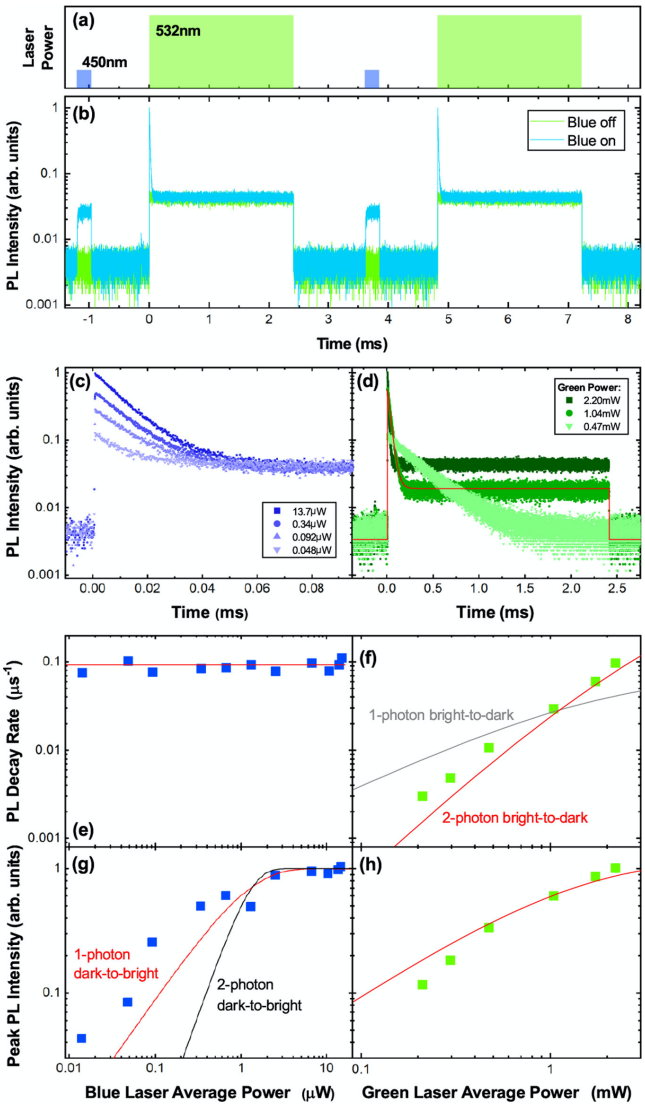

Fig. 5.5 Time-resolved photoluminescence measurements of the zero-phonon line of defect-B. (a) Pulse-sequence used to excite photoluminescence. A blue pulse (450 nm, 2.76 eV) of width 0.5ms is followed by a green pulse (532 nm, 2.33 eV) of 2.5ms, with a repetition frequency of 208 Hz. (b) Example PL intensity time trace. Without the blue pulse, the green laser excites low intensity emission. The blue pulse weakly excites PL, but also prepares the defect in the bright state. The subsequent arrival of a green pulse results in high intensity PL, which rapidly decays, indicating the defect is pumped into the dark state. (c) and (d) PL decay curves resulting from the onset of a green pulse for different (c) blue pump powers (fixed green power of 2.2 mW) and (d) green pump powers (fixed blue power of 10.5 μW). (e) and (f) Exponential decay rate as a function of (e) blue and (f) green pump power. (g) and (h) Peak ZPL intensity from the green laser pulse as a function of (g) blue and (h) green laser power. The red lines in (d) to (h) are calculated using the rate equation model (see Fig. 5.7(c), Table. 5.1).The grey line in (f) is a fit to the data assuming a 1-photon bright-to-dark transition from G to C. The black line in (g) is a fit to the data assuming a 2-photon dark-to-bright transition from S to C.

transitions which link the dark and bright states. For each transition there is a corresponding optical pump: F_B is the bright state pump rate, F_L is the rate at which electrons are pumped out of the bright excited state and F_R is the rate at which the colour centre is pumped out of the shelving state. The resulting system of four differential equations is solved numerically to calculate the photoluminescence, $\propto E\Gamma_R$

The model described by the following differential equations:

$$\frac{dG}{dt} = \Gamma_R E - F_B G \tag{5.1}$$

$$\frac{dE}{dt} = F_B G + \Gamma_{CE} C - \Gamma_R E - F_L E \tag{5.2}$$

$$\frac{dC}{dt} = F_L E + R_R S - \Gamma_{CE} C - \Gamma_{CS} C \tag{5.3}$$

$$\frac{dS}{dt} = \Gamma_{CS} C - F_R S \tag{5.4}$$

which are solved numerically to calculate the photoluminescence intensity, $I \propto \Gamma_E E$.

The radiative lifetime, Γ_R is extracted from a time-resolved photoluminescence measurement and found to be 380 MHz [see Fig. 5.4(b)].

To further validate the chosen model (model 1, Fig. 5.7(c)), we also compare the experimental data to two variations of the model, illustrated in Fig. 5.6. This allows us to determine that a model with a 2-photon bright-to-dark and 1-photon dark-to-bright process best describes the experimental data (See next section).

In model 2, shown in Fig. 5.6(a), the dark-to-bright process is mediated by the pump, F_L, which in this case is directly from G to S. This results in a 1-photon bright-to-dark process, as opposed to the 2-photon process in model 1.

In the case of model 3, shown in Fig. 5.6(b), the bright-to-dark pump, F_R, is proportional to the power squared, rather than linear with power, as is the case with model 1. This allows a comparison of a 2-photon versus 1-photon repump process.

5.4.2 Comparing results with the model

The model is compared to the data in Fig. 5.5 (e) to (h), and shows good agreement with the main experimental observations. Firstly, the rate of the dark to bright process, plotted in Fig. 5.5(f), has an exponent close to 2. Model 1, which has a two-step (two-photon) bright to dark transition, reproduces the data well (red-line), whereas a fit assuming a one-photon

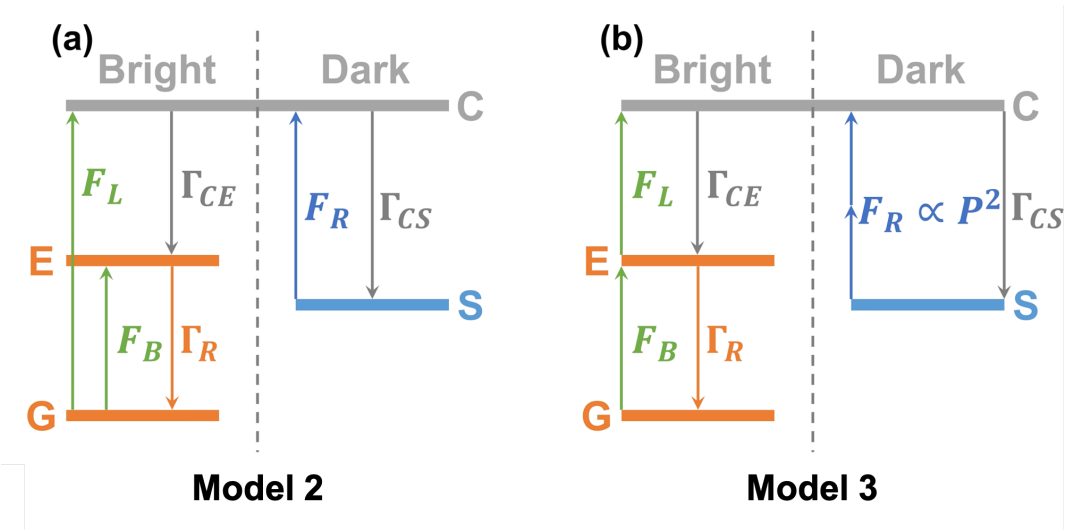

Fig. 5.6 Alternative rate equation models (a) In model 2 there is a direct optical pump from G to C, rather than a two-step pump via E. (b) In model 3 the repump from S to C is a two-photon process.

pump directly from G to C (gray-line) with model 2 does not, showing a clear preference for two-step pumping from the excited bright-state.Secondly, Fig. 5.5(g) plots the peak PL at the beginning of the green pulse as a function of the average power of the blue laser, P_B. At low powers, the exponent is 1, indicating a one-photon repump process that requires an energy >2.33 eV (green), but <2.76 eV (blue). Fits assuming model 1, a one-photon ($F_R \propto P_B$, red-line) and model 3, two-photon ($F_R \propto P_B^2$, black-line) pump from S to C are compared to data, and verify that the model 1 performs best.

Moreover, the peak intensity at the start of the green laser pulse is proportional to the probability that the preceding blue pulse has prepared the colour centre in the bright state. As this is approximately linear with the blue power it indicates a 1-photon dark-to-bright repumping process and therefore better agreement is found for model 1 than model 3.

Similar dynamics have been observed for germanium vacancies in diamond, where resonant excitation results in a two-step pumping of the system to a dark state, whilst a laser of higher energy recovers the system to a bright state with a one-photon process [5]. The non-radiative decay and pump rates are determined from a best fit to the experimental data with model 1 and are given in Table 5.1.

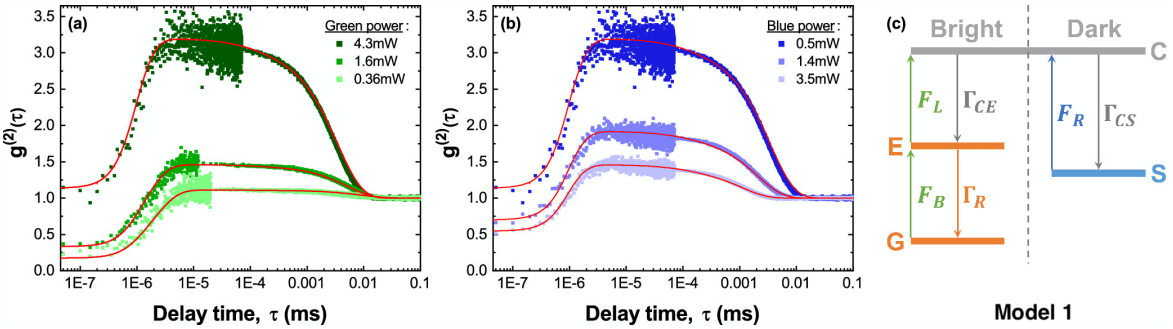

Fig. 5.7 Second order autocorrelation function $g^{(2)}(\tau)$ of defect-B with (a) fixed blue (450 nm, 2.76 eV) power of 0.5 mW and varying green (532 nm, 2.33 eV) power and (b) fixed green power of 4.3 mW and varying blue power. The red lines show fits to the data using the model outlined in the text. (c) Rate equation model of 2-photon photoionization and 1-photon recharging.

5.4.3 Verifying correct model with $g^{(2)}(\tau)$ data

To further verify model 1, $g^{(2)}(\tau)$ measurements of defect-B are made for different blue and green excitation powers. In Fig. 5.7(a), $g^{(2)}(\tau)$ is plotted for fixed blue power of 0.36 mW and three different green powers. For low green power $g^{(2)}(\tau)$ is close to that expected for a two-level emitter. However, increasing the green power leads to pronounced bunching with an exponential decay on the order of microseconds. Similar bunching behavior has been observed previously for colour centres in hBN [19, 20] and other wide bandgap semiconductors [21, 22] and attributed to the presence of metastable dark states. In Fig. 5.7(b), $g^{(2)}(\tau)$ is plotted for fixed green power of 4.3mW and three different blue powers. When the blue power is low, the bunching is strong, but increasing the blue power counteracts the tendency of the green laser to pump the defect into the dark state and $g^{(2)}(\tau)$ close to the 2-level case is recovered. Again, similar observations have been made for the repumping of a colour centre in hBN, but with different emission and pump energies [12]. The $g^{(2)}(\tau)$ function is calculated from the rate equation model with the Quantum Toolkit in Python package [23, 24](QuTiP, www.qutip.org) and convolved with the instrument response function of the photon counting setup. The calculation with QuTip was performed by group member and co-author of [14], Dr. Ralph N. E. Malein. Further information about QuTiP calculation can be found in the S.I section of [14]. By keeping the radiative and non-radiative transition rates constant and varying the pump rates in proportion to the experimental powers (see Table 5.1), good fits to the data could be found, as plotted in Fig. 5.7(a) and (b).

Transition	Rate (MHz)
Γ_R	380 ± 1.0
Γ_{CE}	5.0 ± 0.4
Γ_{CS}	2.75 ± 0.08
F_B	$(246.6 \pm 0.3)P_G + (63.0 \pm 0.4)P_B$
F_L	$(6.9 \pm 0.3) \times 10^{-4} F_B$
F_R	$(0.30 \pm 0.05)P_B$

Table 5.1 Rate equation model parameters. The radiative decay rate, Γ_R, is extracted from a fit to time resolved PL data from Fig.5.4. All other rates are extracted from fits to $g^{(2)}(\tau)$, as shown in Fig. 5.7. P_G and P_B are the power (in mW) of the green (532 nm) and blue (450 nm) lasers used in the experiments.

5.5 Measuring Energy Thresholds

From the two-colour experiments it is clear that the photon energy of the excitation laser determines if the colour centre is bright or dark. We therefore perform PLE spectroscopy, to investigate how the optical pumping depends on photon energy. We first measure the energy threshold of the repump process for defect-A. The PLE spectrum is measured with and without the addition of the blue CW laser, as plotted in Fig. 5.8(a), whilst recording the intensity of the PSB emission. The energy threshold is measured as 2.25 eV by exciting the defect resonantly, whilst simultaneously sweeping the repump laser, as shown in Fig. 5.8(a). To understand why defect-B is dark under green only illumination but bright under green and blue excitation, a similar measurement is made. In Fig. 5.8(b), defect-B is excited by both the green CW laser and the tunable laser and reveals a clear energy threshold for the repump process, of $\sim$2.6 eV. Although the ZPL Energy of defect-A and B differs by only $\sim$50m eV, the repump threshold differs by $\sim$350m eV. Nevertheless, the PLE measurements suggest that the two defects can be described by the same model, but with different energy dependence of the repump rate, F_R.

5.6 Observing high energy level (ZPL_2) via PLE

The PLE measurements also reveal further information about these defects. In Fig. 5.8(c), the PLE spectrum of defect-A is measured, for excitation polarization parallel and perpendicular to the ZPL emission (ZPL_1). When the polarization is parallel to ZPL_1, absorption resonances are observed in two bands detuned by $\sim$170 meV and $\sim$340 meV, which can be attributed to the one and two optical PSBs, respectively. With orthogonal polarization the PLE spectrum

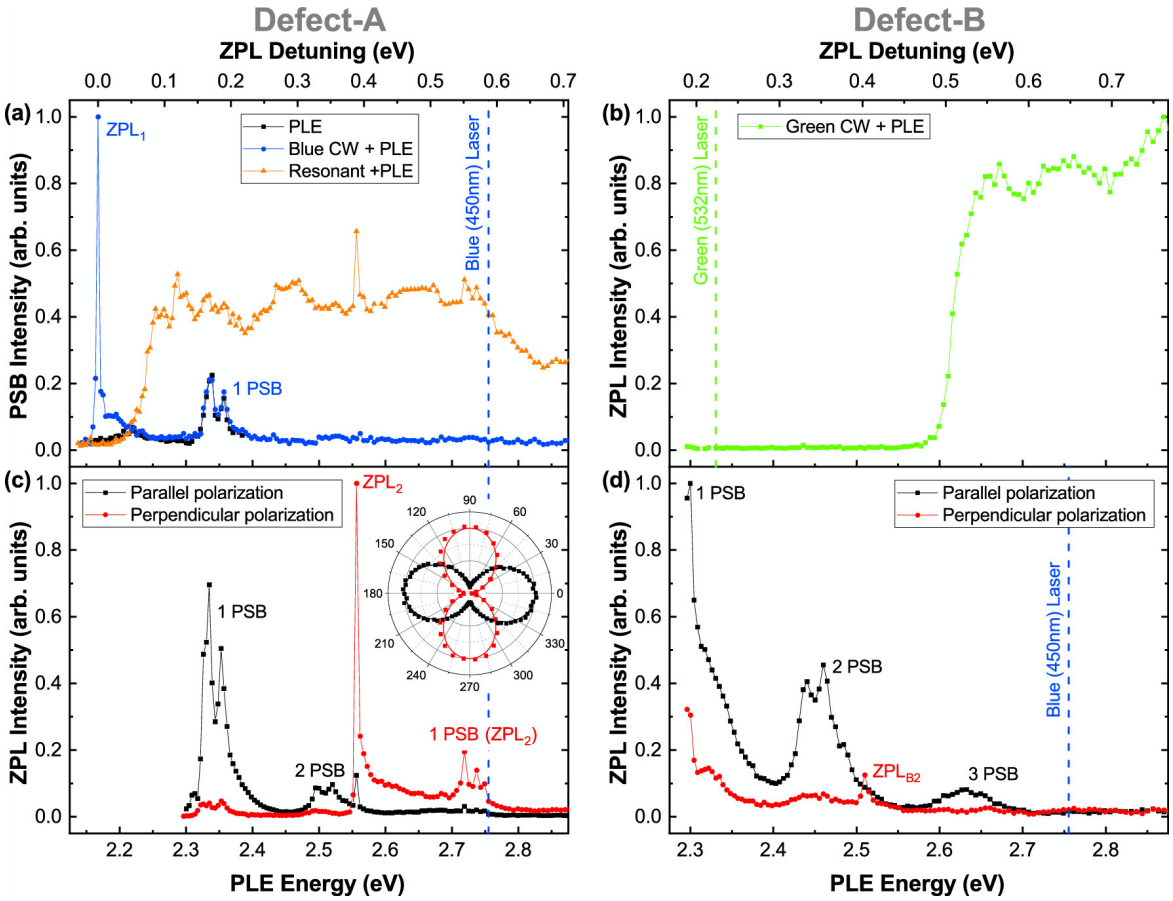

Fig. 5.8 Photoluminescence Excitation (PLE) Spectroscopy. In all experiments, a tunable pulsed laser is swept across the plotted range, with the integrated intensity of the one phonon sideband (a), or zero phonon line (b - d) plotted for each point. (a) PLE spectra of defect-A with (blue circles) and without (black squares) blue CW laser co-excitation and with resonant co-excitation of ZPL_1 (2.167 eV, orange triangles). (b) PLE spectrum of defect-B with fixed green CW laser co-excitation (green squares) (c) and (d) PLE spectra with blue CW co-excitation for PLE laser polarization parallel (black squares) and perpendicular (red circles) to the emission from ZPL_1, for (c) defect-A and (d) defect-B. The inset to (c) shows a polar plot of the intensity of the one phonon sideband of defect-A as a function of the excitation polarization angle when resonant with ZPL_1 (2.167 eV, black squares) and ZPL_2 (2.556 eV, red circles). (c) Inset- The black and red solid lines show $\sin^2\theta$ fits to the absorption polarisation data for dipoles of ZPL_1 and ZPL_2. In (a) - (d) the green and blue dashed lines indicate the energy of the green (532 nm, 2.33 eV) and blue (450 nm, 2.76 eV) CW lasers, respectively.

is very different, with only weak absorption into the PSB, but with a strong and spectrally narrow absorption resonance detuned from ZPL_1 by 400 meV, evidencing a higher energy level in the electronic structure of the colour centre, labelled ZPL_2 in Fig. 5.8(c). The PLE spectrum is similar to that of ZPL_1, including a PSB detuned by $\sim$170 meV. Furthermore, the polar plot in Fig. 5.8(c) shows that the two ZPLs are orthogonally polarised, with an 89° misalignment of the absorption dipoles of ZPL_1 and ZPL_2.

A similar PLE measurement of defect-B is presented in Fig. 5.8(d), where low power blue excitation is used to maintain the colour centre in its bright state. As with defect-A, when the polarization of the tunable laser is aligned parallel to the ZPL, absorption peaks corresponding to phonon assisted processes are observed. In this case, the relative efficiency of the two PSB is greater than for defect-A and the three PSB is also observed. For the orthogonal polarization the absorption is considerably less efficient at all energies, but there is a weak absorption peak at $\sim$2.51 eV, labelled ZPL_{B2} in Fig. 5.8(d). The detuning of this absorption peak is 403 meV, suggesting a similar origin as in defect-A.

5.6.1 Measurements to confirm ZPL_2

Fig. 5.9 summarises some additional measurements of defect-A. Fig. 5.9(a) shows the polarization dependence of the emission and resonant absorption of ZPL_1, which are co-aligned. The PL spectrum of defect-A is shown in Fig. 5.9(b) under blue CW illumination and compared to the PLE spectrum. Although the absorption resonance is clearly observed when detecting at the energy of ZPL_1, there is no PL emission at the energy of ZPL_2 when exciting with the blue laser.

Finally, the PLE data presented in Fig.5.8(c) is replotted in Fig. 5.9(c) and (d) as the polarization angle, $\phi = \tan^{-1}(I_\perp/I_\parallel)$ and polarization contrast, $C = (I_\parallel - I_\perp)/(I_\parallel + I_\perp)$ respectively, where $I_\parallel$ ($I_\perp$) is the intensity of ZPL_1 emission for parallel (perpendicular) excitation polarization. A clear energy dependence can be seen in the alignment of emission and absorption dipoles. When the excitation energy is less (greater) than ZPL_2 (2.556 eV), the emission and absorption dipoles are approximately parallel (perpendicular).

These observations explain previous measurements where, depending on the detuning of the laser energy from the ZPL, the absorption and emission dipoles can be aligned or misaligned by up to 90° [25, 26].

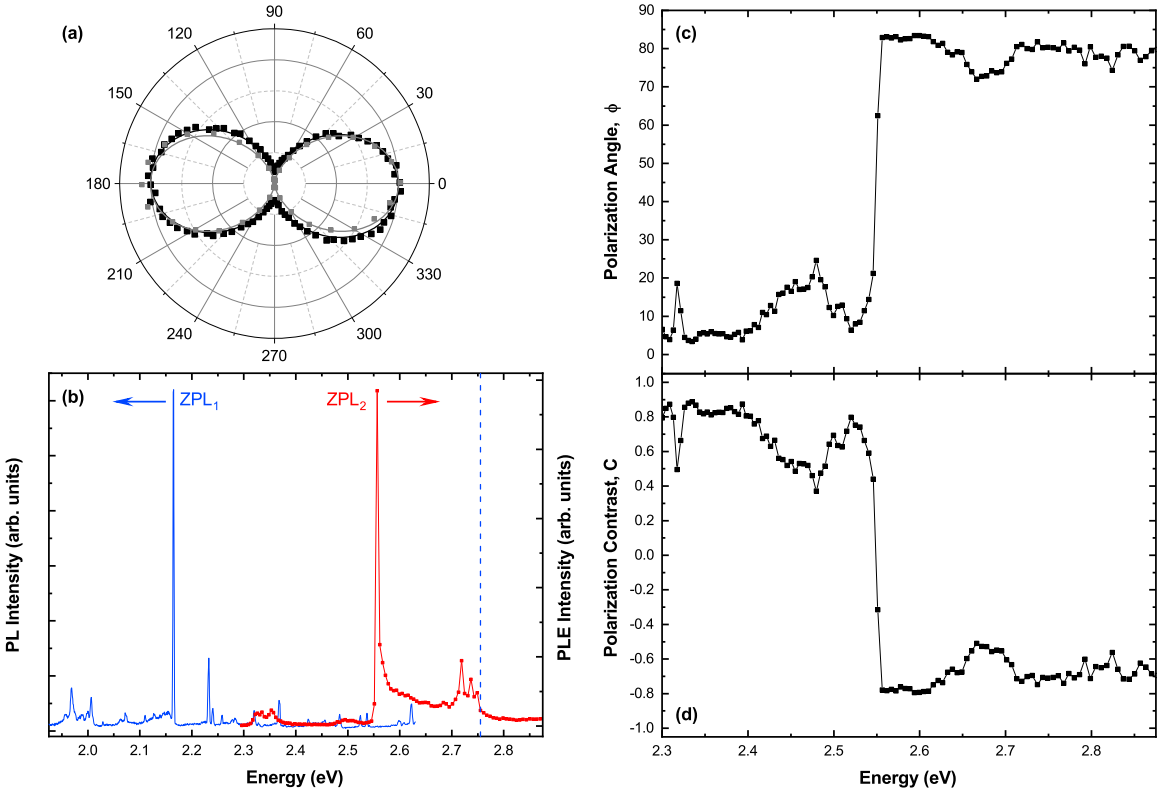

Fig. 5.9 Photoluminescence and Photoluminescence Excitation Spectroscopy of Defect-A. (a) Polar plot of collection polarization angle (grey) and resonant excitation polarization angle (black squares). The grey and black solid lines show $\sin^2\theta$ fits to the data. (b) Comparison of PLE (red) and PL spectrum under blue CW excitation (blue). (c) Excitation polarization angle of maximum absorption and (d) Polarization Contrast as a function of PLE Energy.

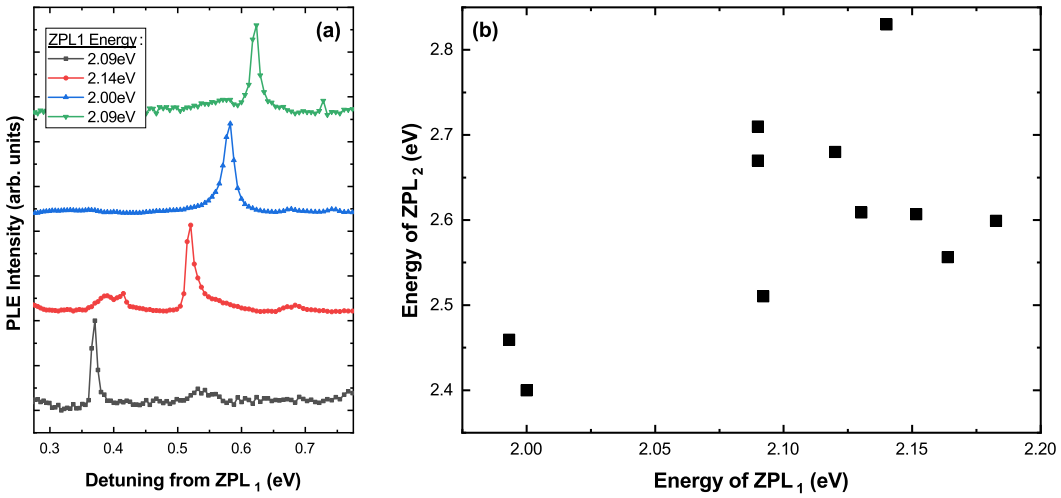

Fig. 5.10 (a) Example PLE spectra of four additional defects. (b) Energy of ZPL_2 absorption resonances as a function of ZPL_1 emission energy.

5.6.2 More examples of ZPL_2

The observation of a second zero phonon line in PLE measurements is a common occurrence. Out of 16 defects measured, 11 were found to show narrow absorption resonances at higher energy and polarized parallel to the ZPL emission. Example PLE spectra are shown for four such defects in Fig. 5.10(a). Fig. 5.10(b) plots the energy of ZPL_2 as a function of ZPL_1 for the 11 defects that display this behavior.

5.7 Possible Identity of the Defect

Regarding the possible identity of the colour centres studied in this work, we compare the observations to Density Functional Theory (DFT) calculations in the literature. The defects have two in-plane polarized ZPL transitions with orthogonal polarization. Whilst several defect species (e.g. Boron dangling bond [27]) have transitions similar to 2 eV, most are out-of-plane polarized and have an orbital degeneracy of one. A possible candidate is the ${}^3A_2^{'}$ $\longleftrightarrow$ ${}^3E'$ transition of the negatively charged boron vacancy, V_B^-. The upper energy level has two orbital states, and a symmetry breaking would result in two orthogonal linearly-polarized transitions at energy of 2.1-2.3 eV [28, 29]. We could not find any calculations of the expected splitting, that we measure to be $\sim$0.4 eV, which seems large. Furthermore, the neutral boron vacancy V_B^0, is predicted to have no optically active transitions below 3.5 eV [30, 31], and the charge transition level for the neutral to negative state of the boron vacancy has been calculated (with reference to the valance band maxima) 1.5 eV [32], and 2.1 eV [33]

for bulk hBN, and 2.4 eV [29] for a monolayer. This is in reasonable agreement with our model of photoionization and recharging. With sufficient energy a photon from the repump laser can convert the dark V_B^0 into the bright V_B^- by promoting an electron from the valence band, whereas two photons are required to remove an electron to the conduction band and convert V_B^- to V_B^0. The $\sim$350 meV variation in the charging threshold could result from local variations, for example, from strain, the number of layers of the flake that hosts the defect, [34] or interaction with the substrate [35].

Very recent experimental work has provided strong evidence for the role of carbon in colour centres emitting around 2 eV and the C_BV_N (carbon substituted for a boron with an associated nitrogen vacancy) is proposed as a likely candidate defect [36]. There is considerable uncertainty in the published theoretical work for the C_BV_N [37]. However, several predictions are consistent with our data. The neutral charge state is predicted to be in-plane polarized [38] with an energy of between 1.6 and 2.3 eV [39, 40]. And the threshold for the positive to neutral charge state transition has been predicted to be 2.5-3.25 eV [38], close to the experimentally measured repump threshold of 2.2-2.6 eV.

Amongst the published theory, evidence can be found to suggest that our experimental results could originate from either the boron vacancy or C_BV_N defects. However, further work is required before any definitive assignment of the defect species can be made.

5.8 Discussion

The simple model describes the data well and we propose the following interpretation in terms of charge state conversion. The green laser efficiently excites the defect from the ground (G) to excited state (E). A second green photon can further excite the electron into the conduction band, C. From C, the electron can be recaptured recharging the colour centre into the bright state; or the electron is lost or trapped by another nearby charge trap, shelving the colour centre in a dark charge state, S. In this picture, the bright state is negatively charged with respect to the dark state. A similar process involving the valence band is also compatible with the data. A similar two-photon ionization process is responsible for photo-switching from the negative to neutral charge state of NV-centres in diamond [1–3] and out of the neutral state of the divacancy in SiC [7, 6]. In the case of NV-centres, a two-photon process is also responsible for repumping. However, in our measurements we find that the repump process is one-photon, assuming the photon energy is sufficiently large to overcome the photo-charging threshold of, 2.25 eV and 2.6 eV for defects A and B, respectively.The sharp, step-like, transition repumping spectra (Fig.5.8(a) and (b)) indicate a repumping transition

between a discrete energy level and a continuum of states, i.e. the conduction or valence band, thus confirming this photocharging picture [6–8]. There are two possible mechanisms underlying the charging process. The first is that the measured threshold corresponds directly to the charge transfer threshold of the colour centre itself, and we see reasonable agreement to calculations for the boron vacancy [29, 33, 32] (1.5 to 2.4 eV) and C_BV_N [32, 38] (2.5 to 3.25 eV) defects. The second explanation is that the repumping threshold represents the charging threshold of a nearby trap state, or states, resulting in free carriers that can then be captured by the colour centre. We note that many defect species have charging thresholds in this region [33, 32]. We further note that in other materials, including silicon vacancies in diamond [4] and SiC [41], the divacancy in 4H-SiC [8, 6], and InGaAs quantum dots [9], nearby defects play a crucial role in the stabilization of the charge state of the target emitter.

Measurements of colour centres in diamond again provide some clues as to the origin of ZPL_2. In the photocharging cycle of NV centres, resonant excitation both at the ZPL energy of NV^0 and at a higher energy level of the NV^-, results in an increase in the PL yield from NV^- [2]. In SiV^- a higher energy level with perpendicular polarization was identified, but was not observed in PL due to selection rules of the energy levels [42]. Further work is required to confirm the origin of the transition reported here, but coupled with the measured energy threshold for repumping, it provides key extra information for the identification of the defect species. When compared to theoretical predictions [27–29, 31, 33, 32, 34, 35] and other experimental work [30, 36] our results suggest that the defects studied here could be boron vacancies or related to carbon impurities.

5.9 Conclusion

In conclusion, illuminating a colour-centre in hBN on, or near, resonance can drive it into a dark state. Applying a second laser, with a photon energy exceeding a defect specific threshold, repumps the colour centre back to the bright state. Phenomenologically, the dynamics can be understood in terms of photoswitching between two different charge states of the same defect, as is the case for colour centres in diamond and SiC [7, 6, 8]. Furthermore, PLE spectroscopy reveals a sharp absorption resonance, at approximately 400 meV higher energy than the ZPL. These results are of practical use for enhancing the PL yields in both future devices and experimental studies, particularly under resonant excitation [43] and can play an important role in the identification of colour centres in hBN.

References

[1] G. Waldherr, J. Beck, M. Steiner, P. Neumann, A. Gali, Th. Frauenheim, F. Jelezko, and J. Wrachtrup. Dark states of single nitrogen-vacancy centers in diamond unraveled by single shot nmr. *Phys. Rev. Lett.*, 106:157601, Apr 2011.

[2] K. Beha, A. Batalov, N. B. Manson, R. Bratschitsch, and A. Leitenstorfer. Optimum photoluminescence excitation and recharging cycle of single nitrogen-vacancy centers in ultrapure diamond. *Phys. Rev. Lett.*, 109:097404, Aug 2012.

[3] N Aslam, G Waldherr, P Neumann, F Jelezko, and J Wrachtrup. Photo-induced ionization dynamics of the nitrogen vacancy defect in diamond investigated by single-shot charge state detection. *New Journal of Physics*, 15(1):013064, jan 2013.

[4] Siddharth Dhomkar, Pablo R. Zangara, Jacob Henshaw, and Carlos A. Meriles. On-demand generation of neutral and negatively charged silicon-vacancy centers in diamond. *Phys. Rev. Lett.*, 120:117401, Mar 2018.

[5] Disheng Chen, Zhao Mu, Yu Zhou, Johannes E. Fröch, Abdullah Rasmit, Carole Diederichs, Nikolay Zheludev, Igor Aharonovich, and Wei-bo Gao. Optical gating of resonance fluorescence from a single germanium vacancy color center in diamond. *Phys. Rev. Lett.*, 123:033602, Jul 2019.

[6] Gary Wolfowicz, Christopher P. Anderson, Andrew L. Yeats, Samuel J. Whiteley, Jens Niklas, Oleg G. Poluektov, F. Joseph Heremans, and David D. Awschalom. Optical charge state control of spin defects in 4h-sic. *Nature Communications*, 8(1):1876, 2017.

[7] D. A. Golter and C. W. Lai. Optical switching of defect charge states in 4h-sic. *Scientific Reports*, 7(1):13406, 2017.

[8] Björn Magnusson, Nguyen Tien Son, András Csóré, Andreas Gällström, Takeshi Ohshima, Adam Gali, and Ivan G. Ivanov. Excitation properties of the divacancy in 4*h*-sic. *Phys. Rev. B*, 98:195202, Nov 2018.

[9] H. S. Nguyen, G. Sallen, C. Voisin, Ph. Roussignol, C. Diederichs, and G. Cassabois. Optically gated resonant emission of single quantum dots. *Phys. Rev. Lett.*, 108:057401, Jan 2012.

[10] Andreas W. Schell, Mikael Svedendahl, and Romain Quidant. Quantum emitters in hexagonal boron nitride have spectrally tunable quantum efficiency. *Advanced Materials*, 30(14):1704237, 2018.

[11] Daniel Wigger, Robert Schmidt, Osvaldo Del Pozo-Zamudio, Johann A Preuß, Philipp Tonndorf, Robert Schneider, Paul Steeger, Johannes Kern, Yashar Khodaei, Jaroslaw Sperling, Steffen Michaelis de Vasconcellos, Rudolf Bratschitsch, and Tilmann Kuhn. Phonon-assisted emission and absorption of individual color centers in hexagonal boron nitride. *2D Materials*, 6(3):035006, apr 2019.

[12] Mehran Kianinia, Carlo Bradac, Bernd Sontheimer, Fan Wang, Toan Trong Tran, Minh Nguyen, Sejeong Kim, Zai-Quan Xu, Dayong Jin, Andreas W. Schell, Charlene J. Lobo, Igor Aharonovich, and Milos Toth. All-optical control and super-resolution imaging of quantum emitters in layered materials. *Nature Communications*, 9(1):874, 2018.

[13] Zav Shotan, Harishankar Jayakumar, Christopher R. Considine, Mažena Mackoit, Helmut Fedder, Jörg Wrachtrup, Audrius Alkauskas, Marcus W. Doherty, Vinod M. Menon, and Carlos A. Meriles. Photoinduced modification of single-photon emitters in hexagonal boron nitride. *ACS Photonics*, 3(12):2490–2496, 2016.

[14] Prince Khatri, Andrew J. Ramsay, Ralph Nicholas Edward Malein, Harold M. H. Chong, and Isaac J. Luxmoore. Optical gating of photoluminescence from color centers in hexagonal boron nitride. *Nano Letters*, 20(6):4256–4263, May 2020.

[15] Xiangzhi Li, Gabriella D. Shepard, Andrew Cupo, Nicolas Camporeale, Kamran Shayan, Yue Luo, Vincent Meunier, and Stefan Strauf. Nonmagnetic quantum emitters in boron nitride with ultranarrow and sideband-free emission spectra. *ACS Nano*, 11(7):6652–6660, May 2017.

[16] Annemarie L. Exarhos, David A. Hopper, Richard R. Grote, Audrius Alkauskas, and Lee C. Bassett. Optical signatures of quantum emitters in suspended hexagonal boron nitride. *ACS Nano*, 11(3):3328–3336, 2017. PMID: 28267917.

[17] P. Khatri, I. J. Luxmoore, and A. J. Ramsay. Phonon sidebands of color centers in hexagonal boron nitride. *Phys. Rev. B*, 100:125305, Sep 2019.

[18] Matthew A. Feldman, Alex Puretzky, Lucas Lindsay, Ethan Tucker, Dayrl P. Briggs, Philip G. Evans, Richard F. Haglund, and Benjamin J. Lawrie. Phonon-induced multicolor correlations in hbn single-photon emitters. *Phys. Rev. B*, 99:020101, Jan 2019.

[19] Bernd Sontheimer, Merle Braun, Niko Nikolay, Nikola Sadzak, Igor Aharonovich, and Oliver Benson. Photodynamics of quantum emitters in hexagonal boron nitride revealed by low-temperature spectroscopy. *Phys. Rev. B*, 96:121202, Sep 2017.

[20] Toan Trong Tran, Christopher Elbadawi, Daniel Totonjian, Charlene J. Lobo, Gabriele Grosso, Hyowon Moon, Dirk R. Englund, Michael J. Ford, Igor Aharonovich, and Milos Toth. Robust multicolor single photon emission from point defects in hexagonal boron nitride. *ACS Nano*, 10(8):7331–7338, 2016. PMID: 27399936.

[21] I. Aharonovich, S. Castelletto, D. A. Simpson, A. D. Greentree, and S. Prawer. Photophysics of chromium-related diamond single-photon emitters. *Phys. Rev. A*, 81:043813, Apr 2010.

[22] Elke Neu, Mario Agio, and Christoph Becher. Photophysics of single silicon vacancy centers in diamond: implications for single photon emission. *Opt. Express*, 20(18):19956–19971, Aug 2012.

[23] J.R. Johansson, P.D. Nation, and Franco Nori. Qutip: An open-source python framework for the dynamics of open quantum systems. *Computer Physics Communications*, 183(8):1760 – 1772, 2012.

[24] J.R. Johansson, P.D. Nation, and Franco Nori. Qutip 2: A python framework for the dynamics of open quantum systems. *Computer Physics Communications*, 184(4):1234 – 1240, 2013.

[25] Nicholas R. Jungwirth, Brian Calderon, Yanxin Ji, Michael G. Spencer, Michael E. Flatté, and Gregory D. Fuchs. Temperature dependence of wavelength selectable zero-phonon emission from single defects in hexagonal boron nitride. *Nano Letters*, 16(10):6052–6057, 2016. PMID: 27580074.

[26] Nicholas R. Jungwirth and Gregory D. Fuchs. Optical absorption and emission mechanisms of single defects in hexagonal boron nitride. *Phys. Rev. Lett.*, 119:057401, Jul 2017.

[27] Mark E. Turiansky, Audrius Alkauskas, Lee C. Bassett, and Chris G. Van de Walle. Dangling bonds in hexagonal boron nitride as single-photon emitters. *Phys. Rev. Lett.*, 123:127401, Sep 2019.

[28] Viktor Ivády, Gergely Barcza, Gergő Thiering, Song Li, Hanen Hamdi, Jyh-Pin Chou, Örs Legeza, and Adam Gali. Ab initio theory of the negatively charged boron vacancy qubit in hexagonal boron nitride. *npj Computational Materials*, 6(1), April 2020.

[29] Mehdi Abdi, Jyh-Pin Chou, Adam Gali, and Martin B. Plenio. Color centers in hexagonal boron nitride monolayers: A group theory and ab initio analysis. *ACS Photonics*, 5(5):1967–1976, 2018.

[30] Jiandong Feng, Hendrik Deschout, Sabina Caneva, Stephan Hofmann, Ivor Lončarić, Predrag Lazić, and Aleksandra Radenovic. Imaging of optically active defects with nanometer resolution. *Nano Letters*, 18(3):1739–1744, 2018. PMID: 29393651.

[31] C. Attaccalite, M. Bockstedte, A. Marini, A. Rubio, and L. Wirtz. Coupling of excitons and defect states in boron-nitride nanostructures. *Phys. Rev. B*, 83:144115, Apr 2011.

[32] L. Weston, D. Wickramaratne, M. Mackoit, A. Alkauskas, and C. G. Van de Walle. Native point defects and impurities in hexagonal boron nitride. *Phys. Rev. B*, 97:214104, Jun 2018.

[33] Jack Strand, Luca Larcher, and Alexander L Shluger. Properties of intrinsic point defects and dimers in hexagonal boron nitride. *Journal of Physics: Condensed Matter*, 32(5):055706, nov 2019.

[34] Tyler J. Smart, Feng Wu, Marco Govoni, and Yuan Ping. Fundamental principles for calculating charged defect ionization energies in ultrathin two-dimensional materials. *Phys. Rev. Materials*, 2:124002, Dec 2018.

[35] Dan Wang and Ravishankar Sundararaman. Substrate effects on charged defects in two-dimensional materials. *Phys. Rev. Materials*, 3:083803, Aug 2019.

[36] Noah Mendelson, Dipankar Chugh, Jeffrey R. Reimers, Tin S. Cheng, Andreas Gottscholl, Hu Long, Christopher J. Mellor, Alex Zettl, Vladimir Dyakonov, Peter H. Beton, Sergei V. Novikov, Chennupati Jagadish, Hark Hoe Tan, Michael J. Ford, Milos Toth, Carlo Bradac, and Igor Aharonovich. Identifying carbon as the source of visible single-photon emission from hexagonal boron nitride, November 2020.

[37] Jeffrey R. Reimers, A. Sajid, Rika Kobayashi, and Michael J. Ford. Understanding and calibrating density-functional-theory calculations describing the energy and spectroscopy of defect sites in hexagonal boron nitride. *Journal of Chemical Theory and Computation*, 14(3):1602–1613, 2018. PMID: 29412670.

[38] Feng Wu, Andrew Galatas, Ravishankar Sundararaman, Dario Rocca, and Yuan Ping. First-principles engineering of charged defects for two-dimensional quantum technologies. *Phys. Rev. Materials*, 1:071001, Dec 2017.

[39] G.D. Cheng, Y.G. Zhang, L. Yan, H.F. Huang, Q. Huang, Y.X. Song, Y. Chen, and Z. Tang. A paramagnetic neutral cbvn center in hexagonal boron nitride monolayer for spin qubit application. *Computational Materials Science*, 129:247 – 251, 2017.

[40] A. Sajid, Jeffrey R. Reimers, and Michael J. Ford. Defect states in hexagonal boron nitride: Assignments of observed properties and prediction of properties relevant to quantum computation. *Phys. Rev. B*, 97:064101, Feb 2018.

[41] Matthias Widmann, Matthias Niethammer, Dmitry Yu. Fedyanin, Igor A. Khramtsov, Torsten Rendler, Ian D. Booker, Jawad Ul Hassan, Naoya Morioka, Yu-Chen Chen, Ivan G. Ivanov, Nguyen Tien Son, Takeshi Ohshima, Michel Bockstedte, Adam Gali, Cristian Bonato, Sang-Yun Lee, and Jörg Wrachtrup. Electrical charge state manipulation of single silicon vacancies in a silicon carbide quantum optoelectronic device. *Nano Letters*, 19(10):7173–7180, 2019. PMID: 31532999.

[42] Lachlan J. Rogers, Kay D. Jahnke, Marcus W. Doherty, Andreas Dietrich, Liam P. McGuinness, Christoph Müller, Tokuyuki Teraji, Hitoshi Sumiya, Junichi Isoya, Neil B. Manson, and Fedor Jelezko. Electronic structure of the negatively charged silicon-vacancy center in diamond. *Phys. Rev. B*, 89:235101, Jun 2014.

[43] Kumarasiri Konthasinghe, Chitraleema Chakraborty, Nikhil Mathur, Liangyu Qiu, Arunabh Mukherjee, Gregory D. Fuchs, and A. Nick Vamivakas. Rabi oscillations and resonance fluorescence from a single hexagonal boron nitride quantum emitter. *Optica*, 6(5):542–548, May 2019.

Chapter 6

STED Spectroscopy

6.1 Introduction

As discussed in chapters 4 and 5, an open question in the field of hBN SPE is the identity of the emitters. The issue is complicated by numerous candidate defects with similar zero-phonon line (ZPL) energies. Techniques such as PSB analysis [1–4], as we used in chapter 4, time resolved PL measurements like in chapter 5 and ODMR [5, 6] are used to study the spectroscopic signatures to comment on emiter identity.

For emitters around 2.0-2.2 eV, the strongest case to date has been made for a carbon-related defect [7]. Calculations about defect symmetry and allowed transitions have been made to comment on the nature of the emitter [8, 2, 9–13, 1, 6, 14]. Experimentally, it is difficult to observe all the calculated transitions in a defect because of reasons like-photocharging, different polarization axis and local strain effects. The confidence in the origin of a defect depends on number of absorption and emission peaks agree with the calculated transitions of that defect. In this chapter we comment on the origins based on the transitions observed in studied emitters and similar emitters from chapter 5. We have demonstrated how PLE can be used to probe the vibronic modes in an excited state. Here, we study a complementary technique to PLE called stimulated emission depletion (STED) for probing vibronic modes in the ground state.

Fig. 6.1 illustrates the principle behind STED by comparison to photoluminescence excitation (PLE). In PLE, the system is driven by a laser at a higher energy than the ZPL, and the ZPL is collected. By tuning the excitation laser, the vibronic spectrum of the excited state can be measured. Conversely, in STED, the system is pumped into the excited state via a resonant excitation and the ZPL is collected. Along with excitation, the system is also probed using a laser at a lower energy than the ZPL (red arrow). As this probe laser

is tuned, stimulated emission via phonon-assisted transitions depletes the population of the excited state, reducing the intensity of the ZPL. The PL signal against probe laser energy shows the vibronic spectrum of the ground state, where dips in the PL signal correspond to phonon resonances. The STED spectrum replicates the PL spectrum, but as STED resonantly probes a specific transition, the spectral selectivity reduces extraneous signals and peaks from adjacent defects or impurities.

If we know for certain that the emission is coming from a single source i.e a single hBN emitter then, theoretically STED and PL profile should be the same because they are probing the same energy levels. In reality, during measurements, a significant portion of photons collected in emission are from a single emitter source but a minor, not negligible, proportion comes from nearby impurities or closely lying defects. This sometimes result in peaks in PSB, which at first instance seems like coupling with a phonon mode but in reality do not belong to the same source. STED is a powerful technique which only probes the ground state of a single emitter and helps in identifying these anomalies.

The most common applications of STED technique are - STED microscopy, which was developed for super-resolution imaging [15–17] (see also chapter 7) and sub-resolution limit photolithography [18–20], and to achieve lasing in NV centres in diamond[21]. Here we apply STED as a spectroscopic probe, in combination with the complementary techniques of PL and PLE, to investigate the electron-phonon interaction of colour centres in hBN and comment on the origins of the emitter.

This work has been published and is here adapted from ACS Photonics, 8, 4, 1007–1012 (2021) Copyright 2021 The Authors. Published by American Chemical Society. For this work, my contributions were- numerical simulation to fit the data, doing measurement remotely (due to covid restrictions) and making LabVIEW programs for automation, inputs for the paper and contribution towards plotting the figures. This paper was written and submitted by Dr. Ralph Malein.

6.2 Sample Preparation and Experimental Setup

The sample for this experiment was exactly the same as the one used for photocharging experiments (See Chapter 5, section 5.2). Fig. 6.2 shows a schematic of the STED experimental set-up. A green DPSS laser (532 nm) is used for resonant excitation and SCL (repetition rate of 78 MHz and pulsewidth of a few ps) is fibre-coupled to an AOTF (430 to 700 nm and a bandwidth of $\sim$ 1-2 nm) to provide a tunable energy for depletion. The lasers are collimated and co-aligned and then coupled to a long working distance objective lens, with numerical

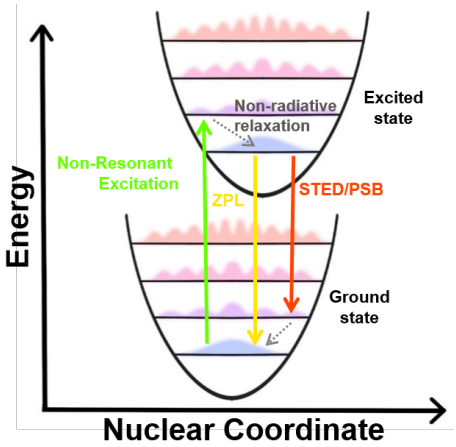

Fig. 6.1 Franck-Condon energy diagram comparing PL, PLE, and STED techniques. In PL, the non-resonant excitation (green) populates the excited state and emission from the ZPL (yellow) and PSB (red) is collected. In PLE, the excitation probes the excited vibronic states and the ZPL is collected. In STED, the non-resonant excitation is again used, and the STED pulses (red) deplete the excited state through stimulated emission into the ground vibronic states, reducing the ZPL intensity. Grey dashed arrows show fast relaxation from higher vibronic states.

aperture of 0.8, which focuses the light to a diffraction-limited spot $< 1\mu$m in diameter. The green laser is triggered by a voltage pulse from the SCL, which has a tunable delay, enabling control of the relative arrival time of excitation and depletion pulses. Light emitted from the samples is collected into the same objective and coupled into a spectrometer and CCD for spectral measurements, or through a series of tuneable long- and short-pass filters for efficient wavelength selection (band pass), then to a single photon avalanche diode (SPAD) to perform photon counting and time-resolved fluorescence measurements via a time-tagging module.

For PLE measurements, the same setup is used and the technique is explained in chapter 5, section. 5.2. To stabilize the PL from the emitter, a weak 450 nm blue CW-laser is also used based on the results in chapter 5 that blue laser keeps the emitter bright by pumping the defect back into the bright state.

In Fig. 6.3, the PL spectrum of emitter-A in hBN is plotted in grey, along with PLE (blue) and STED (red) spectra. To a first approximation, the PLE spectrum is the mirror image of the PL spectrum around the ZPL energy, where PL (PLE) probes the emission (absorption) spectrum. However, in a system such as hBN, the PL spectrum can be contaminated by light from other nearby emitters. Applying STED by scanning a red-detuned laser shows resonances at the PSB but eliminates stray emission from other emitters.

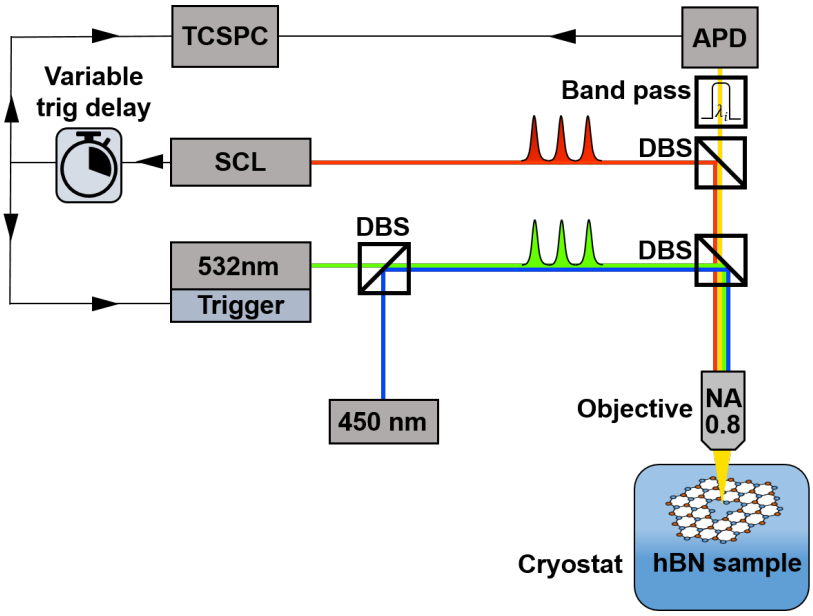

Fig. 6.2 Diagram of the experimental set-up. DBS = dichroic beam-splitter; SCL = super-continuum laser; APD = avalanche photodiode; TCSPC = time-correlated single photon counting electronics. Note that a band pass before APD is made using a series of tuneable long- and short-pass filters.

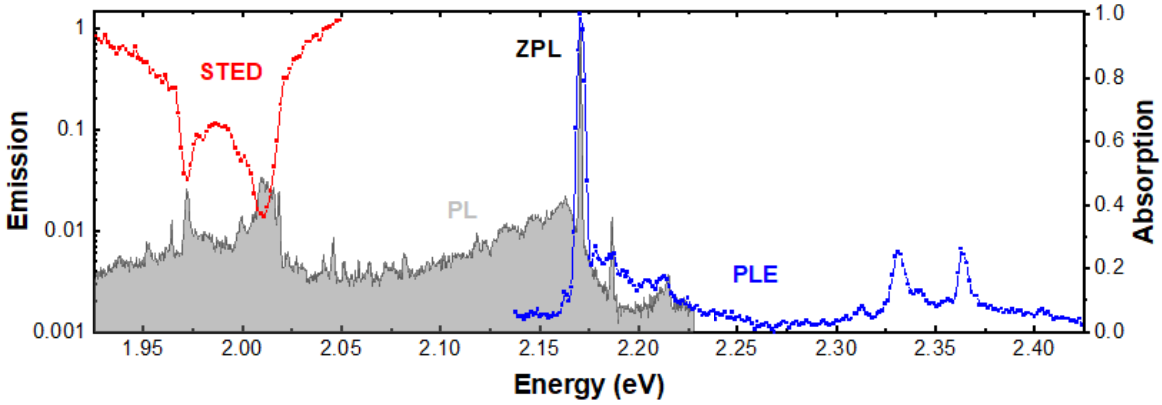

Fig. 6.3 Representative PL (grey), PLE (blue) and STED (red) spectrum from emitter-A with ZPL at ∼2.17 eV, emission OPSB between 1.97 and 2.03 eV and absorption OSPB between 2.32 and 2.38 eV.

6.3 STED Measurements

To perform STED, time-resolved PL is recorded from the ZPL of emitter-A shown in Fig. 6.4. Following non-resonant excitation with a 532 nm PL-pulse, the emission decays exponentially with radiative lifetime of 3.58 ns, which is typical for hBN colour centres [22, 23] . If the STED pulse, resonant with the PSB at $\sim$ 2.02 eV, arrives before the excitation pulse, the PL is not affected (see black trace in Fig. 6.4(b)). However, if the STED pulse arrives after the excitation pulse, the PL is switched-off on the time-scale of the laser pulse (red trace in Fig. 6.4(b)). The STED pulse stimulates phonon-assisted emission, depleting the excited state, and suppressing the PL from the ZPL.

The gating of the ZPL PL spectra by the STED pulse is further illustrated in Fig. 6.4(c), where time-resolved PL spectra from emitter-A are shown for five different values of STED pulse delay time, τ_s. In Fig. 6.4(d) the time-averaged PL is plotted against delay time. With negative τ_s the PL intensity is constant and sharply falls as the pulses overlap, recovering slowly as the STED pulse is moved through the radiative decay tail.

This provides a method of performing STED measurements without varying the SCL laser energy or switching lasers on and off, which can affect the power of the lasers and thus the reliability of measurements:

- "STED on" - Depletion pulse set to arrive 100 ps after the excitation pulse, switching the PL off.
- "STED off" - Depletion pulse set to arrive 100 ps before the excitation pulse, leaving the PL on.

The STED on:off ratio (also known as the inhibition ratio, in the terminology of STED microscopy) is then recorded as the ratio between the STED on and off PL intensities. A power sweep was performed, varying SCL power (Fig. 6.4(e)). Increasing SCL power decreases the STED ratio down to an apparent saturation at about 0.12 showing that STED can not completely switch off the ZPL and available STED power is not a limiting factor.

6.3.1 STED model

To verify that STED is responsible for the experimental observations in Fig. 6.4 , we compare the results to a simple three-level rate equation model based on the level schematic in Fig. 6.5. G and E are the ground and excited state of the radiative transition respectively; M is the intermediary vibronic level, lying above the ground state by the phonon mode energy.

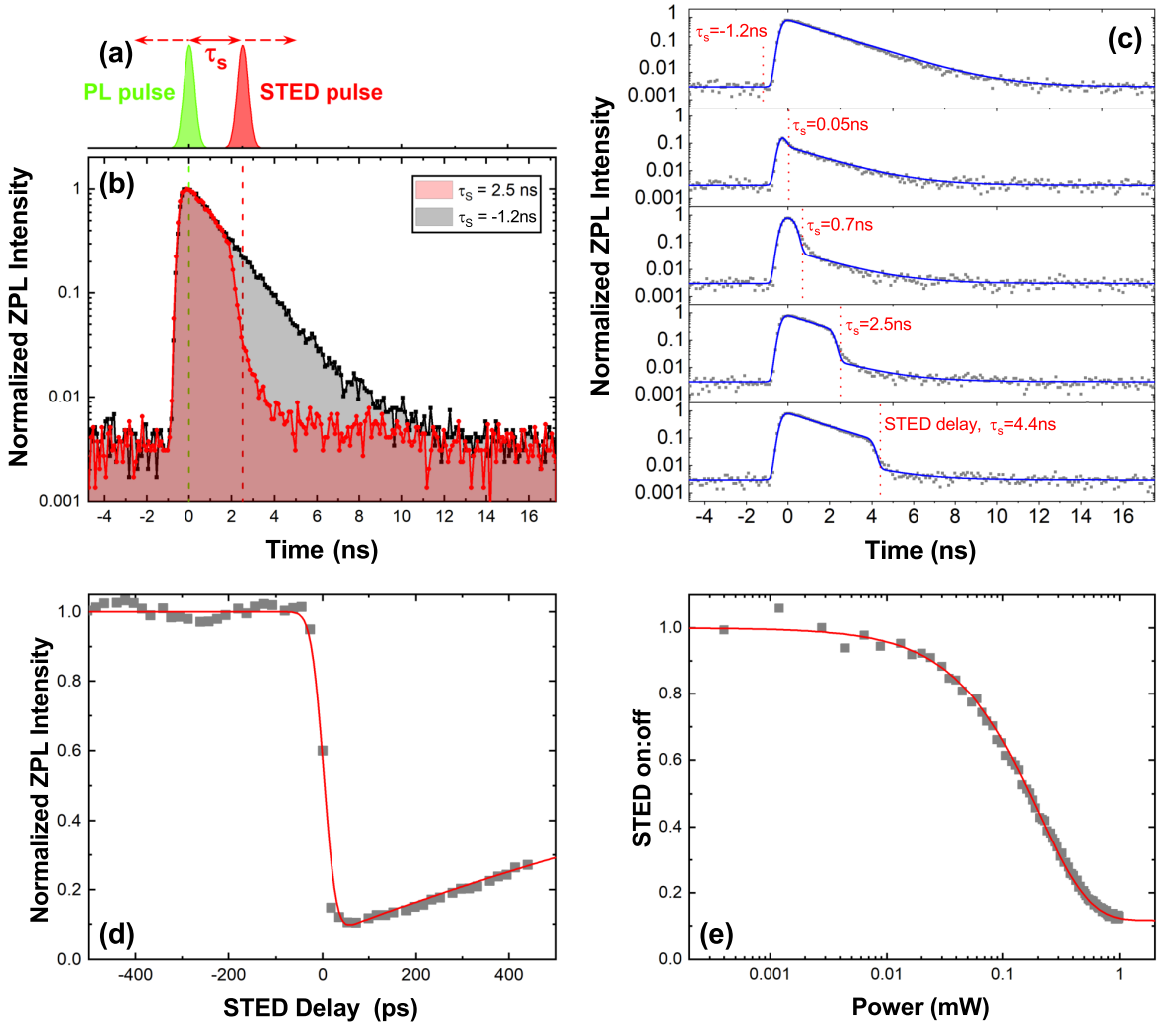

Fig. 6.4 **(a)**: Schematic of arrival times of excitation PL pulse and STED pulse, with delay τ_s between them. **(b)**: Time-resolved ZPL-PL of emitter-A with positive (red) and negative (black) τ_s. The STED pulse switches off the emission **(c)**: Time resolved PL of emitter-A at five different values of τ_s, showing rapid depletion at arrival time of STED pulse. **(d)**: Plot of time-averaged ZPL-PL intensity with varying τ_s. Moving the STED pulse through the PL pulse results in significant quenching of the PL signal that recovers as τ_s is increased. **(e)**: Sweep of STED ratio with varying time-averaged power of the STED laser.

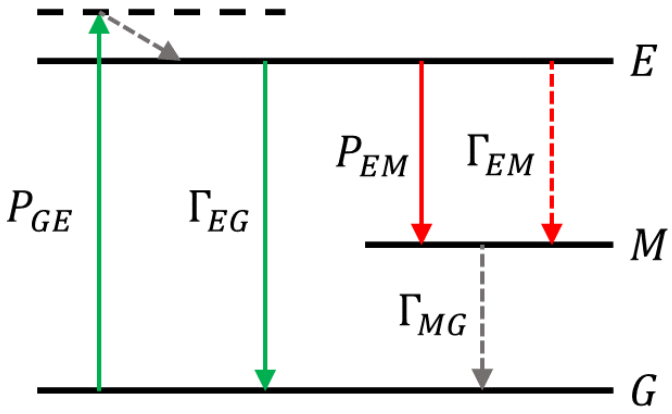

Fig. 6.5 Level schematic of three-level system with rate parameters labelled.

The excitation pulse (P_{GE}) is modelled as a single pump rate encompassing excitation from G to a vibronic state above E followed by rapid relaxation to E, whereas the STED pulse is a pump from E to M (P_{EM}). It is assumed that the non-radiative relaxation from M to G (Γ_{MG}) is fast compared to the other transitions. For time-resolved simulations, the excitation and STED pulses are modelled as Gaussian, and the simulated traces are then convolved with the IRF (Gaussian with 800 ps FWHM) of the APD to better fit to the measurement resolution. The ZPL intensity is then proportional to the population in E multiplied by the radiative decay rate Γ_{EG}. A phonon-mediated spontaneous emission rate Γ_{EM} is also included to model spontaneous emission via the PSB. The rate equations are:

$$\begin{aligned}
\dot{G} &= \Gamma_{EG}E + \Gamma_{MG}M - P_{GE}G \\
\dot{E} &= P_{GE}G - (\Gamma_{EG} + P_{EM} + \Gamma_{EM})E \\
\dot{M} &= -(\dot{E} + \dot{G})
\end{aligned}$$

All simulations show good agreement with experimental data, with consistent model parameters (see Table 6.1): fitting to the time-resolved PL traces in Fig. 6.4(c) (red curve) gives values of the radiative decays and allows accurate determination of the true pulse widths of the 532 nm laser and SCL pulses; fitting the STED pulse delay (Fig. 6.4(d), red curve) and power sweep (Fig. 6.4(e), red curve) shows that the saturation is due to the short delay between excitation and STED pulses which allows a small degree of PL to be emitted before depletion of E. This means that it is difficult to completely switch off the emitter with STED and we will use this important result in next chapter for STED microscopy, where a

gated technique is used to discard the initial PL and photons are counted only after the action of STED.

Note that in Table 6.1, the transition rates $P_{EM} >> P_{GE}$ which suggest that STED pulse is highly efficient in depleting the excited state via PSB because during experiment, the average power of excitation laser $>$ average power of the STED laser.

model parameter	value
Γ_{EG}, Γ_{EM}	279.3 MHz
Γ_{MG}	1 THz
P_{GE}	8 GHz
P_{EM} in delay sweep (Fig. 6.4(d))	1.29 THz
Excitation laser pulse width	50 ps
STED pulse width	2 ps

Table 6.1 Table of simulation parameters for 3-level model shown in Fig. 6.5.

6.4 Comparing STED, PL and PLE

A comparison of STED, PL and PLE spectra for the OPSB of emitter-A is made in Fig. 6.6 For comparison, the magnitude of the detuning from the ZPL is used, because as noted above, PLE uses a laser detuned to higher energies, whereas STED uses a laser detuned to lower energies. As reported previously[25–28], the shape of the PSB corresponds closely to the phonon dispersion relation for bulk hBN (Fig. 6.6(a))[24, 29]. A detailed spectrum of the PL (emission) optical sideband (OPSB) along with corresponding PLE (absorption) data is shown in Fig. 6.6(b). The resolution of the PLE spectrum is limited by the bandwidth of the SCL, and the PL shows sharper features. We note that the PL spectra has additional peaks which are not present in PLE or STED. We attribute this to emission from other nearby emitters that are weakly excited (see also section 6.4.2). Hence, we only compare the PLE and STED spectra. The absorption (emission) PSB maps the coupling of the excited (ground) state of the radiative transition to the single phonon vibronic states. For emitter-A (Fig. 6.6), two main peaks are observed in both PLE and STED. The peak corresponding directly to the maximum of the phonon density of states[27] appears in both PLE and STED at $\sim$ 165 meV. In STED, probing the phonon sideband of the ground state, the peak at 200 meV matches the $LO(E_{1u},\Gamma)$ mode energy in bulk hBN.[24]. In PLE, probing the phonon sideband of the excited state, the peak corresponding to the $LO(E_{1u},\Gamma)$ phonon mode is red-shifted to 195 meV. To confirm this red shift of $LO(E_{1u},\Gamma)$ phonon mode only in PLE data, we did the same PL, PLE and STED measurements on four other defects as shown in Fig. 6.7. The ZPL

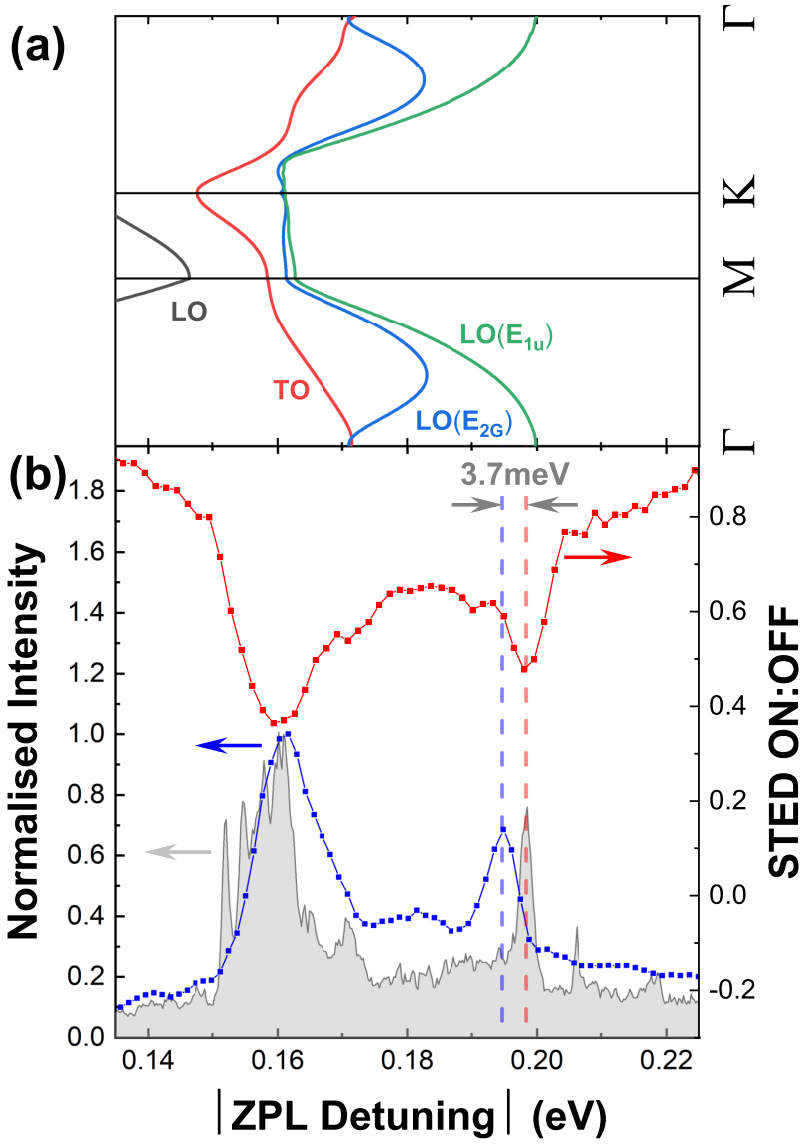

Fig. 6.6 **(a)**: Calculated optical phonon dispersion for bulk hBN with $LO(E_{1u})$ mode highlighted. Taken from Serrano *et al.* [24] **(b)**: Comparison of PL(grey), PLE (blue) and STED (red) OPSB spectra of emitter-A, which has a ZPL energy of 2.170 eV. Red (blue) dashed line shows position of the $LO(E_{1u},\Gamma)$ transition in STED (PLE).

energies for the emitters are similar ~ 2.1 eV. Each one of them show $LO(E_{1u},\Gamma)$ phonon mode peak at same energy for PL and STED but red shifted in PLE.

6.4.1 Analysing the red shift in $LO(E_{1u},\Gamma)$ phonon mode

The red shift in $LO(E_{1u},\Gamma)$ phonon mode, in PLE, can only arise if there's a shift in energy levels once the emitter goes into excited state. To understand this shift we need to think about the movement of layers in E_{1u} and E_{2g} phonon modes. The $LO(E_{1u})$ mode is observed in the PSB because the motion of adjacent planes of the crystal are in phase, resulting in an in-plane electric field. For comparison, in the E_{2g} mode at the Γ-point, the adjacent planes move out-of-phase, resulting in destructive interference [29]. This implies that when the emitter is in the excited state, the lattice is distorted along a lattice coordinate with E_{1u}-like symmetry (in-plane dipole x,y), softening the spring-constant due to the anharmonicity of the bonds.

The distortion in the lattice can be estimated by assuming a softening of the spring constant K of the phonon mode due to the distortion. For simplicity's sake, we consider a 1D diatomic chain whose dispersion is given by

$$\omega^2 = K\frac{m_B+m_N}{m_Bm_N} \pm \sqrt{K^2\left(\frac{(m_B+m_N)^2}{m_B^2m_N^2} - \frac{4}{m_Bm_N}\sin^2\left(\frac{ka}{2}\right)\right)}$$

where k is the phonon momentum, a is the lattice parameter, and $m_{B,N}$ are the masses of the two atoms. As the interaction take place at the Γ point $k=0$, the dispersion simplifies to

$$\begin{aligned}\omega^2 &= K\frac{m_B+m_N}{m_Bm_N} \pm \sqrt{K^2\frac{(m_B+m_N)^2}{m_B^2m_N^2}} \\ &= 0 \quad \text{or} \quad 2K\frac{m_B+m_N}{m_Bm_N}\end{aligned}$$

Thus in the optical branch, $\omega^2 \propto K$. While hBN is not a diatomic chain, considering units of K, this proportionality holds for a 2D hexagonal lattice.

Considering Hooke's law

$$K \propto \left.\frac{\partial^2 V}{\partial q^2}\right|_{q=q_0}$$

where V is the bond potential, q is the normal mode lattice coordinate and q_0 is the equilibrium lattice coordinate. Assuming a form of the potential similar to the Lennard-Jones potential, where it is minimized at the equilibrium position, and expanding around the equilibrium, we

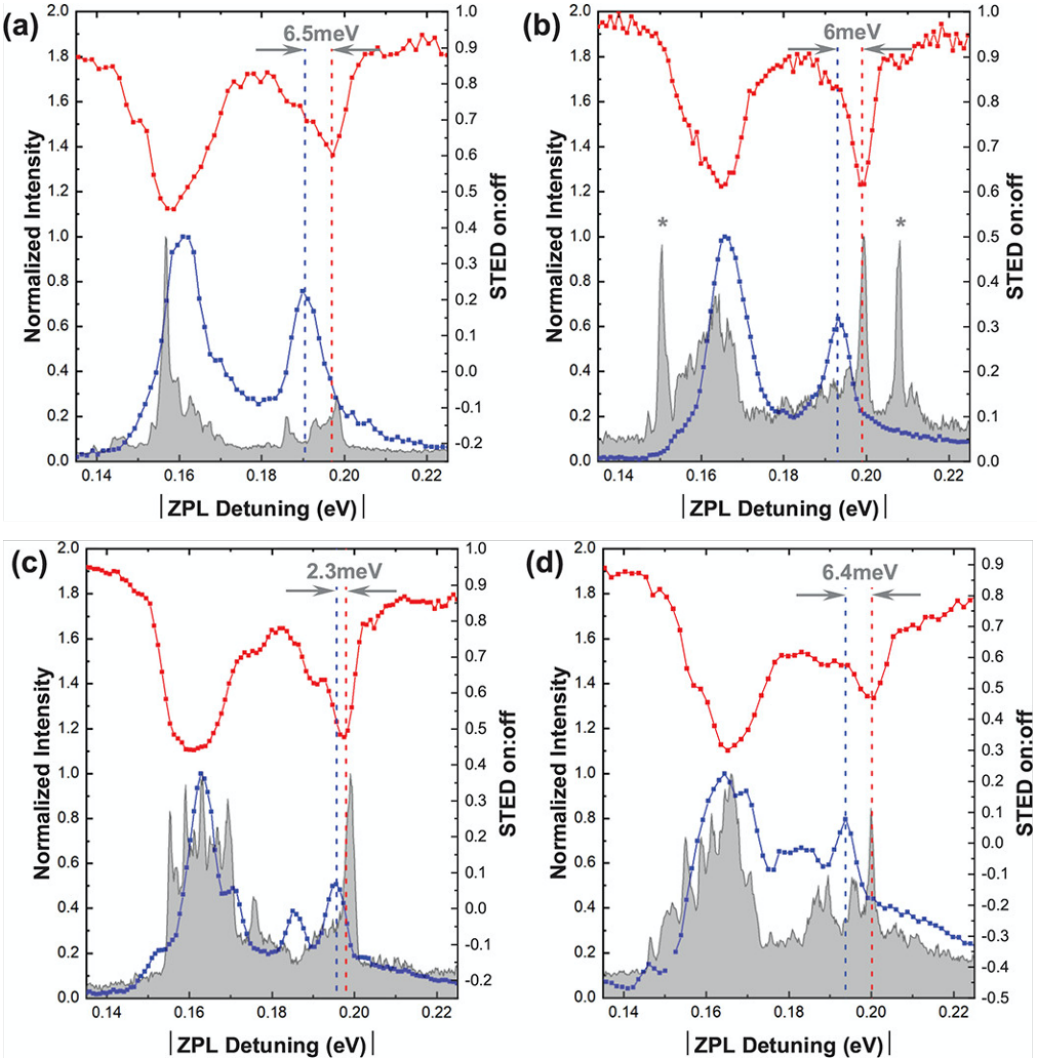

Fig. 6.7 (a)-(d): Comparison of PL, PLE and STED spectra from four similar emitters with ZPL energies of (a) 2.166 eV (b) 2.175 eV (c) 2.142 eV and (d) 2.171 eV. Each emitter shows shift in 200 meV peak between absorption and emission. In (b) the peaks marked with $*$ are from another nearby emitter or impurity.

find that

$$\left.\frac{\partial^2 V}{\partial q^2}\right|_{q=q_0} \propto \frac{1}{q_0^2}$$

so

$$\omega \propto \frac{1}{q_0}$$

Thus, considering excited (ground) phonon mode energies $\hbar\omega_E = 195 \pm 2$ meV ($\hbar\omega_G =$ 200 meV) and equilibrium positions q_E (q_G) we can calculate the excited state lattice equilibrium position as a percentage of the ground state equilibrium:

$$\begin{aligned}\frac{q_E}{q_G} &= \frac{\hbar\omega_G}{\hbar\omega_E} \\ &= \frac{200}{195 \pm 2} \\ &= 102.6 \pm 1\%\end{aligned}$$

Leading to an overall distortion of $+2.6 \pm 1\%$. This result is important because the estimation of lattice distortion can help in engineering hBN heterostructures, for example in moiré-like superstructure [30–33], where lattice mismatch can affect the device performance. The lattice constant of hBN/graphene differs by only 1.8% and at certain angle of rotation, a hBN/graphene heterostructure forms moiré stripes, resulting in new electric properties and changes to Fermi velocity, band gap etc [34, 35]. A 2.6% distortion in hBN lattice upon excitation can distort these properties. Later in section 6.5, we use this result to support our argument that the emitter under question can be a $V_B C_N^-$ defect.

6.4.2 Stray peaks in PL spectrum

An interesting example in Fig. 6.7 is case (b). The two intense peaks in OPSB marked with $*$ are present in PL but not in PLE and STED. In this section we perform PLE and polarisation-resolved PL for all four peaks in the PL spectrum of case (b) to prove that PLE and STED are true, impurity free mapping tools for excited and ground state vibronic levels of an emitter.

Fig. 6.8 shows spectroscopic data of the ZPL and PSB peaks for the emitter in Fig. 6.7(b). In Fig. 6.8(a), the STED and PL spectra for the PSB show good agreement for the features at 0.165 eV (P_B) and 0.20 eV (P_C), but the PL shows two more narrow peaks at 0.15 eV (P_A)

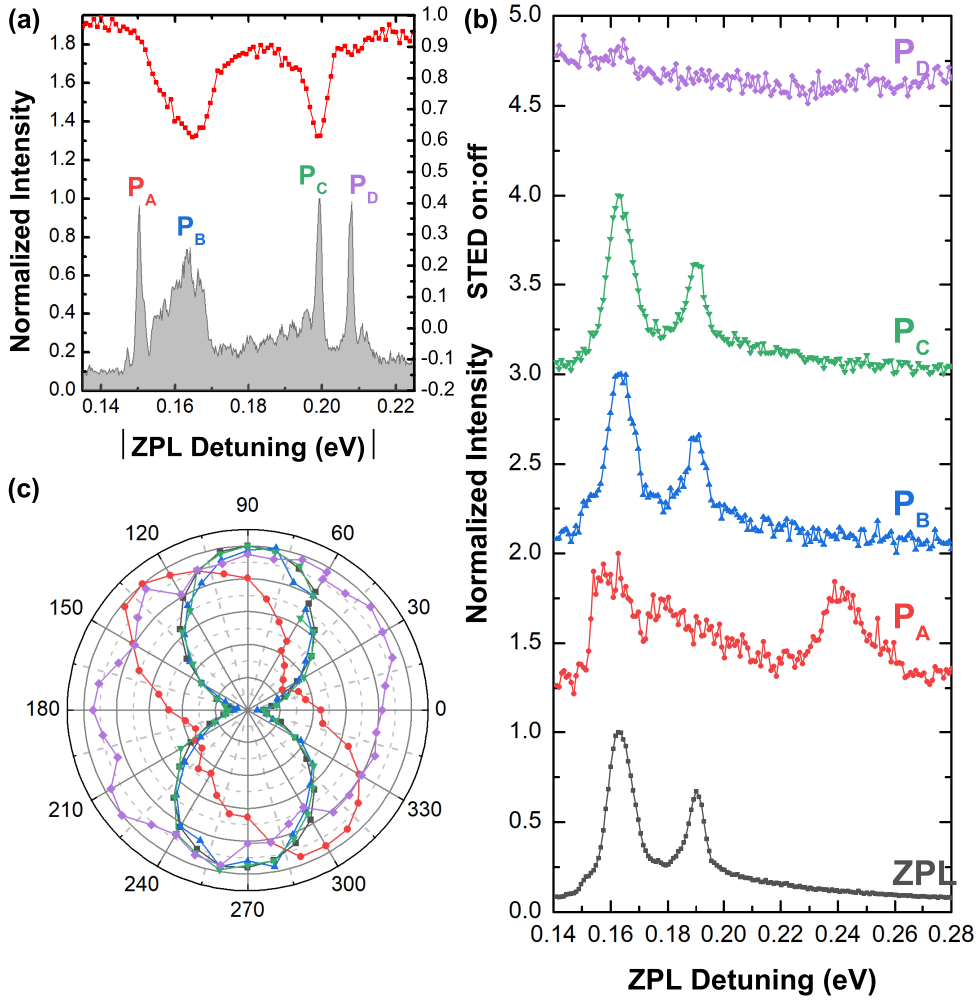

Fig. 6.8 **(a)**: STED (red) and PL (gray) PSB spectra of emitter in Fig. 6.7(b). **(b)**: PLE spectra measured by filtering on energies of ZPL and PSB peaks in **(a)**. **(c)**: Polarisation-resolved PL (excitation at 532 nm) of ZPL and PSB peaks in **(a)**. Colors of lines and markers correspond to PL peaks throughout.

and 0.21ev (P_D), suggesting that these are not due to the emitter in question and linked to the nearby emitters or impurities. This is supported by Fig. 6.8(b) which shows PLE spectra obtained by placing a tunable filter on the peaks indicated (the PL spectrum from each peak is fitted with a Gaussian function and the total area under the peak gives the value of each data point in PLE spectra) and sweeping the excitation laser through the PSB. It is clear that P_B and P_C show clear similarity to the PLE obtained form collecting the ZPL, whereas P_A and P_D show markedly different PLE spectra. Further evidence is given in Fig. 6.8(c), which shows polarisation-resolved PL for these peaks. While the gray (ZPL), blue (P_B) and green (P_C) curves show very similar polarisation, the red curve (P_A) shows polarisation rotated by 30° counterclockwise compared to the ZPL, and the purple curve (P_D) shows no strong polarisation at all. From this data we can conclude that P_A and P_D, the peaks marked with asterisks in Fig. 6.7(b), are not due to phonon-mediated transitions from the emitter being measured, but are due to stray light from another source.

6.5 Tracing the emitter identity

We now compare our spectroscopy results to candidate emitters reported in the literature. Recently, through a series of experiments that introduce carbon to the sample, Mendelson *et al* [7] have demonstrated that there is a carbon related defect emitting at 2.10 ± 0.04 eV with sharp ZPL, in-plane linear polarization, and nanosecond-scale radiative lifetimes, which matches our measurements. Through DFT calculations they determine that $(1)^4B_1 \rightarrow (1)^4A_2$ transition of the $V_BC_N^-$ line defects is the prime suspect. Fig. 6.9 shows a simplified energy level diagram for the suspected $V_BC_N^-$ defect. It has an in-plane linearly-polarized optical dipole perpendicular to the axis of the defect. Our observations are consistent with this claim. In addition, in the previous work (Chapter 5, [14]) on a similar defect to emitter-A, we observe a second ZPL peak in absorption orthogonally polarized to and $\sim 0.5 \pm 0.1$ eV above the emission ZPL, at 2.4-2.8 eV. If the defect is $V_BC_N^-$ with C_{2v} symmetry, this should correspond to the $(2)^4A_2 \leftrightarrow (1)^4A_2$ transition, which is calculated in the supplement of ref. 7 to have a vertical absorption energy between 2.8 and 3.6 eV. Since this state does not appear in emission and was observed in PLE of the ~ 2 eV ZPL, this indicates a fast non-radiative relaxation to the $(1)^4B_1$ state that flips the polarization of the optical dipole, suggesting an intercrossing of the $(2)^4A_2$ and $(1)^4B_1$ states. In this picture, the ground-state is energetically isolated with no in-plane dipole component, and should have a weak lattice distortion compared to the excited state where there are number of orbital states with similar energy available for admixing. This argument is supported by our experimental observation

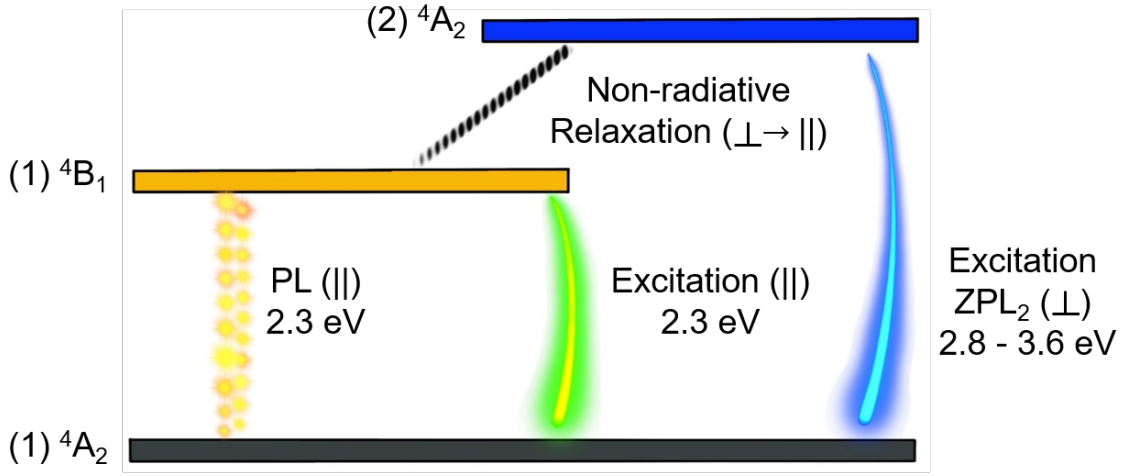

Fig. 6.9 Energy level diagram for $V_BC_N^-$ defect showing the suspected transitions. $(1)^4B_1 \rightarrow (1)^4A_2$ transition gives an in inplane polarized ($\|$) ZPL transition and $(2)^4A_2 \leftrightarrow (1)^4A_2$ orthogonally polarized ($\perp$) excitation gives ZPL$_2$ absorption peak in PLE data [14]. Non radiative relaxation from $(2)^4A_2 \rightarrow (1)^4B_1$ flips the optical dipole polarization.

of red shift in $\sim$ 200 meV, $LO(E_{1u},\Gamma)$ phonon mode peak in PLE which, according to our calculations, gives a lattice distortion of 2.6% in the excited state.

Hayee *et al* [8] report three classes of defect emitters in the $2-2.2$ eV energy range, which they suggest could be the V_NN_B, V_NC_B or V_NO_{2B} defects [2]. All three share C_{2v} symmetry with the V_BC_N, so in principle all could exhibit similar behaviour. We are unaware of any theoretical studies of selection rules for V_NO_{2B} so no concrete statements can be made about it. For all charge states of V_NN_B [9] and V_NC_B [7, 36] (and neutral and positive charge states of V_CB_N), transition energies of $\sim$2 eV are predicted to have out-of-plane optical dipoles, whereas the emitters we study have in-plane optical dipoles.

Hayee *et al* [8] also discuss the V_B defect, and rule it out due to their sample preparation method, but we cannot. By contrast to the other candidate defects, the V_B point defect has D_{3h} symmetry, and the singly negatively-charged V_B^- is the only stable charge state to have in-band-gap transitions [10]. The ground state is calculated to have A_2' symmetry, and there exists an excited state with E' symmetry [13] variously calculated to emit at 2.287 eV [11], 1.92 eV [12] and 2.22 eV [13]. As this state has a two-fold degeneracy in the plane of the crystal, the Jahn-Teller effect occurs, deforming the defect and giving a preferred polarization direction. This deformation could also give rise to the shift in the E_{1u} phonon energy in the excited state. The degeneracy breaking is also expected to result in an orthogonally polarized state, but this is calculated to be at an energy of 2.25 eV [13], which is much lower than the the orthogonally polarized absorption peak previously observed in Ref. 14. While V_B^- has

been proposed as responsible for emission around 2 eV [12, 1], it has also been suggested that the E' excited state undergoes rapid relaxation to a lower E'' energy state, resulting in emission at 1.76 eV [13]. This peak has been observed in PL and ODMR measurements of hBN attributed to V_B^- [6]. Hence, the likelihood of our observations being due to V_B^- is unclear.

6.6 Conclusion

In this work, we have demonstrated the application of STED spectroscopy to the examination of vibronic states of defect emitters in hBN. We have shown that STED spectroscopy replicates the PL spectra, but with the advantage that STED eliminates stray signals from nearby emitters, making it immensely useful for systems with randomly-placed emitters in the solid state, such as defects in 2D materials. We have shown that STED is analogous and complementary to PLE spectroscopy, where the major difference is that STED probes vibronic spectra of the ground state in a two-level system, whereas PLE probes that of the excited state. We have then used STED and PLE to compare the vibronic spectra of the ground and excited states of the radiative transition. For colour centres emitting near 2.2 eV, the main qualitative difference between the ground and excited states is a red-shift in the LO-phonon mode with E_{1u} symmetry. We compare our findings to recent work on different defect species in hBN and show that they are most consistent with the $(1)^4B_1 \rightarrow (1)^4A_2$ transition in the $V_BC_N^-$ defect. In this case, the shift to the phonon mode would be ascribed to a lattice distortion due to admixing between nearby excited states in the defect.

Here, the STED spectral resolution is limited to $\sim$1 nm by the AOTF filtering the SCL, which prevents a detailed examination of the OPSB around 165 meV. However, with a narrower linewidth laser, PLE/STED would enable further investigation of the fine structure of the OPSB and thus shed more light on electron-phonon coupling in hBN emitters.

References

[1] Christopher Linderälv, Witlef Wieczorek, and Paul Erhart. Vibrational signatures for the identification of single-photon emitters in hexagonal boron nitride. *Physical Review B*, 103(11), March 2021.

[2] Sherif Abdulkader Tawfik, Sajid Ali, Marco Fronzi, Mehran Kianinia, Toan Trong Tran, Catherine Stampfl, Igor Aharonovich, Milos Toth, and Michael J. Ford. First-principles investigation of quantum emission from hBN defects. *Nanoscale*, 9(36):13575–13582, 2017.

[3] Daniel Wigger, Robert Schmidt, Osvaldo Del Pozo-Zamudio, Johann A Preuß, Philipp Tonndorf, Robert Schneider, Paul Steeger, Johannes Kern, Yashar Khodaei, Jaroslaw Sperling, Steffen Michaelis de Vasconcellos, Rudolf Bratschitsch, and Tilmann Kuhn. Phonon-assisted emission and absorption of individual color centers in hexagonal boron nitride. *2D Mater.*, 6(3):035006, apr 2019.

[4] Gabriele Grosso, Hyowon Moon, Christopher J. Ciccarino, Johannes Flick, Noah Mendelson, Lukas Mennel, Milos Toth, Igor Aharonovich, Prineha Narang, and Dirk R. Englund. Low-temperature electron–phonon interaction of quantum emitters in hexagonal boron nitride. *ACS Photonics*, 7(6):1410–1417, 2020.

[5] Nathan Chejanovsky, Amlan Mukherjee, Jianpei Geng, Yu-Chen Chen, Youngwook Kim, Andrej Denisenko, Amit Finkler, Takashi Taniguchi, Kenji Watanabe, Durga Bhaktavatsala Rao Dasari, Philipp Auburger, Adam Gali, Jurgen H. Smet, and Jörg Wrachtrup. Single-spin resonance in a van der waals embedded paramagnetic defect. *Nature Materials*, 20(8):1079–1084, May 2021.

[6] Andreas Gottscholl, Mehran Kianinia, Victor Soltamov, Sergei Orlinskii, Georgy Mamin, Carlo Bradac, Christian Kasper, Klaus Krambrock, Andreas Sperlich, Milos Toth, Igor Aharonovich, and Vladimir Dyakonov. Initialization and read-out of intrinsic

spin defects in a van der Waals crystal at room temperature. *Nat. Mater.*, 19(5):540–545, May 2020. Number: 5 Publisher: Nature Publishing Group.

[7] Noah Mendelson, Dipankar Chugh, Jeffrey R. Reimers, Tin S. Cheng, Andreas Gottscholl, Hu Long, Christopher J. Mellor, Alex Zettl, Vladimir Dyakonov, Peter H. Beton, Sergei V. Novikov, Chennupati Jagadish, Hark Hoe Tan, Michael J. Ford, Milos Toth, Carlo Bradac, and Igor Aharonovich. Identifying carbon as the source of visible single-photon emission from hexagonal boron nitride. *Nat. Mater.*, pages 1–8, November 2020. Publisher: Nature Publishing Group.

[8] Fariah Hayee, Leo Yu, Jingyuan Linda Zhang, Christopher J. Ciccarino, Minh Nguyen, Ann F. Marshall, Igor Aharonovich, Jelena Vučković, Prineha Narang, Tony F. Heinz, and Jennifer A. Dionne. Revealing multiple classes of stable quantum emitters in hexagonal boron nitride with correlated optical and electron microscopy. *Nat. Mater.*, 19(5):534–539, May 2020. Number: 5 Publisher: Nature Publishing Group.

[9] A. Sajid, Jeffrey R. Reimers, Rika Kobayashi, and Michael J. Ford. Theoretical spectroscopy of the $v_n n_b$ defect in hexagonal boron nitride. *Phys. Rev. B*, 102:144104, Oct 2020.

[10] L. Weston, D. Wickramaratne, M. Mackoit, A. Alkauskas, and C. G. Van de Walle. Native point defects and impurities in hexagonal boron nitride. *Phys. Rev. B*, 97:214104, Jun 2018.

[11] Viktor Ivády, Gergely Barcza, Gergő Thiering, Song Li, Hanen Hamdi, Jyh-Pin Chou, Örs Legeza, and Adam Gali. Ab initio theory of the negatively charged boron vacancy qubit in hexagonal boron nitride. *npj Comput. Mater.*, 6(1):41, December 2020.

[12] Mehdi Abdi, Jyh-Pin Chou, Adam Gali, and Martin B. Plenio. Color centers in hexagonal boron nitride monolayers: A group theory and ab initio analysis. *ACS Photonics*, 5(5):1967–1976, 2018.

[13] Jeffrey R. Reimers, Jun Shen, Mehran Kianinia, Carlo Bradac, Igor Aharonovich, Michael J. Ford, and Piotr Piecuch. Photoluminescence, photophysics, and photochemistry of the $V_B{}^-$ defect in hexagonal boron nitride. *Phys. Rev. B*, 102:144105, Oct 2020.

[14] P. Khatri, A. J. Ramsay, R. N. E. Malein, H. M. H. Chong, and I. J. Luxmoore. Optical gating of photoluminescence from color centers in hexagonal boron nitride. *Nano Lett.*, 20:4256–4263, May 2020.

[15] Stefan W. Hell and Jan Wichmann. Breaking the diffraction resolution limit by stimulated emission: stimulated-emission-depletion fluorescence microscopy. *Opt. Lett.*, 19(11):780–782, 1994.

[16] Thomas A. Klar and Stefan W. Hell. Subdiffration resolution in far-field fluorescence microscopy. *Opt. Lett.*, 24(14):954–956, 1999.

[17] Hans Blom and Jerker Widengren. Stimulated emission depletion microscopy. *Chem. Rev.*, 117(11):7377–7427, 2017. PMID: 28262022.

[18] Joachim Fischer and Martin Wegener. Three-dimensional direct laser writing inspired by stimulated-emission-depletion microscopy. *Opt. Mater. Express*, 1(4):614–624, Aug 2011.

[19] Joachim Fischer and Martin Wegener. Ultrafast polymerization inhibition by stimulated emission depletion for three-dimensional nanolithography. *Adv. Mater.*, 24(10):OP65–OP69, 2012.

[20] Joachim Fischer and Martin Wegener. Three-dimensional optical laser lithography beyond the diffraction limit. *Laser Photonics Rev.*, 7(1):22–44, 2013.

[21] Jan Jeske, Desmond W. M. Lau, Xavier Vidal, Liam P. McGuinness, Philipp Reineck, Brett C. Johnson, Marcus W. Doherty, Jeffrey C. McCallum, Shinobu Onoda, Fedor Jelezko, Takeshi Ohshima, Thomas Volz, Jared H. Cole, Brant C. Gibson, and Andrew D. Greentree. Stimulated emission from nitrogen-vacancy centres in diamond. *Nat. Commun.*, 8(1):14000, January 2017.

[22] Toan Trong Tran, Mehran Kianinia, Minh Nguyen, Sejeong Kim, Zai-Quan Xu, Alexander Kubanek, Milos Toth, and Igor Aharonovich. Resonant excitation of quantum emitters in hexagonal boron nitride. *ACS Photonics*, 5(2):295–300, November 2017.

[23] Simon White, Connor Stewart, Alexander S. Solntsev, Chi Li, Milos Toth, Mehran Kianinia, and Igor Aharonovich. Phonon dephasing and spectral diffusion of quantum emitters in hexagonal boron nitride. *Optica*, 8(9):1153, August 2021.

[24] J. Serrano, A. Bosak, R. Arenal, M. Krisch, K. Watanabe, T. Taniguchi, H. Kanda, A. Rubio, and L. Wirtz. Vibrational properties of hexagonal boron nitride: Inelastic x-ray scattering and ab initio calculations. *Phys. Rev. Lett.*, 98:095503, Mar 2007.

[25] P. Khatri, I. J. Luxmoore, and A. J. Ramsay. Phonon sidebands of color centers in hexagonal boron nitride. *Phys. Rev. B*, 100:125305, Sep 2019.

[26] T Q P Vuong, G Cassabois, P Valvin, V Jacques, A Van Der Lee, A Zobelli, K Watanabe, T Taniguchi, and B Gil. Phonon symmetries in hexagonal boron nitride probed by incoherent light emission. *2D Mater.*, 4(1):011004, nov 2016.

[27] T. Q. P. Vuong, G. Cassabois, P. Valvin, A. Ouerghi, Y. Chassagneux, C. Voisin, and B. Gil. Phonon-photon mapping in a color center in hexagonal boron nitride. *Phys. Rev. Lett.*, 117:097402, Aug 2016.

[28] Michael Hoese, Prithvi Reddy, Andreas Dietrich, Michael K. Koch, Konstantin G. Fehler, Marcus W. Doherty, and Alexander Kubanek. Mechanical decoupling of quantum emitters in hexagonal boron nitride from low-energy phonon modes. *Sci. Adv.*, 6(40), 2020.

[29] K. H. Michel and B. Verberck. Phonon dispersions and piezoelectricity in bulk and multilayers of hexagonal boron nitride. *Phys. Rev. B*, 83:115328, Mar 2011.

[30] Klaus Hermann. Periodic overlayers and moiré patterns: theoretical studies of geometric properties. *Journal of Physics: Condensed Matter*, 24(31):314210, July 2012.

[31] Patrick Zeller and Sebastian Günther. What are the possible moiré patterns of graphene on hexagonally packed surfaces? universal solution for hexagonal coincidence lattices, derived by a geometric construction. *New Journal of Physics*, 16(8):083028, August 2014.

[32] A. Artaud, L. Magaud, T. Le Quang, V. Guisset, P. David, C. Chapelier, and J. Coraux. Universal classification of twisted, strained and sheared graphene moiré superlattices. *Scientific Reports*, 6(1), May 2016.

[33] S. Günther and P. Zeller. Moiré patterns of graphene on metals. In *Encyclopedia of Interfacial Chemistry*, pages 295–307. Elsevier, 2018.

[34] Jiamin Xue, Javier Sanchez-Yamagishi, Danny Bulmash, Philippe Jacquod, Aparna Deshpande, K. Watanabe, T. Taniguchi, Pablo Jarillo-Herrero, and Brian J. LeRoy.

Scanning tunnelling microscopy and spectroscopy of ultra-flat graphene on hexagonal boron nitride. *Nature Materials*, 10(4):282–285, February 2011.

[35] Jingang Wang, Fengcai Ma, and Mengtao Sun. Graphene, hexagonal boron nitride, and their heterostructures: properties and applications. *RSC Advances*, 7(27):16801–16822, 2017.

[36] A Sajid and Kristian S Thygesen. $V_N C_B$ defect as source of single photon emission from hexagonal boron nitride. *2D Mater.*, 7(3):031007, jun 2020.

Chapter 7

STED Microscopy

7.1 Introduction

Stimulated emission depletion (STED) microscopy [1] is one of a number of super-resolution imaging techniques [2]. A typical STED microscope employs two lasers: one that excites a fluorophore, and a second, with a doughnut-like intensity profile, that deactivates fluorescence via stimulated emission, to effectively reduce the excitation area below the diffraction limit [3]. In the previous chapter we used STED spectroscopy to study the vibronic levels in the ground state, in this chapter we present a practical application of STED technique for high resolution imaging of colour centres in hBN.

For microscopy, the depletion laser pulse profile is changed from Gaussian to doughnut by a vortex phase plate (VPP) [4]. Fig. 7.1 (a) shows a sketch of STED microscopy. The overlapping STED and excitation beams enter the objective and are focused on the hBN sample. The objective, with the help of a piezo stage, moves in a raster fashion to scan the sample. In confocal microscopy the resolution (δd) depends on the spot size of excitation laser beam, which depends on the wavelength (λ) of the pulse and the NA of the objective-

$$\delta d = \frac{0.61\lambda}{NA} \tag{7.1}$$

Fig. 7.1 (b) shows a hypothetical 2D grid of emitters excited via confocal microscopy. The large spot size of the excitation laser excites multiple defects (shown in yellow) at once. In STED microscopy, the doughnut shaped depletion laser pulse is applied soon after the excitation pulse which depletes the emitter from the excited state and reduces the PL signal from the neighbouring fluorophores. The doughnut shaped STED laser depletes all the PL

signal coming from the fluorophores which overlaps with the doughnut ring and only leave the central ones excited, where the doughnut intensity is nearly zero shown in Fig. 7.1 (c). The resolution in STED microscopy can theoretically reach the atomic scale, but is ultimately limited by the properties of the fluorophore [5]. It is therefore important to investigate and characterize potential new fluorophores. The lateral resolution,

$$\delta d \propto \sqrt{\frac{I_{sat}}{I}} \tag{7.2}$$

where I is the optical intensity used to stimulate emission and

$$I_{sat} = \frac{h\nu}{\sigma_s \tau_r} \tag{7.3}$$

is the stimulated-emission saturation intensity of the emitter, with $h\nu$ the photon energy, τ_r the excited state radiative lifetime and σ_s is the STED cross section for stimulated emission [6]. In our STED demonstration, presented in this chapter, we obtained a STED resolution $\sim 10\times$ higher than the confocal technique. This work has been published and is here adapted from ACS Photonics, 8, 7, 2081–2087(2021) Copyright 2021 The American Chemical Society. For this work, my contributions were- numerical calculations and fitting, doing measurement remotely (due to covid restrictions) and making LabVIEW programs for automation, plotting the figures, writing and submitting the paper.

7.2 Search for a new fluorophore

The ideal fluorophore should have large σ_s to enable high resolution, whilst minimising the chance of photodamage to the sample. Fluorophores should also be bright for a low excitation power, photostable, in terms of blinking and bleaching, and physically small such that a high degree of spatial resolution can be achieved.

The most widely used fluorophores are organic dye molecules, which can have a relatively large STED cross-section on the order of 10^{-16} cm^2 [7]. They can be designed to bind to certain biological [8] targets and produce high emission rates [9] at sufficiently low power [10] to enable spatial resolution of ~ 20 nm [11]. However, photobleaching is a significant limitation of these organic dyes, which has stimulated the search for more stable fluorophores [12, 13]. A prime example is the negatively charged nitrogen vacancy (NV) centre in diamond,

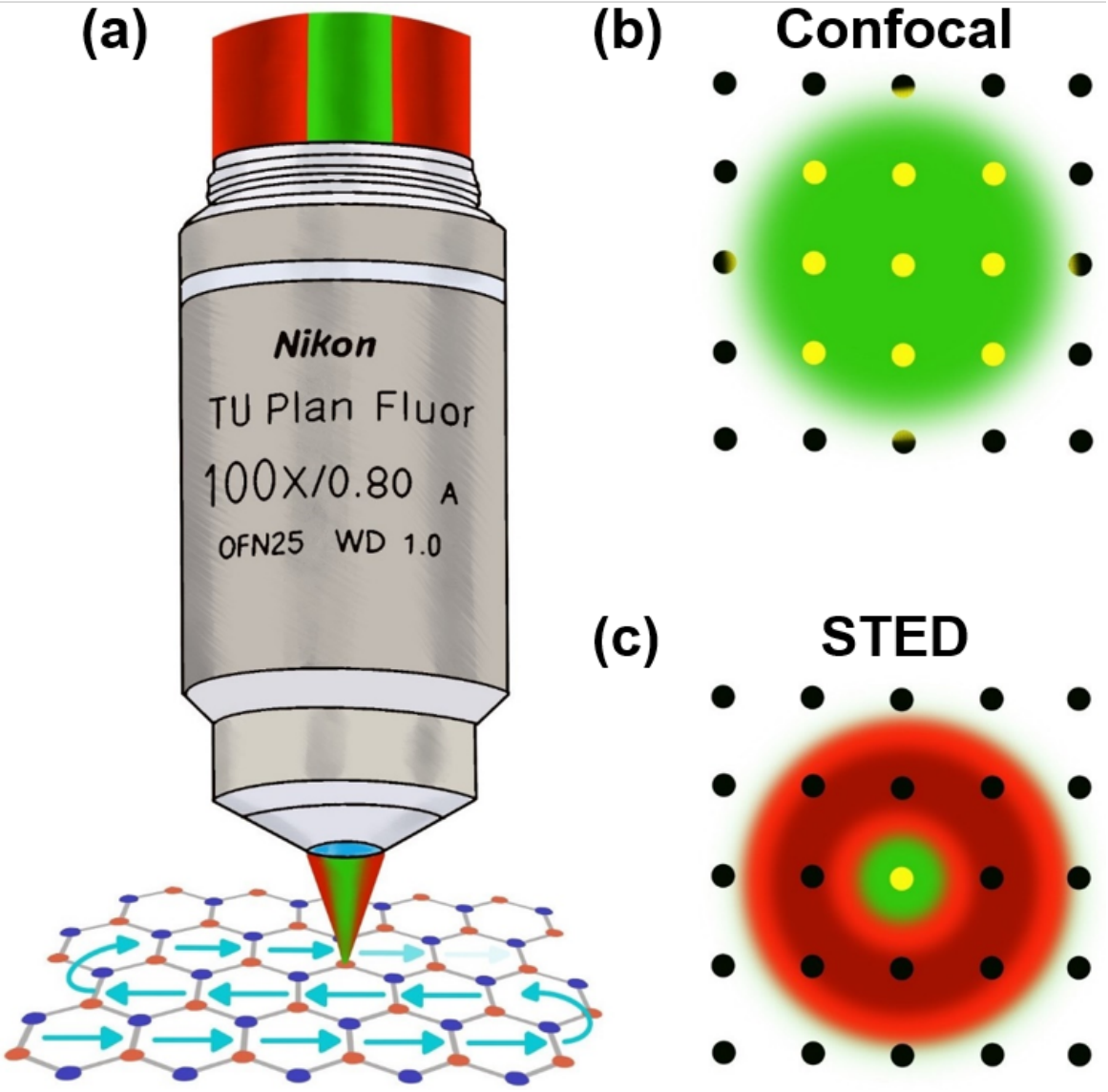

Fig. 7.1 Cartoon sketch to understand STED imaging. (a) Overlapping STED doughnut and Gaussian excitation beam entering the objective which scan the sample in a raster-type pattern. (b) Confocal excitation spot on hypothetical 2D grid of emitters. Excited emitters are highlighted with yellow. (c) Overlapping STED and excitation beam spot on emitter grid shown only one emitter excited while the neighbouring emitters are depleted by the STED doughnut.

where a resolution of 2.4 nm has been demonstrated in bulk diamond [14] and individual NV centres separated by just 15 nm have been resolved in nanodiamonds [15]. Nanodiamonds can be functionalized to bind with biological targets and their relatively non-toxic nature allow their use for target labelling and imaging in living tissues [16]. However, the STED cross-section is smaller than that of dye molecules, at around 10^{-17} cm^2, requiring a larger depletion power [17, 18]. Furthermore, the photoluminescence intensity is low and spans a large spectral range due to phonon assisted emission, and photocharging can result in blinking, particularly in nano-diamonds with diameters < 10 nm [19]. In a recent work, negatively charged silicon vacancies (SiV) have been proposed as an alternative [20], offering the favourable properties of diamond, but with a larger STED cross-section (4×10^{-17} cm^{-2}).

These impressive results with diamond raise the question of whether colour centres in other wide bandgap semiconductors have potential for STED microscopy? In particular, colour centres in hBN appear an interesting candidate, especially after the STED spectroscopy work presented in chapter 6, where we were able to achieve a STED inhibition ratio of $<$ 0.1 [21]. Stable emission has been demonstrated from hBN nanoflakes with thicknesses of just a few atomic layers and lateral dimensions < 10 nm [22]. Colour centres in hBN have previously been studied with super-resolution microscopy [23, 24] but they have not previously been employed in STED microscopy.

7.2.1 Bio-compatibility of hBN

As biological imaging is a major application of STED microscopy, the biocompatibility and functionalization of fluorophores is also an important consideration. Merlo et al. [25] have reviewed the biocompatibility of various forms of boron nitride and conclude that, unlike carbon based nanomaterials, which show different levels of compatibility and toxicity based on shape, preparation method and size of the material, boron nitride in pristine condition is biocompatible in-vivo and in-vitro. Furthermore, Mateti et al. [26] concluded that single boron nitride nano sheets and tubes are non-toxic because of no unsaturated Boron atoms, except at the edges. Functionalization of BN nanostructures [27] holds promise for various applications, including vaccine design [28] and photodynamic cancer therapy [29].

7.3 Sample Preparation and Setup

The samples examined consist of hBN flakes, dropcast from solution onto a Si substrate coated with a 5 nm layer of Al_2O_3[30]. For more details, see chapter 3, section. 3.1. Note

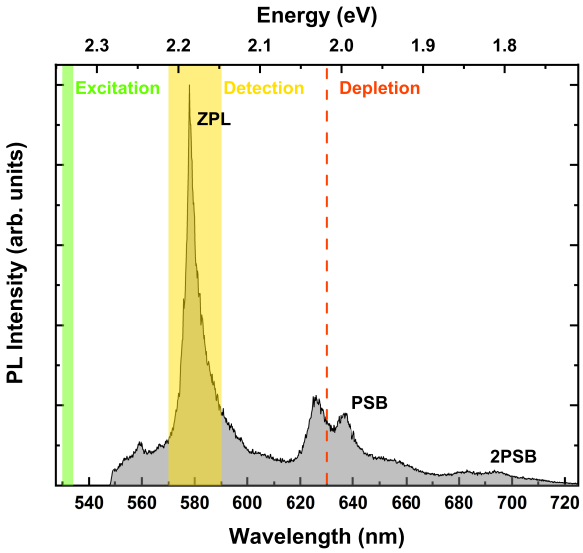

Fig. 7.2 Typical PL spectrum of a colour centre in hBN, showing the excitation, depletion and collection wavelengths. The labels ZPL, PSB and 2PSB indicate the zero-phonon line, one optical phonon sideband and two optical phonon sidebands, respectively.

that this time the sample was not annealed to show that non-annealed hBN flakes are good candidates for STED imaging and holds potential for bio applications.

In this work we focus on a class of defects with zero-phonon line (ZPL) emission at around 580 nm. Fig. 7.2(a) shows the photoluminescence (PL) spectrum from such a defect, under green (532nm) excitation.

The experimental setup for STED-imaging is shown in Fig. 7.3(a) and employs a variant of STED known as time-gated CW-STED [6], where the excitation (depletion) laser is pulsed (continuous-wave [CW]). The excitation is generated by a supercontinuum laser, with a repetition rate of 78 MHz that can be reduced using a built-in pulse-picker. The supercontinuum beam is directed by a pair of dielectric mirrors, which filter-out wavelengths $>$800 nm, through a polarizing beam-splitter and band-pass filter centred at 532 nm (4 nm FWHM), and into a single mode fibre. At the output of the fibre a half-wave plate and linear polarizer maximize the power and ensure a high degree of linear polarization, respectively. The depletion beam is provided by a red CW diode laser, with a wavelength of 630 nm, which is coupled to a single mode fibre, followed by a half-wave plate, linear polarizer and vortex phase plate, which generates the doughnut shaped beam profile necessary for STED microscopy [4]. Two dichroic beam splitters combine the green and red lasers, which are passed to an objective lens with numerical aperture of 0.8 that is mounted on an XYZ-piezo

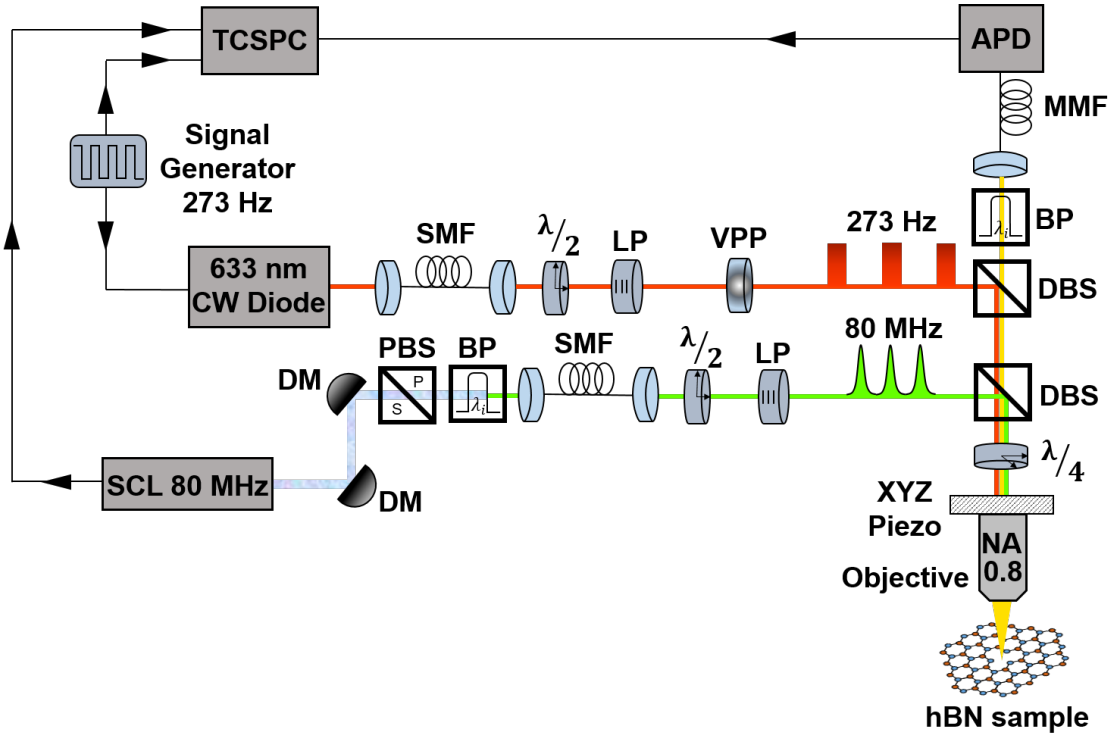

Fig. 7.3 Schematic diagram of the gated CW-STED setup. DM=dielectric mirror; SMF=single-mode fibre; MMF=multi-mode fibre PBS=polarizing beam-splitter; BPF=band-pass filter; VPP=vortex phase plate; LP= linear polarizer; DBS=dichroic beam-splitter; SCL=supercontinuum laser; APD=avalanche photodiode; $\lambda/4$=quarter-waveplate; $\lambda/2$=half-waveplate; TCSPC-time-correlated single photon counting electronics.

stage. The fluorescence from the sample is collected by the same objective, filtered by a pair of tunable long and short pass filters (570-590 nm pass band) and coupled, via a multi-mode fibre, into a single photon avalanche photodiode (SPAD) module. A time correlated single photon counting (TCSPC) module records the arrival time of photons, along with reference pulses from the two lasers. This data is then post-processed to generate time-resolved decay traces and confocal/STED maps. The red depletion laser is switched on and off at 237 Hz with a 50% duty cycle, by controlling the drive current with a function generator. This modulation is much slower than the 78 MHz repetition rate of the excitation laser so enables confocal and STED maps to be acquired simultaneously. Where quoted, the laser power is measured before the objective lens and represents an upper limit, as both excitation and depletion lasers are collimated to a diameter slightly larger than the back aperture of the objective lens.

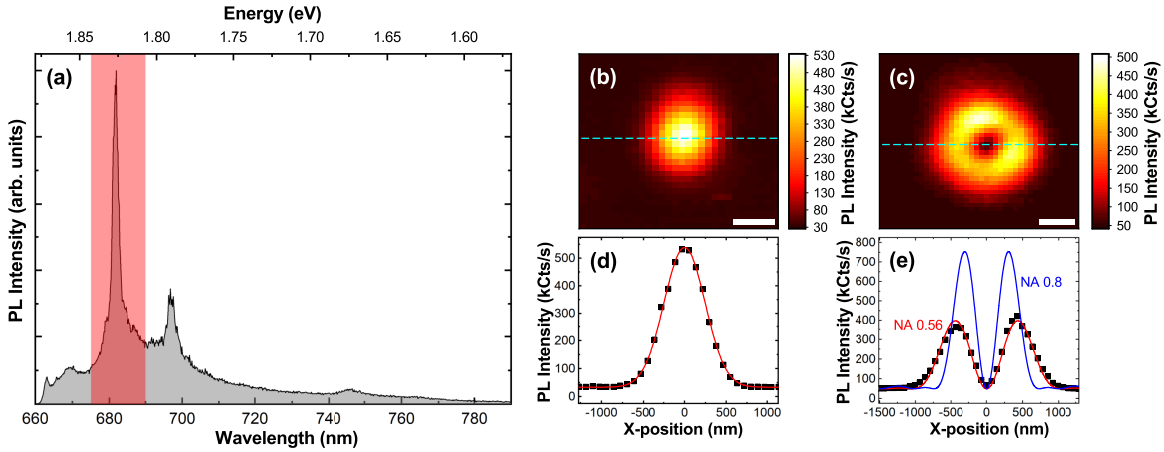

Fig. 7.4 Characterization of STED Laser Beam. (a) PL spectrum of the hBN colour centre used for STED beam characterization. The shaded area indicates the wavelength range used for in the beam characterization. (b) and (c) Confocal images of the hBN colour centre when excited with (b) a Gaussian beam profile and (c) the doughnut beam profile. The scale marker in (b) and (c) is 500 nm and the dashed lines indicate the linecuts shown in (d) and (e). (d) and (e) PL intensity profiles from (d) the gaussian beam and (e) the doughnut beam maps. The solid red line in (d) shows a Gaussian fit to the data with FWHM of 580 nm and in (e) shows a fit to doughnut beam profile calculated with eq. 7.4 giving $\mathrm{NA}_{eff} = 0.56$.

7.3.1 STED beam characterization

To quantify the STED cross-section, the intensity profile of the laser at the focal plane is required. To measure this in our setup, we take advantage of the fact that colour centres emitting over a broad energy range can be found in hBN [31–35]. Using the same sample, we locate a colour centre that can be efficiently excited with the red laser, in this case with ZPL emission at 685 nm, which we then use as an effective point source for mapping the STED laser beam profile. The spectrum of the colour centre is shown in Fig. 7.4(a). The ZPL fluorescence is recorded whilst the beam is scanned over the defect, revealing a Gaussian beam profile, with a FWHM of 580 nm (Fig. 7.4(b) and (d)).

This method is also used to measure the doughnut beam intensity profile, which is required to interpret the achieved STED resolution, and is plotted in Fig. 7.4(c) and (e). The doughnut beam profile, $D(r)$, along the radius, r, is approximated as [20, 36]:

$$D(r) \simeq \frac{2\pi \mathrm{NA}^2}{\lambda_S^2} \left(\pi \frac{H_o(u)J_1(u) - H_1(u)J_o(u)}{u} \right)^2 \tag{7.4}$$

where NA is the numerical aperture of the objective lens, J_o and J_1 are the zeroth and first order Bessel Functions, and H_o and H_1 are the zeroth and first order Struve Functions with normalized radius $u = 2\pi r\mathrm{NA}/\lambda_S$.

In Fig. 7.4(e) the experimental data is shown alongside a fit to the data of eq. 7.4, from which we extract an effective numerical aperture of our microscope, NA_{eff} = 0.56, that is less than the the actual NA of the objective lens (0.8). This reduced NA can be attributed to imperfect circular polarization and the alignment of the doughnut beam into the objective lens. For comparison, eq. 7.4 is also plotted for NA=0.8, which illustrates that larger NA leads to an increase in the intensity and reduction of the distance from the doughnut centre of the two maxima.

7.4 Time Gated CW STED

Time-gated CW-STED is demonstrated in Fig. 7.5(a) for an hBN colour centre. The use of Gaussian-shaped depletion beam from a CW laser, pulsed excitation and time-gated detection, can yield high resolution at low STED intensities [6]. In this approach, the lifetime is reduced by the depletion laser from $1/k_{fl}$ to:

$$\tau = \frac{1}{k_{fl} + (P_S \sigma_S \lambda_S / A_S hc)} \tag{7.5}$$

where k_{fl} is the radiative decay rate of the fluorophore, P_S the power of the STED laser of wavelength λ_S, $A_S = 2\pi(SD)^2$ is the STED beam focal area. A_S is approximated by the standard deviation ($SD = 246$ nm) of the focal spot's Gaussian profile. For photons collected after $\tau_d > \tau$, where the CW laser has depleted the excited state, the STED inhibition factor decreases, and therefore, the STED resolution increases. This enables lower depletion laser power to be compensated by a longer gate delay, as illustrated in Fig. 7.5(c). The trade-off is that with longer gate delays the number of photons in the collection window is reduced, thereby reducing the signal to noise ratio. To some extent this can be compensated by choosing a gate width, τ_W and excitation laser repetition rate, that maximises the fluorescence intensity based on the radiative lifetime of the emitter.

In Fig 7.5.(b) the emitter lifetime is plotted as a function of the depletion laser power and is reduced from ~ 4 ns to ~ 0.5 ns for a STED power, $P_S = 49$ mW, which is the maximum available from this laser. The STED cross-section is extracted from a fit to eq. 7.5 and for this colour centre yields a value of $\sigma_S \geq 2.5 \times 10^{-17}\mathrm{cm}^2$. Note, as the power is measured before the objective lens, the power incident on the sample is less than quoted and hence

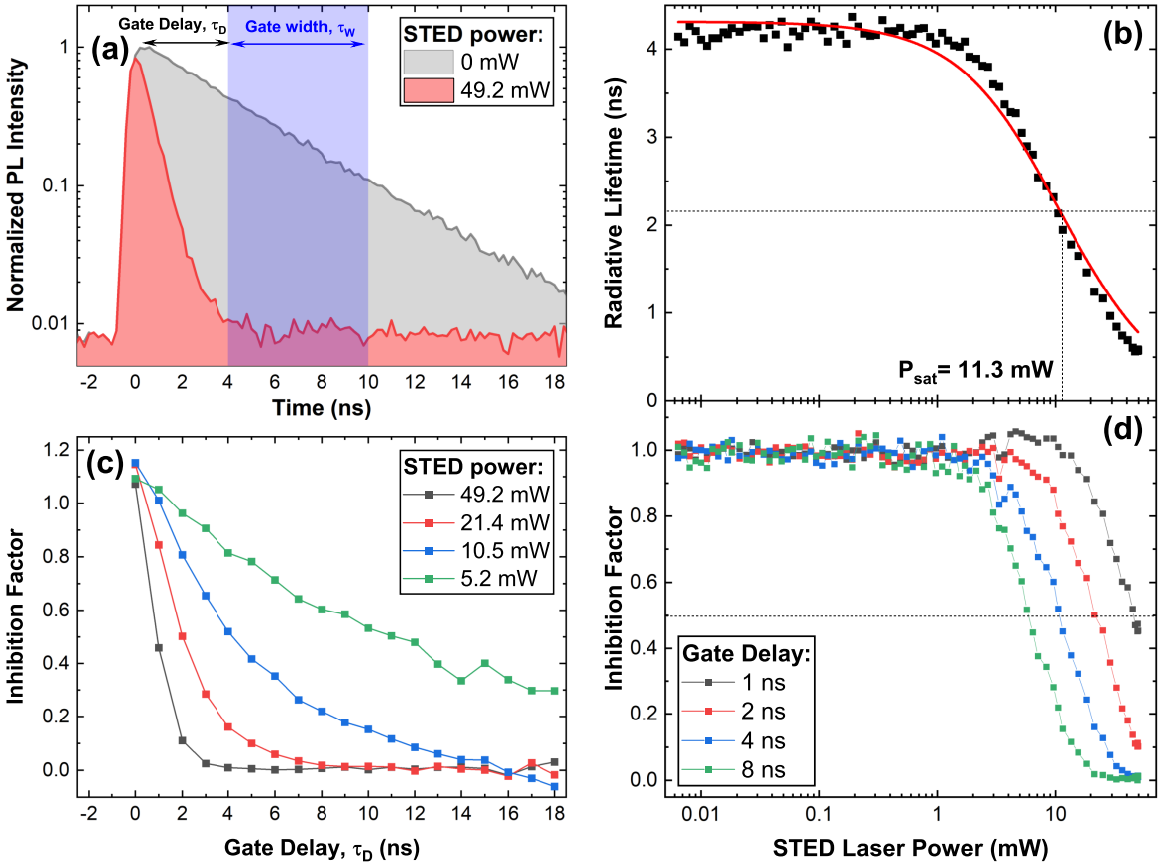

Fig. 7.5 Time-gated CW-STED with a colour centre in hBN. (a) Time-resolved photoluminescence from a single hBN colour centre, under pulsed 532 nm excitation, with and without 633 nm CW-STED laser co-excitation (b) STED laser power dependence of the radiative lifetime of the colour centre. The red line shows a fit to eq. 7.5. (c) and (d) STED inhibition factor as a function of (c) gate delay time and (d) STED laser power with gate width, $\tau_w = 6$ ns. The depletion laser has a Gaussian-shaped intensity profile.

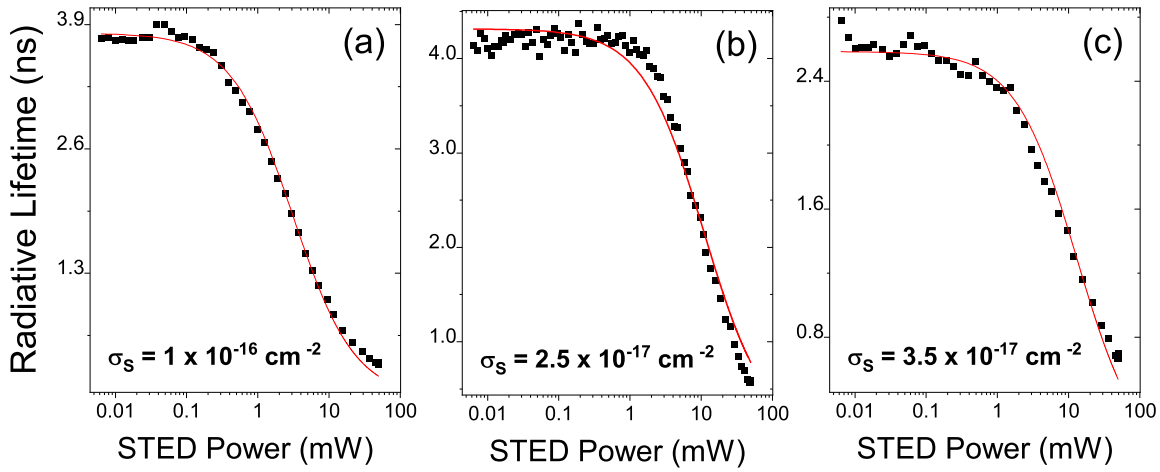

Fig. 7.6 STED laser power dependence on radiative lifetime for 3 example colour centres (a)-(c). σ_S is calculated using eq. 7.5.

our calculation using eq. 7.5 gives a lower limit of the STED cross section. Increasing the time delay of the gate reduces the STED saturation power, defined as the power required to reduced the fluorescence intensity by half, (Fig. 7.5(d)).

The measurements shown in Fig. 7.5 are repeated for ten more colour centres resulting in a mean STED cross-section of $\geq (5.5 \pm 3.2) \times 10^{-17}$cm^2, with a maximum value of $\geq 1 \times 10^{-16}$cm^2. Fig. 7.6(a)-(c) shows lifetime verses STED power plot for three such colour centres. The mean STED cross section for the 10 emitters is $(5.5 \pm 3.2) \times 10^{-17}$ cm^2 with the highest $\sim 1 \times 10^{-16}$ cm^2 shown in 7.6(a). From the same measurement, we also extract the average saturation power $P_{sat} = (14.7 \pm 9.5)$ mW.

These cross-sections compare favourably with centres in diamond [20, 18] and organic dye molecules [7, 6] and demonstrate the clear potential for hBN colour centres to find application in STED microscopy. The relatively large variation in the STED cross-section can be attributed to variations in the efficiency of the optical phonon-assisted depletion from defect to defect [21]. Unlike for NV and SiV centres in diamond, where the ZPL wavelength is well defined, in hBN samples such as ours, there is considerable variation of the ZPL wavelength [32]. In our experiment, the detection bandwidth spans 20 nm, but the STED laser bandwidth is ~ 1 nm. Consequently, the overlap of the STED laser with peaks in the OPSB can vary considerably, leading to the observed defect-to-defect variation in STED cross-section. See chapter 6, section 6.4 for example of OPSB variations among defects. This could be avoided by using a broadband STED laser, such as a filtered supercontinuum [20].

7.5 Resolution Improvement: STED Versus Confocal

To verify that hBN colour centres can be applied to STED microscopy, we use a vortex phase plate to generate a doughnut-shaped depletion laser beam with a central minima co-aligned with the maxima of the Gaussian excitation beam. Scanning confocal and STED images of a single colour centre, presented in Fig. 7.7(a) and (b), respectively, are acquired simultaneously by switching the depletion laser on and off at 237 Hz ($P_S = 49$ mW, $\tau_D = 3$ ns). The images reveal a clear improvement in resolution, which is quantified with Gaussian fits to horizontal intensity profiles through the two images. Fig. 7.7(c) and (e) show confocal and STED profiles along the horizontal and vertical axis of the PL map. The confocal FWHM for the horizontal (vertical) profile is ∼380 nm (∼450 nm), consistent with the diffraction limit of our microscope ($\lambda = 532$ nm, $N.A. = 0.8$). Whereas, with the STED laser applied the FWHM is ∼40 nm (∼60 nm), which is a ∼ 9-fold (7-fold) improvement in resolution. We attribute the asymmetry between the x and y-directions, in both the STED and confocal images, to aberrations [37, 38] and/or drift in our setup.

Fig. 7.7(d) and (f) highlight the value of time-gating in CW-STED, with the Gaussian FWHM plotted as a function of the gate delay time for horizontal and vertical linecuts, respectively. The confocal resolution is independent of the gate delay, whereas the STED FWHM reduces from ∼ 270 nm with no gate delay, to ∼40 nm (∼60 nm) for the horizontal (vertical) linecut when the gate delay is 6 *ns*. The solid lines in Fig. 7.7(d) and (f) show fits to the data of the calculated point spread function (PSF) for time-gated CW-STED. The PSF is calculated following Vicidomini *et al.* [6], but adapted to take into account the gate width, which in this case is comparable to the excited state lifetime of the hBN defects. We start from the inhibition factor, $\eta_S(I_S, \tau_D, \tau_W)$, which is the ratio of fluorescence intensity with and without the STED laser, in the interval defined by the gate delay, τ_D and gate width, τ_W, and can be approximated as:

$$\eta_S(I_S, \tau_D, \tau_W) = \int_{\tau_D}^{\tau_D+\tau_W} e^{-(k_{fl}+k_S)t}dt \Big/ \int_{\tau_D}^{\tau_D+\tau_W} e^{-k_{fl}t}dt \tag{7.6}$$

where $k_S = P_S\sigma_S\lambda_S/A_S hc = \sigma_S I_S$ is the STED induced decay rate. Evaluating eq. 7.6 leads to:

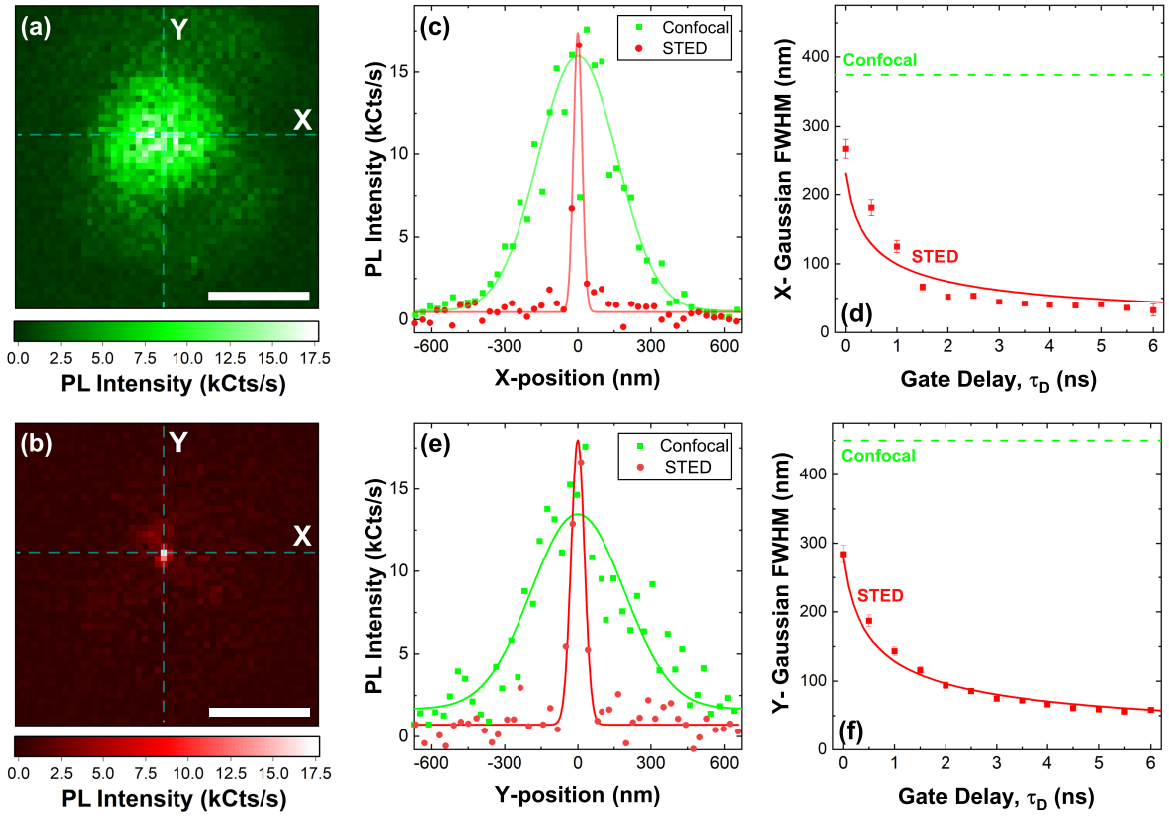

Fig. 7.7 STED microscopy of a single colour centre in hBN. (a) Confocal and (b) STED images of a single hBN colour centre, for a gate delay of 3 ns and a gate width of 7 ns. In (a) and (b) the scale marker is 500 nm. In (b) the STED power is 49 mW. (c) and (e) are Horizontal and Vertical intensity profile through the centre of the confocal and STED images. The solid red and green lines show Gaussian fits to the experimental data with FWHM of 380 nm (450 nm) and 41 nm (63 nm) for Horizontal (Vertical), respectively. (d) and (f) Gaussian FWHM of the STED image as function of gate delay time with fixed gatewidth of 0.5 ns for Horizontal and Vertical intensity profile. The solid red line is a fit to the FWHM of the calculated point spread function for time-gate CW-STED. The fitting parameter, P_{sat} is 1.2 mW (1.6 mW) for Horizontal (Vertical) fit. (See eq. S4 in S. I).

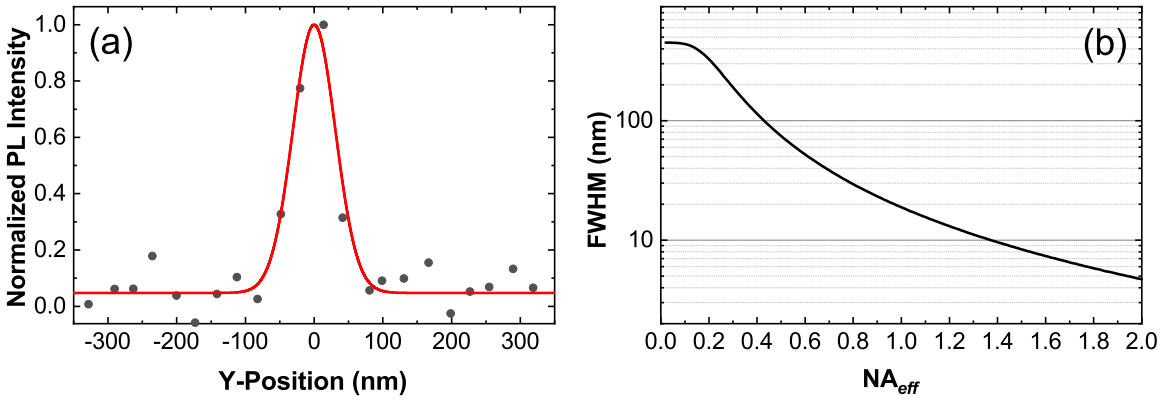

Fig. 7.8 (a) Vertical intensity profile through the centre of the STED image, shown in the Fig. 7.7(e), with fit to the PSF calculated using eq. 7.8 and the parameters $\tau_D = 3$ ns, $\tau_W = 7$ ns, $\tau_{fl} = 1.7$ ns, $d_c = 450$ nm and $P_{sat} = 1.6$ mW. (b) Simulation of FWHM verses NA$_{eff}$ from calculated PSF using Eq. 7.4 and 7.8.

$$\eta_S(I_S, \tau_D, \tau_W) = \frac{1}{1 + I_S/I_{sat}} \left[\frac{\exp(-\frac{\tau_D+\tau_W}{\tau_{fl}} \frac{I_S}{I_{sat}}) - \exp(\frac{\tau_W}{\tau_{fl}} - \frac{\tau_D}{\tau_{fl}} \frac{I_S}{I_{sat}})}{1 - \exp(\frac{\tau_W}{\tau_{fl}})} \right] \tag{7.7}$$

where $I_{sat} = k_{fl}/\sigma_s$ is the saturation intensity, defined as the STED intensity for which the fluorescence is reduced by 50 %. The effective PSF of the STED microscope, $h_S(r)$ arises from the multiplication of the Gaussian excitation profile by the inhibition factor, resulting in:

$$h_S(r) = exp\left[\frac{-r^2 4ln(2)}{d_c^2}\right] \frac{1}{1+S_r} \left[\frac{exp(-\frac{\tau_D+\tau_W}{\tau_{fl}} S_r) - exp(\frac{\tau_W}{\tau_{fl}} - \frac{\tau_D}{\tau_{fl}} S_r)}{1 - exp(\frac{\tau_W}{\tau_{fl}})} \right] \tag{7.8}$$

where d_c is the FWHM of the Gaussian excitation profile and $S_r = P_S D(r) A_S / P_{sat}$ which is a function of NA$_{eff}$. Here P_{sat} is the STED saturation power and is used below as a fitting parameter.

Fig 7.8 (a) shows vertical intensity profiles through the centre of the STED image shown in Fig. 7.7(e). The solid line shows the point spread function calculated using eq. 7.8, where the only fit parameter is $P_{sat} = 1.6$ mW and which is in excellent agreement with the experimental data with FWHM of 61 nm.

In Fig. 7.8 (b), we calculated the FWHM (i.e resolution Δr) from PSF for different values of NA using Eq. 7.4 and 7.8. The calculated FWHM decreases with increase in NA$_{eff}$ as

expected. For an oil-immersion objective, where the NA can reach 1.45, the resolution is predicted to be sub 10 nm.

In Fig. 7.7(d) and (f), the agreement with the experimental data is better for the vertical than the horizontal linecut, which we attribute to under-sampling of the STED image. As the gate delay is increased and the FWHM narrows, the number of pixels contributing to the width of the Gaussian fit also decreases. Due to the asymmetry in horizontal and vertical directions, the under-sampling is more significant for the horizontal linecut, where only two pixels contribute to the width at the maximum gate delay, compared to four pixels for the vertical linecut.

In Fig. 7.7(a) and (b) the maximum PL intensity is approximately the same for the STED and confocal images, whereas in general it is more common for the STED intensity to be lower [20, 6, 15, 17], because the STED intensity does not go to zero at the doughnut centre. This is not observed for all defects (see Fig. 7.9(c)) and we speculate that it is due to optical stabilisation of the charge state, of this particular colour centre in the presence of the STED laser. Photo-charging effects in hBN have been reported for positive detuning of the laser (energy higher than the ZPL) [39, 23]. However, similar behaviour has also been observed for negative detuning, for example in Silicon Carbide defects [40].

There is also some evidence for instability of the photoluminescence, which can be seen in the spread of the confocal data points about the Gaussian fit, particularly in Fig. 7.7(e). This could be related to charge state switching, which is common for colour centres in wide bandgap materials [41, 42], including hBN [23, 39, 43]. This behaviour varies between colour centres and can be detrimental to STED imaging. However, studies have shown stable emission and low rates of blinking and bleaching is possible for hBN colour centres [32] and that the choice of excitation conditions can stabilize the emission [23, 39].

7.6 Practical Example: Distinguishing Multiple Emitters

In Fig. 7.9 we demonstrate that two hBN colour centres, separated by less than the diffraction limit, can be resolved using STED microscopy. In Fig. 7.9(a) and (b), confocal and STED images of the same area of the sample are presented. In the confocal image (Fig. 7.9(a)) a single bright spot is observed, apparently indicating emission from a single colour centre. However, the STED image (Fig. 7.9(b)) clearly reveals two distinct emission centres. From the intensity profiles presented in Fig. 7.9(c), and Gaussian fits to the data, the separation of the two colour centres is 251 ± 8 nm, compared to the diffraction limit of $\lambda/2NA = 333$ nm for our system. The FWHM for the two peaks are 144 nm (lower-left spot) and 190

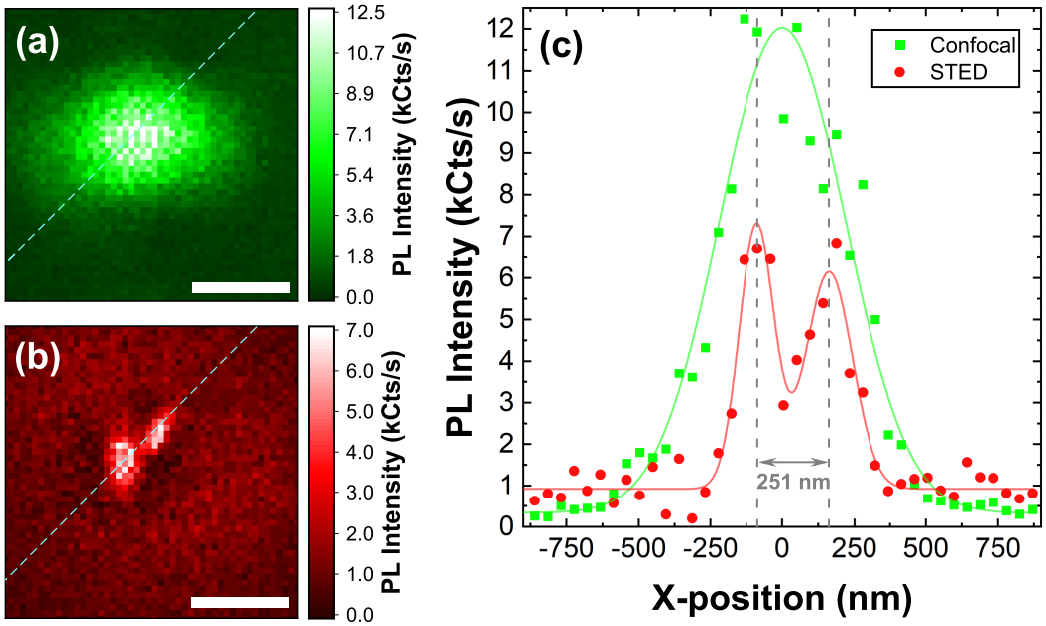

Fig. 7.9 (a) Confocal and (b) STED images of a multiple hBN colour centres, for a gate delay of 3 ns. In (a) and (b) the scale marker is 500 nm and the blue dashed lines indicate the linecuts shown in (c). In (b) the STED power is 49 mW. (c) Linecut intensity profiles from the confocal (green) and STED (red) images along the direction indicated in (a) and (b). The solid green (red) lines in (c) show Gaussian (double Gaussian) fits to the experimental data.

nm (upper-right spot). The resolution here is consistent with the measured average STED cross-section of $(5.5 \pm 3.2) \times 10^{-17}$ cm^2 , which coupled with the numerical aperture of 0.8 and STED laser power of 49 mW, leads to a mean expected FWHM of (202 ± 49) nm. The asymmetry of the two spots in the STED image suggest that one, or both, may contain more than one unresolved emitter.

7.7 Conclusion

In conclusion, these results clearly illustrate the potential of hBN colour centres as a fluorophore for STED microscopy. In our current set-up the resolution is limited by both the numerical aperture of the objective lens (0.8) and the available STED laser power, yet a resolution of ~ 50 nm is still achieved for a power density of 13 MW/cm^2. We calculate that replacing our objective with an oil-immersion lens, widely used in STED microscopy (typical numerical aperture of 1.45), would improve the resolution to <10 nm, comparable to state of the art measurements with diamond NV centres [15]. In this work, we have employed

colour centres with ZPL emission around 580 nm. However, the wide range of emission energies can provide flexibility in the choice of excitation/depletion wavelength and colour centres emitting at shorter wavelengths [44, 31] offer the potential of further improvements in resolution. Photoluminescence from sub-10 nm diameter flakes [22] and the non-toxic nature of hBN [25] show promise for biological applications but further work is required to understand the role of optical pumping on the PL stability [39, 23, 43] so that the excitation scheme can be optimised, and to determine the underlying defect structure so that samples with a single dominant defect species can be produced [45]. Furthermore, STED microscopy can be combined with ODMR [14, 46, 15] to study the spin physics of colour centres in hBN [47, 48], where there is considerable promise for applications in quantum sensing [49].

References

[1] Stefan W. Hell and Jan Wichmann. Breaking the diffraction resolution limit by stimulated emission: stimulated-emission-depletion fluorescence microscopy. *Opt. Lett.*, 19(11):780, 1994.

[2] Giuseppe Vicidomini, Paolo Bianchini, and Alberto Diaspro. STED super-resolved microscopy. *Nature Methods*, 15(3):173–182, January 2018.

[3] Thomas A. Klar and Stefan W. Hell. Subdiffraction resolution in far-field fluorescence microscopy. *Opt. Lett.*, 24(14):954–956, Jul 1999.

[4] Xiang Hao, Cuifang Kuang, Tingting Wang, and Xu Liu. Effects of polarization on the de-excitation dark focal spot in STED microscopy. *J. Opt*, 12(11):8, 10 2010.

[5] Volker Westphal and Stefan W. Hell. Nanoscale resolution in the focal plane of an optical microscope. *Phys. Rev. Lett.*, 94:143903, Apr 2005.

[6] Giuseppe Vicidomini, Gael Moneron, Kyu Y. Han, Volker Westphal, Haisen Ta, Matthias Reuss, Johann Engelhardt, Christian Eggeling, and Stefan W. Hell. Sharper low-power STED nanoscopy by time gating. *Nat. Methods*, 8(7):571–575, 2011.

[7] Lars Kastrup and Stefan W. Hell. Absolute optical cross section of individual fluorescent molecules. *Angew. Chem., Int. Ed. Engl.*, 43(48):6646–6649, 2004.

[8] M. Sameiro and T. Gonçalves. Fluorescent labeling of biomolecules with organic probes. *Chem. Rev.*, 109(1):190–212, 1 2009.

[9] Graham T. Dempsey, Joshua C. Vaughan, Kok Hao Chen, Mark Bates, and Xiaowei Zhuang. Evaluation of fluorophores for optimal performance in localization-based super-resolution imaging. *Nat. Methods*, 8(12):1027–1040, 12 2011.

[10] Margaux Bouzin, Giuseppe Chirico, Laura D'Alfonso, Laura Sironi, Giancarlo Soavi, Giulio Cerullo, Barbara Campanini, and Maddalena Collini. Stimulated emission

properties of fluorophores by cw-sted single molecule spectroscopy. *J. Phys. Chem. B*, 117(51):16405–16415, 2013. PMID: 24298991.

[11] Gerald Donnert, Jan Keller, Rebecca Medda, M. Alexandra Andrei, Silvio O. Rizzoli, Reinhard Lührmann, Reinhard Jahn, Christian Eggeling, and Stefan W. Hell. Macromolecular-scale resolution in biological fluorescence microscopy. *Proc. Natl. Acad. Sci. U. S. A.*, 103(31):11440–11445, 8 2006.

[12] C. Eggeling, J. Widengren, R. Rigler, and C. A.M. Seidel. Photobleaching of Fluorescent Dyes under Conditions Used for Single-Molecule Detection: Evidence of Two-Step Photolysis. *Anal. Chem.*, 70(13):2651–2659, 7 1998.

[13] Joanna Oracz, Volker Westphal, Czesław Radzewicz, Steffen J. Sahl, and Stefan W. Hell. Photobleaching in STED nanoscopy and its dependence on the photon flux applied for reversible silencing of the fluorophore. *Sci. Rep*, 7(1):1–14, 12 2017.

[14] Dominik Wildanger, Brian R. Patton, Heiko Schill, Luca Marseglia, J. P. Hadden, Sebastian Knauer, Andreas Schönle, John G. Rarity, Jeremy L. O'Brien, Stefan W. Hell, and Jason M. Smith. Solid Immersion Facilitates Fluorescence Microscopy with Nanometer Resolution and Sub-Ångström Emitter Localization. *Adv. Mater.*, 24(44):OP309–OP313, 11 2012.

[15] Silvia Arroyo-Camejo, Marie Pierre Adam, Mondher Besbes, Jean Paul Hugonin, Vincent Jacques, Jean Jacques Greffet, Jean François Roch, Stefan W. Hell, and François Treussart. Stimulated emission depletion microscopy resolves individual nitrogen vacancy centers in diamond nanocrystals. *ACS Nano*, 7(12):10912–10919, 2013.

[16] Han B. Man and Dean Ho. Nanodiamonds as platforms for biology and medicine. *J. Lab. Autom.*, 18(1):12–18, 2013.

[17] Kyu Young Han, Katrin I. Willig, Eva Rittweger, Fedor Jelezko, Christian Eggeling, and Stefan W. Hell. Three-dimensional stimulated emission depletion microscopy of nitrogen-vacancy centers in diamond using continuous-wave light. *Nano Lett.*, 9(9):3323–3329, 2009. PMID: 19634862.

[18] Eva Rittweger, Kyu Young Han, Scott E. Irvine, Christian Eggeling, and Stefan W. Hell. STED microscopy reveals crystal colour centres with nanometric resolution. *Nat. Photonics*, 3(3):144–147, 3 2009.

[19] J. R. Rabeau, A. Stacey, A. Rabeau, S. Prawer, F. Jelezko, I. Mirza, and J. Wrachtrup. Single nitrogen vacancy centers in chemical vapor deposited diamond nanocrystals. *Nano Lett.*, 7(11):3433–3437, 11 2007.

[20] Yaser Silani, Forrest Hubert, and Victor M. Acosta. Stimulated emission depletion microscopy with diamond silicon vacancy centers. *ACS Photonics*, 6(10):2577–2582, 2019.

[21] Ralph Nicholas Edward Malein, Prince Khatri, Andrew J. Ramsay, and Isaac J. Luxmoore. Stimulated emission depletion spectroscopy of color centers in hexagonal boron nitride. *ACS Photonics*, 8(4):1007–1012, 2021.

[22] Ngoc My Hanh Duong, Evgenii Glushkov, Andrey Chernev, Vytautas Navikas, Jean Comtet, Minh Anh Phan Nguyen, Milos Toth, Aleksandra Radenovic, Toan Trong Tran, and Igor Aharonovich. Facile Production of Hexagonal Boron Nitride Nanoparticles by Cryogenic Exfoliation. *Nano Lett.*, 19(8):5417–5422, 2019.

[23] Mehran Kianinia, Carlo Bradac, Bernd Sontheimer, Fan Wang, Toan Trong Tran, Minh Nguyen, Sejeong Kim, Zai-Quan Xu, Dayong Jin, Andreas W. Schell, Charlene J. Lobo, Igor Aharonovich, and Milos Toth. All-optical control and super-resolution imaging of quantum emitters in layered materials. *Nat. Commun.*, 9(1):874, February 2018.

[24] Jiandong Feng, Hendrik Deschout, Sabina Caneva, Stephan Hofmann, Ivor Lončarić, Predrag Lazić, and Aleksandra Radenovic. Imaging of Optically Active Defects with Nanometer Resolution. *Nano Lett.*, 18(3):1739–1744, 2018.

[25] A. Merlo, V. R.S.S. Mokkapati, S. Pandit, and I. Mijakovic. Boron nitride nanomaterials: Biocompatibility and bio-applications. *Biomater. Sci.*, 6(9):2298–2311, 2018.

[26] Srikanth Mateti, Cynthia S Wong, Zhen Liu, Wenrong Yang, Yuncang Li, Lu Hua Li, and Ying Chen. Biocompatibility of boron nitride nanosheets. *Nano Res.*, 11(1):334–342, 2018.

[27] Melis Emanet, Özlem Sen, Irem Çulha Taşkin, and Mustafa Çulha. Synthesis, functionalization, and bioapplications of two-dimensional boron nitride nanomaterials. *Front. Bioeng. Biotechnol.*, 7:363, 2019.

[28] Tun Lu, Libo Wang, Ye Jiang, Qiuwen liu, and Caijin Huang. Hexagonal boron nitride nanoplates as emerging biological nanovectors and their potential applications in biomedicine. *J. Mater. Chem. B*, 4:6103–6110, 2016.

[29] Magdalena Jedrzejczak-Silicka, Martyna Trukawka, Mateusz Dudziak, Katarzyna Piotrowska, and Ewa Mijowska. Hexagonal boron nitride functionalized with au nanoparticles—properties and potential biological applications. *Nanomaterials*, 8(8), 2018.

[30] Xiangzhi Li, Gabriella D. Shepard, Andrew Cupo, Nicolas Camporeale, Kamran Shayan, Yue Luo, Vincent Meunier, and Stefan Strauf. Nonmagnetic quantum emitters in boron nitride with ultranarrow and sideband-free emission spectra. *ACS Nano*, 11(7):6652–6660, 2017. PMID: 28521091.

[31] Romain Bourrellier, Sophie Meuret, Anna Tararan, Odile Stéphan, Mathieu Kociak, Luiz H. G. Tizei, and Alberto Zobelli. Bright uv single photon emission at point defects in h-bn. *Nano Lett.*, 16(7):4317–4321, 2016. PMID: 27299915.

[32] Toan Trong Tran, Christopher Elbadawi, Daniel Totonjian, Charlene J. Lobo, Gabriele Grosso, Hyowon Moon, Dirk R. Englund, Michael J. Ford, Igor Aharonovich, and Milos Toth. Robust multicolor single photon emission from point defects in hexagonal boron nitride. *ACS Nano*, 10(8):7331–7338, 2016.

[33] Robin Camphausen, Loris Marini, Sherif Abdulkader Tawfik, Toan Trong Tran, Michael J. Ford, and Stefano Palomba. Observation of near-infrared sub-poissonian photon emission in hexagonal boron nitride at room temperature. *APL Photonics*, 5(7):076103, 2020.

[34] T. Q.P. Vuong, G. Cassabois, P. Valvin, A. Ouerghi, Y. Chassagneux, C. Voisin, and B. Gil. Phonon-Photon Mapping in a Color Center in Hexagonal Boron Nitride-supplementary. *Phys. Rev. Lett.*, 117(9):3–5, 2016.

[35] Kumarasiri Konthasinghe, Chitraleema Chakraborty, Nikhil Mathur, Liangyu Qiu, Arunabh Mukherjee, Gregory D. Fuchs, and A. Nick Vamivakas. Rabi oscillations and resonance fluorescence from a single hexagonal boron nitride quantum emitter. *Optica*, 6(5):542, 2019.

[36] S.N. Khonina, V.V. Kotlyar, M.V. Shinkaryev, V.A. Soifer, and G.V. Uspleniev. The phase rotor filter. *J. Mod. Opt.*, 39(5):1147–1154, 1992.

[37] Yanghui Li, Hui Zhou, Xiaoyu Liu, Yuxue Li, and Le Wang. Effects of aberrations on effective point spread function in sted microscopy. *Appl. Opt.*, 57(15):4164–4170, May 2018.

[38] Jacopo Antonello, Daniel Burke, and Martin J. Booth. Aberrations in stimulated emission depletion (sted) microscopy. *Opt. Commun.*, 404:203–209, 2017. Super-resolution Techniques.

[39] Prince Khatri, Andrew J. Ramsay, Ralph Nicholas Edward Malein, Harold M. H. Chong, and Isaac J. Luxmoore. Optical gating of photoluminescence from color centers in hexagonal boron nitride. *Nano Lett.*, 20(6):4256–4263, 2020. PMID: 32383892.

[40] Gary Wolfowicz, Christopher P. Anderson, Andrew L. Yeats, Samuel J. Whiteley, Jens Niklas, Oleg G. Poluektov, F. Joseph Heremans, and David D. Awschalom. Optical charge state control of spin defects in 4h-SiC. *Nat. Commun.*, 8(1):1876, November 2017.

[41] Disheng Chen, Zhao Mu, Yu Zhou, Johannes E. Fröch, Abdullah Rasmit, Carole Diederichs, Nikolay Zheludev, Igor Aharonovich, and Wei-bo Gao. Optical gating of resonance fluorescence from a single germanium vacancy color center in diamond. *Phys. Rev. Lett.*, 123:033602, Jul 2019.

[42] D. A. Golter and C. W. Lai. Optical switching of defect charge states in 4h-sic. *Sci. Rep*, 7(1):13406, Oct 2017.

[43] Simon J.U. White, Ngoc My Hanh Duong, Alexander S. Solntsev, Je-Hyung Kim, Mehran Kianinia, and Igor Aharonovich. Optical repumping of resonantly excited quantum emitters in hexagonal boron nitride. *Phys. Rev. Appl.*, 14:044017, Oct 2020.

[44] Brian Shevitski, S. Matt Gilbert, Christopher T. Chen, Christoph Kastl, Edward S. Barnard, Ed Wong, D. Frank Ogletree, Kenji Watanabe, Takashi Taniguchi, Alex Zettl, and Shaul Aloni. Blue-light-emitting color centers in high-quality hexagonal boron nitride. *Phys. Rev. B*, 100(15):155419, 2019.

[45] Noah Mendelson, Dipankar Chugh, Jeffrey R. Reimers, Tin S. Cheng, Andreas Gottscholl, Hu Long, Christopher J. Mellor, Alex Zettl, Vladimir Dyakonov, Peter H. Beton, Sergei V. Novikov, Chennupati Jagadish, Hark Hoe Tan, Michael J. Ford, Milos Toth, Carlo Bradac, and Igor Aharonovich. Identifying carbon as the source of visible single-photon emission from hexagonal boron nitride. *Nat. Mater.*, 20(3):321–328, November 2020.

[46] Dominik Wildanger, Jeronimo R. Maze, and Stefan W. Hell. Diffraction unlimited all-optical recording of electron spin resonances. *Phys. Rev. Lett.*, 107:017601, Jul 2011.

[47] Andreas Gottscholl, Mehran Kianinia, Victor Soltamov, Sergei Orlinskii, Georgy Mamin, Carlo Bradac, Christian Kasper, Klaus Krambrock, Andreas Sperlich, Milos Toth, Igor Aharonovich, and Vladimir Dyakonov. Initialization and read-out of intrinsic spin defects in a van der Waals crystal at room temperature. *Nat. Mater.*, 19(5):540–545, 2020.

[48] Nathan Chejanovsky, Amlan Mukherjee, Jianpei Geng, Yu-Chen Chen, Youngwook Kim, Andrej Denisenko, Amit Finkler, Takashi Taniguchi, Kenji Watanabe, Durga Bhaktavatsala Rao Dasari, Philipp Auburger, Adam Gali, Jurgen H. Smet, and Jörg Wrachtrup. Single-spin resonance in a van der waals embedded paramagnetic defect. *Nat. Mater.*, May 2021.

[49] Giulia Petrini, Ekaterina Moreva, Ettore Bernardi, Paolo Traina, Giulia Tomagra, Valentina Carabelli, Ivo Pietro Degiovanni, and Marco Genovese. Is a quantum biosensing revolution approaching? perspectives in nv-assisted current and thermal biosensing in living cells. *Adv. Quantum Technol.*, 3(12):2000066, 2020.

Chapter 8

Conclusion and Future Work

8.1 Conclusions

This thesis has presented a detailed study of the photophysical properties of hBN emitters, from analysing the phonon interaction to demonstrating practical applications in high resolution imaging. The results provided here widens the understanding of hBN as a future 2D material for applications in nanophotonics. An open question in the field of hBN emitters is the identity of the defects. Answering this question can be very rewarding for the wider research community. However, it is not very easy and require an extensive research because hBN emitters show a wide range of ZPL energies and spectrum profiles. Since we started working on this topic, from 2018, we believe that we have made a significant progress towards the answer. We have used PLE and STED techniques to comment on the defect identity while comparing our experimental observations with DFT studies to support the argument with theory.

We made progress on understanding the photophysical processes in the hBN emitter like switching of the defect between dark and bright states which tackles the problem of stability. The engineering steps such as Purcell enhancement and cavity coupling, required to improve the emission quality, rely on the understanding of the phonon interactions with the emitter. We have provided a detailed model for qualitative analysis of phonon coupling mechanisms and the necessary parameters. Furthermore, we have demonstrated a high resolution STED microscopy technique which can resolve two emitters separated by a distance smaller than the diffraction limit. This demonstration can open doors for hBN in the field of bio-imaging.

The chapter-wise conclusion are:

In Chapter 3, we have analyzed the phonon sidebands of two different hBN emitters using an independent boson model. Some striking features about acoustic phonon coupling have

been identified. It can be described by deformation coupling to an effective two-dimensional phonon-bath with exponential form-factor and for phonon energies larger than 10 meV, the acoustic phonon dispersion is degenerate with respect to out-of-plane momentum. The intrinsic sub-Lorentzian broadening of the ZPL limits the achievable photon indistinguishability. The identification of the order of the electron-phonon spectral density is important to determine properties, such as the power laws and ZPL broadening. The 200 meV optical phonon peak can be attributed to Fröhlich coupling to an $LO(E_{1u})$-phonon band where neighboring layers vibrate in anti-phase to each other giving a signature of a multi-layer flake with $\mathcal{N} > 3$. The TO-electron coupling is effectively two-dimensional and can be described by a deformation coupling proportional to in-plane lattice displacement.

In Chapter 4 we presented controllable optical switching between bright and dark states of colour centres emitting around 2 eV. Resonant, or quasi-resonant, excitation of photoluminescence also pumps the colour centre, via a two-photon process, into a dark state, where it becomes trapped. Repumping back into the bright state has a step-like spectrum with a defect-dependent threshold between 2.25 and 2.6 eV. This photocharging mechanism is supported with a multilevel model to understand the experimental observations in time trace and $g^2(\tau)$ data. Furthermore, a second zero phonon line, detuned by +0.4 eV, is observed in absorption with orthogonal polarization to the emission, evidencing an additional energy level in the colour centre.

Chapter 5 shows how STED can probe the vibronic states of the ground state without the interference from neighbouring emitters. The 200 meV optical phonon peak from Fröhlich coupling to an $LO(E_{1u})$-phonon band shows a shift of ~ 3.7 meV for all the emitters emitting around 2.2 meV. This signifies a lattice distortion of 2.6 % when the emitter goes from the ground to excited state. On comparing with latest DFT calculations, the energy transitions agree with that of $V_B C_N^-$ defect.

In Chapter 6, we demonstrated STED microscopy with colour centres in nanoscale flakes of hBN using time-gated CW STED technique. For colour centres with zero phonon line emission around 580 nm we measure a STED cross section of $(5.5 \pm 3.2) \times 10^{-17}$ cm^2, achieve a resolution of ~ 50 nm with power density of 13 MW/cm^2. Compared to commonly used organic dye molecules which suffer from photobleaching due to irreversible chemical reaction, our resolution is ~ 2.5 times larger with similar STED cross section and power density. We were able to resolve two colour centres separated by 250 nm, which is less than the diffraction limit. The achieved resolution is limited by the numerical aperture of the objective lens (0.8) and the available laser power, and we predict that a resolution of sub-10

nm can be achieved with an oil immersion objective lens, similar to state-of-the-art resolution obtained with nitrogen vacancy centres in diamond.

8.2 Future Work

The origin of the hBN emitter should be addressed with more research which support experimental observation along with theoretical modelling. Recently, ODMR has been used to demonstrate that V_B^- defects in hBN are promising candidates for spin based quantum computing [1] and temperature, pressure and magnetic field quantum sensors [2]. An important step could be exploring the ODMR technique to study the energy levels in other optically active defects in hBN and examine the magnetic field dependence, energy level structure and photocharging mechanisms for better estimation of emitter identity.

A rewarding route for further developing the quantum computing front could be controlling the spin state of the emitters electronically which improves the scalability of 2D, spin based quantum information processors. This has been recently demonstrated for NV centres in diamond [3]. An intermediate step can be controlling spin electronically and optical readout of the spin state.

Another aspect of interest to be further explored is creating desired defects via ion implantation or electron beam technique. Recently, Some progress has been made in this front by Mendelson *et al.* [4] with ion implanted carbon defects. To provide a flexible choice of emitters, techniques should be developed to create optically active impurity/lattice defects on demand. The sample we used for the experiments presented in this thesis, consist of emitters with variety of emission wavelengths, intensities and linewidths. It would be interesting to create specific optically active defects at a chosen location in a very pure hBN flake and study them without any interference from nearby charged species or traps.

So far, hBN emitters are optically excited and it would be much more advantageous, in terms of ease in integration with optical devices, to use electrical excitation, like in case of QDs [5]. Optical excitation requires complicated and expensive laser setups which strictly limit hBN to lab use. Whereas, electric excitation is inexpensive and tuning excitation energy can be as simple as changing the voltage. This is a challenging task because hBN is a wide bandgap semiconductor and difficulties in doping hinders electron and hole injection [6]. Some progress has been made in electroluminescence from h-BN by using Al_2O_3/h-BN multiple heterostructure [7] but so far electrically driven quality single photon emission has not been reported. However, it should be noted that a detailed understanding of hBN emitter's

energy level structure with respect to conduction and valance band is important, linking this problem again with the question of emitter identity.

Finally, a major interest in hBN quantum emitters is for QKD application, however, no progress towards a practical demonstration has been made. An effort, specifically targeted toward making room temperature chip scale hBN QKD system can be another aspect of exploiting the commercial applicability of this material [8].

References

[1] Andreas Gottscholl, Mehran Kianinia, Victor Soltamov, Sergei Orlinskii, Georgy Mamin, Carlo Bradac, Christian Kasper, Klaus Krambrock, Andreas Sperlich, Milos Toth, Igor Aharonovich, and Vladimir Dyakonov. Initialization and read-out of intrinsic spin defects in a van der waals crystal at room temperature. *Nature Materials*, 19(5):540–545, February 2020.

[2] Andreas Gottscholl, Matthias Diez, Victor Soltamov, Christian Kasper, Andreas Sperlich, Mehran Kianinia, Carlo Bradac, Igor Aharonovich, and Vladimir Dyakonov. Room temperature coherent control of spin defects in hexagonal boron nitride. *Science Advances*, 7(14):eabf3630, April 2021.

[3] Michal Gulka, Daniel Wirtitsch, Viktor Ivády, Jelle Vodnik, Jaroslav Hruby, Goele Magchiels, Emilie Bourgeois, Adam Gali, Michael Trupke, and Milos Nesladek. Room-temperature control and electrical readout of individual nitrogen-vacancy nuclear spins. *Nature Communications*, 12(1), July 2021.

[4] Noah Mendelson, Dipankar Chugh, Jeffrey R. Reimers, Tin S. Cheng, Andreas Gottscholl, Hu Long, Christopher J. Mellor, Alex Zettl, Vladimir Dyakonov, Peter H. Beton, Sergei V. Novikov, Chennupati Jagadish, Hark Hoe Tan, Michael J. Ford, Milos Toth, Carlo Bradac, and Igor Aharonovich. Identifying carbon as the source of visible single-photon emission from hexagonal boron nitride. *Nature Materials*, 20(3):321–328, November 2020.

[5] C. Bentham, D. Hallett, N. Prtljaga, B. Royall, D. Vaitiekus, R. J. Coles, E. Clarke, A. M. Fox, M. S. Skolnick, I. E. Itskevich, and L. R. Wilson. Single-photon electroluminescence for on-chip quantum networks. *Applied Physics Letters*, 109(16):161101, October 2016.

[6] Menno Bokdam, Geert Brocks, M. I. Katsnelson, and Paul J. Kelly. Schottky barriers at hexagonal boron nitride/metal interfaces: A first-principles study. *Physical Review B*, 90(8), August 2014.

[7] Seung Hee Lee, Hokyeong Jeong, Dong Yeong Kim, Seung-Young Seo, Cheolhee Han, Odongo Francis Ngome Okello, Jen-Iu Lo, Yu-Chain Peng, Chan-Hyoung Oh, Gyeong Won Lee, Jong-In Shim, Bing-Ming Cheng, Kyung Song, Si-Yong Choi, Moon-Ho Jo, and Jong Kyu Kim. Electroluminescence from h-BN by using al2o3/h-BN multiple heterostructure. *Optics Express*, 27(14):19692, June 2019.

[8] Akbar Basha Dhu al-jalali-wal-ikram Shaik and Penchalaiah Palla. Optical quantum technologies with hexagonal boron nitride single photon sources. *Scientific Reports*, 11(1), June 2021.